
ON
THE MISSING DWARF PROBLEM
IN
CLUSTERS
AND
AROUND THE NEARBY GALAXY M33

by

Olivia Keenan

A THESIS SUBMITTED TO CARDIFF UNIVERSITY
FOR THE DEGREE OF DOCTOR OF PHILOSOPHY

MARCH 2017

Author: Olivia Keenan

Title: On
the Missing Dwarf Problem
in
Clusters
and
Around the Nearby Galaxy M33

Date of submission: March 2017

Permission is granted to Cardiff University to circulate and to have copied for non-commercial purposes, at its discretion, the above title upon the request of individuals or institutions. The author reserves other publication rights, and neither the thesis nor extensive extracts from it may be printed or otherwise reproduced without the author's written permission.

Copyright © 2017 by Olivia Keenan

'Opta ardua pennis astra sequi'

VIRGIL

DEDICATION

*'You've got a friend in me
You've got a friend in me
When the road looks rough ahead
And you're miles and miles
From your nice warm bed
You just remember what your old pal said
Boy, you've got a friend in me
Yeah, you've got a friend in me '*

TOY STORY

I owe a great deal of thanks to the inspiring and supportive people I've had the pleasure of working with during my time at Cardiff. In particular, I'd like to thank my AGES collaborators Rhys Taylor and Robert Minchin. They have both been amazingly supportive, have gone above and beyond what anyone could have asked of collaborators, and have become very good friends. Our weekly AGES hangouts were both productive, and hugely enjoyable - sometimes causing me to laugh so hard I cried (greatly to the annoyance of my office mates!). We've made many great plans together, including a proposal of a marriage of convenience (in order to have an excuse at attend someone else's wedding), writing a gossip magazine in LaTeX, and reintroducing roundhouses (with a central wifi hub, naturally). Thanks for everything both, and stay in touch!

I'd like to thank my viva examiners, Haley Gomez and Sugata Kaviraj. They made my viva experience not only bearable, but actually enjoyable at points. They

have also provided my with a set of comments which I believe have greatly improved this Thesis. In addition I'd like to thank my viva chair, Ant Whitworth, who facilitated my eating of a KitKat when I was in dire need, and generally helped me feel calm and at ease.

I'd also like to thank the members of the Galaxies group for being my friends and office mates over the last three and a half years. Due to a huge PhD hiring push in the last few years the group has grown enormously in so I won't include the names of everyone here (*read: I'm terrified of forgetting someone!). However, I'd like to highlight Matt, Mat, Chris and Simon with whom I've shared an office through the entirety of my PhD (well, almost), and I've had some great times. I'll greatly miss office golf (What? We don't do that!), kittencam, putting up the Christmas decorations, the 'Olivia is stupid' bell (cough, Chris...), harry potter quizzing, sporcle sessions, special tea and much much more. I'd also like to wish my protégé Dan Prole the best of luck in living up to the stupendous precedent set by myself(!) - stay cool bro. Please stay in touch everyone, and let me know if you're ever in Lannndaaan (elbows).

I've had a great time in Cardiff, and that was largely due to the fantastic people there. I've made some great friends and had some amazing experiences. Again, there are too many people to name here but I want to thank everyone for making my time in Cardiff so amazing. I'll hugely miss twice daily coffee breaks, postgrad lunches and Friday night (well, any night... or day...) pub trips (RIP poets!). Hopefully I'll find plenty of opportunities to pop back to the department and see everyone!

I'm extremely grateful to have an extremely supportive family who have been there the whole way through my PhD journey. I owe my Mum, Dad and George immense gratitude for being there and putting up with me! My mother has often asked me sharp and probing questions to test my astrophysical knowledge, such as 'Why isn't Pluto a star anymore?', which I'm sure greatly helped my prepare for the viva experience. I can't wait to share my graduation with them and celebrate properly (in fantastic robes and a big, floppy hat). I'd also like to thank my Gramma, Kay and John for always being there for me, and taking part in many entertaining family 'debates'. I love my mildly insane family, and am so lucky to have grown up with them all around me.

Cardiff has been extra special to me because it is where I met my partner, Andrew. I could never put in to words how much thanks I owe Andrew for everything he does. He has constantly supported and believed in me, especially when I haven't believed in myself. He is not only my partner but my best friend, and I'm so glad we got to share our PhD experience. We've had our first home in Cardiff and its been a very happy one (apart from when you get angry at me because of my incapability to do the washing up..), and I can't wait to have many many more. I look forward to us sharing our lives and supporting each other over the coming years. I love you so much. Thank you.

There's one more being I need to thank here, and that's Hathor the cat. Hathor adopted us and moved into our house last year. She provided entertainment, laughter and love and we were distraught when she left. Whether or not we technically owned her, she'll always be my and Andrew's first pet.

Hwyl fawr Caerdydd, diolch yn fawr.

Lastly, I just want to say to everyone out there who thinks they can't do something: Go for it! You can!

ACKNOWLEDGEMENTS

'Knowledge comes, but wisdom lingers.'

ALFRED LORD TENNYSON

This PhD was made possible due to funding from the Science and Technology Facilities Council.

This thesis has used data from the Arecibo Observatory. The Arecibo Observatory is operated by SRI International under a cooperative agreement with the National Science Foundation (AST-1100968), and in alliance with Ana G. MÁl̄ndez-Universidad Metropolitana, and the Universities Space Research Association.

Funding for the Sloan Digital Sky Survey IV has been provided by the Alfred P. Sloan Foundation, the U.S. Department of Energy Office of Science, and the Participating Institutions. SDSS acknowledges support and resources from the Center for High-Performance Computing at the University of Utah. The SDSS web site is www.sdss.org.

SDSS is managed by the Astrophysical Research Consortium for the Participating Institutions of the SDSS Collaboration including the Brazilian Participation Group, the Carnegie Institution for Science, Carnegie Mellon University, the Chilean Participation Group, the French Participation Group, Harvard-Smithsonian Center for Astrophysics, Instituto de Astrofísica de Canarias, The Johns Hopkins University, Kavli Institute for the Physics and Mathematics of the Universe (IPMU) / University of Tokyo, Lawrence Berkeley National Laboratory,

Leibniz Institut für Astrophysik Potsdam (AIP), Max-Planck-Institut für Astronomie (MPIA Heidelberg), Max-Planck-Institut für Astrophysik (MPA Garching), Max-Planck-Institut für Extraterrestrische Physik (MPE), National Astronomical Observatories of China, New Mexico State University, New York University, University of Notre Dame, Observatório Nacional / MCTI, The Ohio State University, Pennsylvania State University, Shanghai Astronomical Observatory, United Kingdom Participation Group, Universidad Nacional Autónoma de México, University of Arizona, University of Colorado Boulder, University of Oxford, University of Portsmouth, University of Utah, University of Virginia, University of Washington, University of Wisconsin, Vanderbilt University, and Yale University.

Parts of this thesis are based on observations obtained with MegaPrime/MegaCam, a joint project of CFHT and CEA/DAPNIA, at the Canada-France-Hawaii Telescope (CFHT) which is operated by the National Research Council (NRC) of Canada, the Institut National des Science de l'Univers of the Centre National de la Recherche Scientifique (CNRS) of France, and the University of Hawaii.

This research made use of Astropy, a community-developed core Python package for Astronomy (Astropy Collaboration et al. 2013).

This research has made use of the NASA/IPAC Extragalactic Database (NED) which is operated by the Jet Propulsion Laboratory, California Institute of Technology, under contract with the National Aeronautics and Space Administration.

This research has made use of the SIMBAD database, operated at CDS, Strasbourg, France.

This research has made use of NASA's Astrophysics Data System Bibliographic Services.

This research has made use of NASA's Astrophysics Data System.

This research has made use of the Miriad data reduction package (Sault et al. 1995a).

This research made use of Montage. It is funded by the National Science Foundation under Grant Number ACI-1440620, and was previously funded by the National Aeronautics and Space Administration's Earth Science Technology

Office, Computation Technologies Project, under Cooperative Agreement Number NCC5-626 between NASA and the California Institute of Technology.

This work includes material reproduced under the terms of the Creative Commons Attribution ShareAlike 3.0 Unported license¹.

¹ <http://creativecommons.org/licenses/by-sa/3.0/deed.en>

PRINCESS OLIVIA AND THE MAGICAL MOOSE

This story has been reproduced from the FRELLED manual by kind permission of Rhys Taylor.

Once upon a time, the fair Princess Olivia was bored and decided to look in her magic mirror.. "Mirror, mirror, on the wall," said the Princess, "who has the best HI data of them all ?"

"You, O Princess", said the mirror, "but it would be even better if you looked at it with FRELLED."

The Princess decided that this was a good idea and would go to the library to learn all about it. It was a long way to walk, but luckily a magical moose appeared from nowhere. That's what magical mooses do.

"Climb aboard !" said the moose, "I'll take you to the library in no time at all."

The moose ran to the library at an amazing speed. "Thanks, moose !" said the Princess, "I don't suppose you know where I could find out about FRELLED ?"

"Why yes," said the moose, "for I am a magical moose." The moose and the Princess sat down in front of one of the library's many computers.

"First," said the moose, "you should decide whether you want the data to be in 3D or 2D, and push the little blue button accordingly."

The Princess sighed a disdainful sigh. "You can't be a very magical moose," she said. "Why would I want to look at data in 2D ? I am a Princess, you know !"

"Ah, quite," said the moose, who magically blushed and shuffled his feet in an embarrassed manner. "How silly of me. Anyway, next you should press the '99'

button".²

"Why ?" asked Princess Olivia.

"This will work out how much of the data should be transparent," said the moose, "and then automatically set the appropriate data value in the 'maximum data value' box. '99' means that 99% of the data will be transparent, which usually looks quite nice."

"How very convenient," declared Princess Olivia in a regal manner. "Anything else ?"

"Yes," said the moose, "You must choose which projections to export. Let's try just the XY projection for now, it will be faster. Then you need to press the 'Map 1' button in the top part of the panel."

The Princess did as she was bid, and gasped.

"Gasp !" said Princess Olivia, "I see that something else happened when I pressed map 1 !"

"Yes," said the magical moose, "The top part controls how the data is converted, but it also sets defaults for how to display the data. That's what the buttons at the bottom are for."

The Princess was delighted that her regal fingers would be saved from the excessive manual labour of pressing more buttons than were absolutely necessary. "I suppose you are quite a magical moose, after all," she said, grudgingly. "What's next, moose ?"

"All you have to do now is press 'Go' !" said the magical moose.

"Alright," said the Princess, "but will this take long ? I have to go and fight off an invading horde of goblins this afternoon."³

"Not at all !" said the moose, proudly, "The code is parallelised. It shouldn't take more than a couple of minutes." And indeed, in almost no time at all, the Princess marvelled to see a wonderful three-dimensional image appear on the screen. "Wow !" she exclaimed, "This is better than Avatar ! Especially since it doesn't have any 9ft tall smurfs. But what about all these other buttons ?"

"There isn't any time to explain. This is only a quick start guide," said the moose, magically breaking the fourth wall. But he tipped his head and something white and fluttery fell from his antlers. "Try reading this manual. That should answer

² The moose had the magical ability to pronounce quotation marks.

³ Princess Olivia was a warrior princess.

all your questions."

Princess Olivia thought about this and adjusted her tiara in a haughty fashion. She wasn't sure that Princesses were allowed to read manuals. Perhaps she could find a servant to read it for her.

"Oh, alright," she said. "Goodbye moose!"

The moose magically disappeared. Later on, Princess Olivia decided that fighting the goblins was too much effort. Instead she decided to teach them all about FRELLED. And they all analysed HI data ever after.

THE END.

PUBLICATIONS

'I am sick to death of cleverness. Everybody is clever nowadays.'

OSCAR WILDE, THE IMPORTANCE OF
BEING EARNEST

FIRST AUTHOR

Keenan O. C., Davies J. I., Taylor R. and Minchin R. F. 2016, *The Arecibo Galaxy Environment Survey - X. The structure of halo gas around M33*, MNRAS, 456, 951

Keenan. Olivia, Davies., Jonathan., Taylor. Rhys., and Minchin. Robert. 2016, *The Structure of Halo Gas Around M33*, published in Proceedings of the IAU Symposium No. 321, 2016, Formation and Evolution of Galaxy Outskirts, eds. Gil de Paz A., Knapen J. and Lee J.

CO-AUTHOR

Taylor R., Davies J. I., Jáchym P., Keenan O., Minchin R. F., Palouš J., Smith R. and Wünsch, R. 2017, *Kinematic clues to the origins of starless HI clouds : dark galaxies or tidal debris?*, MNRAS, 467, 3648

Davies J. I., Davies L. J. M. and Keenan O. C. 2016, *Probing the low surface brightness dwarf galaxy population of the virgo cluster*, MNRAS, 456, 1607

Minchin R. F., Auld R., Davies J. I., Karachentsev I. D., Keenan O. C., Momjian E., Rodriguez R., Taber T., and Taylor R. 2016, *The Arecibo Galaxy Environment Survey IX: the isolated galaxy sample*, MNRAS, 455, 3430

Taylor R., Davies J. I., Jáchym P., Keenan O., Minchin R. F., Palouš J., Smith R. and Wünsch, R. 2016, *Attack of the flying snakes: formation of isolated H I clouds by fragmentation of long streams*, MNRAS, 461, 3001

ABSTRACT

'Brief let me be.'

WILLIAM SHAKESPEARE, HAMLET

This thesis explores possible solutions to the dwarf galaxy problem. This is a discrepancy between the number of dwarf galaxies we observe, and the number predicted from cosmological computer simulations. Simulations predict around ten times more dwarf galaxy satellites than are currently observed. I have investigated two possible solutions: dark galaxies and the low surface brightness universe.

Dark galaxies are dark matter halos which contain gas, but few or no stars, hence are optically dark. As part of the Arecibo Galaxy Environment Survey I surveyed the neutral hydrogen gas around the nearby galaxy M33. I found 32 gas clouds, 11 of which are new detections. Amongst these there was one particularly interesting cloud. AGESM33-32 is ring shaped and larger than M33 itself, if at the same distance. It has a velocity width which is similar to the velocity dispersion of gas in a disk galaxy, as well as having a clear velocity gradient across it which may be due to rotation. The fact that it also currently has no observed associated stars means it is a dark galaxy candidate.

Optically, dwarf galaxies may be out there, but too faint for us to detect. This means that with newer, deeper, images we may be able to unveil a large, low surface brightness, population of dwarf galaxies. However, the question remains as to how these can be distinguished from background galaxies. I have used Next Generation Virgo Survey (NGVS) data to carry out photometry on 852 Virgo galaxies in four bands. I also measured the photometric properties of galaxies on a background (non-cluster) NGVS frame. I discovered that a combination of colour,

magnitude and surface brightness information could be used to identify cluster dwarf galaxies from background field galaxies. The most effective method is to use the surface brightness-magnitude relation.

CONTENTS

Dedication	vii
Acknowledgements	xi
Princess Olivia and the Magical Moose	xv
Publications	xix
Abstract	xxi
List of Tables	xxvii
List of Figures	xxviii
1 Introduction	1
1.1 Island Universes	2
1.2 Galaxy Evolution	3
1.2.1 Hierarchical Structure Formation	4
1.2.2 Cosmic Downsizing	4
1.3 The Galaxy Red Sequence	5
1.4 Λ CDM	7
1.5 Simulations	8
1.6 The Dwarf Galaxy Problem	10
1.7 Proposed Observational Solutions	12
1.7.1 Dark Galaxies	13
1.7.2 Low Surface Brightness Galaxies	17
1.7.3 Dwarf Galaxy Populations	17
1.7.4 The Coma Cluster : Ultra Diffuse Galaxies	18

1.7.5	The Fornax Cluster: Ultra Compact Dwarfs	19
1.7.6	The Virgo Cluster	20
1.8	Summary	21
2	M33	25
2.1	M33 and the surrounding area	25
2.2	The Arecibo Galaxy Environment Survey	28
2.3	M33 Observations and Data Reduction	29
2.4	Source Extraction	32
2.5	Identifying Clouds	36
2.6	Column density maps, velocity maps and spectra of the clouds around M33	37
2.7	The Ring Cloud	56
2.8	A Plane of Clouds	59
2.9	How are the clouds distributed?	59
2.10	Could our clouds be dwarf galaxies?	61
2.11	Summary of M33 work	66
3	Dwarf Galaxies in Clusters	67
3.1	The Cluster Environment	68
3.2	The Virgo Cluster Catalogue	69
3.3	The Extended Virgo Cluster	70
3.4	The Next Generation Virgo Cluster Survey	71
3.5	The Low Surface Brightness Virgo Cluster Catalog	72
3.6	Summary	76
4	Photometry of Virgo Cluster Galaxies	79
4.1	Preparing the Data for Photometry	80
4.1.1	Making Galaxy Cutouts	80
4.1.2	Measuring the Galaxies' Position Angles and Axial Ratios . .	80
4.2	Performing Photometry on a Test Sample	82
4.3	NGVS Photometric Calibration	82
4.3.1	VCC galaxies sample	82
4.3.2	LSBVCC galaxies	83
4.3.3	Removing Stars from the Frames	84

4.4	The Photometry Code	85
4.5	Fixing Problems in the LSB photometry	89
4.6	Perfecting the VCC photometry	95
4.7	Photometric Errors	99
4.8	Serendipitous Discoveries	100
4.8.1	VCC 652's Companion	101
4.9	Photometry Results	102
5	Virgo Cluster Results and Analysis	105
5.0.1	Virgo Cluster Luminosity Function	105
5.1	Comparison with colours of local group dwarfs	107
5.2	Exploring Virgo Cluster Galaxy Properties	109
5.2.1	Colour-Colour plots	109
5.2.2	Colour-Magnitude relation	110
5.2.3	Colour-Surface Brightness plots	114
5.2.4	Surface Brightness - Magnitude relation	116
5.2.5	Surface Brightness - Radius relation	118
5.3	Comparison with background field population	119
5.3.1	Colour-Colour Diagrams	122
5.3.2	Colour-Magnitude Diagrams	124
5.3.3	Surface Brightness	126
5.4	The Virgo Red Sequence	127
5.5	Can we identify dwarfs based on their properties?	133
6	Conclusion	135
6.1	The gas cloud population of M33	136
6.2	AGESM33-31	137
6.2.1	Potential further observations	138
6.3	The LSB population of the Virgo Cluster	138
6.3.1	What did we find?	139
6.3.2	How could this be used in the future?	139
6.4	Comments on how my work could impact the Dwarf Galaxy Problem	140
6.4.1	Dark Galaxies	140
6.4.2	The LSB Universe	141

Bibliography	142
7 Appendix	151
7.1 Photometry Data Tables	151

LIST OF TABLES

2.1	Properties for all M33 ‘isolated’ clouds.	34
2.2	Properties of all M33 clouds which fall within the disk.	35
4.1	Mean and median magnitudes of the VCC sample compared to the SDSS.	82
4.2	The SDSS band calibration uncertainties.	100
4.3	The SDSS magnitudes of the two objects that the companion of VC652 is split into.	102
4.4	Our values for the SDSS-band magnitudes for the companion of VCC652.	102
5.1	Median colours for local dwarfs as well as the Virgo dwarfs.	108
7.1	The VCC number, RA, Dec, magnitudes in the u, g, i and z bands with errors.	153
7.2	The VCC number, all colours and errors on colours.	168
7.3	The VCC number, radius measured at the 28 mag arcsec ⁻² isophote in the g band, mean surface brightnesses within that radius in each band and errors on all surface brightnesses.	184
7.4	The LSBVCC number, RA, Dec, magnitudes in the u, g, i and z bands and errors.	200
7.5	The LSBVCC number, all colours and errors on colours.	206
7.6	The LSBVCC number, radius measured at the 28 mag arcsec ⁻² isophote in the g band, mean surface brightnesses within that radius in each band and errors on all surface brightnesses.	212

LIST OF FIGURES

1.1	The Hubble tuning fork diagram	3
1.2	A galaxy merger tree representing the hierarchical structure formation model.	6
1.3	The red sequence and blue cloud.	7
1.4	The cosmic microwave background.	9
1.5	The Millenium-II simulation.	11
1.6	The Schechter function.	13
1.7	VIRGOHI21	16
1.8	UDGs from van Dokkum et al. (2015a).	20
1.9	UDGs from Koda et al. (2015).	21
1.10	Virgo LSB dwarfs from Davies et al. (2016).	22
2.1	The Arecibo Telescope	29
2.2	Position-Velocity plot of the AGES HI data cube.	31
2.3	Renzogram of M33.	38
2.4	The discrete clouds of M33.	39
2.5	AGESM33-1	40
2.6	AGESM33-2	40
2.7	AGESM33-3	41
2.8	AGESM33-4	42
2.9	AGESM33-5	43
2.10	AGESM33-6	43
2.11	AGESM33-7	44
2.12	AGESM33-8	44
2.13	AGESM33-9	45
2.14	AGESM33-10	45

2.15 AGESM33-11	46
2.16 AGESM33-12	46
2.17 AGESM33-13	47
2.18 AGESM33-14	47
2.19 AGESM33-15	48
2.20 AGESM33-16	48
2.21 AGESM33-17	49
2.22 AGESM33-18	49
2.23 AGESM33-19	50
2.24 AGESM33-20	50
2.25 AGESM33-21	51
2.26 AGESM33-22	51
2.27 AGESM33-23	52
2.28 AGESM33-24	52
2.29 AGESM33-24	53
2.30 AGESM33-25	53
2.31 AGESM33-26	54
2.32 AGESM33-27	54
2.33 AGESM33-28	55
2.34 AGESM33-29	55
2.35 AGESM33-30	56
2.36 AGESM33-31	57
2.37 AGESM33-32	57
2.38 Aplane of clouds in the M33 region.	60
2.39 Plot of the number of clouds in each velocity band.	61
2.40 The mass of our clouds against the mass of LG galaxies.	62
2.41 The velocity width distribution of our clouds plotted against the model distribution.	65
3.1 The position of VCC galaxies.	69
3.2 Positions of EVCC galaxies.	71
3.3 The observing fields of the NGVS.	72
3.4 The coverage in each of the five bands of the NGVS.	73
3.5 The distribution of the magnitudes of Davies et al. (2016) 443 galaxies.	74

3.6	Positions of LSBVCC galaxies compared to the VCC. Number density of Virgo galaxies.	75
3.7	The positions of LSBVCC galaxies compared to EVCC galaxies.	75
3.8	Example LSBVCC galaxies.	77
4.1	Example nebulised background map.	81
4.2	The magnitudes measured for the VCC galaxies against values given by the SDSS.	84
4.3	VCC585	85
4.4	LSBVCC115	86
4.5	LSBVCC428	87
4.6	VCC1876	88
4.7	25 mag arcsec ⁻² isophotal magnitudes for the LSB galaxy sample against those from Davies et al. (2016).	90
4.8	26 mag arcsec ⁻² isophotal magnitudes for the LSB galaxy sample against those from Davies et al. (2016).	91
4.9	27 mag arcsec ⁻² isophotal magnitudes for the LSB galaxy sample against those from Davies et al. (2016).	91
4.10	28 mag arcsec ⁻² isophotal magnitudes for the LSB galaxy sample against those from Davies et al. (2016).	92
4.11	LSBVCC004	93
4.12	Radial surface brightness profiles for LSBVCC galaxies.	94
4.13	28 mag arcsec ⁻² isophotal magnitudes for the LSB galaxy sample against those from Davies et al. (2016).	95
4.14	The VCC magnitudes from Binggeli et al. (1985) plotted against the CFHT g-band magnitudes.	96
4.15	The SDSS data release 9 g-band magnitudes plotted against the CFHT g-band magnitudes.	97
4.16	The VCC magnitudes from Binggeli et al. (1985) plotted against those from the SDSS data release 9.	97
4.17	The VCC magnitudes from Binggeli et al. (1985) plotted against our g band 28 mag arcsec ⁻² isophotal magnitudes.	98
4.18	VCC 652 and it's companion.	101

5.1	A luminosity function for the Virgo galaxies.	107
5.2	Colour-colour diagrams showing all colour combinations of the Virgo photometric data.	111
5.2	Continued. Colour-colour diagrams showing all colour combinations of the Virgo photometric data.	112
5.3	A u-g,g colour-magnitude diagram for the Virgo cluster.	114
5.4	Colour-magnitude diagrams showing all of our Virgo colours against g-band magnitude.	115
5.5	Colours are plotted against the g-band mean surface brightness within the 28th magnitude arcsec ⁻² isophotal radius.	117
5.6	Surface brightness - magnitude plots of all the Virgo galaxies in four bands.	119
5.7	Surface Brightness- radius plot for the VCC and LSBVCC galaxies. .	120
5.8	Colour-colour diagrams showing the cluster dwarf ellipticals and LSBVCC sample, as well as the background field galaxies.	122
5.8	Continued. Colour-colour diagrams showing the cluster dwarf ellipticals and LSBVCC sample, as well as the background field galaxies.	123
5.9	Colour-magnitude diagrams for the Virgo dwarfs and the background field.	125
5.10	Surface Brightness - magnitude plot for the Virgo galaxies and the background field.	127
5.11	Surface Brightness - magnitude plot for the Virgo galaxies and all of the sources in the background field.	128
5.12	The red sequence plots from Roediger et al. (2017).	130
5.13	The red sequence plots using my Virgo photometry data.	131
5.14	The red sequence of the Virgo cluster separated by core and non-core galaxies.	132

CHAPTER 1

INTRODUCTION

'There is a theory which states that if ever anybody discovers exactly what the Universe is for and why it is here, it will instantly disappear and be replaced by something even more bizarre and inexplicable. There is another theory which states that this has already happened.'

DOUGLAS ADAMS

SINCE ancient times mankind has looked up at the sky and pondered its' place in the Universe. From the pyramids of Giza being perfectly aligned with the stars of Orion's belt, to the Mayan civilisation measuring the cycle of Venus with stunning accuracy, it is clear that the heavens have always played a crucial role in civilization. The heliocentric model of the solar system, the idea that the Earth revolves around the Sun, can be traced back to Aristarchus in the third century BC. However, it wasn't until the sixteenth century that a mathematical model of a heliocentric system was produced by Nicolaus Copernicus. This was followed by Johannes Kepler expanding the framework to include elliptical orbits in order to explain observations of the paths of the planets across the sky. These ideas were cemented by Galileo's telescopic observations of the planets and their moons.

It took until the seventeenth century, with William Herschel and Friedrich Bessel, for it to be realised that the Sun was only the centre of the solar system, and there was a greater Universe outside of this. The first observed galaxies were

simply perceived to be nebulous patches on the sky, and this eventually led to the great debate on 'island universes'.

1.1 ISLAND UNIVERSES

By the eighteenth century astronomers had entered 'The Realm of the Nebulae', to borrow Hubble's magnanimous book title (Hubble, 1936). The French Mathematician and Philosopher M. de Maupertius described the nebulae as such (de Maupertius, 1742):

"These are small luminous patches, only slightly more brilliant than the dark background of the sky; they have this in common, that their shapes are more or less open ellipses; and their light is far more feeble than that of any other objects to be perceived in the heavens."

It was noted that one possible explanation for these Nebulae was that they were not single stars, instead they were systems of many stars which, due to their distance, could not be resolved into separate stars and so resembled faint patches of light in the sky. Hence, the theory was proposed that these groups of stars did not reside within our own 'stellar system' (the Milky Way) but were further out in space. This became known as the theory of 'Island Universes', however it existed solely in the realms of philosophical speculation until the late nineteenth century. At this point the cumulation of observational data brought the problem of the Nebulae to the forefront of astronomy and the theory of island universes was one possible solution.

The Curtis-Shapley debate brought the issue to a head in 1920. Shapley believed that the Nebulae were part of the Milky Way. The crux of his argument rested upon the fact that if the Andromeda galaxy wasn't a part of the Milky Way then its distance would be of the order of 10^7 light years (around 3Mpc), which at the time seemed laughable to many astronomers (Shapley and Curtis. 1921). Curtis, on the other hand, argued for the island universes interpretation. His main evidence were the fact that Andromeda had more Novae than the Milky Way, dark lanes in other galaxies resembling the dust clouds in the Milky Way and the Doppler shifts of light from other galaxies.

A resolution to this debate was at least partially reached in the mid-1920s. The astronomer Edwin Hubble observed Cepheid variable stars in the Andromeda galaxy. Cepheid variable stars were discovered by Henrietta Swan Leavitt when studying variable stars in the Magellanic clouds. She found that these pulsating

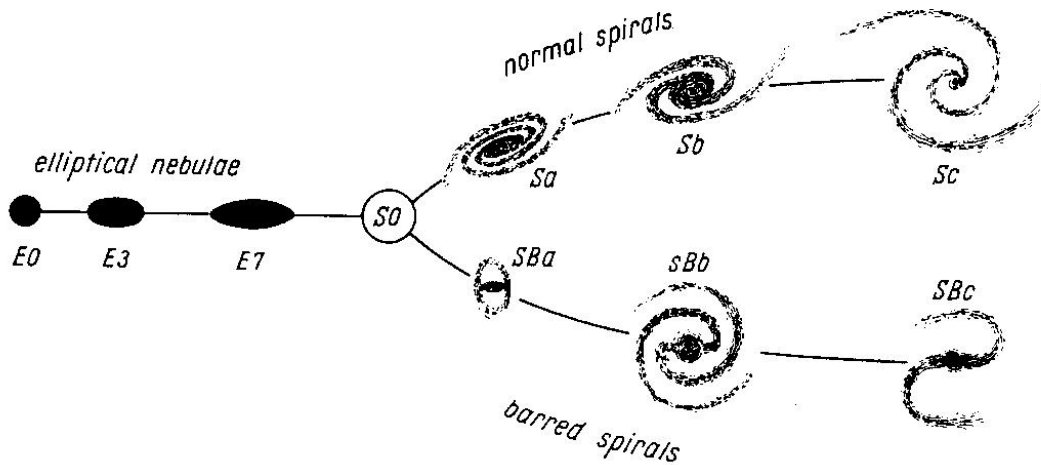


FIGURE 1.1 The Hubble tuning fork diagram, Sandage (1975). Elliptical galaxies appear to the left of the diagram, with a number to denote their ellipticity (0 is perfectly circular and 9 is extremely elongated). The diagram then splits into barred (SB) and non-barred (S) spirals, with the small letters denoting flocculence (a is the least flocculent, c is the most).

stars have a well defined relationship between their luminosity and pulsation period; this means they can be used as distance estimators. Using this technique Hubble measured Andromeda to be 1.5 million light years away, therefore placing it far outside the confines of the Milky Way.

1.2 GALAXY EVOLUTION

At the same time that this debate raged, astronomers noticed that the nebulous objects had a range of varying morphologies. The Hubble sequence is a system for morphological classification of galaxies invented by Hubble in 1926. He divided galaxies into three main classes based on their physical appearance: spiral galaxies, elliptical galaxies and lenticular (or S0) galaxies. It was thought that elliptical galaxies were 'early type', and these moved through the lenticular phase to become spirals or 'late type' galaxies, as can be seen in fig 1.1. Ellipticals are denoted by the letter 'E', followed by a number which is indicative of ellipticity (0 is entirely spherical and 9 is the most elongated). Spiral galaxies are split into two classes : barred and non-barred spirals, labelled 'S' and 'SB'. These labels are followed by a lower case letter denoting how tightly wound the spiral arms are, 'a' is for the most tightly wound and 'c' is for the most flocculent.

We now know that the majority of galaxies are actually dwarf galaxies.

These were not known about in Hubble's time and do not appear in his classification system. Most dwarfs are dwarf ellipticals, having similar properties to elliptical galaxies. However, dwarf irregular galaxies and dwarf spirals also exist. These dwarf galaxies are crucial to this thesis, and will be discussed in much more detail later.

1.2.1 HIERARCHICAL STRUCTURE FORMATION

The belief that ellipticals form first and evolve into spirals was later called into question. In 1962 Olin Eggen, Donald Lynden-Bell and Allan Sandage (Eggen et al. 1962) proposed that disk galaxies formed from the monolithic collapse of a gas cloud: the cloud would collapse and settle into a rapidly rotating disk. This was known as the 'top-down' formation scenario. However, it would later give way to a 'bottom-up' formation model. This is where small things form first and merge to make bigger things. This 'bottom-up' formation method, also known as hierarchical structure formation, was first suggested by Leonard Searle and Robert Zinn (Searle & Zinn 1978). They looked at metallicities of globular clusters at the outskirts of the halo of the Milky way and discovered that they could not have formed in-situ. The result of this is the theory that larger galactic halos are built up from many smaller ones (e.g. Lacey & Cole 1993), this can be represented by the merger tree diagram shown in fig 1.2. Under the hierarchical structure formation model the early and late type galaxies appear to be the wrong way round: spirals would merge to make ellipticals.

Ellipticals can therefore be seen as having resulted from mergers of spiral galaxies: their stars are randomly distributed and don't sit in disk like planes and they have little gas or ongoing star formation. This has led them to be thought of as 'old, red and dead', as due to their lack of continued star formation, they have no young blue stars and appear red in colour.

1.2.2 COSMIC DOWNSIZING

Cosmic downsizing provides an explanation for this colour bi-modality in galaxy populations. Larger galaxies have older stellar populations due to active galactic nuclei (AGNs) having evacuated large proportions of these galaxies' gas reservoirs, hence quenching their star formation relatively early. However, smaller galaxies do not have AGNs and so hold on to their cold gas, needed for star formation. Downsizing is the migration of star forming activity over cosmic time from

larger to smaller halos due to the AGN activity (e.g. Neistein et al. 2006, Juneau et al. 2005). From a downsizing point of view the stars in higher mass galaxies on the red sequence appear redder because they are older, whereas dwarf galaxies would be less red because they have formed more recently. There is no conflict between downsizing and the Λ CDM model (see below) as massive galaxies do continue to accrete smaller companions, but they do not contain enough gas to alter the stellar populations of the ellipticals. Boselli et al. (2001) state that dwarf galaxies do have large gas reservoirs per unit mass, when compared to massive spirals. There have been many studies which have claimed to have observed direct evidence for downsizing. Kriek et al. (2007) have used emission lines to study the evolution of stellar populations in AGN host galaxies, and Rigby et al. (2011) use simulations to investigate the radio luminosity function; they state that their results provide clear evidence for downsizing in the radio-AGN population. However, Boselli et al. (2008) state that, when trying to reproduce galaxy properties observed in the Virgo cluster using a starvation scenario which includes downsizing, they do not reproduce the observed H_I deficient population. Additionally Smith et al. (2009) state that the core of the Coma cluster does not exhibit the effects of downsizing.

There have been some recent observations of massive objects at high redshift. Fu et al. (2013) have discovered an elliptical galaxy with a mass of $4 \times 10^{11} M_{\odot}$ at a redshift of 2.3. It has a gas-to baryon fraction which is far higher than the mean for galaxies with masses of $10^{11} M_{\odot}$ at $z \sim 2$. Fu et al. (2013) state that gas rich major mergers at high redshift can form the most massive galaxies observed by $z \sim 1.5$. Therefore, the existence of these galaxies at high red shift is not inconsistent with hierarchical structure formation. This fits in with a downsizing scenario, as these massive elliptical galaxies at high red shift would have their gas exhausted at early epochs by AGN feedback processes.

1.3 THE GALAXY RED SEQUENCE

The red sequence is the region in which red galaxies, generally elliptical or dwarf elliptical types, sit on a colour magnitude diagram. Their colours are redder as they have little to no current star formation occurring and have old, metal rich, stellar populations. This means that they lack young blue stars and are largely made up of an older red population. Figure 1.3 shows the relative positions of the red sequence and blue cloud on a colour-luminosity diagram. It is believed that galaxies begin life in the blue cloud as star forming galaxies. As they age their gas

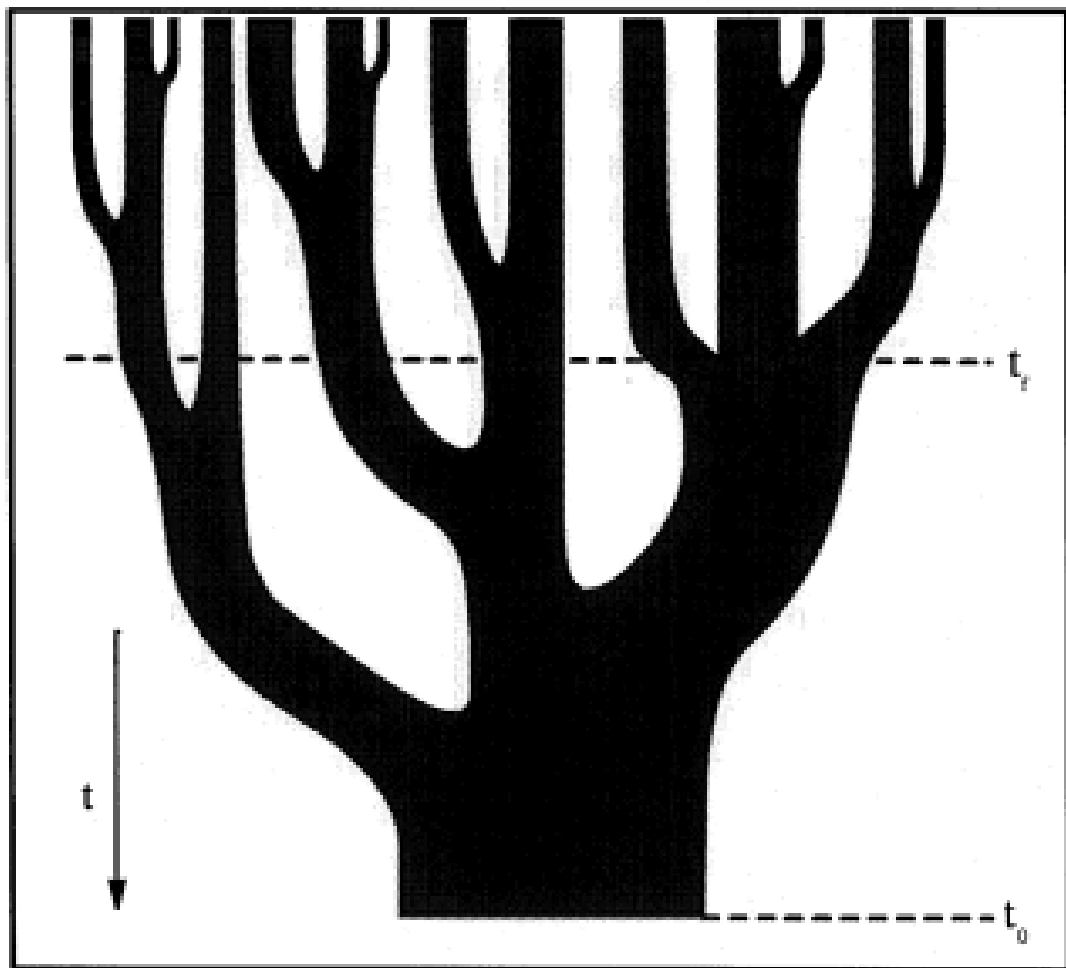


FIGURE 1.2 A galaxy merger tree representing the hierarchical structure formation model. Small halos merge to form larger ones, and these then merge in turn. In this diagram the top of the tree represents a time when there were a lot of small halos, and these merge to eventually form the trunk of the tree, or a large cluster sized halo. t_0 denotes the present time, and t_f is the time at which a parent halo containing more than half the mass of the final halo was created, (Lacey & Cole 1993).

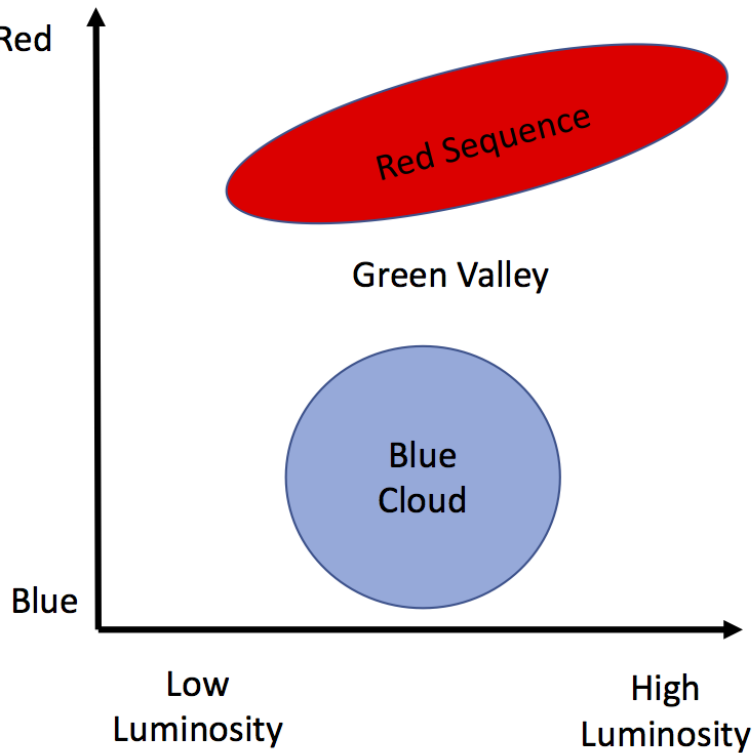


FIGURE 1.3 The positions of the galaxy red sequence and blue cloud on a colour - luminosity diagram. Galaxies with current star formation tend to sit in the blue cloud. When star formation has stopped, and a galaxy's stars are older the galaxy moves onto the red sequence.

is consumed through star formation. When their gas reservoir is so depleted that star formation stops they evolve onto the red sequence. In between the blue cloud and red sequence is a region sometimes named the green valley, it is believed that galaxies may evolve across this green valley to get from the blue cloud to the red sequence. Galaxy clustering in these regions has been observed in SDSS studies (e.g. Zehavi et al. 2011). It is a subject of debate if and how galaxies evolve across this green valley to join the red sequence (e.g. Guo et al. 2016b, Schawinski et al. 2014).

1.4 Λ CDM

The Λ CDM cosmological model is the leading explanation of how our Universe works. It is a paradigm of the the Big Bang model and states that we live in a cold dark matter Universe with a cosmological constant, Λ . The model starts with the Big Bang, when the Universe exploded out of a point of infinite density. The

afterglow of the Big Bang can be observed in the cosmic microwave background (CMB), see fig 1.4. As can be seen from the figure, the temperature across the CMB is not uniform, but has fluctuations. These are the imprint of quantum fluctuations in matter which occurred shortly after the Big Bang, and were measured by the COBE satellite in 1992 to be \sim one part in 10^5 (Boggess et al. 1992). After this there was a period of massive inflation meaning that these initial fluctuations became the seeds for the large scale structure observed in the Universe today. As the early Universe cooled, matter began to form, with the first stars forming 400 Myrs after the Big Bang.

The Λ CDM model incorporates Big Bang cosmology into a model which includes a cosmological constant and cold dark matter. The dark matter is described as cold because its particles move slowly when compared to the speed of light. The cosmological constant gives the energy density value of space and it's magnitude and sign dictates the expansion timescales of the universe. A Λ CDM Universe is described by a set of cosmological parameters. It has an energy density parameter $\Omega_0 = 1$, corresponding to a flat geometry. Three different fluids contribute to this energy budget: matter with $\Omega_{M,0} = 0.27$, dark energy with $\Omega_{\Lambda,0} = 0.73$, and radiation with $\Omega_{R,0} = 4 \times 10^{-5}$. The matter term is the sum of contributions from ordinary baryonic matter ($\Omega_{B,0} = 0.045$) and Cold Dark Matter ($\Omega_{CDM,0} = 0.225$). Additionally, dark energy is very well described by an equation of state parameter, $\omega = -1$, which necessitates the introduction of the cosmological constant.

These model parameters have the same values as those observed, by missions such as WMAP (Hinshaw et al. 2013) and Planck (Planck Collaboration et al. 2016), so the Λ CDM model is extremely effective at describing the universe we live in. Further predictions arising from the Λ CDM model are the abundances of the elements hydrogen, helium and lithium; the large scale structure of the Universe and the accelerating expansion of the Universe (Riess et al. 1998).

In the Λ CDM model the Universe forms as a great mesh of filaments, with galaxy groups and clusters forming where these filaments intersect. Material travels down the filaments to the clusters and hence, they continue to grow. We observe this structure from our position in the Milky Way: we see the galaxy clusters Virgo, Coma and Fornax from within our Local Group of galaxies.

1.5 SIMULATIONS

Simulations are a vital tool for astronomers to test theories on the evolution of the universe. For instance, in testing the Λ CDM model, it is possible to simulate

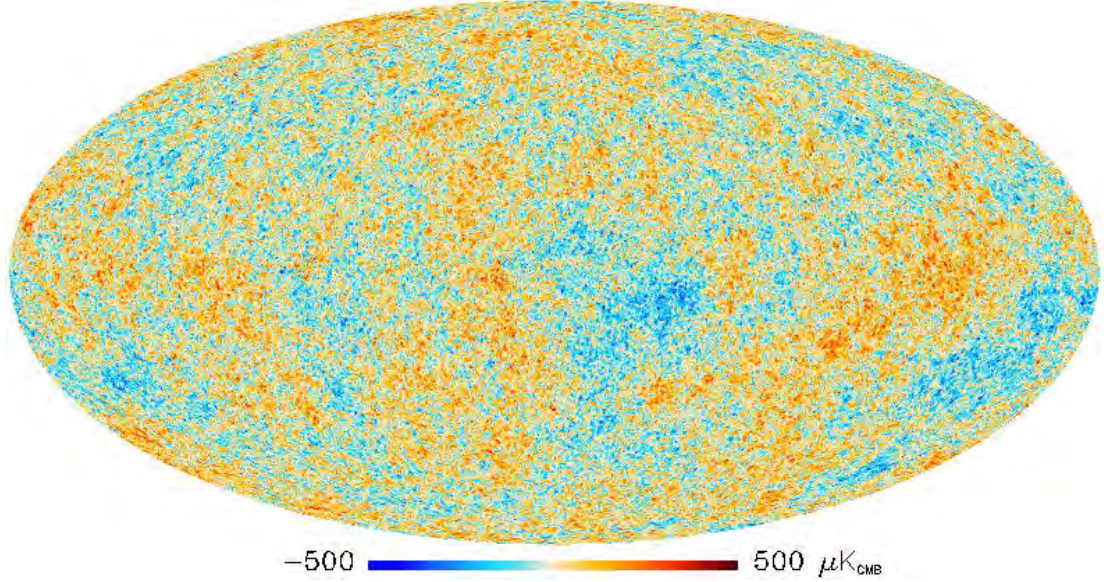


FIGURE 1.4 A Planck Collaboration map of the cosmic microwave background. The red areas of the map correspond to warmer regions and the blue areas to cooler regions, (Planck Collaboration et al. 2014).

a universe with all the cosmological constants set to their most accurately known value and see what the universe should look like at the present time. Until recently, these simulations have been made up of solely dark matter particles (e.g. Lemson & Virgo Consortium 2006, Klypin et al. 1999a). There are two main reasons for this: the first is that these simulations are extremely computer power heavy, so until recently it has not been possible to incorporate any baryonic physics in to them. The second reason is that our Universe is made up largely of dark matter, so dark matter simulations are thought of as a good approximation to our Universe. The dark matter density cosmological parameter is 0.23, compared to 0.05 for baryonic matter density, which makes it clear to what degree dark matter dominates. Therefore, in simulations such as those done by Klypin et al. (1999a) (see also Kravtsov et al. 1997) only dark matter particles are used and the only active force is gravity. Klypin et al. (1999a) follow the evolution of the dark matter particles in the simulations and use these to predict the subsequent appearance of the universe. These models predict that in a simulated galaxy group similar to the Local Group we should see about 300 satellites in a 1.5Mpc radius- observationally however, we only see around 40 in the local group. This problem is seen consistently across these Λ CDM dark matter simulations, and will be discussed in more detail later (see section 1.6).

More recent simulations, such as the Virgo Consortium’s Evolution and Assembly of GaLaxies and their Environments (EAGLE) project (e.g. Schaye et al. 2015) and Illustris (e.g. Vogelsberger et al. 2014b), are hydrodynamical simulations. Hydrodynamical simulations are able to account for the baryonic component of the Universe by calculating fluid motion, as well as gravity. This allows effects such as feedback to be incorporated, which is believed to be vital in galaxy evolution. Feedback is a process that regulates the growth of galaxies, in which the interstellar medium is heated (e.g. as a result of a supernova explosion) and halts further star formation.

1.6 THE DWARF GALAXY PROBLEM

The dwarf galaxy problem arises when these simulations are compared to our observable Universe. When examined on large scales the results of the dark matter only simulations seem to largely echo the Universe we live in: there are great filaments with clusters of galaxies at the intersections and large voids of empty space in between. However, when examined on galactic scales they show around an order of magnitude, or ten times more, dwarf galaxies than we observe (e.g. Klypin et al. 1999a, Bullock 2010). Klypin et al. (1999a) carry out dark matter only Λ CDM simulations of a region the size of the Local Group, within a radius of ~ 1.5 Mpc. Using a particle size of 1.66×10^7 they predict around 9 times more satellites than are observed in the Local Group. Moore et al. (1999) also use dark matter numerical simulations to examine substructure. They investigate the dark matter sub halo population of a Milky Way sized galaxy halo and predict that we should find around 500 halos with masses larger than $10^8 M_\odot$; in reality around 50 are observed.

One proposed solution to the dwarf galaxy problem is that the simulations that predictions come from do not mirror our Universe closely enough, as they have not incorporated enough baryonic physics. Recently the EAGLE team (Schaye et al. 2015) have run suits of hydrodynamical simulations, which incorporate a lot more baryonic physics. Their APOSTLE (A Project Of Simulating The Local Environment) simulations focus on a Local Group sized region (Sawala et al. 2016). From these simulations they state that the number of luminous satellites now agrees with the number observed, however they still predict around ten times more dark matter halos. This means that these halos may have matter in them, but have not had enough mass to form stars in the simulations. There are currently ~ 60 known galaxies with masses above $10^5 M_\odot$ within 2 Mpc of the Local Group

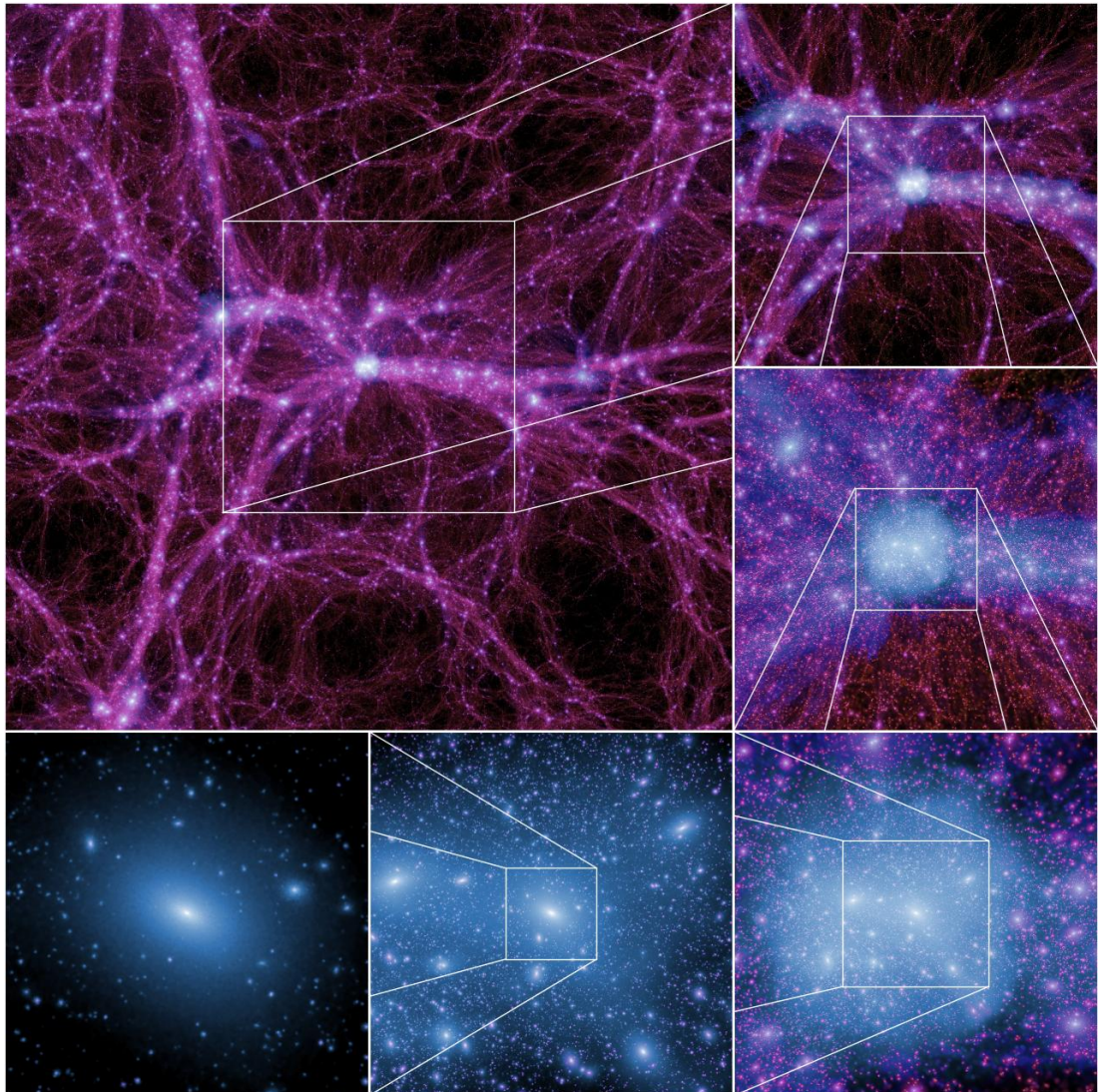


FIGURE 1.5 zoom sequence from 100 Mpc/h to 0.5 Mpc/h through the Millenium-II simulation at redshift 0.

The top-left panel shows the super-cluster scale. The top, middle and bottom panels on the right hand side show a cluster. The bottom-middle and -left hand panels show an individual galaxy whose dwarf companions can be seen,(Boylan-Kolchin et al. 2009).

barycentre, comparatively in their simulation Sawala et al. (2016) produce 90^{+20}_{-15} in the same area. However, they still generate vast numbers of satellite galaxy halos, especially when compared to the number of luminous satellite galaxies they predict. This raises the question of why there are so many empty halos, and if they are truly empty or whether their luminous mass is smaller. Additionally, the APOSTLE simulations do not probe the lowest mass end of the dwarf galaxy population. They run three simulations with different particle sizes, respectively $1 \times 10^4 M_{\odot}$, $1.2 \times 10^5 M_{\odot}$ and $1.5 \times 10^6 M_{\odot}$. However, faint satellites of the Milky Way have been discovered with masses as low as $10^3 M_{\odot}$ (Drlica-Wagner et al. 2015).

Vogelsberger et al. (2014a) discuss results from the Illustris simulation. They have compared populations of satellite galaxies brighter than $r < -20.5$ mags for host systems similar to SDSS groups and clusters. Their results appear to reproduce the distributions seen in the SDSS, however, their magnitude cut-off is bright compared to many known dwarf galaxies. Additionally they present a corresponding dark matter only simulation (Illustris-Dark) and state that in this simulation the satellite distribution does not resemble the SDSS sample as well, therefore highlighting the importance of baryonic physics in cosmological simulations.

The magnitude of this problem can be shown using a Schechter function (fig 1.6). This function takes the following form:

$$n\left(\frac{L}{L^*}\right)d\frac{L}{L^*} = \phi^* \frac{L}{L^*}^{\alpha} e^{-\frac{L}{L^*}} d\frac{L}{L^*}$$

where L^* is the characteristic luminosity of typical massive galaxy, corresponding to a halo mass of $10^{13} M_{\odot}$ (Cooray & Milosavljević 2005), ϕ^* is the number density of galaxies and α defines the faint end slope. The simulations tend to obtain an α of ~ -2 (Klypin et al. 1999a), however, observationally α values of between -0.7 and -1.5 have been measured (e.g. Marzke et al. 1994, Loveday et al. 1992, Lin et al. 1996, Efstathiou et al. 1988, Ratcliffe et al. 1998).

1.7 PROPOSED OBSERVATIONAL SOLUTIONS

There are many proposed solutions to the dwarf galaxy problem. One of these is that the Λ CDM model is flawed, this is beyond the scope of this thesis and I will not discuss it any further here. Some other suggested solutions are 1. that the dwarf galaxies are out there and we have thus far been unable to detect the majority of them and 2. that the simulations don't include enough physics to accurately represent our universe.

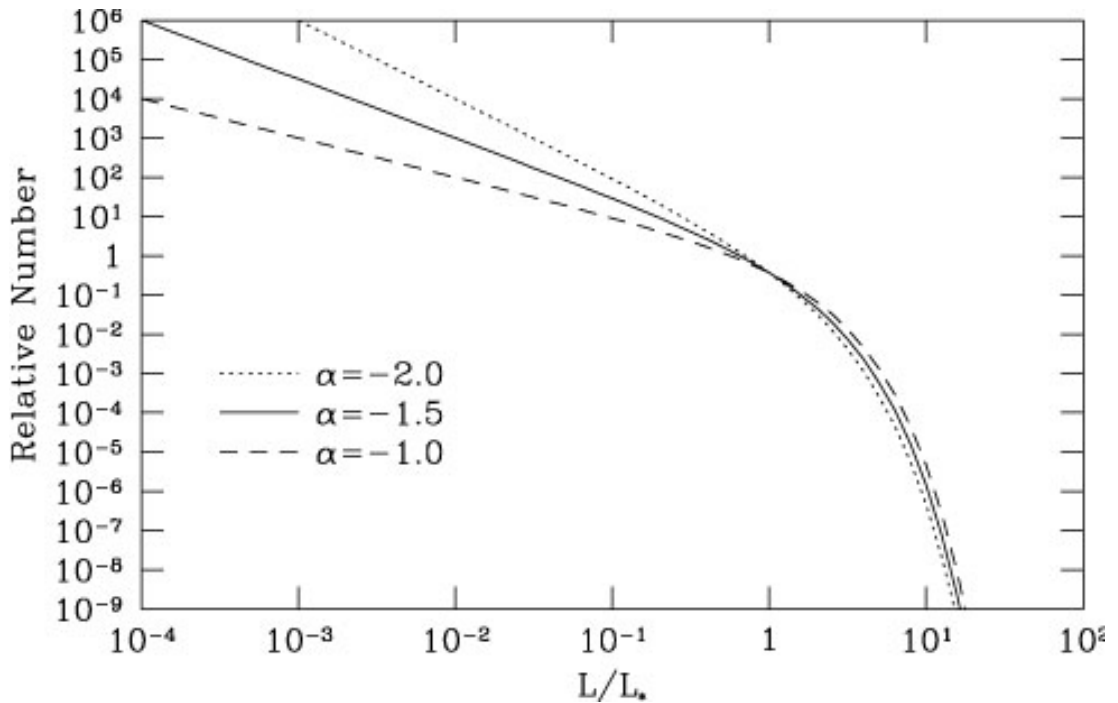


FIGURE 1.6 A Schechter function, with luminosity plotted on the x-axis and number on the y-axis. The shape of the function is shown for α values of -1, -1.5 and -2. Dark matter only models predict an α value of -2 however, observationally α values of around -1 to -1.5 have been measured. This does not show results from models, just a schechter function with varying alpha values.

image from <https://ned.ipac.caltech.edu/level5/March01/Schneider/Schneider3.html>

1.7.1 DARK GALAXIES

As mentioned above, the Λ CDM simulations have been, at least until recently, largely dark matter only simulations. This means they predict that each L^* galaxy size dark matter halo should have many dark matter subhalo companions. This raises the question as to whether these halos are out there, but have little to no baryonic matter within them. Halos like this have been termed 'dark galaxies' .

It has been proposed that many of these halos could be detectable through their neutral gas content (e.g. Davies et al. 2006). If a dwarf galaxy has had one generation of star formation, then it is possible that when one of these stars died, and went supernova, this removed the majority of the gas reservoir and hence quenched future star formation. This galaxy would then be largely devoid of stars, yet still have some neutral gas which didn't meet the conditions for further star formation. It is possible to detect neutral hydrogen by looking for its 21cm line emission (H I emission). This emission line is emitted due to electron spin in the ground state of hydrogen. An electron has both an electron spin and a nuclear spin

component. When these two spins are parallel they are in a higher energy state, so when they become anti-parallel a 21cm photon is released. The 21cm line is a forbidden line with a low probability for spontaneous 1 to 0 transition, however, due to the vast amounts of hydrogen in the universe it is easily detectable. This makes the 21cm line a fantastic tracer for large amounts of neutral hydrogen in the Universe. Therefore, in observing the 21cm line in the regions around L* galaxies it is possible to look for any dark satellite galaxies which may be devoid of stellar material but still have H I gas.

Attempts have been made to predict the amount of dark galaxies that should exist in the universe. Davies et al. (2006) predict that 20% of the total galaxy population is dark, and 15% of the total H I currently residing in galaxies is in dark galaxies. However, they also flag some issues with detecting these galaxies: they are rare compared to galaxies with stars; although dark galaxies appear to have the same range of masses and sizes as normal galaxies, a higher fraction of them are small and of low mass which makes them difficult to detect; and if dark galaxies cluster in the same way normal galaxies do then it is very easy for them to be assigned an incorrect optical counterpart.

Although no dark galaxy detections have been confirmed to date there are many candidate dark galaxies, these include HVC 127-41-330, Smith's cloud and VIRGOHI21.

HVC 127-41-330 is a rotating disk of HI located between the Andromeda galaxy and M33 which was discovered in 1982 using the Dwingeloo 25m telescope (Christian & Tully 1983), it was then rediscovered by Blitz & Robishaw (2000) as part of the Leiden/Dwingeloo Survey of Galactic Neutral Hydrogen (Hartmann & Burton 1997). It was thought that the cloud was associated with the nearby local group dwarf galaxy, LGS3, however Blitz & Robishaw (2000) pointed out that it was larger and had a higher H I mass than LGS3, as well as being offset both spatially and in velocity. Further observations were carried out in 2000 using the Arecibo telescope (Simon 2005) which resolved the cloud into a double lobed H I cloud with a velocity width of 24km s^{-1} . It is located $30'$ away from LGS3 with a velocity difference of -45km s^{-1} and shows a clear velocity gradient across it. Due to these features Simon (2005) proposes it is a dark galaxy.

Smith's cloud was discovered in 1983 by Gail Bieger (née Smith) (Smith 1963). Observations of Smith's cloud in 2008 using the Green Bank Telescope revealed it to have 10^6 M_\odot of H I (Lockman et al. 2008). It has a cometary appearance and is moving towards the galactic plane with a velocity of $73 \pm 26 \text{ km s}^{-1}$ (Lockman et al. 2008), suggesting that it is a gas cloud in the process of being accreted by

the Milky Way. Projecting the cloud's trajectory backwards it has been estimated that it survived a pass through of the Milky Way around 70 Myrs ago. To have survived this previous encounter it has been suggested that the cloud must have a massive dark matter halo (Smith 1963), hence it is a strong dark galaxy candidate.

VIRGOHI21 was detected by Davies et al. (2004) using the Jodrell Bank Multibeam instrument, it is a cloud in the Virgo cluster with a H I mass of $10^8 M_\odot$ and a velocity width of 220 kms^{-1} (Minchin et al. 2005). No optical counterpart has been detected for VIRGOHI21 down to a surface brightness level of $27.5 \text{ B mag arcsec}^{-2}$ and, if it is bound, it has a dynamical mass of $\sim 10^{11} M_\odot$. Minchin et al. (2007a) imaged VIRGOHI21 using the Westerbork Synthesis Radio Telescope and confirmed the detection of a dark, edge-on spinning disk with the mass and size of a typical spiral galaxy. VIRGOHI21 appears to have previously interacted with the galaxy NGC 4254, see fig 1.7. Minchin et al. (2007a) have ruled out, through modelling, the possibility that VIRGOHI21 is tidal debris, formed through ram pressure stripping, through long range interactions or being the result of a group gravitational field. The only interpretation they are left with is that VIRGOHI21 contains a massive, dark disk. However, other studies have concluded that VIRGOHI21, and objects like it, could be tidal in origin. Duc & Bournaud (2008) state that harassment in galaxy clusters may produce extended gaseous tails. Galaxies in crowded environments interact in different ways, one of these being high speed fly-bys, this is called 'harassment'. Tails formed in this way could then fragment off and appear to have properties very similar to proposed dark galaxies. Duc & Bournaud (2008) present numerical models of VIRGOHI21 to explore whether it may have a tidal origin: they show that the observed properties of VIRGOHI21 can be reproduced in material ejected from NGC 4254 from a flyby from a massive companion. They propose that high speed collisions of this nature are a much simpler explanation for features such as VIRGOHI21 than the dark galaxy hypothesis.

Recently work has been carried out to investigate whether dark galaxies could have formed through the fragmentation of long H I streams (Taylor et al. 2016). A suite of numerical simulations have been carried out to determine whether harassment could have caused the high velocity widths of known dark H I clouds. They find that harassment is not able to explain the existence of these clouds and therefore one possibility is that they are primordial dark galaxies. Some of their arguments for these clouds not being tidal debris, and instead being dark galaxies are as follows; H I streams are believed to be long lived, so if the H I clouds are unbound and transient then they should not survive longer than the streams in which they may have originated, therefore the lack of detected associated streams

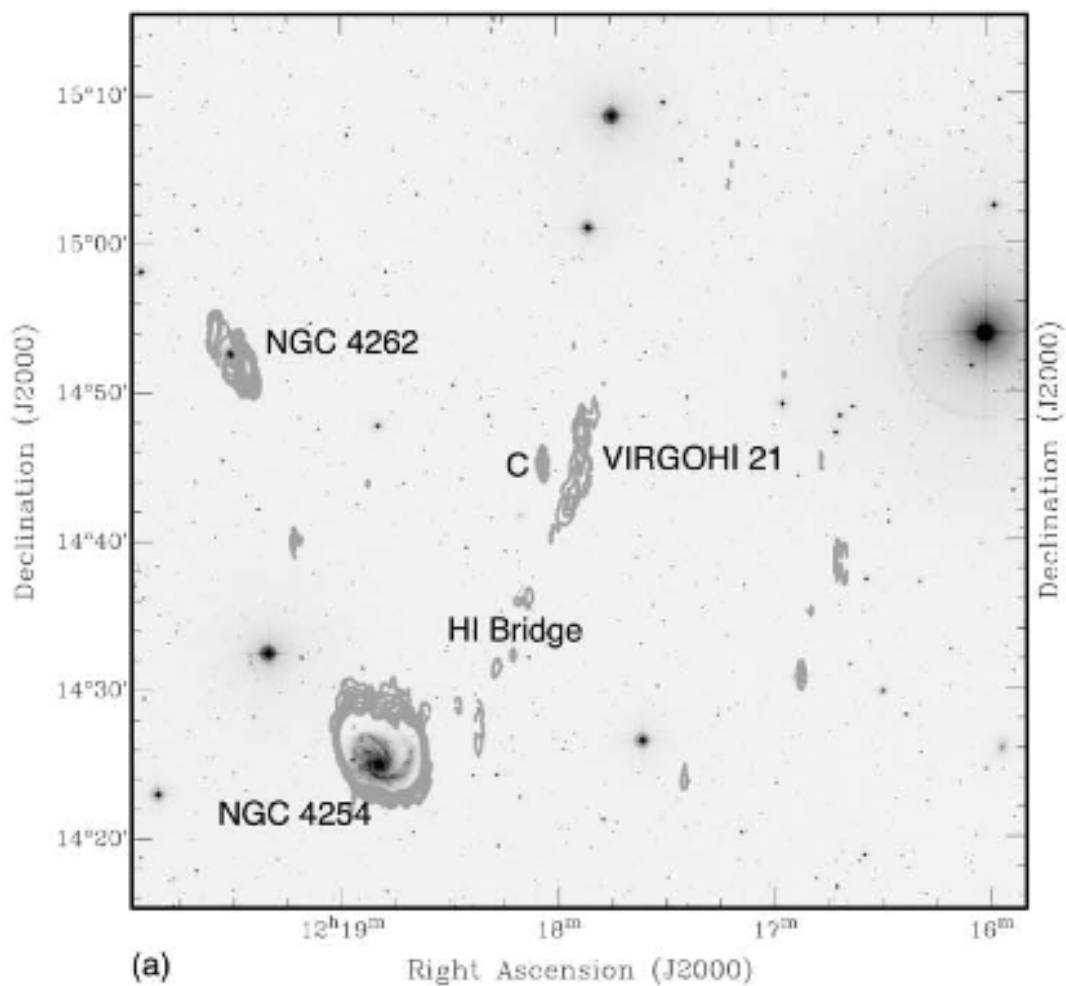


FIGURE 1.7 A H_I map of VIRGOHI21 overlaid onto an optical image. It can be seen that VIRGOHI21 is a massive H_I gas cloud with no optical counterpart which may have previously interacted with NGC 4254, (Minchin et al. 2007a).

is surprising; isolated dark galaxy candidates exist which are very difficult to explain as tidal debris; and the objects signal to noise ratios and velocity widths are consistent with them being rotating disks. Although a lot more work needs to be done in this area, it is starting to look as if the most plausible explanation for many known dark H_I clouds is that they are, in fact, dark galaxies.

Part of the content of this thesis is a further investigation into the possibility of dark galaxies. This can be found in Chapter 2.

1.7.2 LOW SURFACE BRIGHTNESS GALAXIES

Although the depth and resolution of optical galaxy surveys is constantly improving, their surface brightness limits can be problematic for those investigating the low surface brightness (LSB) universe. The obvious rule when looking for galaxies is the bigger and brighter something is, the easier it is to detect. Therefore, faint dwarf galaxies can be difficult to find. For instance the faintest of the classical satellites (those which were known prior to optical CCD surveys) of the Milky Way has a central surface brightness of 27.1 mags arcsec⁻² (McConnachie 2012a), with the average being \sim 24.7 mags arcsec⁻² (McConnachie 2012a). The surface brightness of the night sky can vary depending on weather conditions, location and altitude, however, we are reaching the limit with observations where the surface brightnesses of faint objects blend in with the sky surface brightness. Therefore, many more low surface brightness galaxies and dwarf galaxies may exist which are extremely difficult to detect.

Recently, with more and more sensitive optical surveys, progress is being made in this field. There have been recent discoveries of new LSB galaxies in the Virgo, Coma and Fornax clusters, such as those by van Dokkum et al. (2015a), Mihos et al. (2015) and Drinkwater et al. (2000), which are discussed below.

1.7.3 DWARF GALAXY POPULATIONS

In the last few years there have been many studies focused on finding new galaxy populations in clusters (e.g. van Dokkum et al. 2015a, Koda et al. 2015, Mihos et al. 2015). However, they largely rely on inspection by eye, and photometric redshifts, to define cluster membership. Photometric data is not always available, and inspecting sources by eye quickly becomes impractical with large population sizes.

1.7.4 THE COMA CLUSTER : ULTRA DIFFUSE GALAXIES

One interesting galaxy population which had been discovered recently are the Ultra Diffuse Galaxies (UDGs). van Dokkum et al. (2015a) discovered 47 new low surface brightness objects in the Coma cluster, using the Dragonfly Telephoto Array. The objects have central surface brightnesses of between 24 and 26 mag arcsec⁻² and effective radii of 1.5 - 4.6 kpc; this means that they have sizes comparable to L* galaxies, although their mean stellar mass is only $\sim 6 \times 10^7 M_\odot$. For comparison, the stellar mass of the Milky Way is $\sim 6 \times 10^{10} M_\odot$ (Licquia & Newman 2014). These features have led to them being named Ultra Diffuse Galaxies (UDGs). Unlike the giant low surface brightness galaxies these UDGs are reasonably red and round, with $\langle g - i \rangle = 0.8$ and $\langle b/a \rangle = 0.74$ ($\langle b/a \rangle$ is the ratio of the semi major and semi minor axes, and so defines a galaxy's ellipticity.)(van Dokkum et al. 2015a). UDGs have only recently been predicted by a formation model (Rong et al. 2017) and van Dokkum et al. (2015a) state that they are not likely to be the products of galaxy harassment or tidal stripping, as these processes tend to shrink galaxies. van Dokkum et al. (2015a) suggest that UDGs could be "failed" L* galaxies, which have lost their gas after early generations of star formation at high redshift. If this scenario proves true, then UDGs may have very high dark matter fractions, which would help explain their survival in the cluster. The positions of these galaxies relative to the cluster, and examples of a selection of the sources, are shown in figure 3.1. van Dokkum et al. (2015a) can only infer cluster membership of these objects based on their spatial distribution within the cluster, and serendipitous Hubble Space Telescope ACS imaging of one source: they attain a lower limit for its distance from the fact that it is not resolved into stars. They then modelled this galaxy, leaving the distance as a free parameter. When this model was inserted into the original image it took on the same smooth appearance as the original source, and so they concluded that it is likely that the UDGs are associated with Coma. In van Dokkum et al. (2015b) they then present Keck spectrometry of one of the objects, and therefore confirm its cluster membership. This highlights the difficulty in confirming galaxies' cluster memberships, as in spite of all of the above van Dokkum et al. (2015a) have only confirmed the membership of one of their sample, and must then infer that the other sources are also cluster members.

Motivated by the work of van Dokkum et al. (2015a), Koda et al. (2015) used the Subaru telescope to search for UDGs in the Coma cluster. They find 854 UDGs in the Coma cluster, 332 of which are Milky Way sized with effective radii $> 1.5\text{kpc}$. They propose that this suggests that the Coma cluster has > 1000 UDGs, when the

smaller field size of Subaru compared to Dragonfly is taken into account. Koda et al. (2015) find these galaxies to be concentrated around the cluster centre, which suggests that they have been members of the cluster long term. They find them to be red in colour, with no active star formation. They have exponential light profiles, effective radii ranging from 800 pc to 5kpc, effective surface brightnesses between 25 and 28 mag arcsec⁻², and stellar masses $\sim 1 \times 10^7 M_\odot - 5 \times 10^8 M_\odot$. As also concluded by van Dokkum et al. (2015a), Koda et al. (2015) note that their survival close to the cluster centre indicates that they are extremely dark matter dominated. Due to the fact that UDGs have been found in much larger numbers in the Coma cluster than in the field, Koda et al. (2015) conclude that the cluster environment must play a role in their formation and evolution. Again, however, Koda et al. (2015) do not confirm that these galaxies are cluster members - in fact they state that at least one of the objects they have classified as a UDG may be a background spiral galaxy. This galaxy is the third circled source from the top of figure 1.9. This reiterates the problem that we are attempting to solve: currently without spectroscopy it is not possible to confirm cluster membership.

UDGs have not only been found in the Coma cluster, but also in the Virgo cluster. Mihos et al. (2015) announced the discovery of three UDGs in the Virgo cluster; they have half light radii of 3-10 kpc and surface brightnesses of ~ 27 mag arcsec⁻². These objects appear to be projected directly onto the cluster core, and only one of them shows any sign of tidal disruption. This again may imply that these UDGs have very high dark matter fractions, and so can survive in the dense cluster environment. Mihos et al. (2015) only infer cluster membership due to the fact that Next Generation Virgo Survey imaging of one of the objects does not resolve red giant branch stars, which yields a lower distance limit of 2.5 Mpc.

1.7.5 THE FORNAX CLUSTER: ULTRA COMPACT DWARFS

Another recently discovered type of dwarf galaxy are the ultra compact dwarfs, a population of which were discovered by Drinkwater et al. (2000) at the centre of the Fornax cluster. They have spectra typical of stellar systems, are unresolved and are more luminous than any Galactic globular clusters, but fainter than any known compact dwarf galaxies. Drinkwater et al. (2000) appear to use these criteria alone to claim cluster membership for these galaxies. Drinkwater et al. (2000) suggested that they may be a new class of low-luminosity compact elliptical dwarf galaxy. The distribution of these objects is more centrally clustered than we see in galaxy clusters in general. Bekki et al. (2003) revisited the findings of

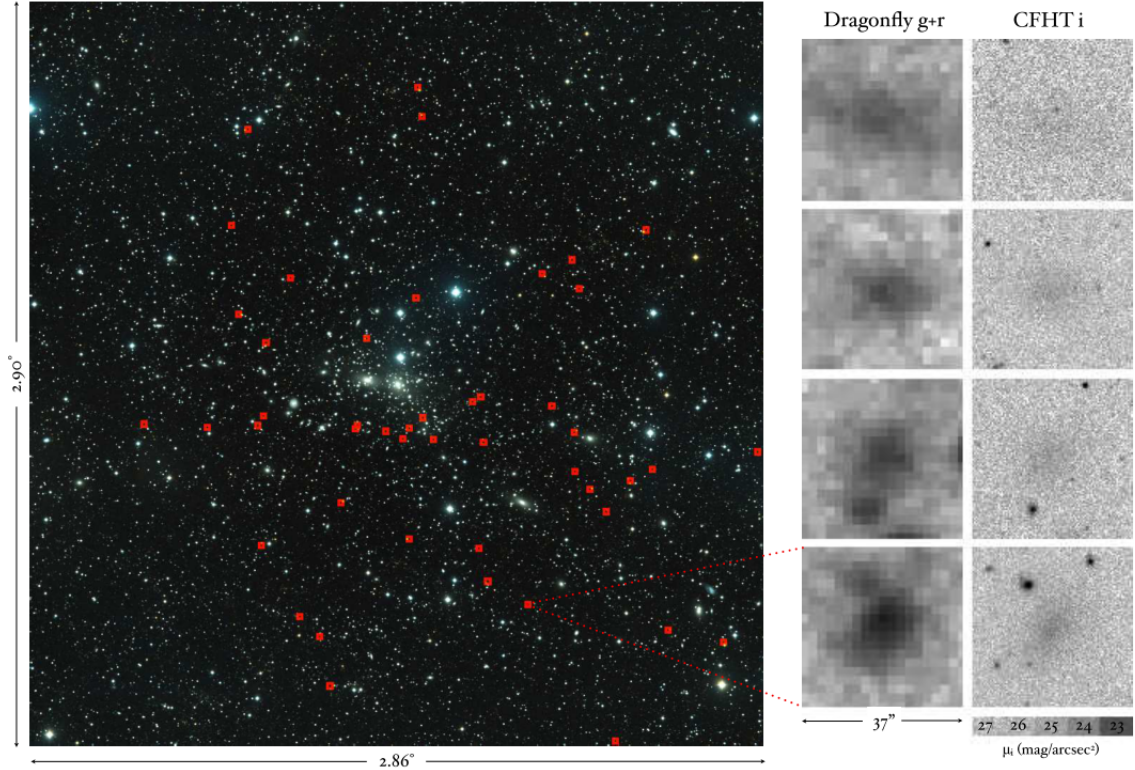


FIGURE 1.8 Figure showing the spatial positions of the UDGs detected by van Dokkum et al. (2015a). They are shown with red squares which are overlaid on a Dragonfly g and r band image of the Coma Cluster. The right panel shows some examples of the van Dokkum et al. (2015a) galaxies, in both Dragonfly and CFHT images. Figure from van Dokkum et al. (2015a).

Drinkwater et al. (2000), and termed the galaxies ‘Ultra-Compact Dwarfs’ (UCDs). Bekki et al. (2003) carried out numerical simulations in order to clarify the origins of the objects. They simulated the effects of the Fornax Cluster’s strong tidal field on nucleated dwarf galaxies. It was found that the tidal field of the cluster would remove the outer stellar components of these nucleated dwarfs. Due to its compact nature the nucleus would survive, and is found to have very similar physical properties to UCDs. Therefore, Bekki et al. (2003) state that this is a likely formation mechanism for the Fornax UCDs. They also conclude that UCDs are most likely to be formed in massive Galaxy groups, or clusters, as their stronger tidal fields make the stripping of outer components more efficient.

1.7.6 THE VIRGO CLUSTER

Additionally, LSB galaxies have been recently found in the Virgo cluster by both Mihos et al. (2015) and Davies et al. (2016). Mihos et al. (2015) discover 3

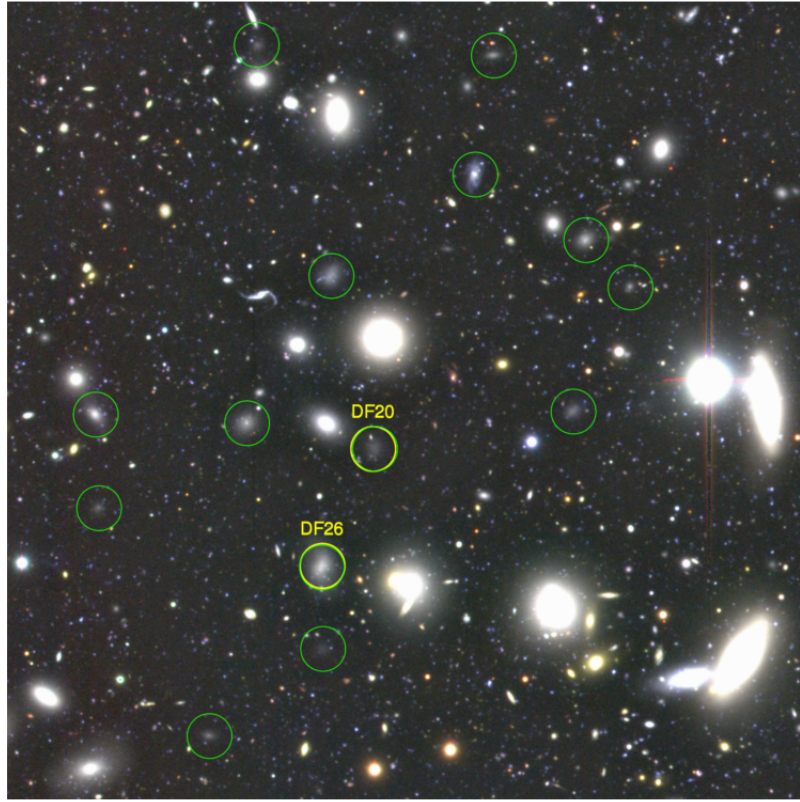


FIGURE 1.9 Figure showing some of the UDGs detected by Koda et al. (2015). The galaxies are indicated by green and yellow circles on the Subaru BRi colour image. Koda et al. (2015) claim that the third galaxy from the top may be a background spiral. Figure from Koda et al. (2015).

large LSB galaxies using wide-field imaging of the Virgo cluster from the Burrell Schmidt telescope. They have similar sizes to L* galaxies and their surface brightnesses are ~ 27 mags arcsec $^{-2}$. On the opposite end of the size scale, in Davies et al. (2016) we detect 303 new dwarf galaxies in the Virgo cluster using Next Generation Virgo Survey data (NGVS) (Ferrarese et al. 2012). These galaxies have surface brightnesses of 22.5 - 26 mags arcsec $^{-2}$ and exponential scale lengths of 3 - 10 arcsec. Two examples of these galaxies can be seen in fig 1.10. The work from Davies et al. (2016) is discussed in more detail in Chapter 3.

1.8 SUMMARY

This chapter has introduced the Dwarf Galaxy problem as a discrepancy between observations of the number of dwarf galaxies in our universe, and predictions from theoretical models. The possible solutions to this problem include the idea that more realistic treatment of baryonic physics and feedback is needed

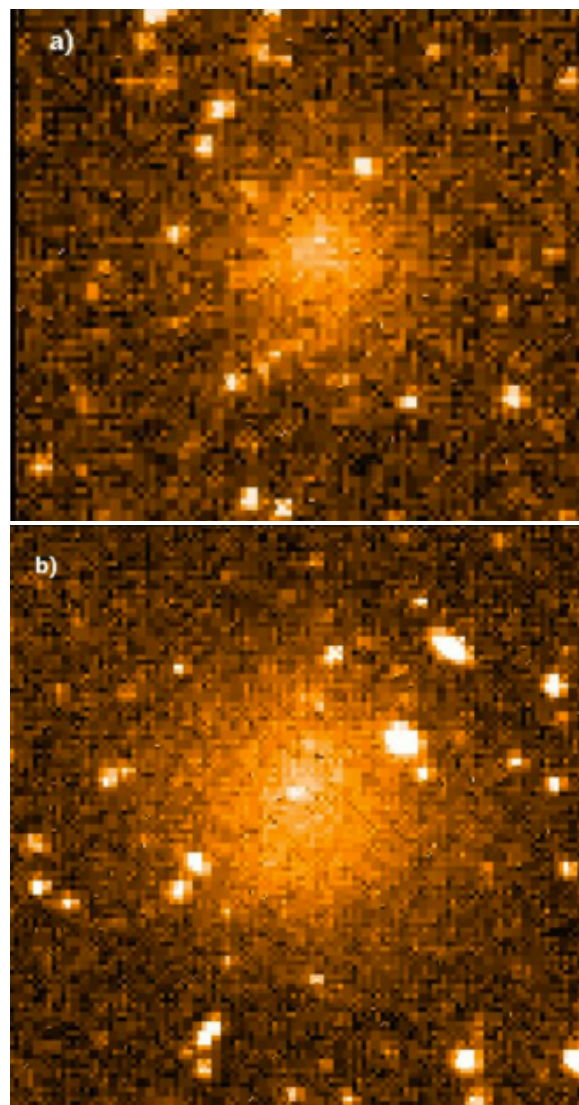


FIGURE 1.10 Examples of two of the Virgo LSB dwarf galaxies detected in Davies et al. (2016) (a) a galaxy with central surface brightness $25.0 \text{ mags arcsec}^{-2}$ and a size of 38 arcsec (b) a galaxy with central surface brightness $24.4 \text{ mags arcsec}^{-2}$ and a size of 46 arcsec .

in simulations to make them more accurate as well as observational solutions.

Observationally, there are two main proposed solutions to the dwarf galaxy problem. The first is dark galaxies, and the second is the LSB universe.

In chapter 2 of this thesis, the dark galaxy solution is explored. HI observations of the nearby galaxy M33 are investigated to hunt for gas clouds, which display features of being dark galaxies.

Chapter 3 introduces the cluster environment, and discusses previous work done on the Virgo cluster. In chapters 4 and 5 of this thesis data from the Next Generation Virgo Survey is used to explore whether it is possible to use photometric properties to distinguish cluster dwarf galaxies from those in the background. This would allow the discovery and classification of many more dwarf galaxies, thus helping solve the dwarf galaxy problem.

CHAPTER 2

M33

*'That Light whose smile kindles the Universe,
That Beauty in which all things work and move'*

PERCY BYSSHE SHELLEY

As discussed in the introduction, there is a lack of observed satellite galaxies when compared to simulations: this is called the dwarf galaxy problem. One potential solution is that some galaxies may be 'dark galaxies'. Dark galaxies are dark matter halos which contain gas but few to no stars. In this chapter I will explore the idea of dark galaxies being a potential solution to the dwarf galaxy problem.

Here I present HI survey data of the galaxy M33 and its surrounding area. This data was taken as part of the Arecibo Galaxy Environment Survey (AGES). Our aim was to explore the gas in the region around M33, investigate any clouds found and assess our discoveries in respect to the idea of dark galaxies.

2.1 M33 AND THE SURROUNDING AREA

M33 is the third most massive galaxy in the Local Group (after Andromeda (M31) and the Milky Way). It is generally thought that M31 and M33 are closely associated with each other, for example they may have gravitationally interacted with each other in the relatively recent past (e.g. Bekki 2008). The M31-33 system collectively has around 30 known satellite (dwarf galaxy) companions (Martin et al. 2009), almost all of which are confirmed satellites of M31 and have no obvious association with M33. However, Martin et al. (2009) recently announced the discovery of two new dwarf galaxies in close proximity to both M31 and M33.

One of these (And XXI) they classified as a definite M31 satellite, but the other, Andromeda XXII, is the first proposed satellite of M33 (e.g. Chapman et al. 2013). And XXII is a lot closer in projection to M33 (~ 40 kpc) than to M31 (~ 220 kpc) and lies in a region where M33's dark matter halo would appear to dominate gravitationally over that of M31. The PAndAS CUBS optical survey was used to discover the two new dwarf galaxies by searching for spatial over densities of stars. In fact, the majority of surveys searching for faint Local Group dwarf galaxies have relied upon optical detection of these stellar over densities.

In the region around M33 extended star clusters have been found, which Chapman et al. (2013) propose may be tidally stripped dwarf galaxies because of their structure: they are extremely sparse stellar clusters with elongated distributions of stars. Other objects have also been detected around M33 and in its halo. Huxor et al. (2009) show that the globular cluster population of M33 is weighted towards the far side of M33 with respect to M31, they believe this is further evidence that an interaction with M31 has affected M33's halo population. Additionally, Sarajedini et al. (2006) have identified RR Lyrae stars in the halo of M33. RR Lyrae stars are found in stellar populations that are older than 10 Gyrs. This helps to determine the age of the halo population of M33 and therefore place a limit on when an interaction with M31 may have occurred. As we will see below these stars are considerably older than derived ages for a M31/M33 interaction suggesting that M33's halo may well have been rather unperturbed over reasonably long timescales.

Given the proximity of M33 (we use a distance of 840 kpc (Freedman et al. 1991)) and the past optical searches for stars, e.g. Martin et al. (2009), it is surprising that M33 currently has only one known possible dwarf galaxy companion. This seems even more remarkable when it is taken into account that the standard galaxy formation models predict many hundreds of dwarf satellite galaxies surrounding larger galaxies like M33 (Stadel et al. 2009 and references therein).

There has been considerable previous work, utilising 21cm observations, that has been used to investigate the halo of M33 and the nature of its relationship with M31. As part of the Arecibo Legacy Fast ALFA (ALFALFA) survey, Grossi et al. (2008) examined the neutral hydrogen in a $3^\circ \times 3^\circ$ area centred on M33, as well as deeper pointed observations of two fields near the edge of M33's HI disk. They attain a 1σ HI column density sensitivity of $5 \times 10^{-17} \text{ cm}^{-2}$ over a velocity resolution of 10 kms^{-1} . They detect 24 HI clouds in the region around M33, as well as mapping the outskirts of the HI disk. They consider two possible origins for these clouds: 1.) they are dark matter dominated gaseous satellites, and 2.)

they are debris from filaments flowing into M33 from the intergalactic medium, or from a past encounter with M31. Grossi et al. (2008) state that both these scenarios could explain the observed cloud properties.

Braun & Thilker (2004) used the Westerbork array to detect HI over a 1800 deg² region of the sky that covered both M31 and M33. Their survey had a very low HI column density sensitivity of 1.5×10^{17} cm⁻² over a 30 km s⁻¹ velocity width, but a rather large spatial resolution of 49 arcmin (FWHM). They detected 95 HI clouds almost all of which seem to be clearly associated with M31. They also identified a faint HI stream seemingly joining M33 and M31 however, they were unable to trace this all the way to M33 due to confusion with HI in the outskirts of the Milky Way. They detected one HI cloud in the region of M33 with a HI mass of a few times 10^5 M_⊙ - this cloud has properties similar to the High Velocity Clouds (HVCs) found around the Milky Way. HVCs are clouds of HI with velocities that cannot be explained with a simple model of galactic rotation - Galactic HVCs typically have velocities which deviate from expectations of rotation by > 50 kms⁻¹ (Wakker 1991). Westmeier et al. (2005) present high-resolution (~ 2 arcmin) follow up observations of the previously identified M31/M33 HI clouds and again conclude that the single M33 HVC displays very similar characteristics to Galactic HVCs. A possible link between HVCs and the missing dwarf galaxy population as either progenitors of, or failed, dwarf galaxies has previously been proposed by Blitz et al. (1999) and Blitz et al. (2004).

Braun & Thilker (2004) suggest two possible mechanisms for the origin of the HI stream between M31 and M33: (1) that it is a pre-existing filament extending between the two galaxies, filaments like this are a prediction arising from high resolution numerical models of structure formation (Davé et al. 1999, Davé et al. 2001) or (2) the stream has arisen from a past tidal interaction between M31 and M33. Braun & Thilker (2004) use the measured systemic velocities of M33 and M31 to conclude that the two galaxies are currently moving towards each other, indicating that no recent (< 2 Gyr) interaction has taken place. Putman et al. (2009) have used similar methods to Braun & Thilker (2004) (they have assessed possible orbits given the observed velocities) and conclude that the galaxies are likely to have interacted between 1 and 3 Gyr ago, which is roughly consistent with Braun & Thilker (2004). Putman et al. (2009) list distinct features of the gaseous disc of M33 including: an extended warp in the disc, a filament from the northern part of the disc, diffuse gas surrounding the galaxy, and a cloud with a filament extending from the galaxy. They say that all of these features strongly indicate a past interaction between the two galaxies and state that this interaction is the probable

origin of the M31-M33 stream. Bekki (2008) have carried out a suite of simulations of possible orbits for M33 and M31; their conclusion is that an interaction occurred even longer ago than proposed above - between 4 and 8 Gyr.

However, using observations of the stream down to a column density limit almost identical to that of Braun & Thilker (2004) ($2.7 \times 10^{17} \text{ cm}^{-2}$ for a line width of 25 km s^{-1}), Wolfe et al. (2013) report that about 50% of the atomic hydrogen in the stream is composed of distinct clouds whilst what remains is made up of an extended, diffuse component. They use their much improved spatial resolution of 9 arcmin to identify these distinct clouds; comparably Braun & Thilker (2004) had a spatial resolution of 49 arcmin. Wolfe et al. (2013) propose an intergalactic filamentary origin of the stream. They argue that the collapse timescale for the individual clouds they identify is much shorter ($\sim 400 \text{ Myr}$) than the likely time since an interaction (a few Gyr). Wolfe et al. (2013) propose that the clouds may have several possible origins: (1) they may be primordial gas rich objects similar to dwarf spheroidal or dwarf irregular galaxies, (2) the clouds may be gas accreting into sub-halos, (3) the clouds may be tidal dwarf galaxies in formation and (4) the clouds may be transient objects condensing from a pre-existing intergalactic filament.

Clearly, there is still some lack of agreement as to the origin of the HI stream/filament. If it is tidal then at first sight it is difficult to see how distinct clouds along its length will not have already collapsed into much smaller denser structures. However, this is based on the assumption that the observed velocity widths measure the 'local' gravitational field and are not highly biased by streaming motions along the filament - something that cannot be ruled out. The question also remains open as to whether any of the HI condensations could eventually become dwarf galaxies and so help explain the discrepancy between the numbers that theory predicts and the observations.

2.2 THE ARECIBO GALAXY ENVIRONMENT SURVEY

The Arecibo Galaxy Environments Survey (AGES) (Minchin et al. 2007b) is a neutral hydrogen (HI) survey using the Arecibo L-band Feed Array (ALFA) multibeam instrument at the Arecibo Observatory. The Arecibo Telescope, at the Arecibo Observatory in Puerto Rico, is an 305 m single dish radio telescope, see fig.2.1. The installation of ALFA made it possible to survey the sky with higher sensitivity and higher spatial resolution than was previously possible (Auld et al.



FIGURE 2.1 The Arecibo Telescope

2006). AGES covers 200 square degrees of sky looking at a range of galactic environments; from the local galaxy M33 to the Virgo Cluster and regions where isolated galaxies are found (e.g. Keenan et al. 2016, Taylor et al. 2012, Minchin et al. 2016). The survey was carried out over a total of 2391 hours between the 21st of December 2005 and the 2nd of December 2015. The survey's aims included: exploring the nature of High Velocity Clouds (HVCs) and their link to dwarf galaxies; measuring the contribution of HI to the global baryonic mass density; identifying gaseous tidal features and investigating their relation to mergers and interactions; and comparing AGES results with numerical models of galaxy formation (Auld et al. 2006).

2.3 M33 OBSERVATIONS AND DATA REDUCTION

Observations of the M33 field began in August 2008 and were completed in August 2013. The field observed to full depth spans approximately 5 degrees

of R.A. by 4 degrees of declination centred on M33. The full spatial range of the data is from 1:23:36 to 1:44:39 in R.A, and from +28:23:50 to 32:53:54 in declination (J2000).

Observations were performed with the telescope in drift scan mode, which means that the array is kept at a fixed azimuth and elevation whilst the sky drifts overhead. Each drift lasts for 20 minutes and covers about 5 degrees of RA. The 3.5 arcmin resolution element takes about 13 seconds to cross the beam when observing at 1.4 GHz, so 25 scans are required for an integration time of ~ 330 sec. Each beam records every second data in two polarisations with 4096 channels, spanning a velocity range of approximately -2,000 km/s to +20,000 km/s. The two polarisations are combined and then the data are gridded into 1' spatial pixels (the Arecibo beam has a FWHM of 3.5' at this wavelength) and into velocity channels of width 5.2 kms^{-1} .

The data was reduced using the AIPS++ packages LIVEDATA and GRIDZILLA, which are extensively described in Barnes et al. (2001). LIVEDATA is used to perform bandpass estimation and removal, Doppler tracking and it calibrates the residual spectrum. We also fit and subtract a sigma-clipped second-order polynomial to each spectrum, which, as shown in Taylor et al. (2014) (hereafter AGES VII), can significantly improve the baseline quality. GRIDZILLA is a gridding package which co-adds all of the spectra to produce the data cube described above. It also performs side lobe correction so that in the final gridded data cube each beam contributes equally to each pixel, with the exception of the edges of the map where sky coverage is incomplete.

We obtain an approximate 1σ HI column density sensitivity of $1.5 \times 10^{17} \text{ cm}^{-2}$ over a velocity of 10 kms^{-1} . Our column density sensitivity is around three times better than the ALFALFA data of Grossi et al. (2008). Additionally, we cover a much larger area than Grossi et al. (2008). Braun & Thilker (2004) have a comparable column density ($1.5 \times 10^{17} \text{ cm}^{-2}$), however this is over a velocity width of 30 kms^{-1} , whereas the AGES observations have the same column density sensitivity over a velocity width of 10 kms^{-1} . Sources of any given mass will be detected with lower S/N levels if their velocity width is large or equally, if they have the same intrinsic velocity widths but are discs with higher inclination angles, since their flux is spread out over more channels.

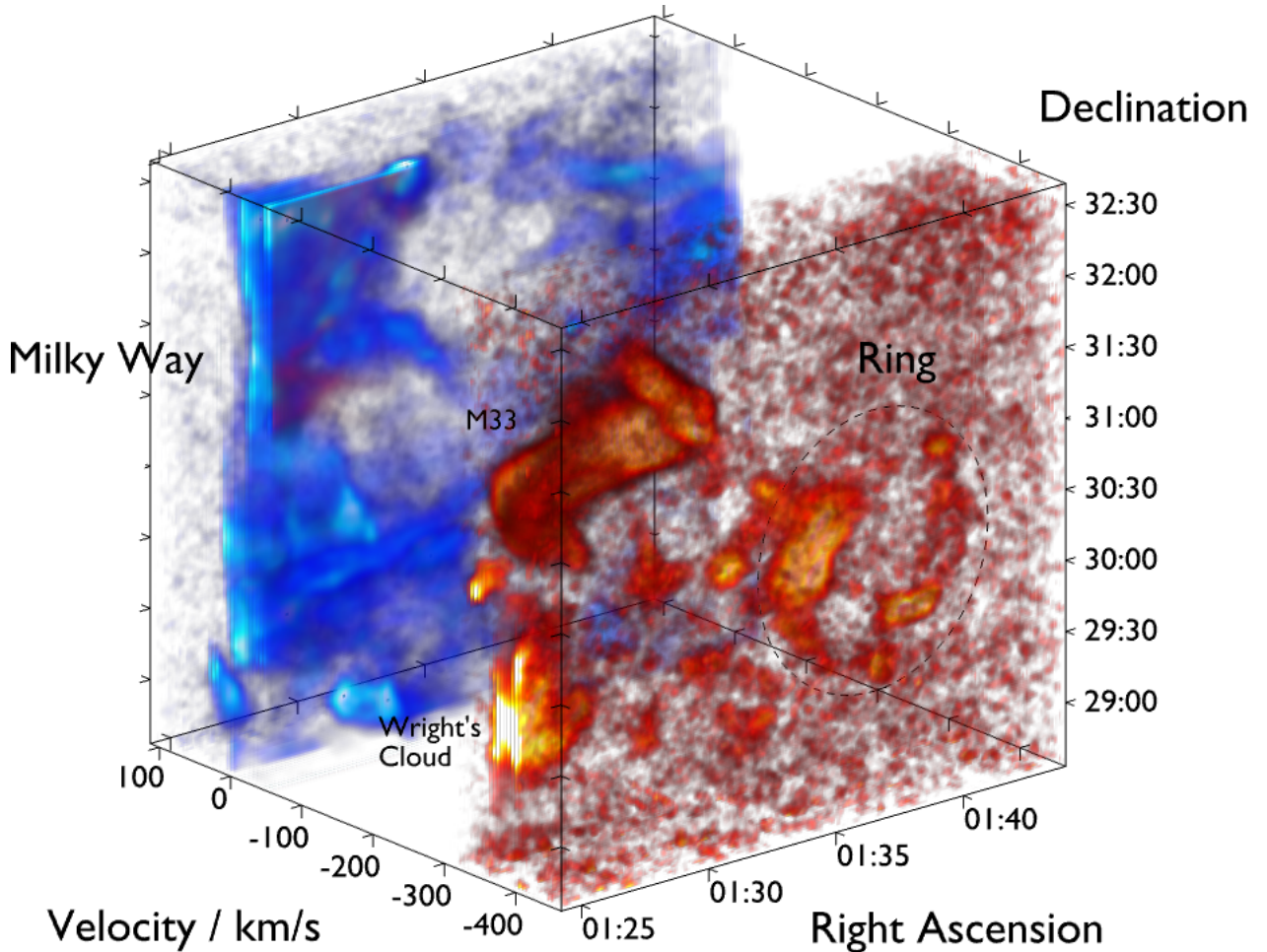


FIGURE 2.2 Position-Velocity plot of the AGES HI data cube. The HI from M33 and the Milky Way are confused over the approximate velocity range of $-75 < v < 0 \text{ km s}^{-1}$ so we have used blue for velocities $v > -75 \text{ km s}^{-1}$ (Milky Way) and red for everything else. Some of the distinct HI structures referenced in the text are labelled. The figure shows just a single, representative still image. A full movie of the rotating cube as supplementary online material for Keenan et al. (2016).

2.4 SOURCE EXTRACTION

To isolate the HI associated with M33 we selected a region of the cube spanning a velocity range of $\sim 600 \text{ kms}^{-1}$. The systemic velocity of M33 is $\sim -180 \text{ kms}^{-1}$ and as the Milky Way is centred at 0 kms^{-1} distinguishing HI in M33 from that in the Milky Way is not straightforward (all velocities given are barycentric except where stated otherwise). Each channel was inspected to determine the extent of the Milky Way contamination. HI from the Milky Way appears as extended emission spread across the spatial extent of the cube and is continuously connected, it also appears outside of the region in which one would expect to find M33. The systemic velocities of the two galaxies, along this line of sight, differ by only about 200 kms^{-1} , which is of the order of their internal velocities, so they 'bleed together' in the cube (fig. 2.2). This means that any sources in this crossover area (from around 0 kms^{-1} to 75 kms^{-1}) must be inspected by eye to determine whether they are likely to be a cloud associated with M33. If we find a compact source as opposed to extended emission across the field then we conclude that the source does not appear to be associated with the Milky Way. This process led to a final data cube analysed here that spanned a velocity range of -500 to 100 km s^{-1} , see fig. 2.2. This cube is available as an MP4 movie through the online materials for Keenan et al. (2016). Initially source identification was carried out by visual inspection of the data cube. The cube was split into moment 0 maps each of width $\sim 50 \text{ kms}^{-1}$ and these were inspected for individual sources. Visual examination is also preferable to automated source extraction when attempting to distinguish between real sources and radio frequency interference (RFI) (see Taylor et al. 2013 - AGES VI). However, visual inspection does suffer from our subjectivity and is generally slower than most algorithms. In AGES VII we describe a new data cube viewer, which has been specifically designed to assist visual extraction of sources from HI data cubes. The data cube viewer is called FRELLED (FITS Realtime Explorer of Low Latency in Every Dimension). Full details are given in AGES VII appendix A and the source code is available through our website at www.naic.edu/~ages/. FRELLED was used to visualise and catalogue all of our detections.

We then used the MIRIAD task MBSPECT to view the spectra of each identified HI cloud and confirm our detections. Miriad is a radio interferometry data reduction package which can be used for reduction of observations through to image synthesis, analysis and display (Sault et al. 1995b). MBSPECT is particularly useful in this case as it can be used to determine whether a cloud is distinct from the Milky Way (and possibly M33) by confirming that they have separate

spectral peaks i.e.whether our identified HI clouds appear to be distinct both spatially and in velocity. We define a cloud as an object detected after a 3σ clip has taken place on the data cube and channel smoothing has been applied (the channels are smoothed to 10 kms^{-1}). After this the detection is checked with both FRELLED and MBSPECT- for it to be included in our detections it must appear in MBSPECT as a single peak at 3σ , but may separate into more peaks above this level. MBSPECT was also used to measure the velocity widths (at 50 and 20% of peak flux density) of the identified HI clouds. We then used the image display and processing package DS9 to fit ellipses to each of the identified sources. From this we obtained the central coordinates of each cloud and the lengths of the semi-minor and semi-major axes of the fitted ellipse as measured at a column density of 3σ - the noisiest pixel has a 3σ noise value of $\sim 0.1 \text{ Jy}$. The cloud sizes given were calculated using the measured values of the semi-major and semi-minor axes. We used these positions and sizes to measure the total flux density and HI mass within the detection aperture using the standard formula:

$$M = 2.36 \times 10^5 d_{Mpc}^2 \sum f_v \Delta V$$

d_{Mpc} is the distance to the source in Mpc, which we assume to be the same as M33 i.e 0.84 Mpc (Freedman et al. 1991), f_v is the flux density in Jy and ΔV is the velocity width in kms^{-1} . Uncertainties in fluxes and systemic velocities are calculated using equations from Auld et al. (2006). The error on the systemic velocity is given by:

$$\sigma(F_{HI}) = 4 \times SN^{-1}(S_{peak}F_{HI}\delta v)^{1/2}$$

Where S_{peak} is the peak flux, SN is the ratio of S_{peak} to $\sigma(S_{peak})$, F_{HI} is the integrated flux and δv is the velocity resolution of the data.

Errors on fluxes are given by:

$$\sigma(V_{sys}) = 3 \times SN^{-1}(P\delta v)^{1/2}$$

where $P = 0.5 \times (W_{20} - W_{50})$, which is a measure of the steepness of the profile edges.

In addition we can create integrated flux maps by summing pixel values over velocity. Full details of the sources detected and their derived parameters are given in tables 2.1 and 2.2.

AGES ID (AGES M33-) (1)	RA (J2000) (2)	Dec (J2000) (3)	Velocity Width 50 (km s ⁻¹) (4)	Systemic Velocity (km s ⁻¹) (5)	Velocity Relative to M33 (km s ⁻¹) (6)	HI Mass (M _⊙) (7)	Flux (Jy km s ⁻¹) (8)	Size (a,b kpc) (9)	Column Density (cm ⁻²) (10)	Previous Detection? (11)
1	01:34:51.3	+ 30:59:59	51.0	-86 ± 3	94 ± 3	1.18×10^6	7.1 ± 0.4	3.0×1.7	3.9×10^{18}	G08-AA1
2	01:40:13.2	+ 30:50:57	26.0	-111 ± 15	69 ± 15	1.62×10^6	9.7 ± 2.5	4.9×2.4	2.4×10^{18}	G08-AA2
3	01:44:03.7	+ 31:14:33	30.5	-121 ± 3	59 ± 3	1.48×10^6	8.9 ± 0.2	3.7×2.4	2.9×10^{18}	none
5	01:39:31.4	+ 30:41:30	32.8	-126 ± 3	54 ± 3	2.13×10^6	12.8 ± 0.2	2.4×2.4	6.2×10^{18}	G08-AA5
9	01:39:42.4	+ 31:27:32	28.5	-180 ± 7	0 ± 7	3.00×10^5	1.8 ± 0.2	3.2×1.7	9.5×10^{17}	none
10	01:41:00.8	+ 30:05:17	21.0	-164 ± 3	16 ± 3	2.33×10^5	1.4 ± 0.1	2.4×2.4	6.9×10^{17}	none
12	01:33:27.8	+ 29:14:49	29.2	-186 ± 4	-6 ± 4	6.66×10^5	4.0 ± 0.3	3.7×2.4	1.3×10^{18}	G08-AA9
14	01:31:18.3	+ 30:00:54	22.7	-188 ± 3	-8 ± 3	1.91×10^6	11.5 ± 0.2	1.7×1.7	1.1×10^{19}	G08-AA10
19	01:29:52.0	+ 31:04:23	34.1	-288 ± 3	-108 ± 3	9.99×10^4	0.6 ± 0.1	3.7×1.2	3.5×10^{17}	G08-AA17
20	01:34:27.6	+ 29:30:00	38.4	-315 ± 6	-135 ± 6	2.00×10^6	12.0 ± 0.5	6.1×3.7	1.6×10^{18}	none
21	01:39:41.7	+ 29:58:32	32.6	-307 ± 5	-127 ± 5	1.67×10^5	1.0 ± 0.1	1.7×1.7	1.0×10^{18}	none
22	01:33:41.3	+ 30:57:00	32.8	-338 ± 15	-158 ± 15	9.99×10^5	6.0 ± 0.6	6.6×3.7	7.2×10^{17}	none
23	01:37:47.2	+ 30:23:48	49.5	-352 ± 4	-172 ± 4	2.53×10^6	15.2 ± 0.4	6.6×3.7	1.8×10^{18}	none
24	01:34:37.0	+ 30:08:00	26.7	-328 ± 3	-148 ± 3	1.18×10^6	7.1 ± 0.3	4.9×3.7	1.1×10^{18}	G08-AA18
25	01:31:36.5	+ 30:13:55	36.9	-324 ± 5	-144 ± 5	1.78×10^6	10.7 ± 0.4	6.1×4.4	1.2×10^{18}	G08-AA20
26	01:24:32.8	+ 30:36:43	56.4	-359 ± 5	-179 ± 5	5.99×10^5	3.6 ± 0.2	3.2×2.4	1.3×10^{18}	none
27	01:27:17.8	+ 30:05:21	16.9	-377 ± 3	-197 ± 3	6.66×10^5	4.0 ± 0.2	7.3×2.4	6.5×10^{17}	none
28	01:38:04.7	+ 29:56:46	44.8	-335 ± 5	-155 ± 5	2.26×10^6	13.6 ± 0.5	9.7×3.7	1.1×10^{18}	none
29	01:33:18.6	+ 29:29:59	71.1	-335 ± 7	-155 ± 7	5.16×10^5	3.1 ± 0.2	3.7×2.4	9.9×10^{17}	G08-AA19
30	01:40:20.3	+ 29:11:24	24.5	-341 ± 3	-161 ± 3	5.00×10^5	3.0 ± 0.2	3.7×2.4	9.8×10^{17}	none
31	01:37:00:2	+ 30:01:52	17.7	-374 ± 3	-194 ± 3	1.22×10^7	73.5 ± 0.5	18.2×14.6	7.9×10^{17}	G08-AA21a, 21b
32	01:24:06.1	+29:38:35	25.4	-383 ± 3	-203 ± 3	4.54×10^7	272.6 ± 0.7	10.9×10.9	6.5×10^{18}	Wright's cloud

TABLE 2.1 Properties for all 'isolated' clouds. 1) name, 2) and 3) RA and Dec (J2000), 4) velocity width at FWHM (50%), 5) central velocity of cloud from MBSPECT, 6) velocity relative to M33 (M33 velocity = -180 km s⁻¹, 7) HI mass at M33 distance, 8) total measured flux density, 9) measured size of cloud along the semi-major and semi-minor (kpc). Measured to the nearest pixel which corresponds to ~0.2 kpc 10) the peak column density of cloud as measured by our 3.5 arcmin beam and 11) whether the cloud has been previously detected by another survey. N.B. values for AGESM33-32 (Wright's cloud) only measure amount of cloud visible in our cube. Where necessary a distance to the clouds of 840 kpc is assumed (Freedman et al. 1991). Errors on velocities and fluxes were calculated with parameters from MBSPECT, equations given in Auld et al. (2006). Where velocity error was <3 km s⁻¹, error is given as 3 km s⁻¹. This is because the central velocity is accurate to with half a channel.

AGES ID (AGES M33-) (1)	RA (J2000) (2)	Dec (J2000) (3)	Velocity Width 50 (km s ⁻¹) (4)	Systemic Velocity (km s ⁻¹) (5)	Velocity Relative to M33 (km s ⁻¹) (6)	HI Mass (M _⊙) (7)	Flux (Jy km s ⁻¹) (8)	Size (x,y kpc) (9)	Column Density (cm ⁻²) (10)	G08 ID (11)
AGESM33-4	01:37:56.4	+ 30:10:15	29.4	-136 ± 3	44 ± 3	5.08×10^6	30.5 ± 0.3	6.1×2.2	6.60×10^{18}	AA4
AGESM33-6	01:32:30.6	+ 29:26:56	22.7	-149 ± 3	31 ± 3	5.48×10^6	32.9 ± 0.4	3.2×3.1	9.4×10^{18}	AA6
AGESM33-7	01:38:11.8	+ 29:47:11	57.7	-137 ± 3	43 ± 3	1.08×10^6	6.5 ± 0.3	2.2×2.4	3.5×10^{18}	AA7
AGESM33-8	01:36:15.0	+ 29:58:10	42.3	-158 ± 3	22 ± 3	5.33×10^5	3.2 ± 0.1	1.5×1.2	5.2×10^{18}	AA8
AGESM33-11	01:34:18.8	+ 31:32:00	43.8	-191 ± 3	-11 ± 3	7.49×10^5	4.5 ± 0.1	1.9×1.2	5.50×10^{17}	AA13
AGESM33-13	01:38:26.0	+ 30:50:37	36.6	-191 ± 6	-11 ± 6	2.33×10^5	1.4 ± 0.1	1.2×1.2	2.7×10^{18}	AA11
AGESM33-15	01:29:56.6	+ 31:16:46	35.6	-199 ± 3	-19 ± 3	2.61×10^6	15.7 ± 0.2	2.4×2.4	7.6×10^{18}	AA12
AGESM33-16	01:27:51.3	+ 31:31:21	34.1	-245 ± 3	-65 ± 3	3.73×10^6	22.4 ± 0.2	3.7×3.1	5.6×10^{18}	AA14
AGESM33-17	01:28:49.8	+ 31:40:37	27.9	-263 ± 3	-83 ± 3	1.15×10^6	6.9 ± 0.1	3.7×2.4	2.2×10^{18}	AA15
AGESM33-18	01:35:28.9	+ 30:43:17	34.6	-292 ± 6	-112 ± 6	9.66×10^5	5.8 ± 0.5	2.4×2.4	2.8×10^{18}	AA16

TABLE 2.2 The above table gives our derived properties of all clouds listed by Grossi et al 2008 which are either part of the disc of M33 or joined to M33 by low column density HI . All columns are the same as in table 2.1, with the exception of column 11 which is the cloud ID given in G08.

2.5 IDENTIFYING CLOUDS

As a check of our calibration compared to other surveys we measured the HI mass of M33 in the same way as the other HI clouds identified - we obtain a total HI mass for M33 of $4.7 \times 10^9 M_{\odot}$. To compare this result with a previously derived value we reduced our aperture to approximately the same size as that given in Putman et al. (2009). When this was done a HI mass of $2.0 \times 10^9 M_{\odot}$ was obtained, this compares well with the value given in Putman et al. (2009), which is $1.4 \times 10^9 M_{\odot}$ - the masses agree to within 30%, though defining exactly the same apertures both spatially and in velocity is not possible.

Using the source extraction methods described above we have identified 32 clouds that have a probable association with M33. Below are moment zero (integrated flux maps), moment 1 (velocity field) and spectra for each detected source. The sources are split into two groups: those that appear discrete and those that clearly show an extended connection to M33. One clear initial result is that some of the features identified by Grossi et al. (2008) as discrete clouds are actually connected to the HI disc of M33 by areas of low column density HI in the AGES data, which has a better column density sensitivity. This is demonstrated in fig. 2.3 which shows the positions of clouds, which fall within the disk of M33.

We employed a similar distinguishing criterion to Braun and Thilker (2002) to separate what are described as discrete objects from those that are clearly linked to M33 by low column density HI i.e they describe them as discrete if there is no connection observed down to a column density of $1.5 \times 10^{17} \text{ cm}^{-2}$. Table 2.1 is a full list of the 22 HI clouds that are identified as being discrete down to our column density sensitivity limit of $\sim 1.5 \times 10^{17} \text{ cm}^{-2}$. Table 2.2 lists 10 additional clouds from Grossi et al. (2008), which we detect but are either clearly part of the disc of M33 or joined to M33 by low column density HI . These latter objects have been listed in a separate table as they cannot be classified as independent clouds due to their obvious connection to M33. These objects may be of an entirely different nature to those in table 2.1, for example the result of tidal interactions rather than potential primordial objects. Of course, future more sensitive observations may reveal low column density HI between objects considered here to be discrete.

We detected all clouds listed in Grossi et al. (2008), with the exception of their clouds AA3, AA22 and AA23, which do not appear in this data at the coordinates and velocities specified. Grossi et al. (2008) state that their clouds AA4, AA6, AA12, AA13 and AA14 are connected to M33, this list is here extended to include AA7, AA8, AA11, AA15 and AA16. In addition to this, the clouds Grossi et al.

(2008) designate as AA21a and AA21b appear in our data to be a single ring like structure (AGESM33-31, see below). A moment zero map of our data is shown in fig. 2.4. The outline of M33's HI disc is shown, with all discrete clouds overlaid. The figure was made by integrating the flux over the velocity range of each cloud, then filling in the lowest contour. The colour indicates the central velocity of each cloud. The large structure to the bottom right of fig. 2.4 has previously been identified and is known as Wright's cloud (Wright 1979).

These results can also be compared to those of Braun & Thilker (2004). As stated above their survey covers the much larger M33/M31 region, but is somewhat compromised compared to our survey by the large spatial resolution of 49 arcmin. Using the Braun & Thilker (2004) sensitivity limits we calculated that their minimum detectable HI mass at the distance of M33 is about $10^5 M_\odot$, which is smaller than the mass of most of the clouds we have detected (see tables 2.1 and 2.2). Braun & Thilker (2004) only detect two discrete clouds over the region where our data overlaps (as listed in Thilker et al. 2002), so the limitation of their data compared to ours must be their spatial resolution. We detected both of the clouds described in Braun & Thilker (2004) using the AGES data. Wright's cloud (AGESM33-32), which is a previously known HI cloud, is either associated with M33 or possibly extended debris from the Magellanic stream. Wright's cloud has a total mass of $\sim 10^8 M_\odot$ (Wright 1979), but our cube only contains part of it (fig. 2.4), it is fully described in Wright 1979. The second cloud, AGESM33-31, will be discussed in detail in section 2.7.

The detected clouds range in HI mass from $1.0 \times 10^5 M_\odot$ to $4.5 \times 10^7 M_\odot$ and have velocity widths of between ~ 17 and ~ 72 km s^{-1} at 50% of their peak flux density. The smallest of the clouds is just over 1 kpc in size and, as the Arecibo beam size is about 1 kpc on the sky at the distance of M33 (840 kpc), we wouldn't expect to measure sizes any smaller than this.

2.6 COLUMN DENSITY MAPS, VELOCITY MAPS AND SPECTRA OF THE CLOUDS AROUND M33

For figures 2.5 to 2.37 below image (a) is an integrated flux map, (b) is a velocity map and (c) is the spectrum taken from MBSPect with the cloud marked. In all instances except AGESM33-8, AGESM33-15 and AGESM33-18 the peak can be clearly distinguished (these are clouds detected by G08 as AA8, AA12 and AA16). The integrated flux maps show clouds AGESM33-8 and AGESM33-15 to

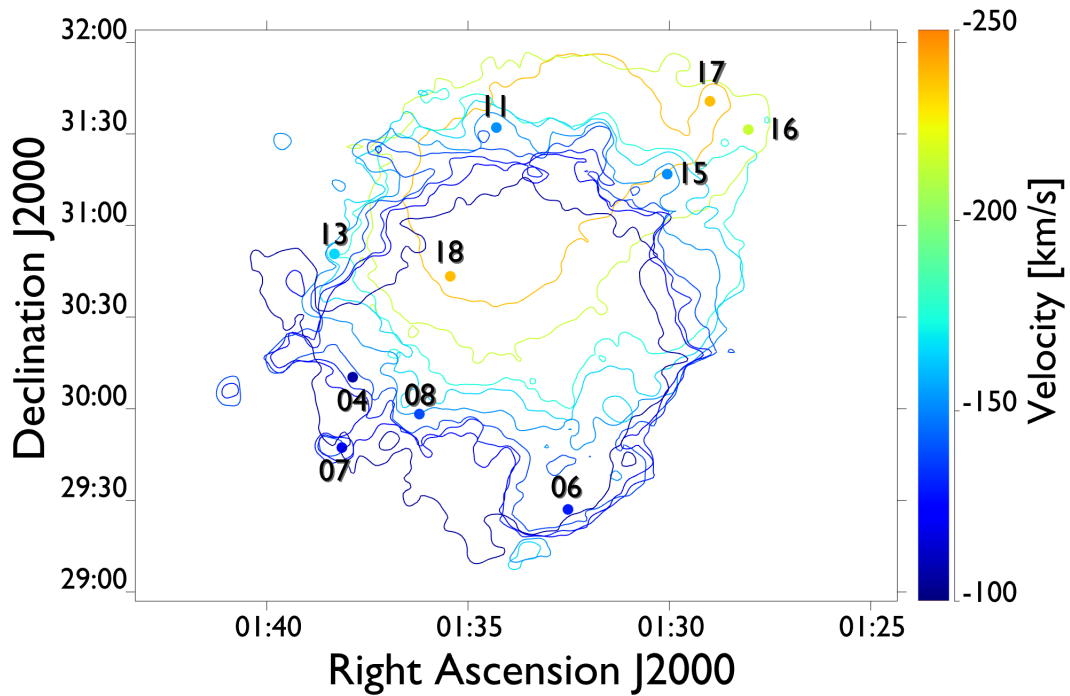


FIGURE 2.3 A Renzogram of M33 across a velocity range of 150km s^{-1} . Labelled dots indicate the positions of clouds which appear to form part of the disk of M33 (table 2.2). Colours are indicative of velocity.

be joined to the disk of M33 by low column density hydrogen. On inspection of the integrated flux map AGESM33-18 is indistinguishable from the disk of M33. It has been included as it can be seen as a very small peak in the spectra of M33.

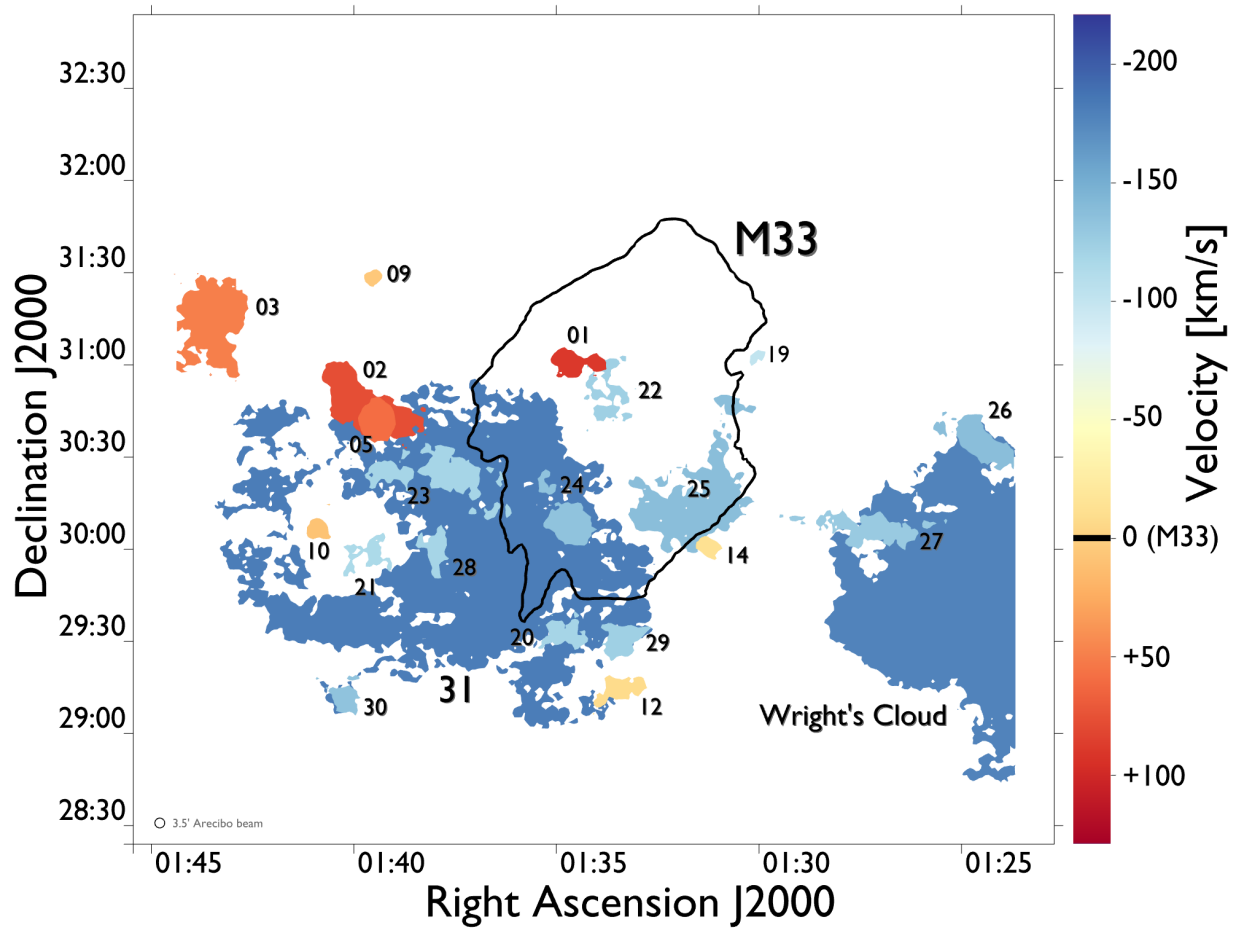


FIGURE 2.4 The outline of M33's HI disk is shown, with all of the discrete detected clouds overlaid. The figure was made by integrating the flux over the velocity range of each cloud, then filling in the lowest contour. The central velocity of each cloud was used so the colours are indicative of this velocity. The black line shows the approximate extent of M33. Velocities shown are relative to M33.

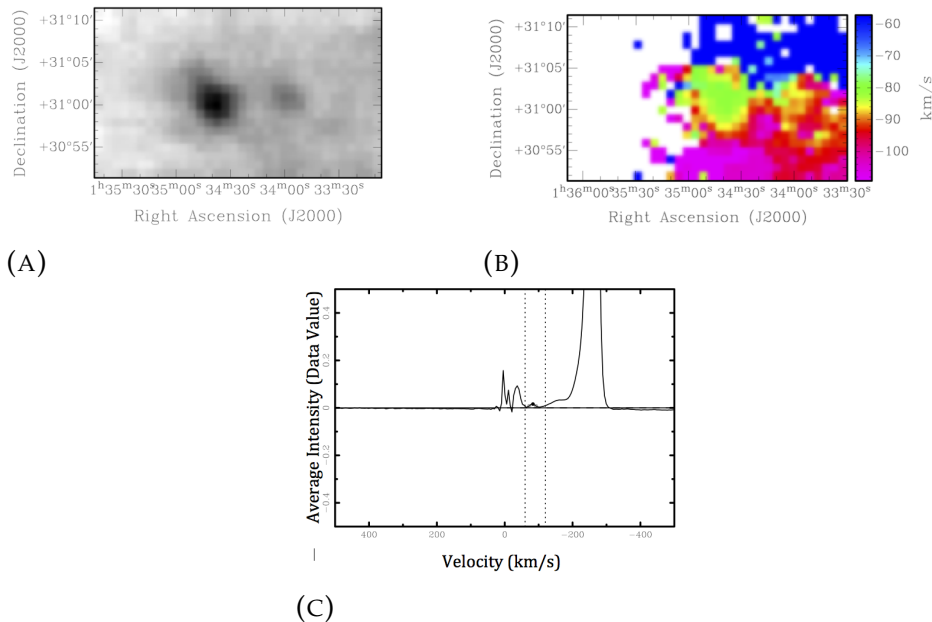


FIGURE 2.5 AGESM33-1

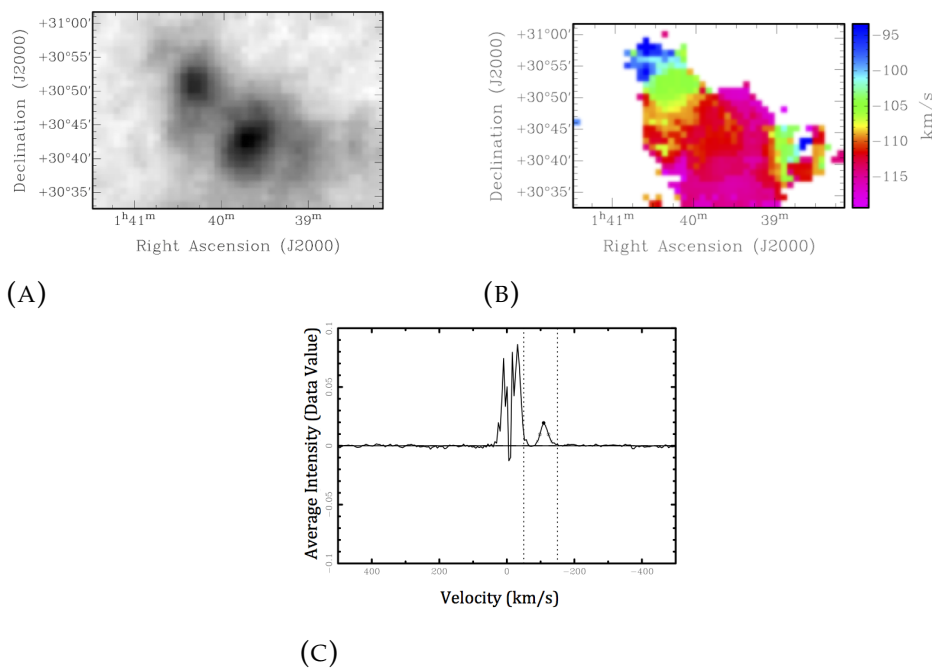


FIGURE 2.6 AGESM33-2

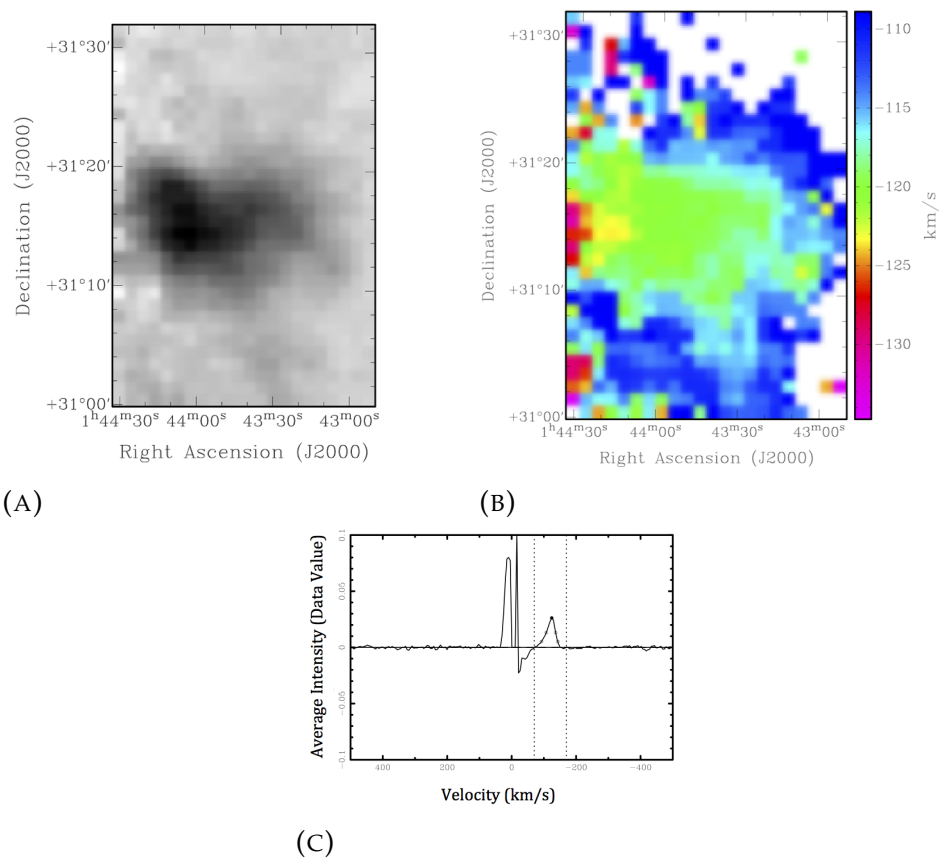


FIGURE 2.7 AGESM33-3

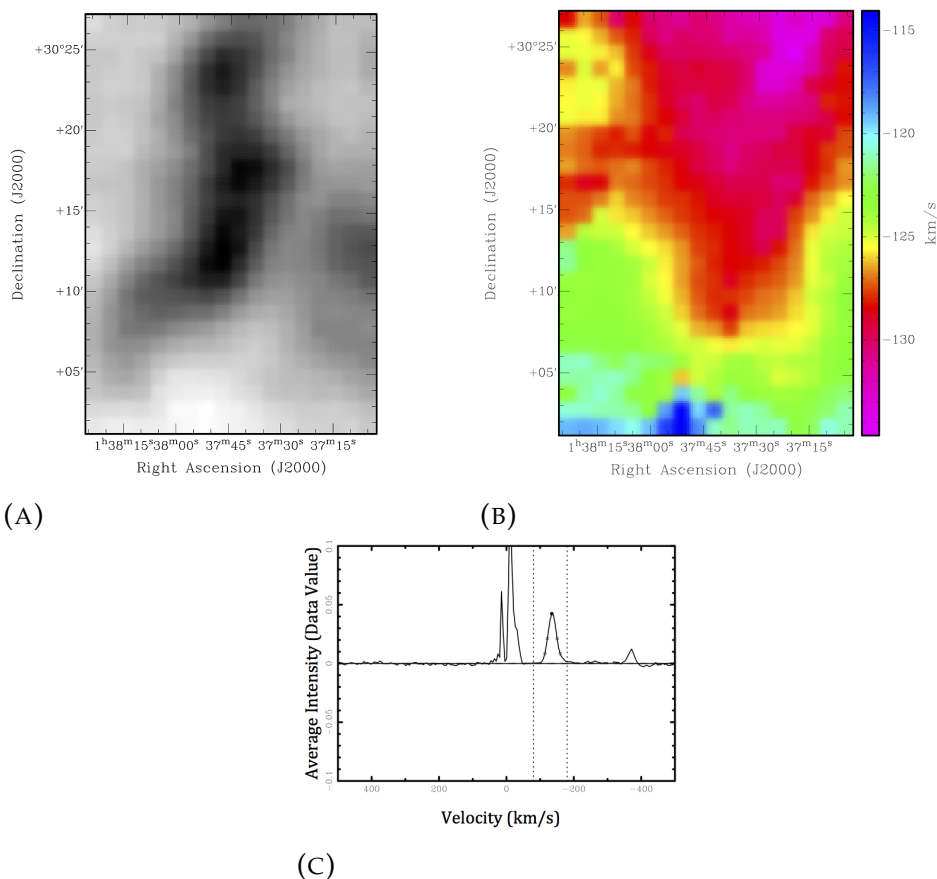


FIGURE 2.8 AGESM33-4

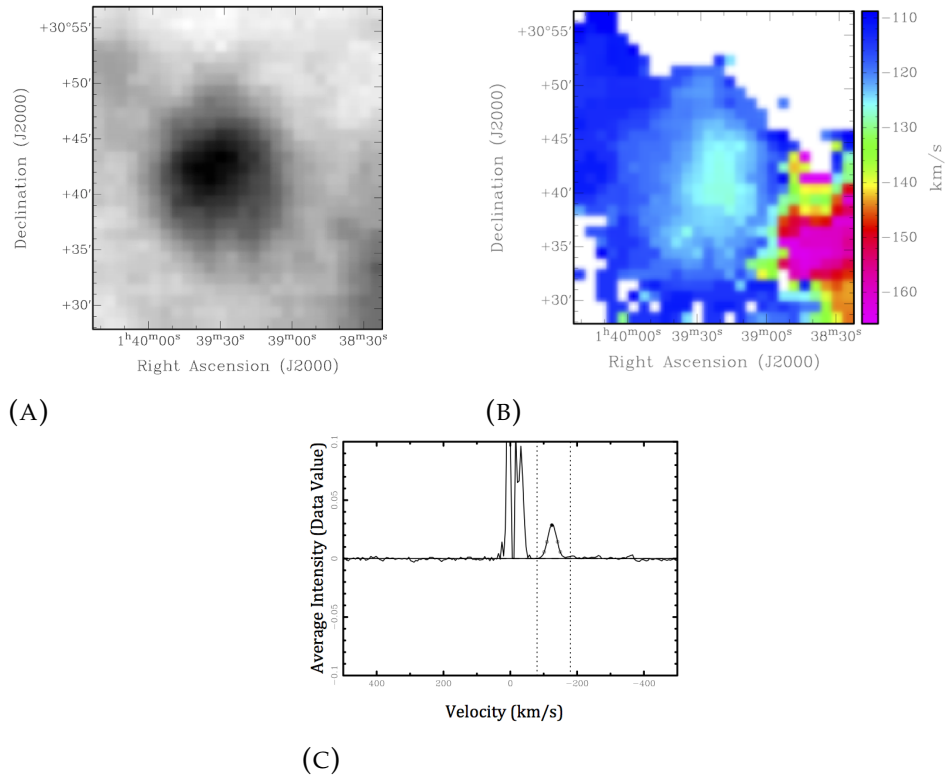


FIGURE 2.9 AGESM33-5

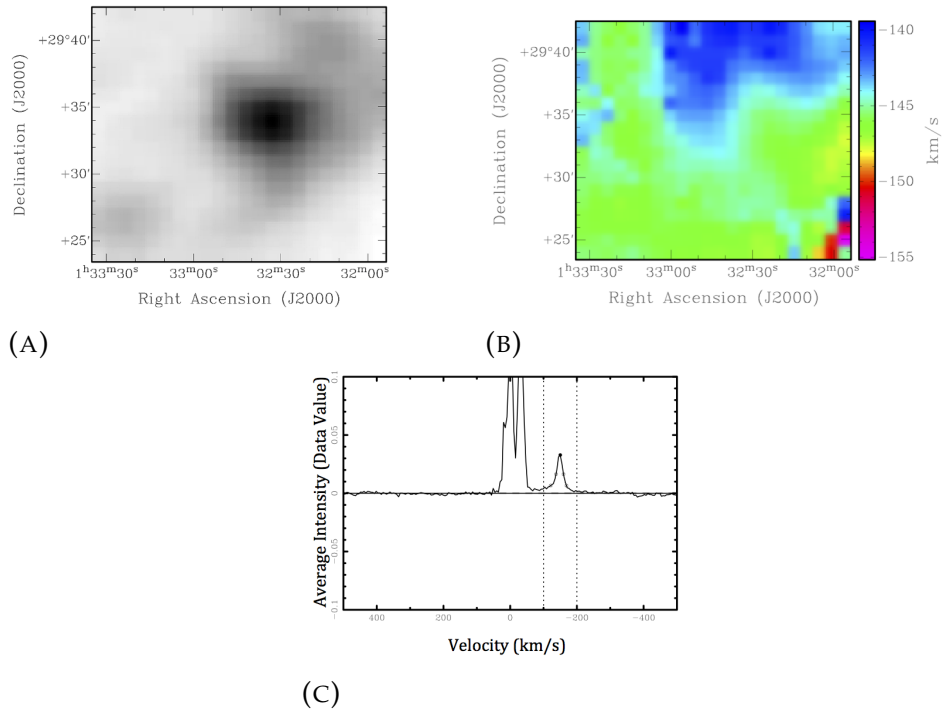


FIGURE 2.10 AGESM33-6

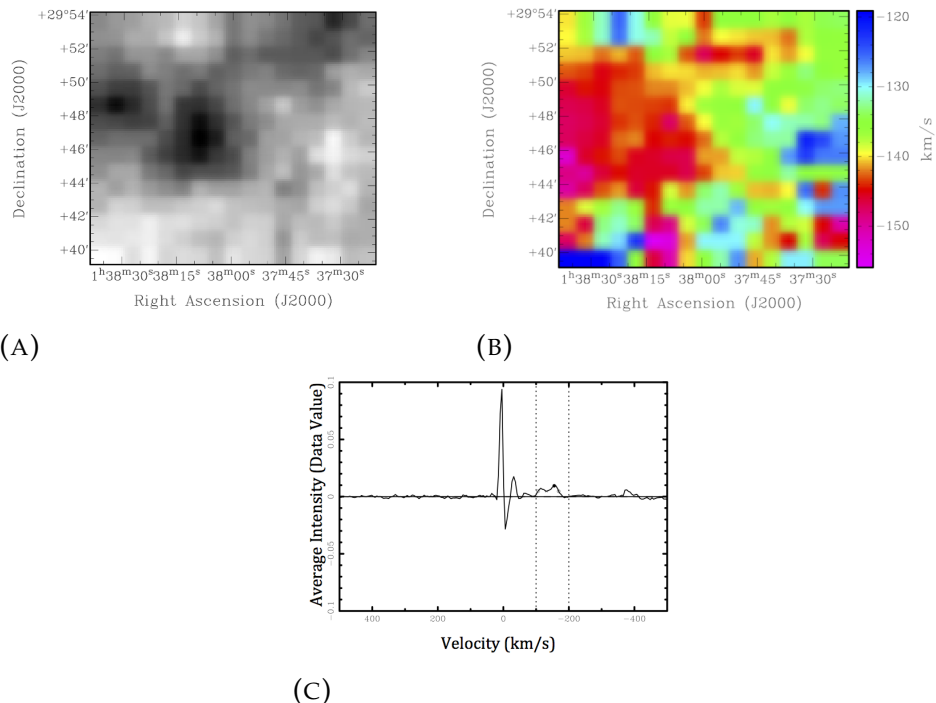


FIGURE 2.11 AGESM33-7

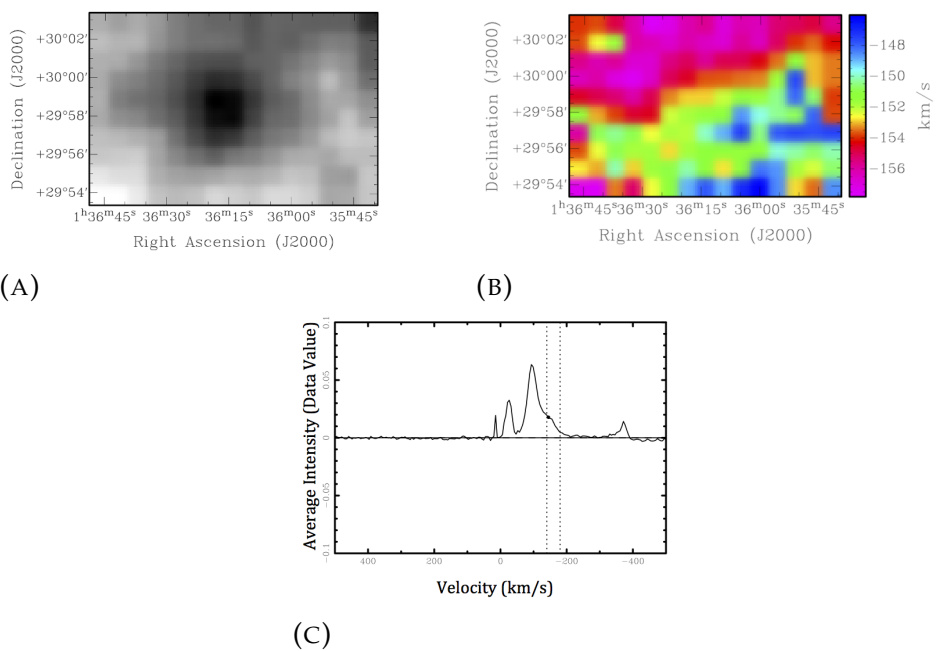


FIGURE 2.12 AGESM33-8

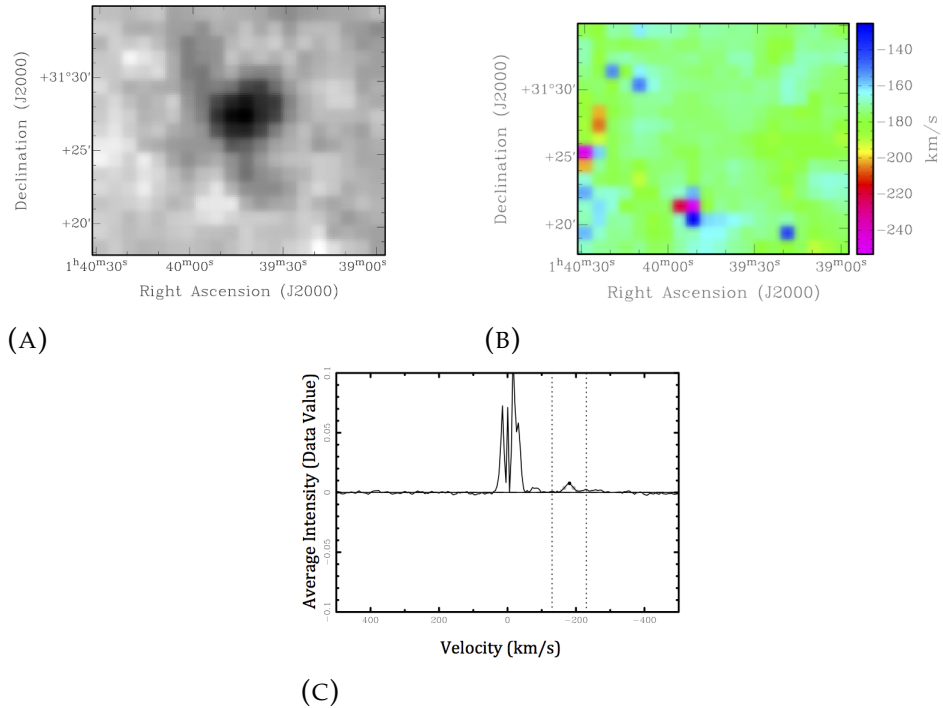


FIGURE 2.13 AGESM33-9

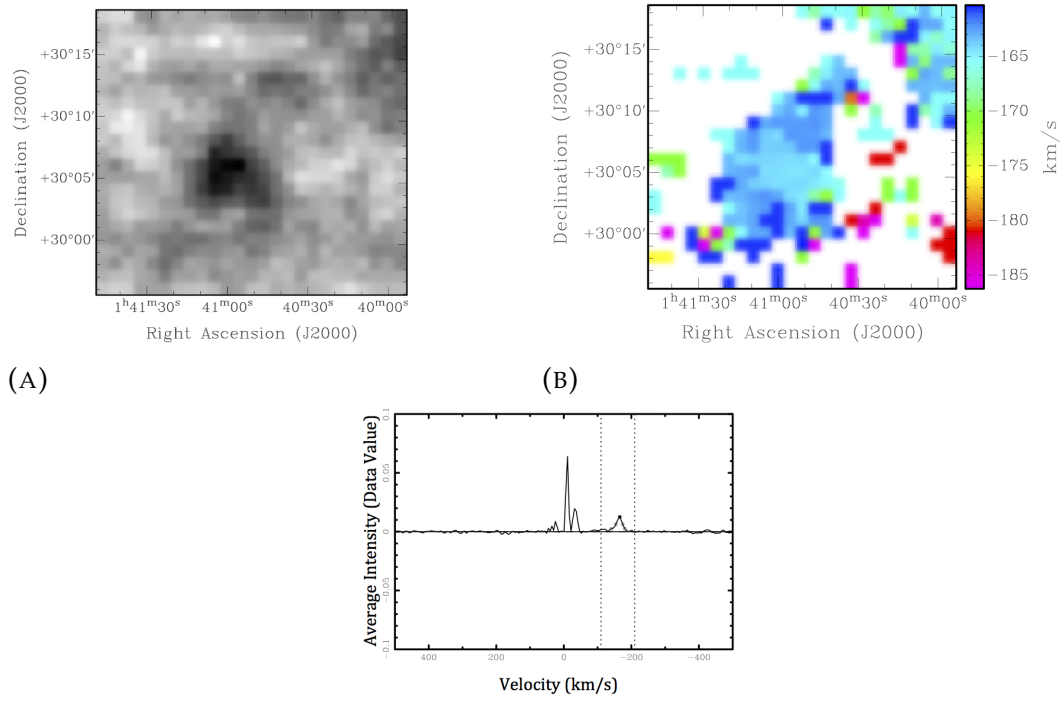


FIGURE 2.14 AGESM33-10

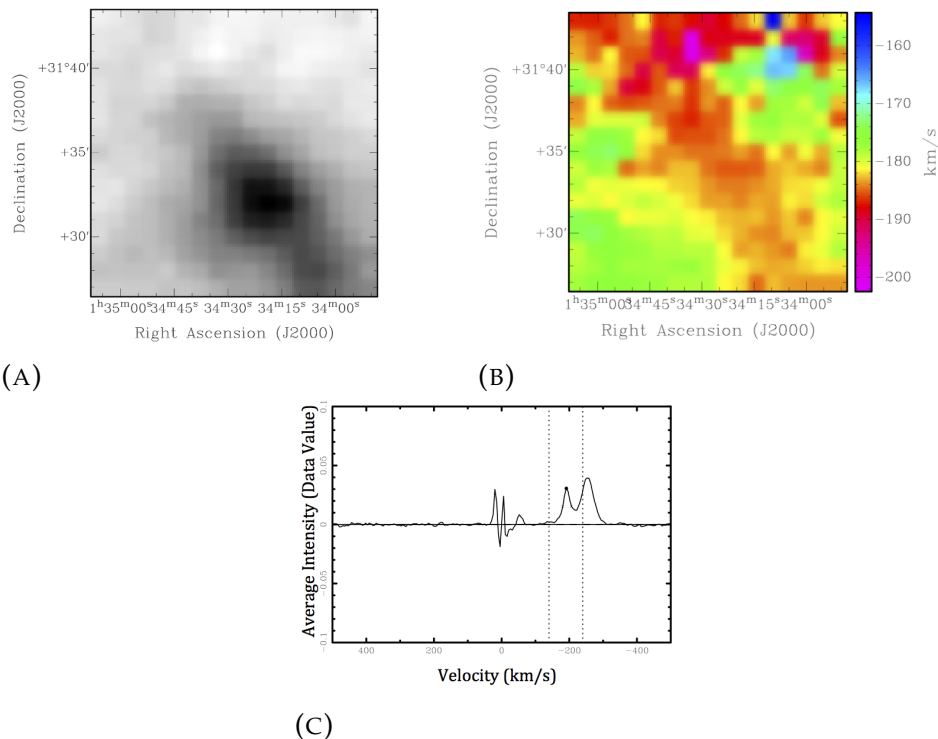


FIGURE 2.15 AGESM33-11

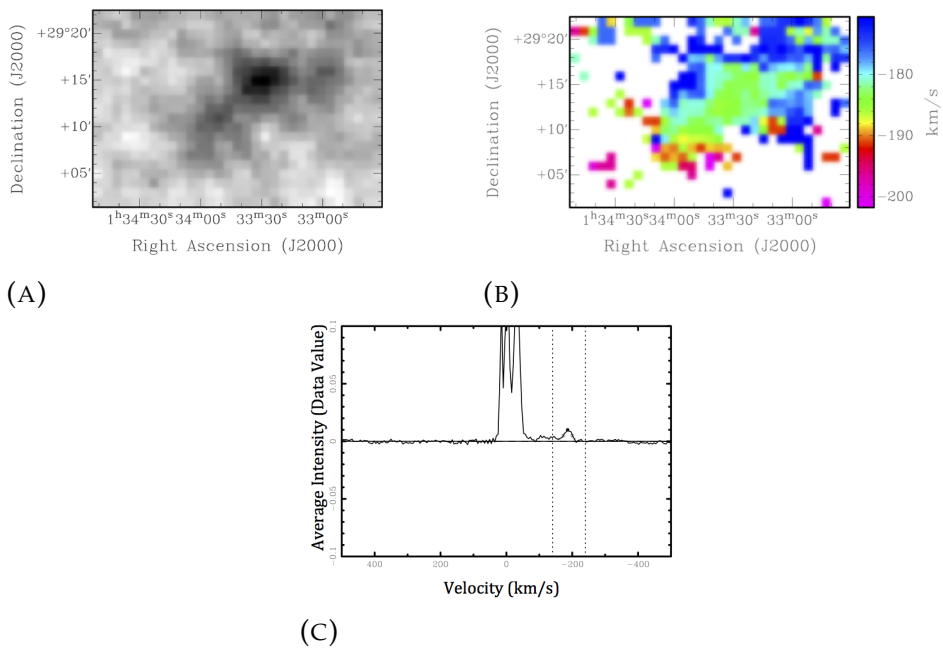


FIGURE 2.16 AGESM33-12

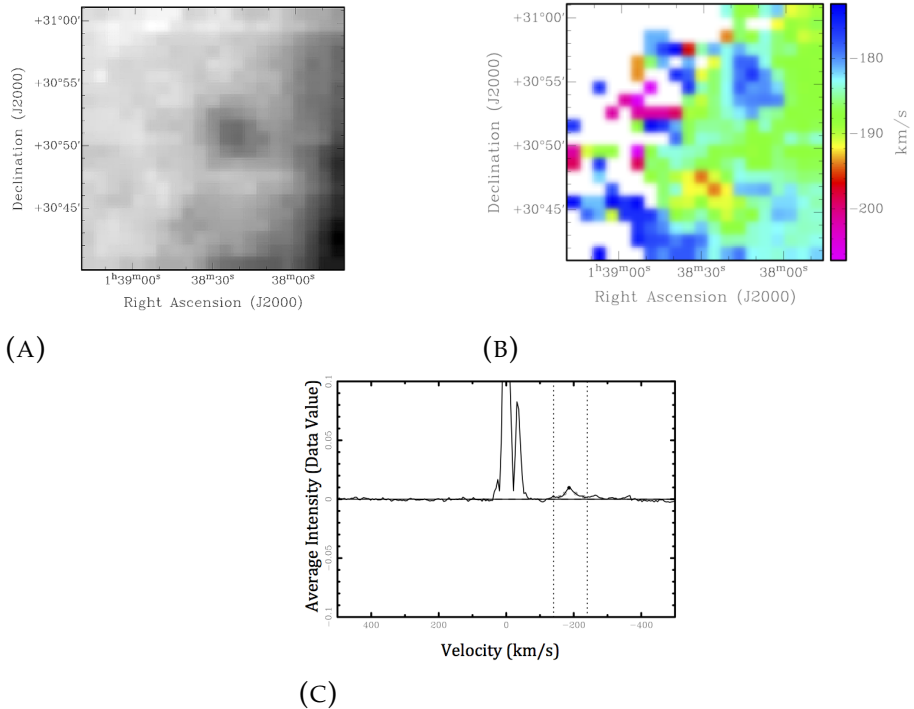


FIGURE 2.17 AGESM33-13

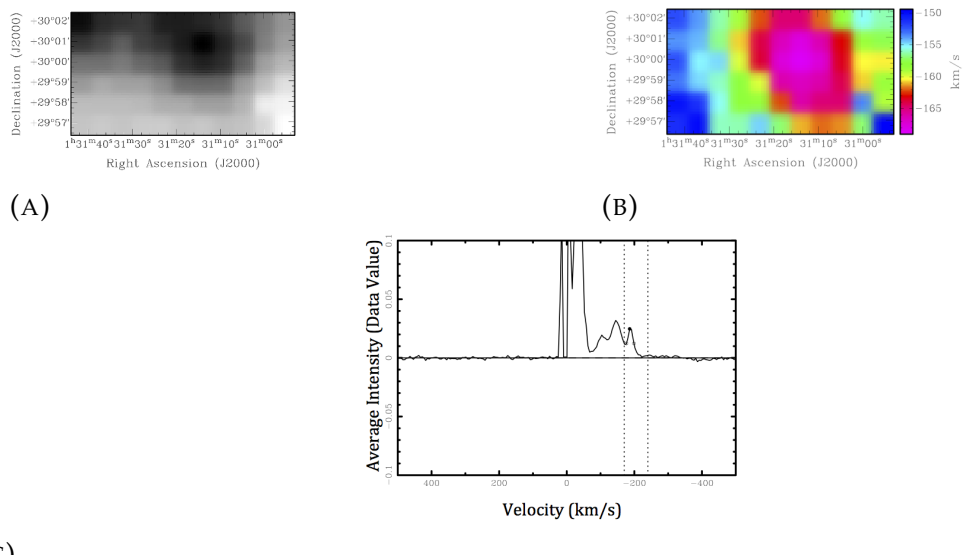


FIGURE 2.18 AGESM33-14

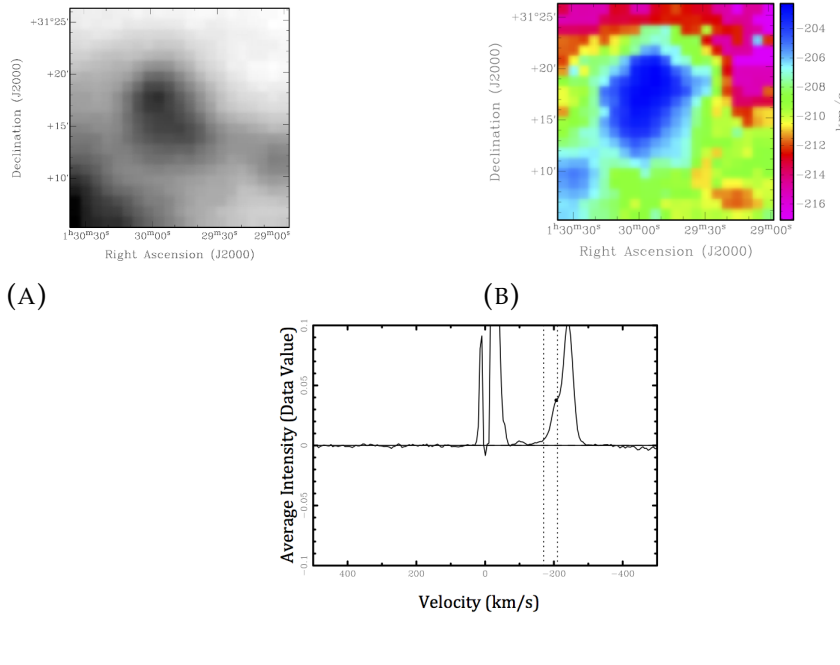


FIGURE 2.19 AGESM33-15

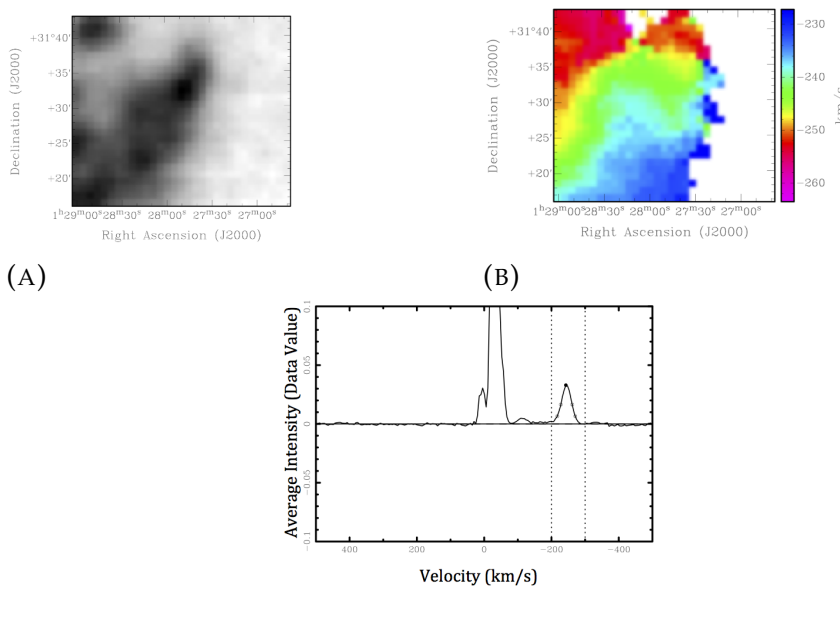


FIGURE 2.20 AGESM33-16

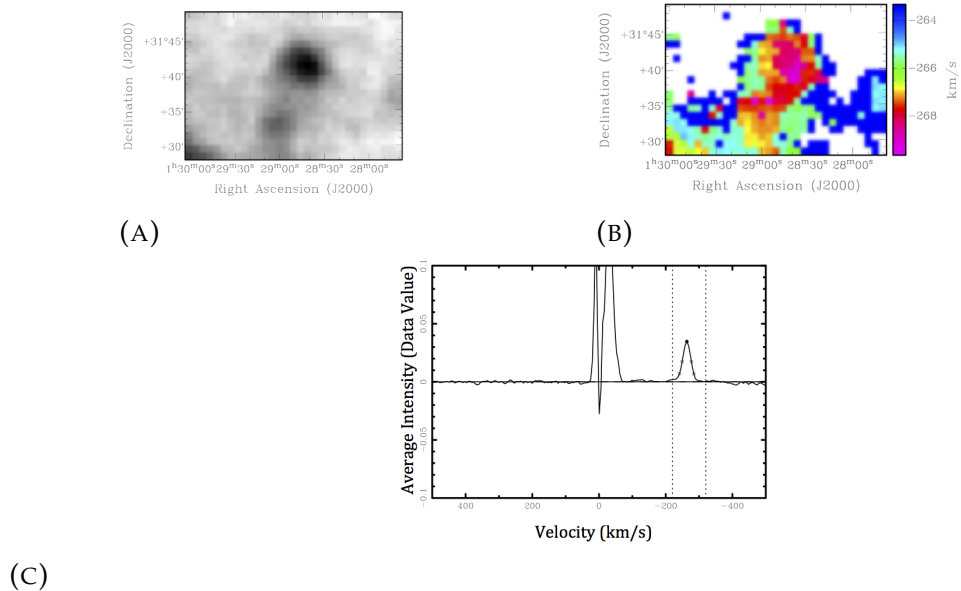


FIGURE 2.21 AGESM33-17

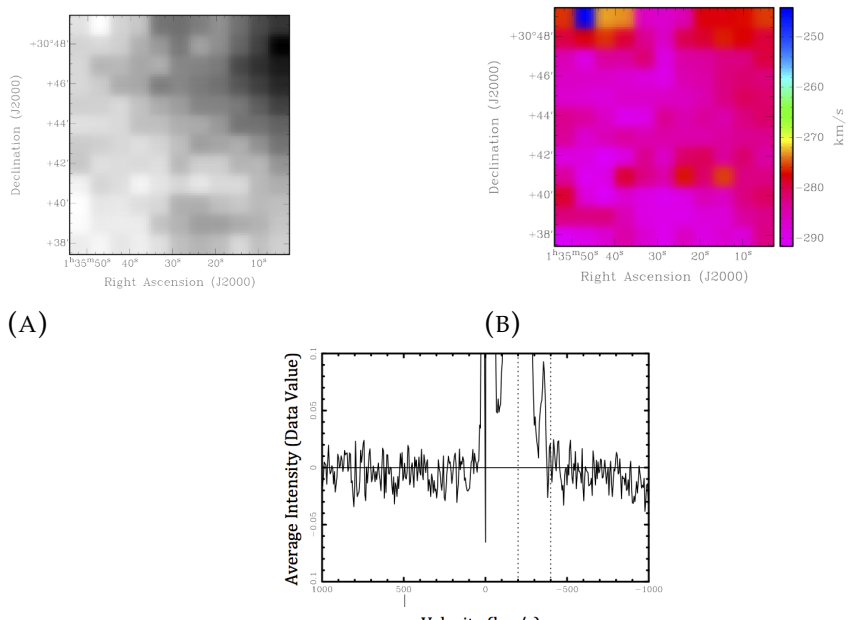


FIGURE 2.22 AGESM33-18

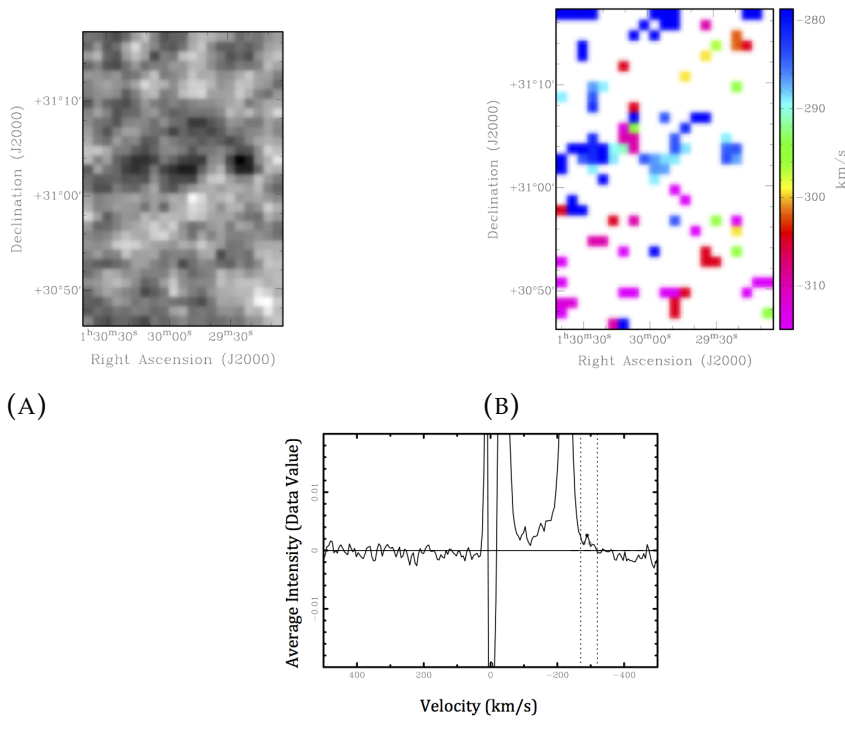


FIGURE 2.23 AGESM33-19

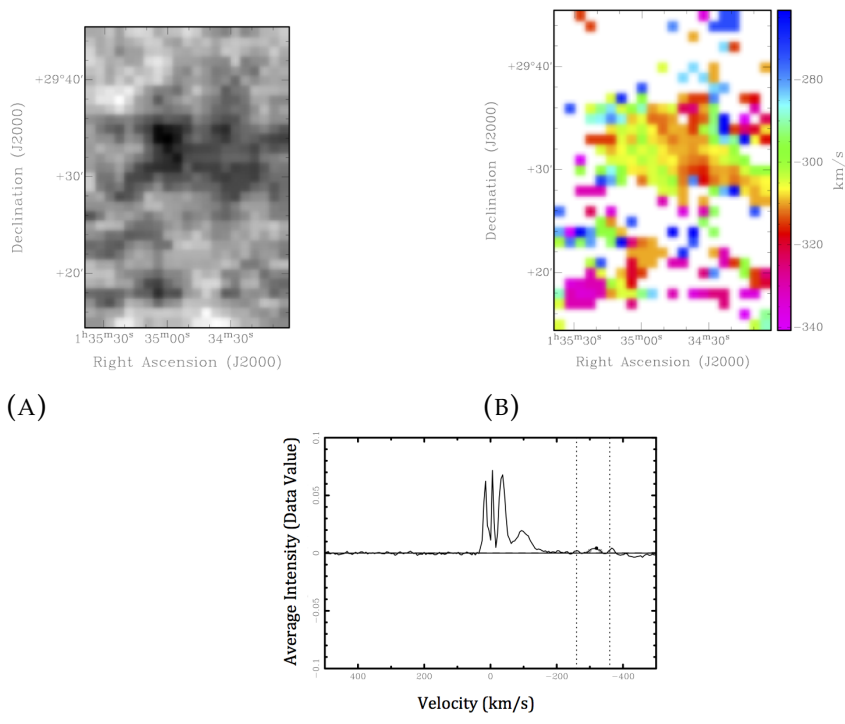


FIGURE 2.24 AGESM33-20

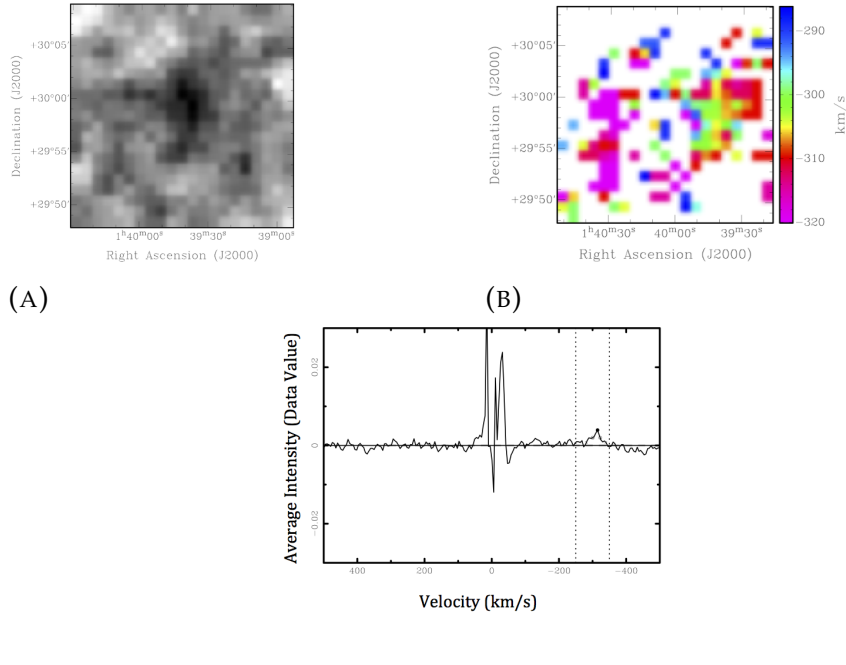


FIGURE 2.25 AGESM33-21

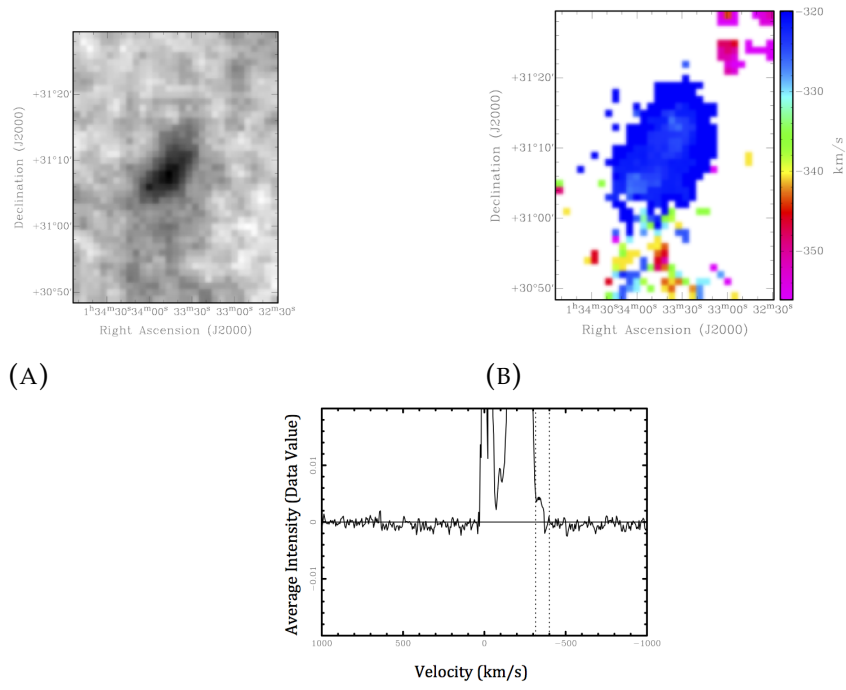


FIGURE 2.26 AGESM33-22

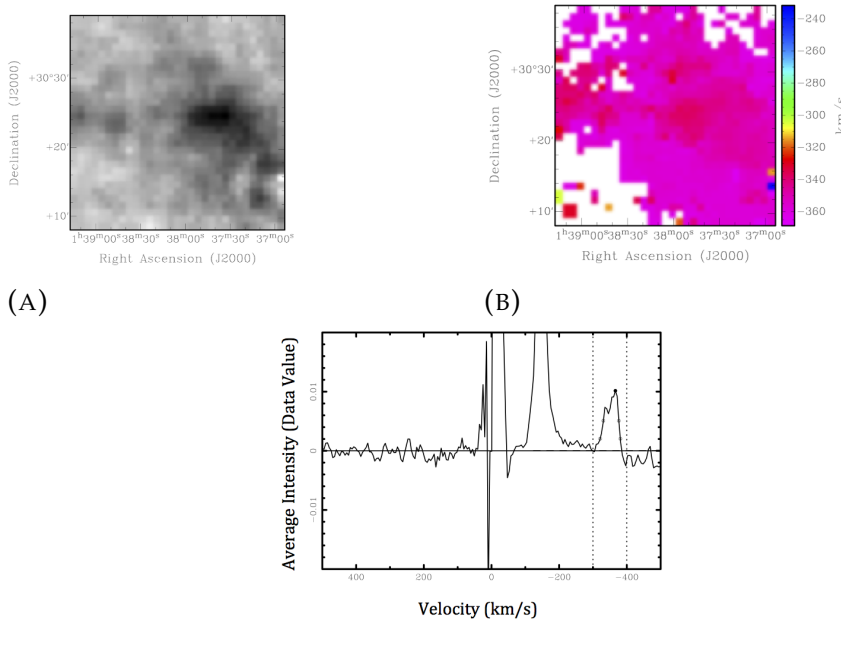


FIGURE 2.27 AGESM33-23

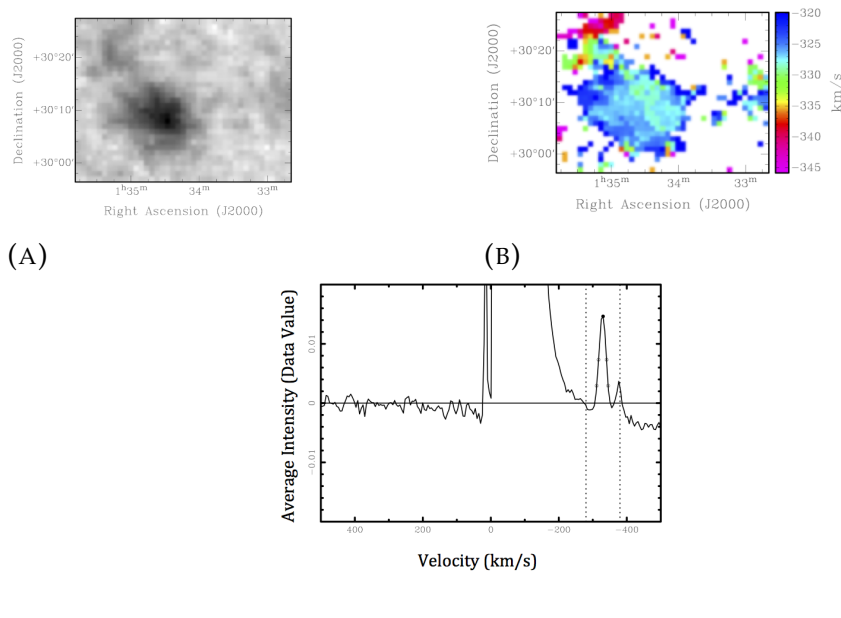


FIGURE 2.28 AGESM33-24

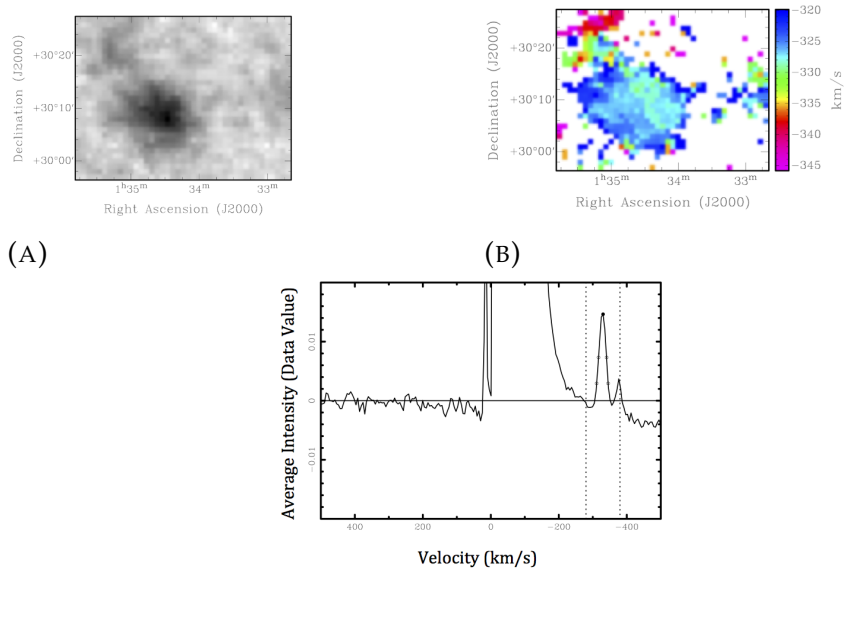


FIGURE 2.29 AGESM33-24

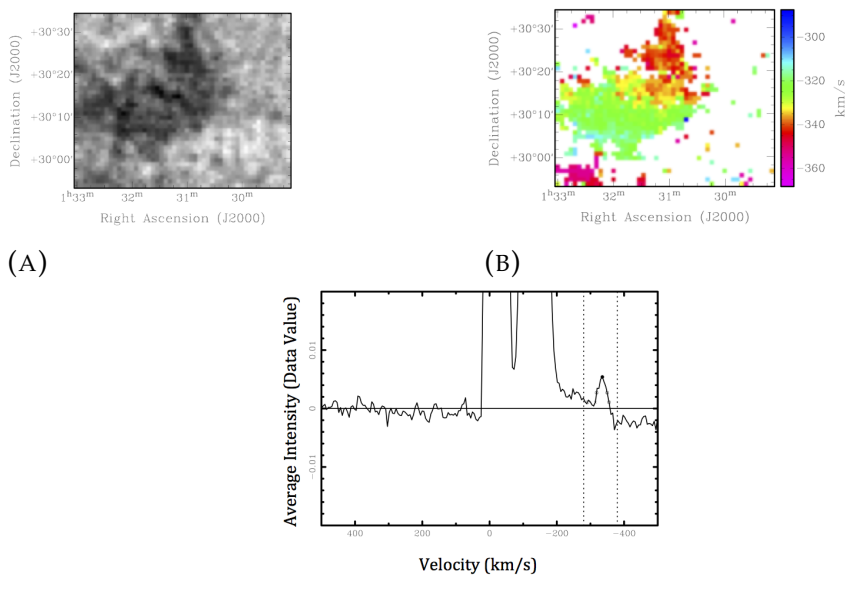


FIGURE 2.30 AGESM33-25

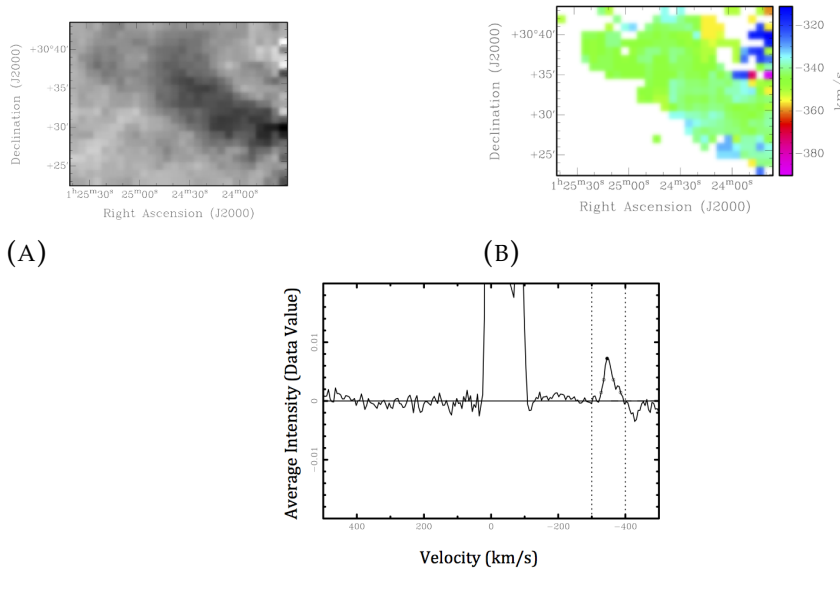


FIGURE 2.31 AGESM33-26

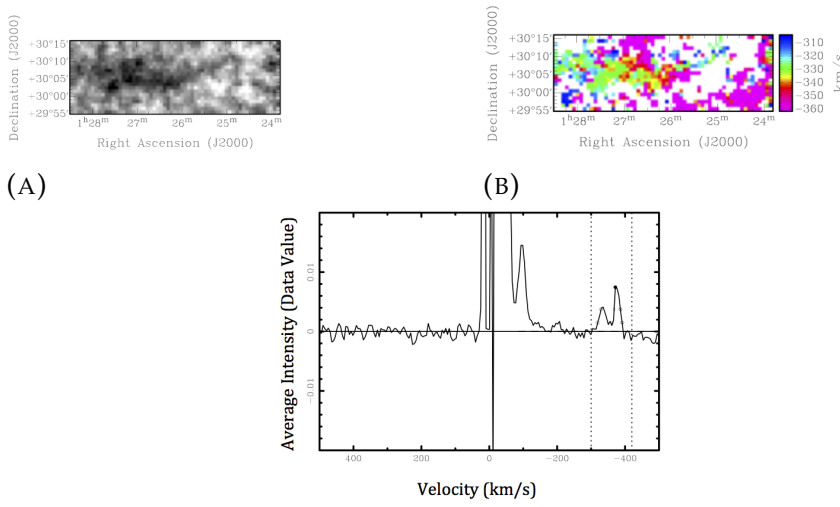


FIGURE 2.32 AGESM33-27

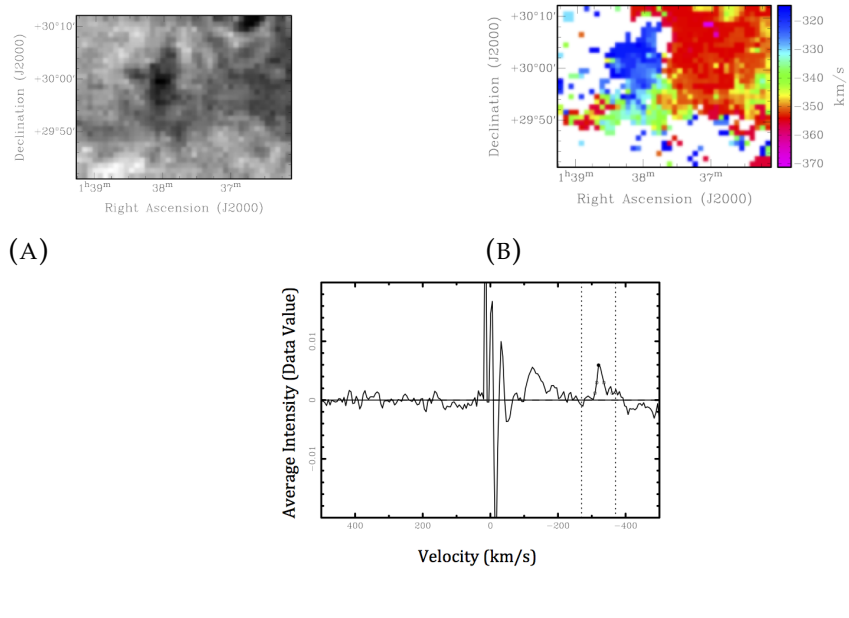


FIGURE 2.33 AGESM33-28

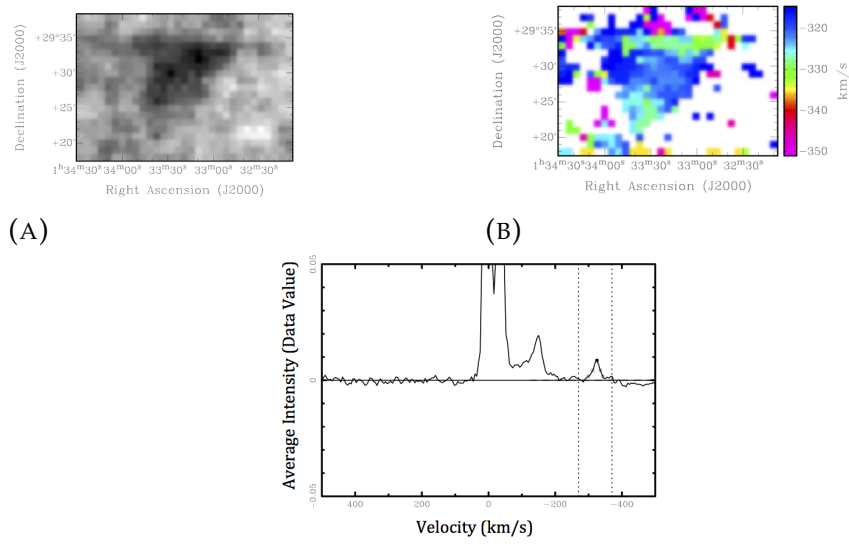


FIGURE 2.34 AGESM33-29

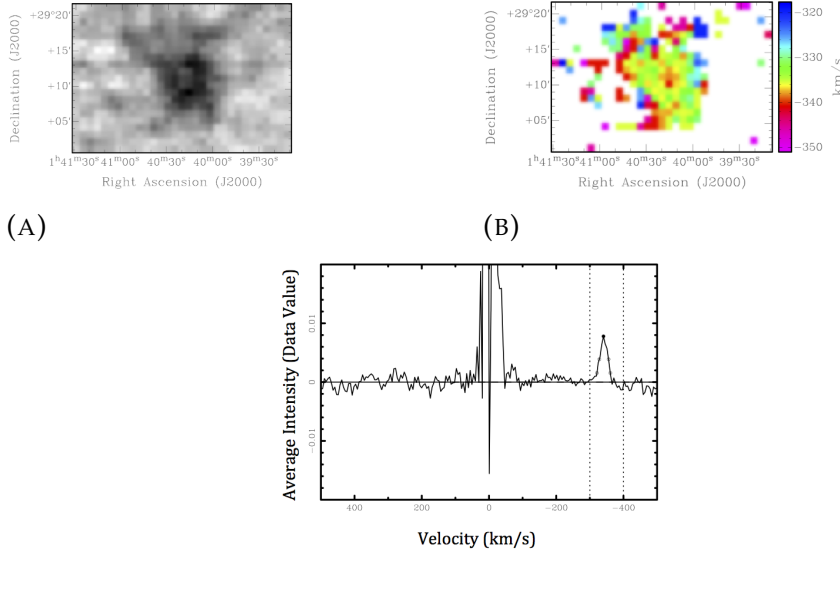


FIGURE 2.35 AGESM33-30

2.7 THE RING CLOUD

Cloud AGESM33-31 is particularly interesting. If at the same distance as M33 (840 kpc, Freedman et al. 1991) it has a diameter of over 18kpc, making it of a comparable size to M33 itself. The cloud is ring shaped with a large central hole of about 10kpc across. It has been previously detected in two separate surveys, but never resolved into one ring-shaped cloud. Firstly, it was detected by Thilker et al. (2002) as 'M33CHVC' but was unresolved. Then, Grossi et al. (2008) detected it as two separate clouds, AA21a and AA21b, as they did not have the column density sensitivity to make out the less dense sections. Our moment 1 (velocity map) of the ring cloud shows a small velocity gradient of 30 km s^{-1} .

The ring cloud is an extremely intriguing object, which leads us to question its origin. Wright's cloud (Wright 1979) also appears in our data cube (it is labelled in figure 2.4). It has been suggested that this previously discovered large HI cloud is associated with the Magellanic stream. However, it is around 50 kpc away from the main structure of the stream and $\sim 30\text{kpc}$ from the stream's S0 filament (Nidever et al. 2010). As AGESM33-31 has a similar column density to Wright's cloud and has the same central velocity then it is possible that it is somehow related to the Magellanic stream. However, as it is even further from the stream than Wright's cloud, and the stream at this distance has become extremely sparse and flocculant, it seems somewhat unlikely that a cloud the size of AGESM33-31 would be related

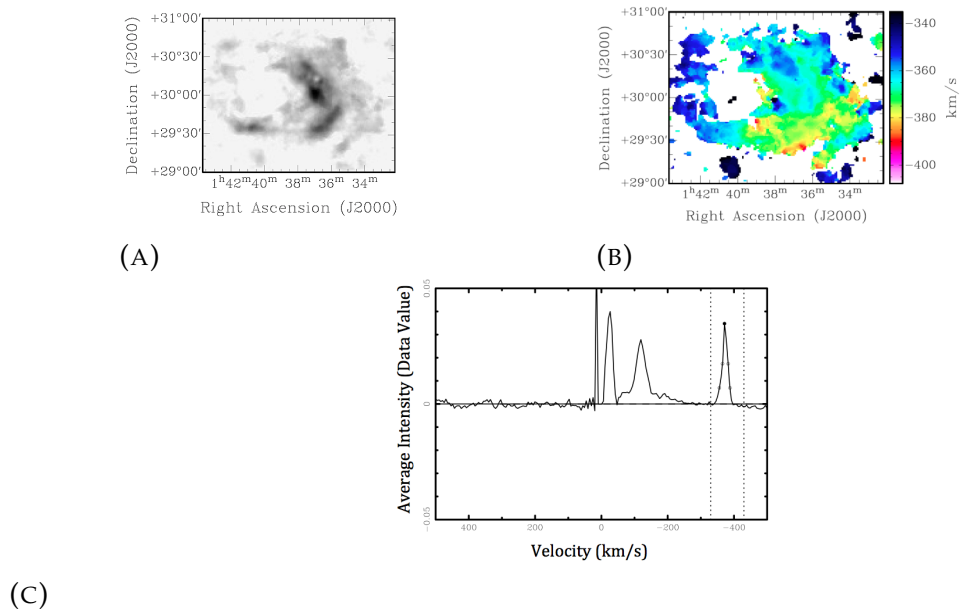


FIGURE 2.36 AGESM33-31

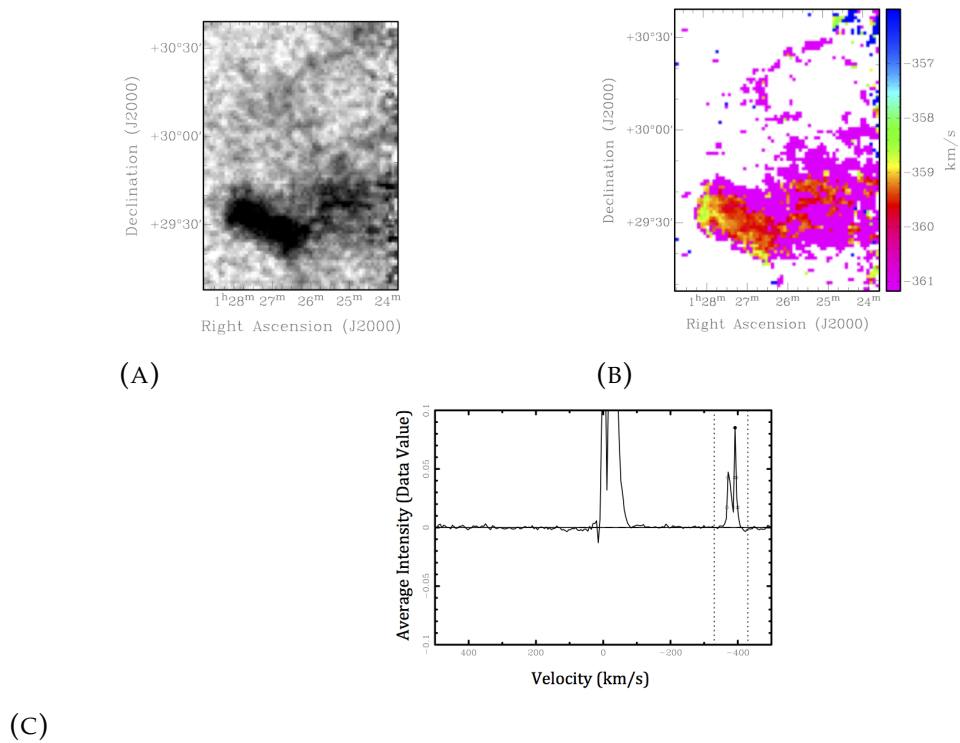


FIGURE 2.37 AGESM33-32

to it. Another interpretation is that AGESM33-31 is a galactic HVC projected along the line of sight. At M33 distance we measure AGESM33-31 to have a size of $\sim 18\text{kpc}$ and a HI mass of around 1% that of M33. If it were nearer the galaxy the HI mass and size of the cloud would be reduced to values more similar to a HVC. This cannot be ruled out, although the presence of Wright's cloud at the same velocity, and so near in position, cannot be explained by this scenario. Another question that must be considered is how AGESM33-31 came to have a large hole in it. This sort of a hole could be interpreted as the aftermath of stellar winds or a supernovae explosion (e.g Oey et al. 2002). Similar HI holes and shells were discovered in the disk of M33 by Thilker et al. (2002). However, if the cloud is at the distance of M33 then the hole is $\sim 10\text{kpc}$ in diameter, which is an order of magnitude larger than one would expect if it had been formed in either of these ways. If the origin were associated with stellar winds then it would imply the presence of stars, so could provide a link between these HI clouds and what we would normally consider a galaxy. We searched the literature for any stars, or star clusters, that could be associated with AGESM33-31. Huxor et al. (2009) identify a globular cluster, HM33-B, which is within the coordinate range of AGESM33-31. However, no mass or distance is given for this cluster so we are unable to draw any conclusions as to its possibility of association. Additionally, Grossi et al. (2011) carried out follow up observations of the regions around M33 searching for stellar populations. They report no evidence for young stellar populations in any of their detected clouds, and conclude that there has been no in-situ star formation. Further searches for stellar populations in this area will greatly benefit from upcoming survey data releases, such as that from PAndAS CUBS (e.g. Martin et al. 2009). If we continue to consider the idea that AGESM33-31 could be in some way akin to a galaxy; we observe that the very low measured velocity width of AGESM33-31 of 18 kms^{-1} is consistent with the velocity dispersion of atomic gas seen perpendicular to the plane of a typical disk galaxy. This is of order 10 kms^{-1} and, for example, Putman et al. (2009) give the velocity dispersion of the atomic hydrogen in M33 to be 19 kms^{-1} . This raises the possibility that we are seeing a face on disk in HI. The velocity map of AGEM33-31 shows a gradient across the disk of $\sim 30\text{ kms}^{-1}$, but we cannot be sure as to whether this is due to rotation or some form of streaming motion. Bearing this in mind, if the ring cloud is a similar structure to a disk galaxy, we need to consider whether other galaxies have been found with this sort of hole in them. There is a class of interacting galaxies named collisional ring galaxies (e.g Lavery et al. 2004), such as the pair Arp 147. This sort of an interaction could explain the

size of the hole in AGESM33-31, so it is a possibility worth being explored. However, as stated above, the velocity width of AGESM33-31 is only 18 kms^{-1} . If there had been an interaction in which another galaxy had passed directly through the centre of AGESM33-31's face-on disk, we would expect to see much more disturbance in the velocity of gas in this direction. Additionally, for most collisional ring galaxies the interaction partner is close by, whereas there is no obvious interaction companion near AGESM33-31. Therefore, it is unlikely that the hole was formed in this way. When Thilker et al. (2002) observed AGESM33-31 as M33CHVC they describe it as a 'dark companion' to M33, which echoes the ideas we are presenting here.

2.8 A PLANE OF CLOUDS

As can be seen in table 2.1, the clouds designated AGESM33-23 to 30 all lie at very similar velocities. This is particularly striking as they span 4° in position, or around 60kpc across the sky (see fig 2.38). The velocities of these clouds are also not too dissimilar from those of AGESM33-31 and Wright's cloud (they differ by around 40 kms^{-1}). This raises the question as to whether they are all part of the same structure, of which we are only detecting the higher column density areas. If this were the case then it would be a truly vast HI structure.

2.9 HOW ARE THE CLOUDS DISTRIBUTED?

We have investigated how the clouds around M33 are arranged with respect to velocity. Figure 2.39 shows a plot of the number of clouds in each velocity band with respect to M33. The blue bars represent the clouds which we categorise as joined to M33, and the black-outlined bars represent the discrete clouds. Unsurprisingly, the clouds which are joined to M33 sit at velocities close to its central velocity: all of them are within the velocity range covered by the galaxy. The discrete clouds tend to sit at more extreme velocities; those with velocities similar to M33 are detached in position and have RA and Dec values which differ significantly from the galaxy. As figure 2.39 shows, the majority of the detached clouds have velocities which are more negative than that of M33. This could be a true bias, however, due to confusion with HI in the Milky Way we could not detect clouds with velocities much more than 100 kms^{-1} greater than that of M33. Therefore, we

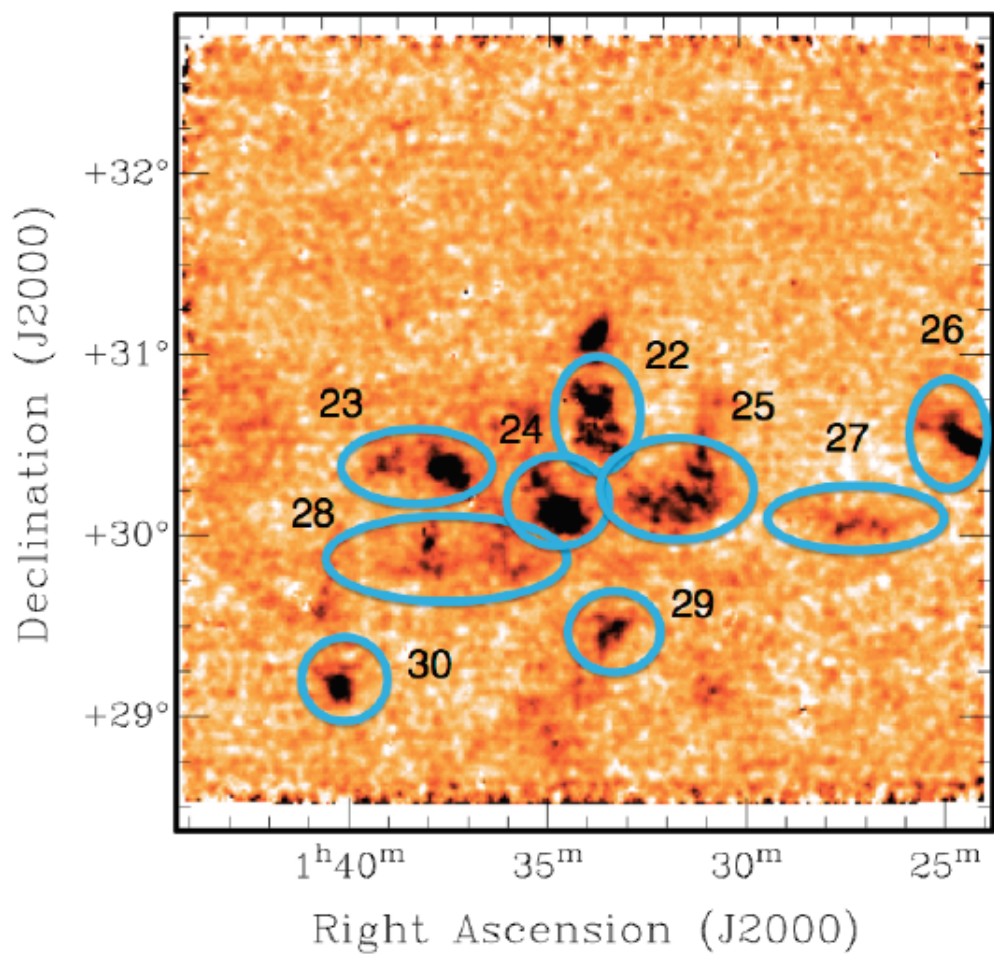


FIGURE 2.38 This figure shows 9 of the M33 clouds which all lie at very similar velocities, despite spanning 4° in position. They form a 'plane of clouds'. It is possible that all of these clouds are connected with low column density hydrogen which is below our detection limit.

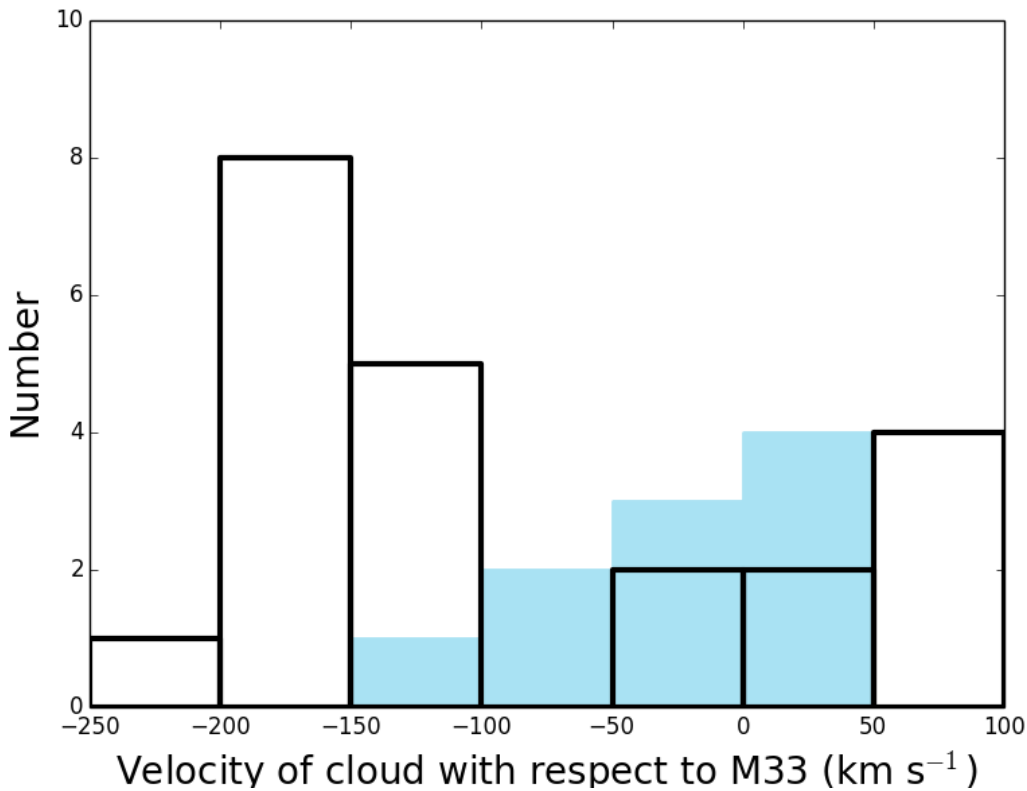


FIGURE 2.39 A plot of the number of clouds in each velocity band with respect to M33. The blue bars represent the clouds which we categorise as joined to M33, and the black-outlined bars represent the discrete clouds.

are unable to comment further on this. We have noted that there is a large over-abundance of clouds in the velocity range -150 to -200 km s^{-1} , these are the clouds discussed as the ‘plane of clouds’ in the previous section.

2.10 COULD OUR CLOUDS BE DWARF GALAXIES?

As mentioned previously, M33 is distinctly lacking in dwarf companions when compared to models, and even when compared to other galaxies. The clouds we have detected around M33 have comparable masses to known dwarf galaxies. To investigate this we have compared the masses of our clouds to those of the dwarf galaxy population of the Milky Way. In figure 2.40 we have plotted histograms of the masses of both sets of objects. We used data from McConnachie (2012b) for the masses of the Milky Way dwarf galaxies. As figure 2.40 shows, the masses of our clouds are consistent with those of the dwarf galaxies, but do not extend to the highest masses. Therefore, our clouds do appear to be massive enough to be dwarf galaxies. However, they have no detectable stellar component

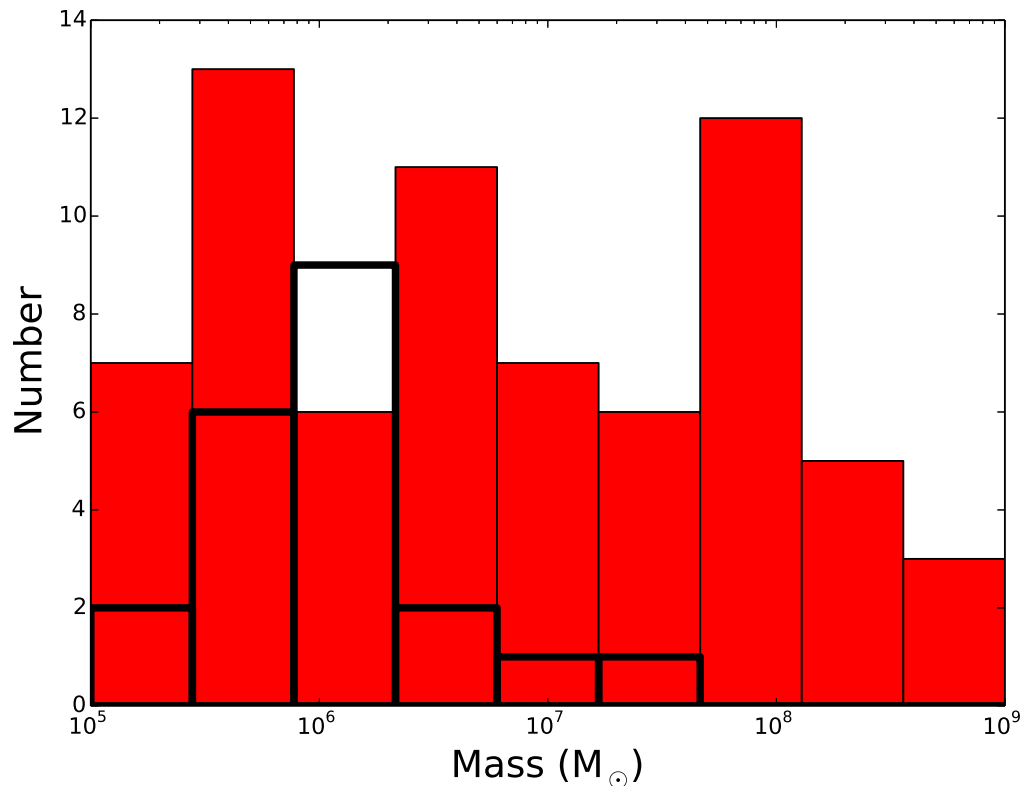


FIGURE 2.40 Number of members of a certain HI mass for both our clouds and the Local Group dwarf galaxies. Our clouds are represented by the black-outlined bars, Local Group galaxies are represented by the red bars. It can be seen that the M33 clouds' masses are in the same range as Local Group galaxies', however do not extend to the highest masses. Masses of Local Group galaxies from McConnachie (2012b). The Local Group dwarfs are catalogued by McConnachie (2012b) and are all dwarf galaxies lying within 3Mpc of the Sun.

and also no signs of ordered rotational motion. This can be seen in figures 2.5b to 2.37b: these are velocity maps of all of our clouds. It can be seen that none of the clouds has a strong velocity gradient across it (cloud AGESM33-31 has a small velocity gradient which will be discussed again later), and therefore none of them seem to have ordered rotational motion which would be a strong indicator of them being bound objects.

Even in the absence of ordered rotation, the clouds could still be supported by velocity dispersion. To assess this possibility we made an estimation of their dynamical masses (M_{dyn}). To do this we have assumed spherically virialised clouds (Blitz et al. 1999). We use the FWHM of the velocity profile (Δv_{50}) to estimate the 3D velocity dispersion of the gas and take the size of the HI cloud to be a measure of the geometric mean of the semi-major and semi-minor axes (r_{geo}). We can then use the following formula to estimate the dynamical mass:

$$M_{Dyn} = \Delta v_{50}^2 r_{Geo} / G$$

Using this formula we obtain dynamical masses between 10^9 and $10^{11} M_\odot$. Therefore, if these objects were bound they would have mass-to-light ratios of $\sim 10^4$. We would expect a correlation between the HI masses and dynamical masses if our clouds had a constant ratio of dark matter to baryonic matter, but we find no such correlation. These extremely high mass-to-light ratios were calculated with the assumption that we have detected all of the hydrogen in the cloud. HI clouds immersed in an ionising background have been modelled by Sternberg et al. (2002), we might expect this sort of background near M33 due to its star formation. Sternberg et al. (2002) state that HI remains neutral for column densities of 10^{19} cm^{-2} or above, and that only 10% of typical HVCs remain in neutral form. Therefore, it is possible that there is 10 times more hydrogen present than is observed in HI. If this is the case, for our clouds we would still need mass-to-light ratios of 10^3 in order for them to be bound. Although this is high, similar mass-to-light ratios have been observed in Local Group dwarf galaxies (McConnachie 2012b).

We have also investigated the extent to which the number of objects we have detected around M33 is consistent with galaxy formation models. Klypin et al. (1999b) report on the results of a numerical simulation which models the dark-matter sub-halo population around large galaxies; it assumes Λ CDM cosmology. Sternberg et al. (2002) have parametrised the results of this simulation into an equation which can be used to predict the number of dark matter halos expected around a galaxy of a given mass.

$$N(> v_s, < d) =$$

$$1.06 \times 10^3 \left(\frac{M_{\text{vir,p}}}{10^{12} \text{ M}_\odot} \right) \left(\frac{v_s}{10 \text{ km s}^{-1}} \right)^{-2.75} \left(\frac{d}{1 \text{ Mpc}} \right)$$

Here $N(> v_s, < d)$ is the total number of sub-halos with velocity widths greater than v_s (we use $\frac{\Delta w_{50}}{2}$). d is the distance from the centre of the halo of the parent halo and $M_{\text{vir,p}}$ is the virial mass of the parent galaxy. We take $5 \times 10^{11} \text{ M}_\odot$ to be the mass of M33 (Corbelli 2003). We observe out to $\sim 2.25^\circ$ from M33, which corresponds to a distance of about 33 kpc at a distance of 840 kpc. Assuming that we have detected all HI clouds with velocities greater than our minimum detected velocity (Δv_{50}) we have $v_s \approx 9 \text{ km s}^{-1}$. This is therefore a reasonable value to use based on the observed widths of our gas clouds. Putting these numbers into the above equation the model predicts ~ 25 sub-halos. This compares remarkably well with the 22 HI clouds detected. We can actually do a little better than this and compare the distribution of sub-halo velocities widths with that predicted by the model. Figure 2.41 shows a histogram of the distribution of the velocity widths predicted by the formula (blue histogram) against the velocity-width distribution of our observed clouds (black-outlined histogram). The distribution in figure 2.41 follows a power law and is reasonably well described by the Pareto principle (e.g. Hosking & Wallis 1987), which states that for a power law distribution 80% of the data will fall within 20% of the bins. As can be seen from figure 2.41 most of our clouds cluster at the low velocity width end of the distribution. 50% of the clouds fall with the smallest velocity width bin, from $20 - 30 \text{ km s}^{-1}$. A Kolmogorov-Smirnov test on the data shown in figure 2.41 gives a KS statistic of 0.166 and a P-value of 0.999 indicating that we cannot reject the hypothesis that the two samples are from the same distribution. In summary, the numbers of HI clouds and the distribution of their velocity widths is consistent with the properties of sub-halos produced in numerical cosmological simulations.

Due to the unique nature of the M33 region there are no simulations that model areas like it. M33 is a relatively small galaxy and, as previously discussed, currently has no observed satellites. However, groups have simulated regions similar to the halo of the Milky Way and the Local Group (e.g. Klypin et al. 1999a, Moore et al. 1999 and Sawala et al. 2016). They predict an overabundance of satellite halos in these regions compared to observations. Full details of these simulations, including scale and particle sizes, are given in the introduction.

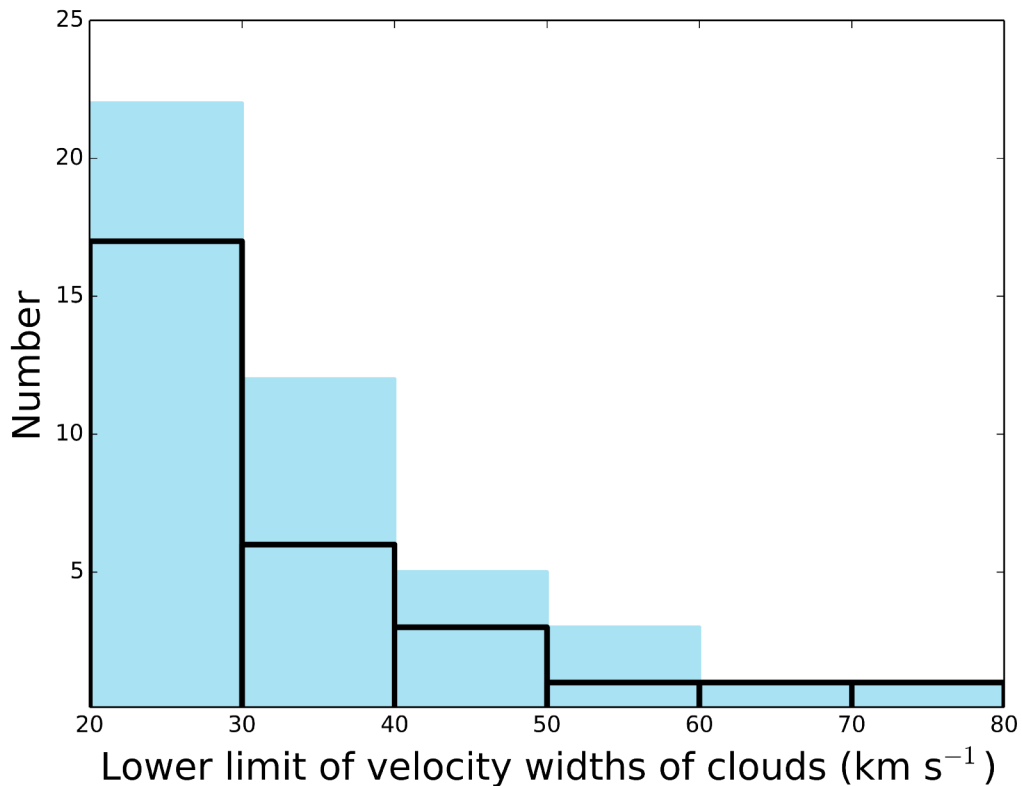


FIGURE 2.41 Histograms showing the number of objects within each velocity-width band. The blue histogram shows the distribution of velocity widths for the sub-halos predicted from the equation and the black-outlined histogram shows the distribution of velocity widths of the M33 clouds.

On the whole, there is not enough evidence to claim that it is likely that the majority of the M33 clouds are starless galaxies. Their unusual shapes and lack of ordered rotation do not suggest that they are gravitationally bound objects. Additionally, the plane of clouds we observe at similar velocities may not be separate clouds at all, but a large area of HI of which we can only make out the highest column density areas. However, the ring cloud, AGESM33-31, remains a perplexing object and potential dark galaxy candidate. Its size, mass and velocity dispersion is comparable to that of a galaxy. Therefore it is an extremely unusual object due to its lack of stars and the large hole in the gas at its centre. One possible explanation is that it is a dark galaxy, an idea similar to one reached by Thilker et al. (2002) who described it as a 'dark companion to M33'.

2.11 SUMMARY OF M33 WORK

In this chapter I have described work carried out using data from the Arecibo Galaxy Environment Survey (AGES) to investigate the HI gas in the halo of Local Group galaxy M33. We have detected 22 discrete HI clouds around M33, 11 of which were previously undetected. We have studied the properties of these clouds and have concluded that, although they have similar masses and sizes to dwarf galaxies, we find no strong evidence that they are gravitationally bound. Additionally, none of these clouds have any detected stellar component. AGESM33-31, or the ring cloud, is particularly intriguing due to its large size; it has a diameter of 18kpc if at the distance of M33. It also has a large hole in it with a diameter of \sim 10kpc. We have proposed some explanations for this object: it could be a galactic HVC projected along the line of sight to M33, it may be an extension of the Magellanic stream, or it could be something more akin to a dark galaxy.

CHAPTER 3

DWARF GALAXIES IN CLUSTERS

*'Young Hodge the drummer never knew –
Fresh from his Wessex home –
The meaning of the broad Karoo,
The Bush, the dusty loam,
And why uprose to nightly view
Strange stars amid the gloam.'*

THOMAS HARDY, DRUMMER HODGE

Having looked into the possibility of finding dwarf galaxies through their HI gas content, I will now discuss methods of detecting them using stellar light emission. Due to their small sizes and low surface brightnesses dwarf galaxies are notoriously difficult to detect. Until around 2005 only about ten Milky Way dwarf galaxy satellites were known. However, in the last ten years or so this number has exploded so that today it sits closer to fifty. The majority of these satellites have been found in the Sloan Digital Sky Survey (SDSS) (e.g. Willman et al. 2005, Zucker et al. 2006). This demonstrates that the potential for finding dwarfs in group and cluster environments is massive. Most of these discoveries have been made by looking for stellar over-densities. The colours of the stars in these over-densities are then examined to see if they resemble a single stellar population, and are therefore likely to be bound as a satellite.

Unfortunately, outside of our Local Group discovering dwarf galaxies as stellar over-densities is impossible: we do not have the capability to resolve individual stars. As image resolution and processing techniques have improved new

populations of dwarf galaxies have been discovered outside of the Local Group, including in the Coma and Fornax Clusters. These galaxies have been detected with surface brightnesses as low as 28 mag arcsec⁻² and many have very extreme mass to light ratios, some reaching M/L \sim 1000 (e.g. Muñoz et al. 2015, Peng & Lim 2016). For comparison, a typical galaxy has a mass to light ratio of around 10 (Dickel & Rood 1978) and a surface brightness of \sim 22-23 mag arcsec⁻². In this chapter I will explore the recently discovered populations of dwarf galaxies, as well as the challenges faced in classifying their cluster membership. I will then introduce previous work on the Virgo cluster, before going on to discuss my own work on the cluster in chapters 4 and 5.

3.1 THE CLUSTER ENVIRONMENT

As evidenced in the introduction, galaxy clusters are hotbeds for dwarf galaxy discoveries. Recently discovered dwarfs have largely been found by either using automated detection programs such as SExtractor (e.g. Koda et al. 2015), or by eye (e.g. Mihos et al. 2015). Their cluster membership has been confirmed based on visual inspection (e.g. Drinkwater et al. 2000), and occasionally some spectroscopy (e.g. van Dokkum et al. 2015b). However, as we enter the age of big data astronomy, with the rise of instruments like the Large Synoptic Survey Telescope (LSST, Ivezic et al. 2008), it will become impractical to inspect data by eye to detect objects and determine cluster membership. We will need a robust automated method to distinguish cluster member dwarf galaxies from galaxies in the background. Therefore, a set of physical constraints using which we can differentiate between these populations will be essential. I will explore whether such constraints exist, and how they can be used to achieve this purpose. To do this I will use data recently made publicly available by the Next Generation Virgo Survey (NGVS, Ferrarese et al. 2012) to perform accurate photometry on known Virgo Cluster members. To identify known cluster members the Virgo Cluster Catalog (VCC, Binggeli et al. 1985) and the Low Surface Brightness Virgo Cluster Catalog (LSBVCC, Davies et al. 2016) will be used. I will then compare the properties of these cluster members to the properties of a background sample of galaxies. This will hopefully enable the discovery of a method by which cluster dwarf galaxies can be distinguished from those in the background.

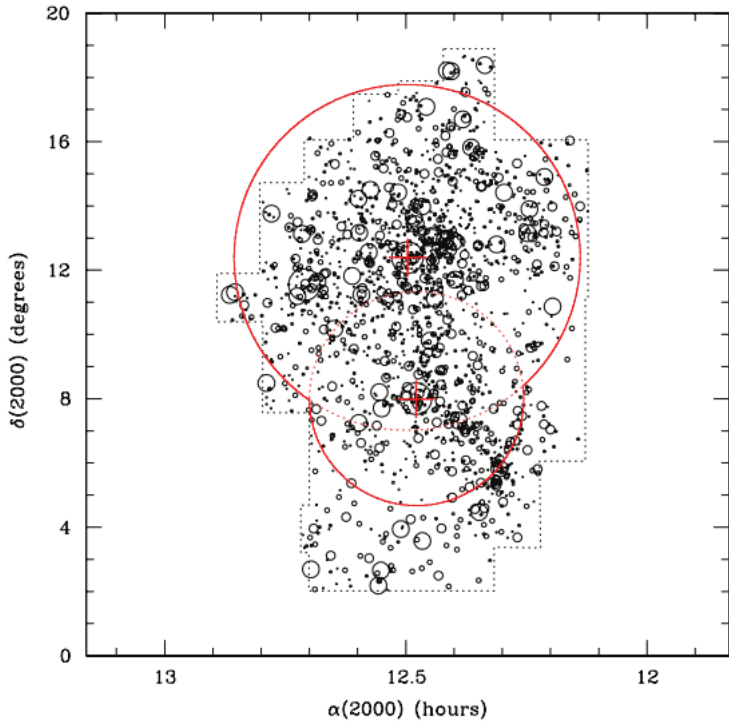


FIGURE 3.1 The position of galaxies in the Virgo Cluster Catalogue (VCC, Binggeli et al. 1985). 1762 galaxies are shown which are classified as certain or probable cluster members. The dotted lines indicate the Binggeli et al. (1985) survey size. The red crosses indicate the position of M87, at the centre of subcluster A, and M49 at the centre of subcluster B. The red circles show their respective virial radii. Figure from Ferrarese et al. (2012).

3.2 THE VIRGO CLUSTER CATALOGUE

Binggeli et al. (1985) produced the first substantial catalogue of Virgo galaxies. They produced a catalogue of 2096 galaxies over an area of $\sim 140^\circ$ squared centred on the Virgo Cluster. They claim to be complete down to $M_{BT} \sim -13.7$ assuming a Virgo distance modulus of $(m-M) = 31.7$. The catalogue was compiled by inspecting 67 photographic plates taken using the du Pont 2.5m reflector telescope of the Las Campanas Observatory. They state that of the 2096 detected galaxies, 1277 are cluster members, 574 are possible cluster members, and 245 are background galaxies. They determine cluster membership primarily by considering galaxy morphology. They give four criteria on which their decisions are based: 1. They use surface brightness to decide whether dE and Im galaxies are cluster members. These have typically low surface brightnesses which would be undetectable if they were outside the Virgo Cluster. 2. If they can resolve stellar associations and HII regions in spiral and irregular type galaxies then they class them

as cluster members. These features in background galaxies would appear unresolved. 3. Luminosity was also used as a determinant of membership. 4. They looked at radial velocities of the galaxies, where available, and determined that cluster members had an observed v (minimum) of $\sim 700 \text{ kms}^{-1}$ and $v(\text{mean}) \sim 960 \text{ kms}^{-1}$. They assume a symmetrical velocity distribution and therefore calculate a $v(\text{maximum})$ of $\sim 2700 \text{ kms}^{-1}$. They also state that the catalogue membership essentially represents a morphological selection, and the radial velocity information is solely used to confirm membership assignments. Binggeli et al. (1985) go some way to constrain their completeness limits. They define a mean surface brightness of $25.3 \text{ B mags arcsec}^{-2}$ as the limit at which they cannot distinguish galaxies from the sky background. Effectively, this means that any galaxy with a fainter surface brightness than this will not be detected by their survey. They also state that they have a problem with high surface brightness dwarf galaxies. They would be able to detect such galaxies, however, they cannot distinguish them from background galaxies as their morphologies are not sufficiently distinct.

3.3 THE EXTENDED VIRGO CLUSTER

More recently Kim et al. (2014) presented a new catalogue of galaxies in the Virgo Cluster region: they named it The Extended Virgo Cluster Catalog (EVCC). The EVCC covers an area of 725 deg^2 , which is 5.2 times larger than that of Binggeli et al. (1985)'s VCC and reaches out to more than 3.5 times the virial radius of the Virgo Cluster. Kim et al. (2014) used the Sloan Digital Sky Survey (SDSS) Data Release 7 to select 1324 target galaxies with radial velocities less than 3000 km s^{-1} . Additionally, they selected 265 galaxies not included in the SDSS but with redshifts available in the NASA Extragalactic Database (NED). The fact that Kim et al. (2014) could only pick galaxies with redshift measurements highlights the need for an independent method to verify cluster membership. Due to the fact Kim et al. (2014) only picked galaxies with available spectroscopic surface brightnesses they are biased toward selecting reasonably high surface brightness sources. They have a total of 1589 galaxies, 676 of which aren't included in the VCC. Figure 3.2 shows the spatial distribution of the 676 galaxies detected only in the EVCC. As the figure shows, the majority of their new detections lie outside of the footprint of the original VCC. The red circles indicate certain cluster members and the blue circles possible members. The red dashed line indicates the size of the VCC. Kim et al. (2014) state that around 19% of the new EVCC galaxies lie outside of the footprint of the VCC. These galaxies are both smaller and fainter than the VCC galaxies and

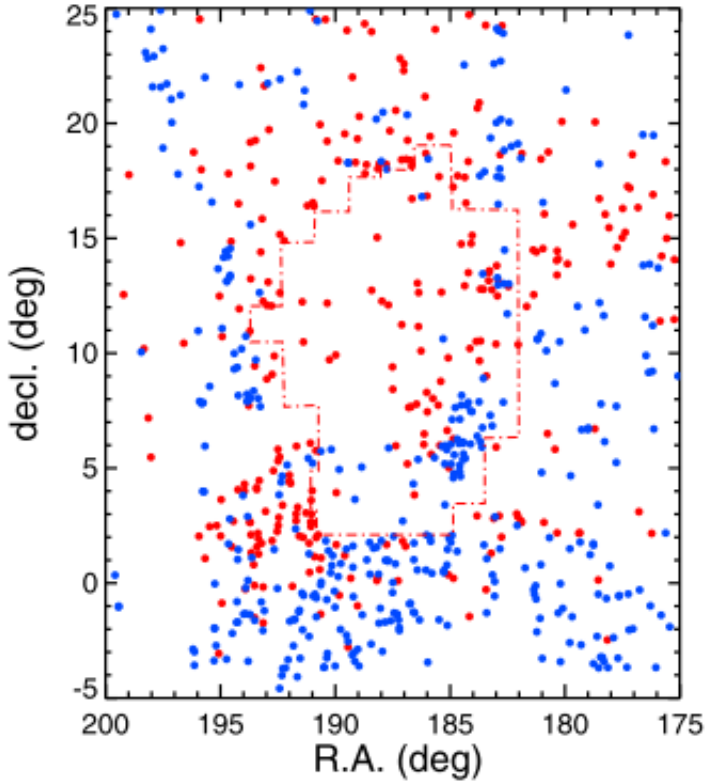


FIGURE 3.2 Figure showing the spatial distribution of the 676 galaxies detected only in the EVCC. The red circles indicate certain cluster members and the blue circles possible members. The red dashed line indicates the size of the VCC. Image from Kim et al. (2014).

show Irr and dE/dS0 morphologies. Unfortunately, the NGVS (see below) does not cover the majority of the EVCC, so we will not be using the EVCC galaxies in our study.

3.4 THE NEXT GENERATION VIRGO CLUSTER SURVEY

The Next Generation Virgo Cluster Survey (NGVS) used the 1 degree² MegaCam instrument on the Canada France Hawaii Telescope (CFHT) to obtain deep optical imaging of the Virgo cluster (Ferrarese et al. 2012). The survey covers an area of 104 degree², from the Virgo cluster’s core to its virial radius, with total coverage in the g band and partial coverage in the u, r, i and z bands. Ferrarese et al. (2012) give the NGVS’s point-source limiting depth to be $g \sim 25.9$ mag at 10σ and a surface brightness limit of $\mu_g \sim 29$ mag arcsec⁻² at 2σ above the mean sky level. Using the NGVS data, I measure the 1σ noise level of the sky background to be 26.9 mag arcsec⁻². The NGVS covers a similar area to the VCC (Binggeli et al. 1985), yet is designed to probe much deeper than previous observations. Binggeli

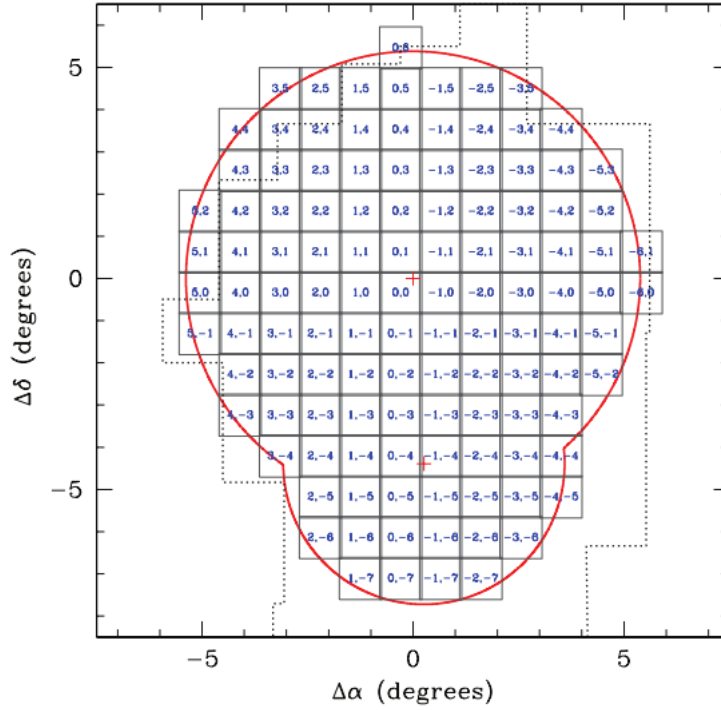


FIGURE 3.3 The observing fields of the NGVS. The dotted black lines show the survey area of the VCC (Binggeli et al. 1985), the red lines show the virial radii of subclusters A and B, and the red crosses mark the positions of M87 and M49. Taken from Ferrarese et al. (2012).

et al. (1985) give 23.5 B mags arcsec^{-2} to be their mean limiting surface brightness, whereas in the NGVS galaxy profiles can be reliably traced out to 28 mags arcsec^{-2} . Therefore the NGVS is an extremely powerful data set for discovering and measuring low surface brightness galaxies. Figures 3.3 and 3.4 show the observing fields of the NGVS and the coverage of those fields in each band.

3.5 THE LOW SURFACE BRIGHTNESS VIRGO CLUSTER CATALOG

Davies et al. (2016) use the g-band NGVS data to search for new dwarf galaxies. As discussed in chapters 4 and 5 of this thesis, the four-band NGVS data was later used to carry out photometry on known Virgo galaxies, with the aim of identifying a method of separating cluster dwarfs from background galaxies. The Davies et al. (2016) work was done to test whether there were still any Virgo dwarfs to find. If they had not identified any then there would have been little justification for the work done in chapters 4 and 5 of this thesis. Figures 3.7

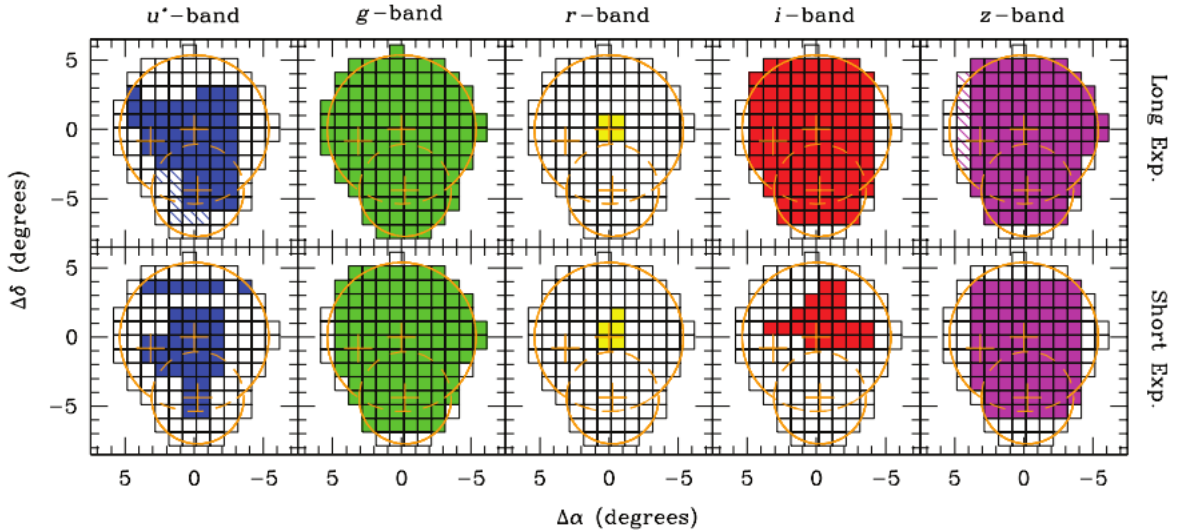


FIGURE 3.4 The coverage in each of the five bands of the NGVS. The orange lines indicate the virial radii of subclusters A and B, orange crosses mark the positions of M87, M49 and M60. Taken from Ferrarese et al. (2012).

to 3.9 have been taken from Davies et al. (2016), to illustrate the work done in that paper.

Davies et al. (2016) continue to explore the LSB population of the Virgo Cluster by extending the catalogue of galaxies in the Virgo cluster to lower surface brightness levels. Next Generation Virgo Cluster Survey data is used in the g -band to detect new LSB dwarf galaxies. 443 cluster dwarf galaxies were detected, 303 of which are new detections. This produced a catalogue of detections which will be referred to as the Low Surface Brightness Virgo Cluster Catalog (or LSB-VCC). To do this the object detection algorithm *SExtractor* was used on the g -band frames of the NGVS. *SExtractor* input parameters were chosen which best select low surface brightness galaxies; central surface brightness values of $22.5 \leq \mu_0 \leq 26.0 \text{ mag arcsec}^{-2}$ and exponential scale lengths of $3.0 \leq h \leq 10.0 \text{ arcsec}$. It was found that the density of the newly detected galaxies decreases radially from the cluster centre. As discussed previously, one major problem when looking for LSB galaxies is distinguishing them from background objects. To try and overcome this the following selection criteria were used, although all sources will subsequently need to be inspected by eye:

- i.) We have only selected objects with an area equal to or less than 800 pixels: this equates to a radius of 3 arcsec if the object is circular. We have also only selected objects that are reasonably circular, with an ellipticity ≤ 0.4 . This should ensure we do not include extended objects such as satellite trails and diffraction spikes from stars.

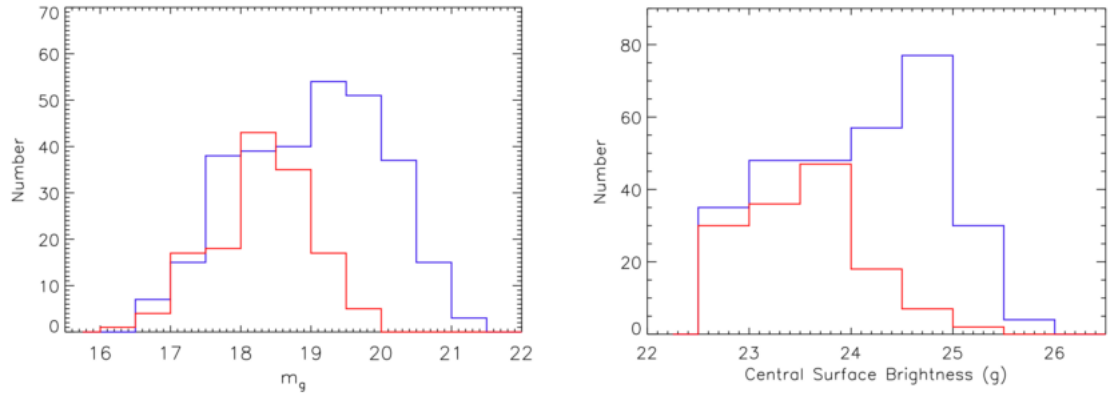


FIGURE 3.5 The distribution of the magnitudes of our 443 galaxies. The red histogram represents galaxies also in the VCC and the blue histogram represents our new LSB galaxies. From Davies et al. (2016).

ii.) We have used the measured isophotal magnitudes and areas to calculate central surface brightnesses (μ_0), scale sizes (h) and apparent magnitudes (m_g). We have done this by assuming an exponential surface brightness profile.

iii.) We only select galaxies with $\mu_0 \geq 22.5 \text{ mag arcsec}^{-2}$ and $h \geq 3.0$.

After visual inspection of all objects which met this selection criteria we were left with 443 objects. 140 of these were listed in the VCC, which left us with 303 new LSB dwarf galaxies. Figure 3.5 shows the distribution of the magnitudes of our 443 galaxies. The red histogram represents galaxies also in the VCC and the blue histogram represents our new LSB galaxies. This demonstrates how the NGVS allows us to probe much fainter magnitudes and surface brightnesses than has been previously possible. The left panel of figure 3.6 shows positions of our galaxies (blue) compared to all VCC galaxies (red). The black ellipses represent the virial radii of subclusters A and B, and the black crosses mark the positions of M87 and M49. The right panel of figure 3.6 shows the number density of galaxies plotted against distance from M87. Again, our detections are shown in blue and VCC galaxies are in red. Figure 3.7 shows the positions of our galaxies in green, compared to the positions of galaxies in the EVCC (red are certain cluster members and blue are possible members). Again the black ellipses represent the virial radii of subclusters A and B, and the black crosses mark the positions of M87 and M49. Figure 3.8 shows typical examples of two of the galaxies from Davies et al. (2016). Due to using SExtractor to detect sources, with preset detection criteria, the majority of the galaxies in the LSBVCC resemble those in fig 3.8 meaning that they are dwarf galaxies with elliptical profiles. This means that SExtractor will have struggled to detect galaxies which have very different properties.

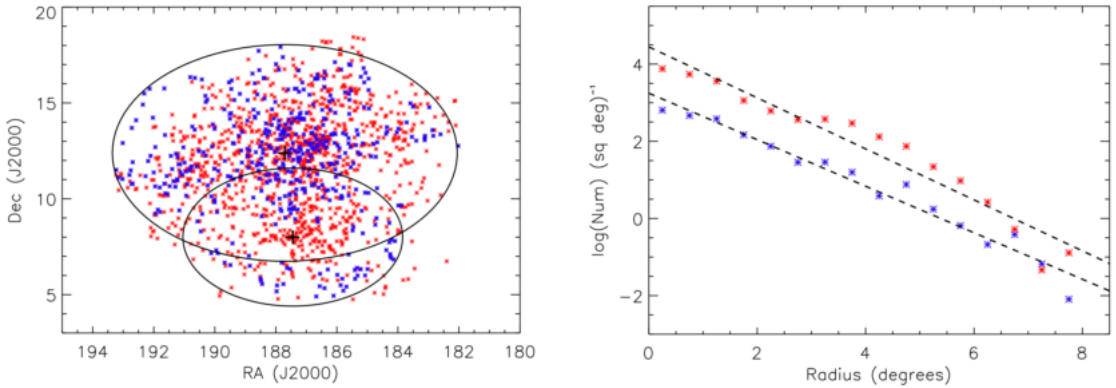


FIGURE 3.6 Left: positions of our galaxies (blue) compared to all VCC galaxies (red). The black ellipses represent the virial radii of subclusters A and B, and the black crosses mark the positions of M87 and M49. Right: The number density of galaxies plotted against distance from M87. Again, our detections are shown in blue and VCC galaxies are in red. From Davies et al. (2016).

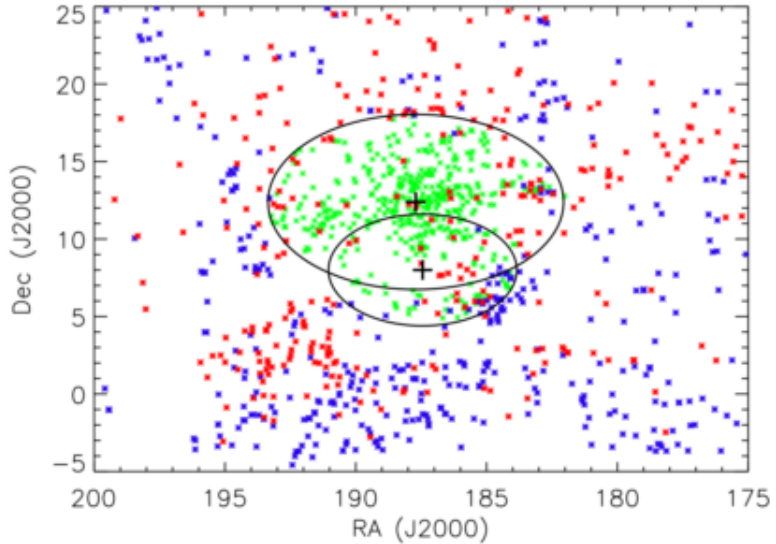


FIGURE 3.7 The positions of our galaxies in green, compared to the positions of galaxies in the EVCC (red are certain cluster members and blue are possible members). Again the black ellipses represent the virial radii of subclusters A and B, and the black crosses mark the positions of M87 and M49. From Davies et al. (2016).

Many other studies have used similar detection methods to Davies et al. (2016) to find dwarf galaxies. For example, Merritt et al. (2014) identified seven new LSB galaxies near M101. Six of these were initially identified by eye, and subsequently SExtractor was used to identify an additional LSB galaxy, as well as also detecting those already found by eye. Even with conservative constraints set in SExtractor, they found 529 objects which needed visual inspection. Additionally, Koda et al. (2015) used SExtractor to identify around 1000 ultra diffuse galaxies in the Coma cluster. They defined pre-set radii and surface brightnesses in SExtractor, and had to inspect all objects visually. Therefore, they will only have found dwarfs with a narrow range of properties and this method will quickly become impractical with large data sets.

Using SExtractor to identify dwarf galaxies is not an effective or efficient method as we increasingly have large quantities of deep CCD data. SExtractor relies on user input to define the objects it finds, using parameters such as central surface brightness, and radius. This means that the user will only detect galaxies which fit a pre-defined range of characteristics, and rules out speculative detections. SExtractor is also not very good at separating out objects which are close together. This highlights the need for new detection methods which do not rely on pre defined characteristics and which can trace galaxies profiles to low surface brightness levels, and hence not blend them with nearby objects. Additionally, detections made by SExtractor need to be visually inspected, as usually only a small proportion of them are significant. The work in chapters 4 and 5 has been done to explore whether there are photometric qualities that can be used to define LSB galaxies, as opposed to relying on physical qualities. This information will be used to help train a new automated detection programme to find vast numbers of dwarf galaxies in data coming from new large area optical surveys, without the need to visually inspect every object identified.

3.6 SUMMARY

This chapter has explored previous optical surveys of the Virgo cluster and their scope. It has also provided an introduction to the Next Generation Virgo Survey, which provides the data used in the subsequent chapters.

As discussed above, the work of Davies et al. (2016) was used to lay a groundwork for the work presented in chapters 4 and 5 of this thesis. The primary aim of the work in Davies et al. (2016) was to discover whether there were

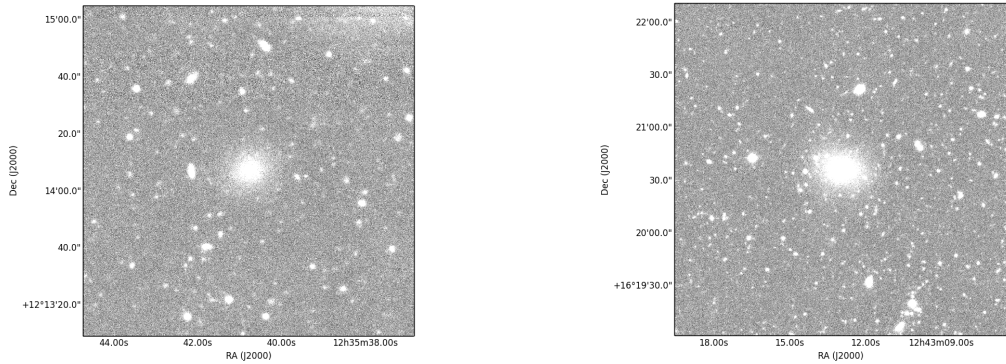


FIGURE 3.8 Examples of galaxies from the LSBVCC (Davies et al. 2016). Left: LSBVCC059. Right: LSBVCC120.

still new dwarf galaxies to be found in the Virgo cluster. Utilising a simple detection method by using the programme SExtractor Davies et al. (2016) discovered 303 new Virgo dwarfs. However, SExtractor could only be used with strict input parameters and all sources required visual inspection. This highlighted the need for a new detection method to identify dwarfs accurately and efficiently. In order to do this we will need to train it to identify dwarf galaxies based on the properties of known dwarf galaxies, and it will need to be able to separate these from background sources. The work presented in chapters 4 and 5 explores whether photometric properties of dwarf galaxies can be identified which separates them from background galaxies. If such properties can be found, they will be used to identify dwarf galaxies from within future large surveys.

CHAPTER 4

PHOTOMETRY OF VIRGO CLUSTER GALAXIES

'And God said, 'Let there be light' and there was light, but the Electricity Board said He would have to wait until Thursday to be connected.'

SPIKE MILLIGAN

As evidenced in chapter 3, a lot of progress is being made in the field of LSB galaxies. Using superior optical surveys, with better depth, it has been possible to unveil many previously unknown galaxy populations. However, there is still a distinct problem when it comes to identifying distances of optically detected galaxies, and hence whether they belong to a particular group/cluster, or are in the background.

With this in mind, we are using the NGVS data to revisit the VCC (Binggeli et al. 1985) and the LSBVCC (Davies et al. 2016). We are carrying out photometry on confirmed member VCC galaxies, and the LSBVCC sample. The aim of doing this is to 1. have a new coherent set of photometry for Virgo galaxies using the new, deep data and 2. to look for identifying features which set cluster dwarfs apart from background galaxies, hence aiding the identification of them as cluster galaxies. The NGVS team have only carried out photometry on cluster core galaxies (Roediger et al. 2017 and Ferrarese et al. 2016), and have not released a catalogue of Virgo galaxies from the data. Therefore, the photometry presented here is a novel result and a vast improvement on what was previously available (the last time photometry was carried out such a large sample of Virgo galaxies

was in Binggeli et al. 1985). We are using the four NGVS bands with a reasonable amount of coverage (u , g , i and z) in order to do this. We have 763 frames in the u -band, 1214 in the g -band, 1131 in the i -band and 1165 in the z -band (see figure 3.4, top row). This gives us 763 VCC galaxies in all four bands, with 1131 in three bands, 1165 in two bands and 1214 in one band. Additionally, we have 278 LSB-VCC galaxies in all four bands, 384 in three bands, 390 in two bands and 441 in one band.

4.1 PREPARING THE DATA FOR PHOTOMETRY

4.1.1 MAKING GALAXY CUTOUTS

As the NGVS frames are $1^\circ \times 1^\circ$ cut-outs were made of all the VCC member galaxies covered by the NGVS, as well as all of the LSBVCC galaxies from Davies et al. (2016). On inspection of these cut-outs a problem was discovered: for cut-outs of galaxies that sat near frame boundaries the galaxies were not centred and black space appeared at the original frame boundary. This affected around 10% of the galaxies. In order to rectify this a code was written to identify galaxies near frame boundaries: it was given the co-ordinates of each galaxy, and the corresponding cut-out radius, and identified galaxies which were within this radius of the frame edge. A programme named MONTAGE was then used to produce cut-outs of the galaxies near frame edges, it takes the coordinates of a galaxy and makes the cut-outs by stitching together the frame with the next one. This then meant that, for all galaxies covered in each band by the NGVS, we had cut-outs centred on each galaxy. All galaxies with frame edges remaining in the cut-out, or where the montaged frame divide did not perfectly match up, were removed from the sample.

4.1.2 MEASURING THE GALAXIES' POSITION ANGLES AND AXIAL RATIOS

In order to perform accurate photometry of our sources the axial ratios and position angles needed to be measured. The code used for this was initially developed by Christopher Clark (Clark (2015)). It calculates the noise in the frame, and looks for pixels which are 2.5 sigma above the noise level. It then uses the coordinates of the galaxy to look for contiguous pixels above this

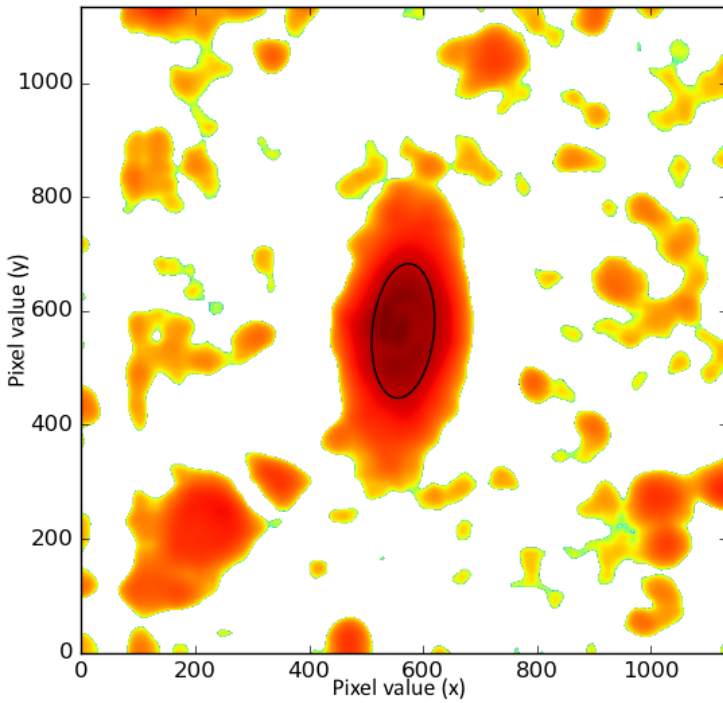


FIGURE 4.1 A nebulised background map of one galaxy (VCC504) showing the measured position angle and axial ratio. Note that this wasn't used to define the size of the photometry aperture, just the angle and axial ratio.

signal-to-noise limit. The best fit ellipse to this region is fitted and the code outputs the position angle of the galaxy and the axial ratio of the ellipse. When this code was first run a random sample of the galaxies were checked by measuring their position angles and axial ratios by hand. Many of the results from the code were quite drastically different to those measured by hand. On inspection, the galaxies affected had many background objects or artefacts on the CCD. To reduce the effects of these objects the cut-outs were smoothed in order to measure them. This was done using a programme called NEBULISER, full information on which can be found at <http://casu.ast.cam.ac.uk/surveys-projects/software-release/background-filtering>. This program is designed to remove background variations from an input image, it outputs two things: a nebulised map and a background map. The nebulised map will remove much low surface brightness structure, however the background map returns a smoothed image of the galaxy. These background maps were ideal for us to use to measure the position angles and axial ratios of our galaxies. Figure 4.1 displays one of these nebulised maps with the ellipse showing the measure position angle and axial ratio.

band	median mag	SDSS median mag	mean mag	SDSS mean mag	maximum difference
u	19.83	17.70	19.51	17.67	8.77
g	18.47	16.40	17.97	16.53	9.81
i	17.57	15.61	17.04	15.55	8.05
z	17.52	15.49	16.93	15.53	8.46

TABLE 4.1 The mean and median magnitudes of galaxies in the test sample from my measurements compared to the SDSS. The last column gives the maximum difference (in magnitudes) for a galaxy in that band.

4.2 PERFORMING PHOTOMETRY ON A TEST SAMPLE

4.3 NGVS PHOTOMETRIC CALIBRATION

The NGVS images have a photometric zero point of 30, so AB magnitudes are calculated using the following equation, from Ferrarese et al. (2012):

$$m(\text{AB}) = -2.5 \times \log(F) + 30.0$$

Here F is the flux measured from the frame, after background subtraction. This is how all magnitudes from the NGVS data in this thesis have been calculated.

4.3.1 VCC GALAXIES SAMPLE

A basic photometry code was written, results from which could be tested to highlight any problems. For each galaxy the measured position angle and axial ratio, as well as the galaxy size from the VCC, were used to create an aperture. When the sizes of some of these apertures were checked they were found to be too small. Due to the NGVS's much superior sensitivity over the VCC, the galaxies appear a lot bigger in the NGVS data, so the apertures were missing a large amount of the galaxy flux. Therefore the VCC measurements were scaled to account for this and the size of the aperture was set to 1.5 times the VCC size. To measure the sky background in the frames an annulus was placed around our aperture. To ensure there was no galactic contamination in this aperture the radius of its inner ellipse was set to 1.5 times that of the aperture radius.

Due to the size of the data set, an initial sample of 62 galaxies were tested (100 were selected in the g-band, of which we had data for 62 in all four bands) using this basic photometry code. This flagged up some issues which needed to be addressed. A summary of the magnitude results from this sample can be seen

in table 4.1. The mean and median magnitudes are given for the galaxies in the test sample, both for my measurements and the SDSS. Additionally, the maximum magnitude difference for any galaxy in each band is given. These results have all been converted to the SDSS magnitude system, to eradicate discrepancies due to the differing filter systems, however this difference would amount to a change in magnitude of less than 1%. As this demonstrates, when the sample is examined as a whole there are large discrepancies between the values I attained and those in the SDSS. However, figure 4.2 shows the test sample magnitudes plotted against SDSS magnitudes for the galaxies. The red, blue, green and purple points represent galaxies in the g, u, i and z bands respectively. As this plot shows, our magnitudes actually largely correlate well with the SDSS magnitudes, however, there is a population of galaxies which appear to be significantly brighter in the NGVS data. To investigate this, all of these galaxies were examined by eye, and photometry was carried out by hand to confirm the results. These galaxies could be split into two types of object:

- 1.) Galaxies with bright stars in the frame, some flux from which was being included in the photometry.
- 2.) Galaxies with some bright star forming regions, but also some extended LSB structure.

In the latter case our photometry can be trusted over the SDSS. This is due to the fact that the SDSS has measured the galaxy to be solely the star forming region, as the extended structure is below their detection limit. An example of one of these galaxies is shown in figure 4.3. To resolve the former case software was used to mask stars in the frames, hence greatly reducing this problem (the star removal software is discussed in section 4.3.3.)

4.3.2 LSBVCC GALAXIES

Photometry was then carried out on the LSBVCC galaxies from Davies et al. (2016). Due to their small cut-out size, these galaxies could be processed quickly. The basic photometry code was run on the LSBVCC frames, and their magnitudes used to calculate colours.

This initial run highlighted galaxies with unusually high or low colour values. These galaxies were inspected in order to ascertain the reason for these extreme values. This led to two galaxies being removed from the sample: LS-BVCC115 and LSBVCC428. When the image of LSBVCC115 was inspected no galaxy was found, instead it appears that SExtractor identified part of a stellar

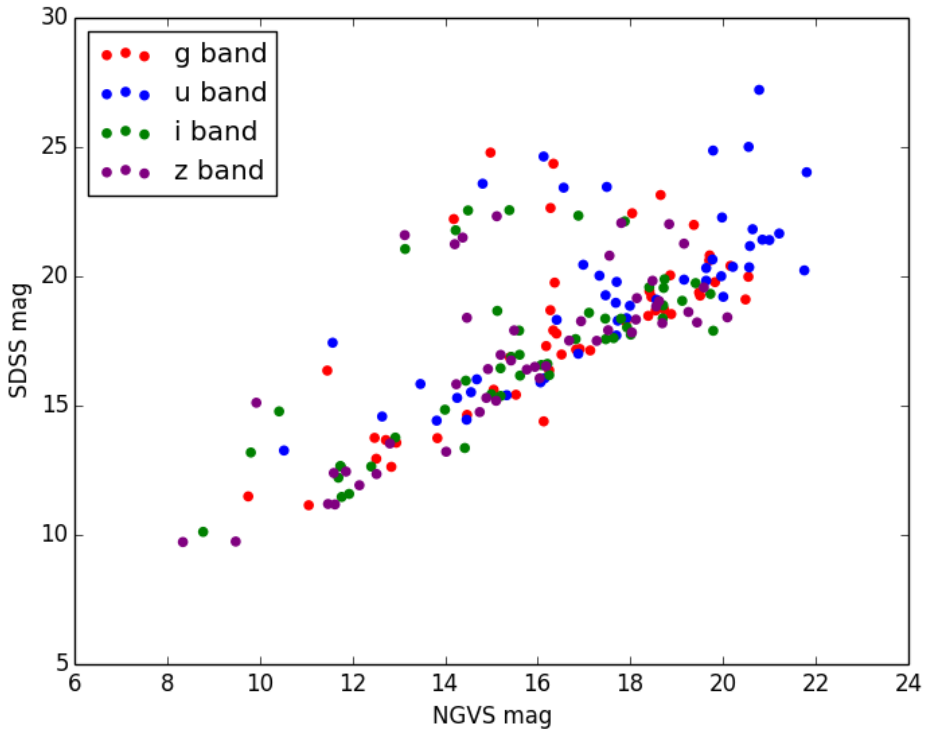


FIGURE 4.2 The magnitudes measured for the initial VCC sample plotted against those in the SDSS. The red points are the g-band magnitudes, the blue are u-band, green i-band and purple z-band. It can be seen that for many of the galaxies we obtained magnitudes much brighter than those in the SDSS.

halo (see figure 4.4). LSBVCC428 is an entirely different case - on inspection of the g-band image it looks like a plausible dwarf elliptical (figure 4.5), however, in the z-band it appears as a dense streak across the frame (figure 4.5). The u- and i-bands were also inspected: in the i-band the object appears similar to the g-band image, except fainter, whereas, in the u band it disappears entirely. After close inspection of the frame and its neighbour (LSBVCC428 lies near a frame boundary), we discovered a bright star which was having an effect on the surrounding area and caused the object we initially detected as LSBVCC428. Therefore, both LSBVCC115 and LSBVCC428 were removed from the sample.

4.3.3 REMOVING STARS FROM THE FRAMES

The issue of bright stars in the frame is the curse of CCD astronomy - both when they are too close to an object of interest and when they saturate surrounding pixels, leaving artefacts on the frame. In order to minimise this problem a star removal program was run on the cut-outs. This was done using the star removing

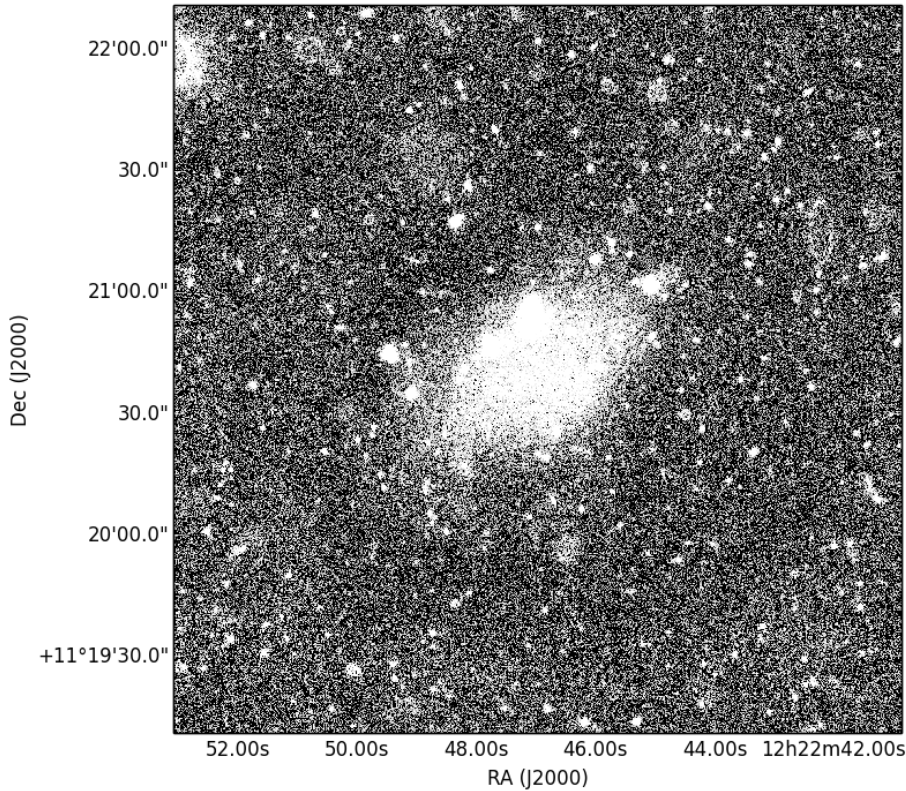


FIGURE 4.3 VCC585. The SDSS only detect the bright upper region of this galaxy, and so it's g-band magnitude is given to be 21.13 in SDSS data release 13. Conversely, we measure it to have a magnitude of 16.25 with the initial photometry code.

functionality of the PTS (PYTHON Toolkit for SKIRT) modules for SKIRT (Camps & Baes (2015), Verstocken et al. in prep.)¹. The wcs information is used to query catalogues and identify bright stars in the frame. It then masks these, as well as associated diffraction spikes, by replacing them with regions mimicking the background noise of the frame. Figure 4.6 shows an example of the star removal. As can be seen, it does not perfectly remove the stars but it greatly improves them.

4.4 THE PHOTOMETRY CODE

The initial photometry code was then expanded to include more functionality. This was written using some aspects of the photometry pipeline described in Clark (2015). Specifically, Clark (2015)'s functions were used for creating ellipses

¹ <http://www.skirt.ugent.be/pts/>

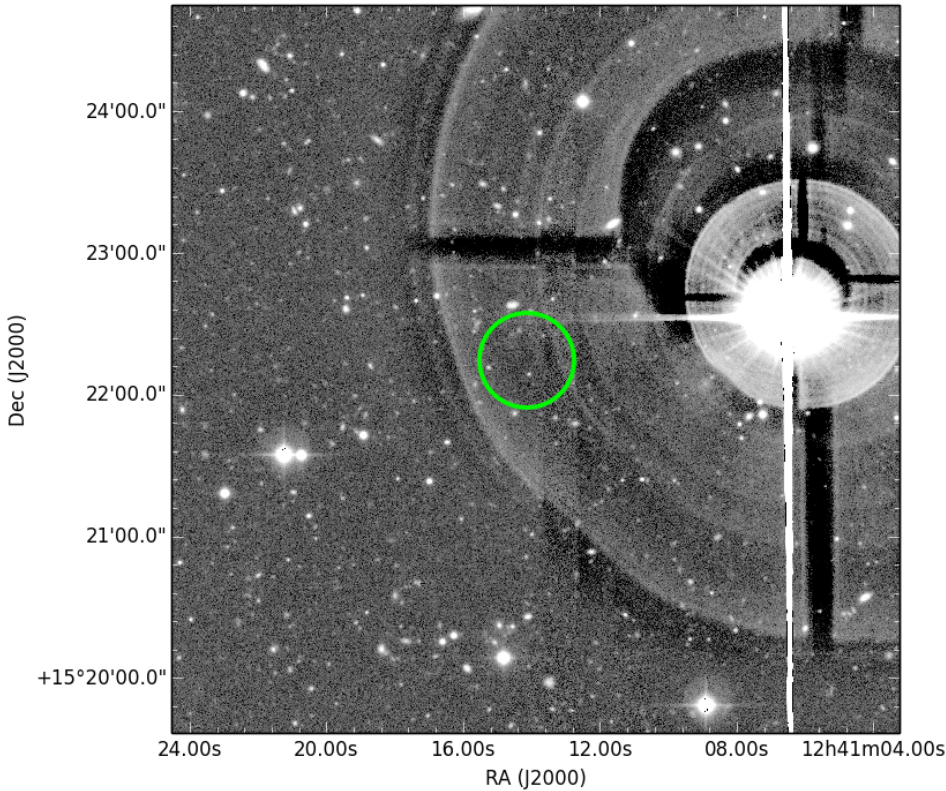


FIGURE 4.4 LSBVCC115, g-band image. The green circle represents the coordinates given in the LSBVCC. As can be seen from the image, there is no discernible galaxy and it is likely that SExtractor detected the stellar halo.

and annuli. The input parameters were the source ID, radius of the ellipse, axial ratio, position angle and the ra and dec of the galaxy. These are used to define the aperture from inside of which the flux will be taken. The background is measured using an annulus which has an inner radius of 1.5 times the aperture radius, and has a width of the aperture radius. A mean pixel background is calculated from this. The background per pixel times the number of aperture pixels is deducted from the aperture flux value: this gives the flux in the galaxy with the background removed. These apertures were defined in the g band and then used for all bands, this ensured the consistency of our measurements.

We have used this code to do two additional things:

- 1.) define the size of the galaxy to a range of surface brightness isophotes.
- 2.) measure the galaxy flux at varying isophotal radii.

This uses concentric annuli of increasing size - for each one it calculates an average surface brightness and prints out the magnitude and radius when the

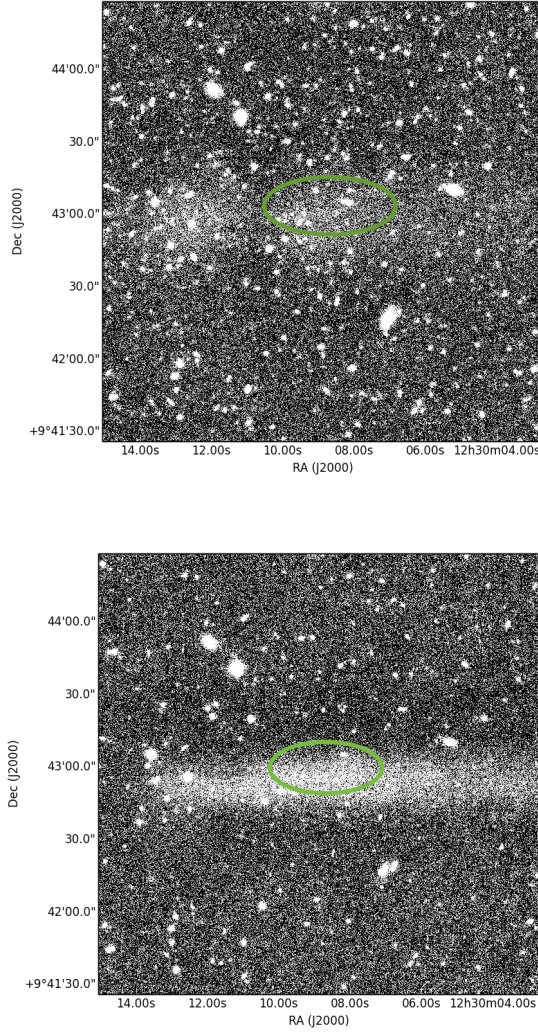


FIGURE 4.5 Upper: LSBVCC428, g-band image. The green ellipse marks the position and size of the catalogue galaxy. This galaxy appears to be a LSB elliptical galaxy in the g-band, perhaps with a second similar galaxy to the left. Lower: LSBVCC428, z-band image. The green ellipse marks the position and size of the catalogue galaxy. However, in the z-band the structure looks distinctly different. On inspection of the neighbouring frame (LSBVCC428 is near the edge of its frame), a bright star was found to be the cause of this unusual object.

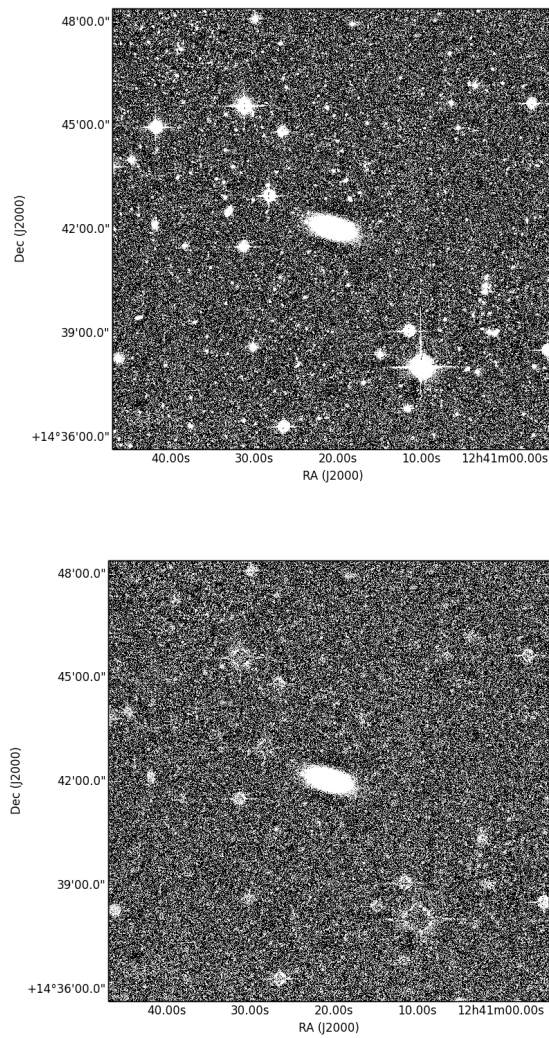


FIGURE 4.6 Upper: g-band cut-out of VCC1876. A number of stars, with diffraction spikes, can be seen in the frame. Lower: g-band cut-out of VCC1876 after the star removal package has been run. As can be seen, the stars and their diffraction spikes have been masked by noise which mimics the background noise in the frame.

required surface brightness is reached. We do this for 25 mag arcsec $^{-1}$, 26 mag arcsec $^{-1}$, 27 mag arcsec $^{-1}$ and 28 mag arcsec $^{-1}$. Although we record all of these measurements, only those in the g-band are used to define apertures when calculating magnitude, colour and mean surface brightness. The g band was chosen because it is the only NGVS band that has complete coverage in the Virgo cluster. We inspected this aperture on a sample of galaxies by eye to ensure that we were not going to miss flux in the other bands. Using one band to define aperture sizes ensures our measurements are consistent and comparable across all four bands.

With all of these aspects taken together we can calculate the magnitude, colour, size and surface brightness of all galaxies in our sample.

4.5 FIXING PROBLEMS IN THE LSB PHOTOMETRY

As the LSBVCC contains far fewer galaxies than the VCC it was decided that problems would be identified on this data set first, and then what was learnt could be applied to the whole VCC.

For the LSBVCC sample it was found that for many galaxies we obtained magnitudes far fainter than those given in Davies et al. (2016). This comparison was done in the g-band as this is the band in which Davies et al. (2016) give magnitudes. On inspection of the radii being measured for the isophotal galaxy sizes it was realised that, especially for the fainter surface brightnesses, many of the galaxies sizes were only the width of the first annuli iterated over. This was due to the fact that many of the LSB galaxies either don't reach 25 mag arcsec $^{-2}$, or, are so clumpy in texture that they fall below 25 mag arcsec $^{-2}$, and then rise above it again. This was caused by the fact that many LSB galaxies have bright HII regions joined together by extremely low surface brightness material.

Initially we tried to fix this problem by altering the code to look for all instances where the surface brightness in an annulus was 25 mag arcsec $^{-2}$ or above. It would then look for when the distance between one instance of the surface brightness having this value and the next instance was double the distance from the previous one. However, this then over-measured the size of many of the galaxies as it ended up selecting a point with a bright background contaminant, rather than a point within the LSB galaxy.

The next approach used was smoothing the galaxy images to attempt to negate the effect caused by the clumpy nature of the galaxies - effectively smoothing out the HII regions with the interconnecting LSB structure. The images were smoothed on a pixel-by-pixel basis using a Gaussian with a standard deviation of

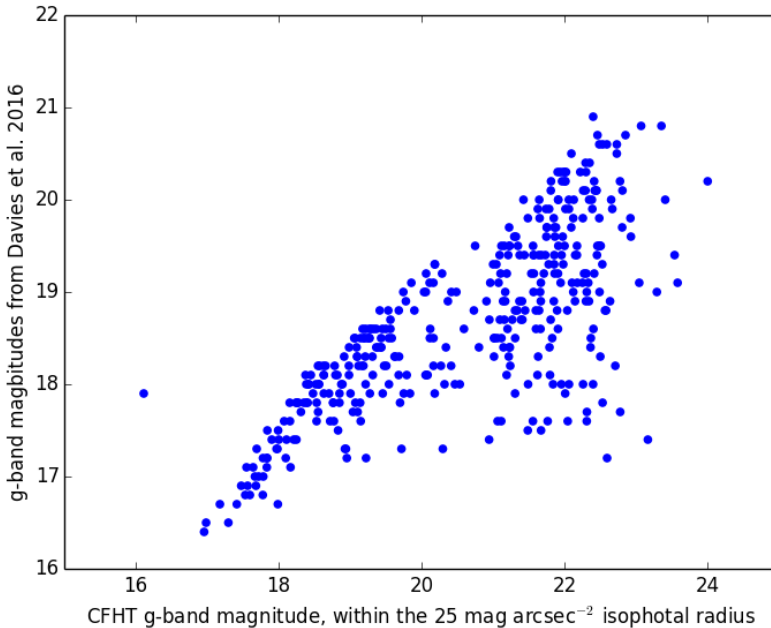


FIGURE 4.7 A plot showing the $25 \text{ mag arcsec}^{-2}$ isophotal magnitudes for the LSB galaxy sample plotted against those from Davies et al. (2016). As shown by the plot this isophote cannot be used to reliably measure LSB galaxies. (the x axis shows the values measured from the NGVS data.)

4 pixels- this did not over-smooth the images and any errors introduced fell within the size of the radial annuli.

This worked well, and fixed the problems being caused by the flocculent internal structure of the LSB galaxies. However, we still faced the problem of which isophotal size to pick to carry out colour calculations with. The photometry code was run on the smoothed galaxies in order to inspect the results, and pick the most appropriate aperture size.

As can be seen from the plots in figures 4.7 to 4.10, the g-band 28 mag arcsec^{-2} isophotal magnitudes produce results which correlate extremely well with those from Davies et al. (2016). When the brighter magnitude isophotes are used the fainter galaxies are often undermeasured. This is due to many of these galaxies not reaching surface brightnesses of 25 or 26 mag arcsec^{-2} , or reaching these magnitudes but dropping below them rapidly. When the 28 mag arcsec^{-2} data set was compared to that of Davies et al. (2016), a median value of 1.004 was attained. Initially, a few outliers were removed from the sample which, on inspection, had bright stars near the galaxy meaning flux was being over measured.

All remaining outlying points in figure 4.10 were then inspected. For a few of these there had been an issue with the star removal: in some cases where a

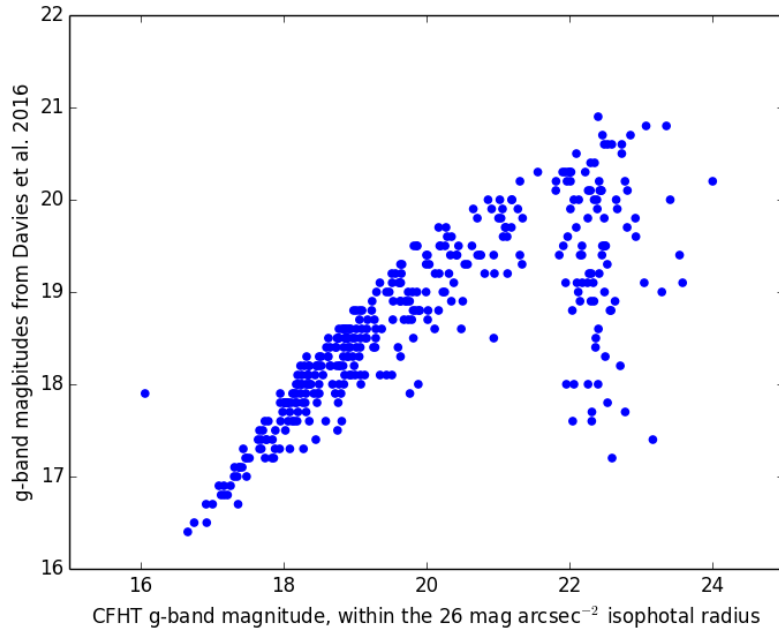


FIGURE 4.8 A plot showing the 26 mag arcsec⁻² isophotal magnitudes for the LSB galaxy sample plotted against those from Davies et al. (2016). This is an improvement to the 25 mag arcsec⁻² plot, but the faintest LSB galaxies are still not well measured. The x axis shows the values measured from the NGVS data.

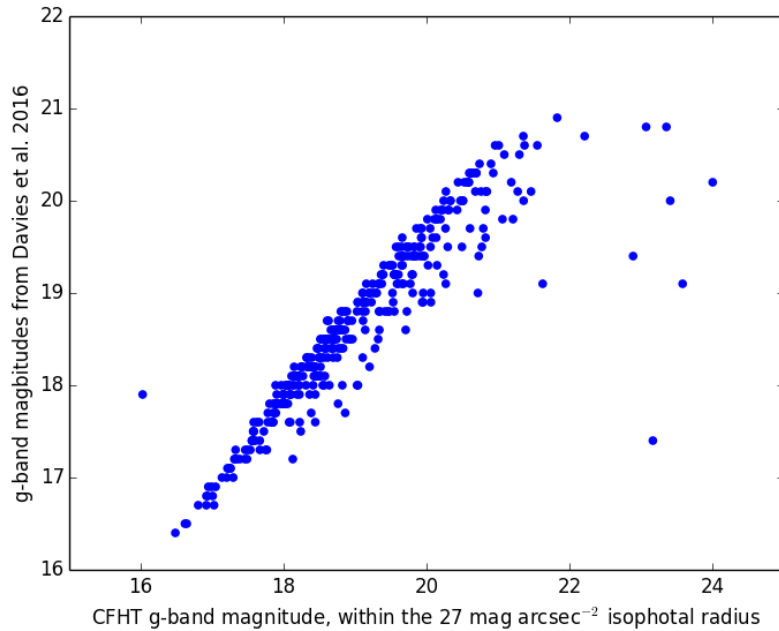


FIGURE 4.9 A plot showing the 27 mag arcsec⁻² isophotal magnitudes for the LSB galaxy sample plotted against those from Davies et al. (2016). Here only a few galaxies have been clearly mis-measured within the isophotal radii. The x axis shows the values measured from the NGVS data.

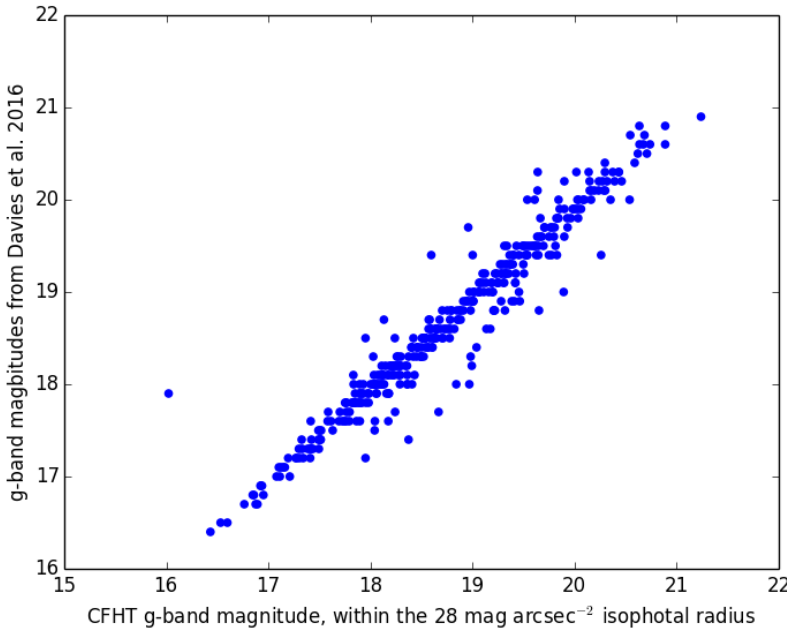


FIGURE 4.10 A plot showing the 28 mag arcsec^{-2} isophotal magnitudes for the LSB galaxy sample plotted against those from Davies et al. (2016). This produces a good correlation between the two sets of results. The x axis shows the values measured from the NGVS data.

star's coordinates were very close to those of the central galaxy some of the galactic light had been removed with the stellar light. In these cases, the non-star-removed frames were inspected and used. The photometry was re-run on these and the magnitudes checked. Where photometry had clearly been affected by the stars in the frame the results were removed from the sample. In the remaining cases the target galaxies were sharing a frame with another galaxy, in these cases the 'companion' galaxy was found to be affecting the background subtraction and these frames were also removed from the sample.

The outlying point to the bottom left of figure 4.10 represents LSBVCC004. This is an unusually shaped galaxy for which we measure a magnitude of 16.02 and Davies et al. (2016) measure a magnitude of 17.9. There are some remaining points which don't sit on a perfect 1:1 line. This can be explained by the fact that the Davies et al. (2016) magnitudes were measured using *SExtractor*, whereas we have fit our galaxies to obtain accurate position angles and axial ratios and used these to define our apertures. This means that in some cases the Davies et al. (2016) photometry misses flux, or contains extra background flux, whereas we have minimized the effects of this.

As can be seen from the isophotal results for the LSBVCC sample the 28 mag

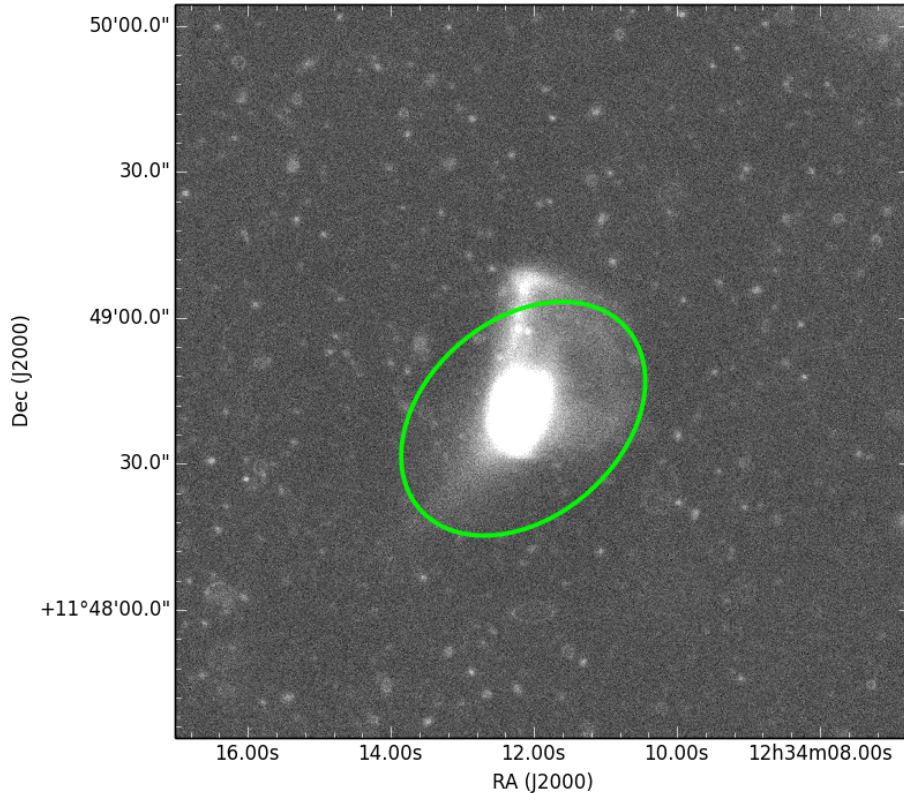


FIGURE 4.11 LSBVCC004. Due to the galaxy's unusual shape, we measure a much more accurate magnitude than Davies et al. (2016). The green ellipse is the annulus within which we have measured flux. It contains much more of the extended emission that it would if it were fit to the bright core of the galaxies, as in Davies et al. (2016). The SDSS model-Mag magnitudes were used throughout this thesis. To attain these the SDSS first fits both de Vaucouleurs and exponential profiles to a source in the r-band and then use the best fit to define the aperture for all bands. Therefore, it is not possible to recreate the exact SDSS aperture on this plot, as the surface brightness they measure down to will change by galaxy. The SDSS data has a surface brightness noise limit of between 22 and 24 mag arcsec $^{-2}$ in all bands, whereas the limiting surface brightness in the NGVS is 26.9 mag arcsec $^{-2}$, meaning that the photometry in this thesis probes much lower surface brightness levels than that of the SDSS. The galaxy is not included in the photometry results tables in the appendix, as it was not covered in all four bands.

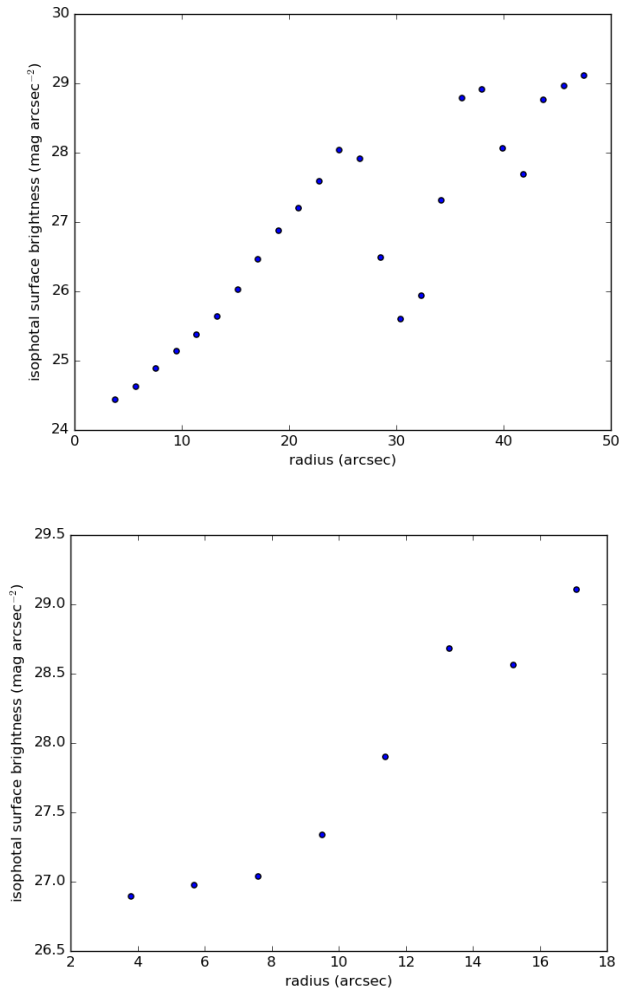


FIGURE 4.12 Upper: Radial surface brightness profile of LSBVCC431. The profile is traced nicely to 28 mag arcsec⁻² but after this background sources dominate. Lower: Radial surface brightness profile of LSBVCC414. Again the profile is traced to a little fainter than 28 mag arcsec⁻² before being affected by background variation.

arcsec^{-2} isophotal radii are the most accurate for measuring the magnitudes: they allow us to probe the lowest surface brightness limit of the data. In order to further demonstrate this the surface brightness profiles of the galaxies were checked to verify that the data was reliable down to the 28 mag arcsec⁻² isophotal radii. To do this the g-band isophotal radii and surface brightnesses were plotted against each other, to give galaxy profiles. Although some could be traced to fainter magnitudes many profiles did not remain smooth after the 28 mag arcsec⁻² surface brightness isophote. Some example profiles are shown in figure 4.12.

The final plot of the magnitudes calculated using the 28 mag arcsec⁻² isophotal radii against those from Davies et al. (2016) is shown in figure 4.13.

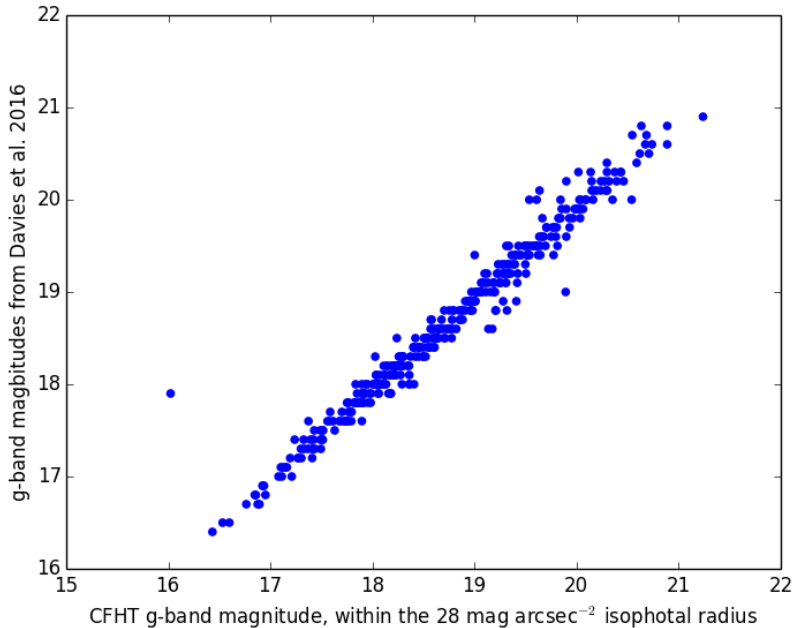


FIGURE 4.13 A plot showing the 28 mag arcsec⁻² isophotal magnitudes for the LSB galaxy sample plotted against those from Davies et al. (2016). Here, all outlying points caused by problematic star removal, or bright stars and galaxies in the frame, have been removed from the sample. The x axis shows the values measured from the NGVS data.

Therefore, these are the sizes being used to attain colours for the LSB galaxies. As we have the largest sample of LSBVCC galaxies in the g-band, the g-band 28 mag arcsec⁻² isophotal radii are being used to obtain colours. An aperture of this radius will be used for all bands, to ensure that we are measuring magnitude within a consistent radii.

4.6 PERFECTING THE VCC PHOTOMETRY

The photometry code was then run on the entire VCC sample of galaxies. To check these initial outputs, and identify sources of error, the 25 mag arcsec⁻² isophotal magnitudes were plotted against both the magnitudes from the original VCC (Binggeli et al. 1985) (figure 4.14) and those from the SDSS data release 9 (Ahn et al. 2012) (figure 4.15). The 25 mag arcsec⁻² was used here initially as for bright, L* galaxies this works very well - they have bright enough central regions that the 25 mag arcsec⁻² isophote contains the majority of the galaxy's light. As an initial rough check we looked at the number of galaxies for which we got magnitude values which differed by more than 2 magnitudes from those in the VCC or

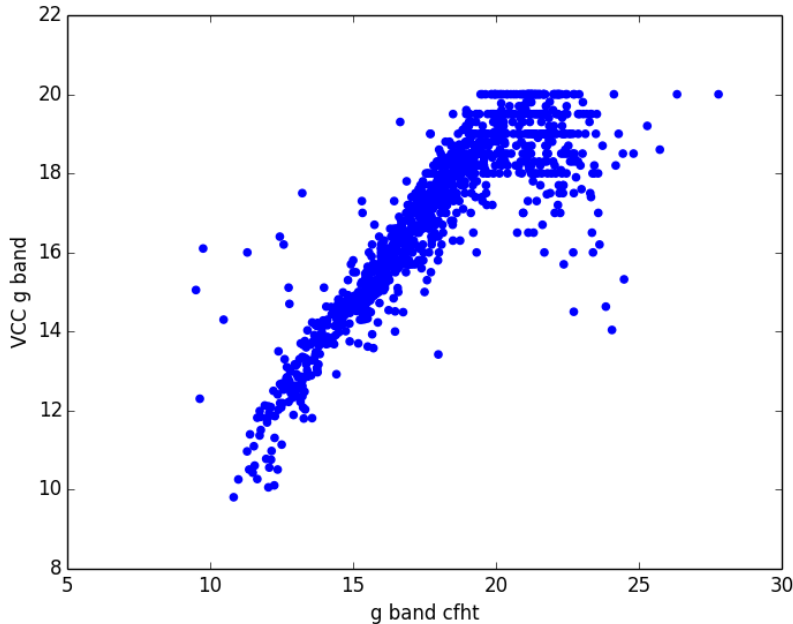


FIGURE 4.14 The VCC magnitudes from Binggeli et al. (1985) plotted against the CFHT g-band magnitudes. The y axis shows the values measured from the NGVS data.

SDSS. We used the SDSS g-band magnitudes. The VCC magnitudes (Binggeli et al. (1985) magnitudes are given in the B band: we do not have B band frames for the NGVS but the g-band is comparable. For the VCC we found that there were 238 galaxies with magnitudes differing by more than 2 ($\sim 21\%$ of the sample), and for the SDSS we found 280 galaxies ($\sim 25\%$). Additionally, the magnitudes from the VCC were then plotted against those from the SDSS (figure 4.16) and 278 galaxies were found with a magnitude difference of more than 2 (again, $\sim 25\%$ of the sample). Therefore, although we did not have a perfect correlation, all outlying galaxies were examined to understand why the magnitudes differ from those in the SDSS and VCC.

We found 128 galaxies where the magnitude differed by 2 or more from both the VCC and the SDSS. These were checked by eye to isolate any issues which could be causing these differences. Some frames were found to have defects - the frames had frame divides, or badly fitted together edge frames; 12 frames were removed from the sample because of this. An additional 4 frames were removed as the galaxies did not appear at the coordinates specified in the VCC. In some circumstances the star removal process had affected light from the target galaxy - this was due to stars/galaxies in close proximity being removed, or effects from the removal of diffraction spikes. 66 frames had been affected by this. These were

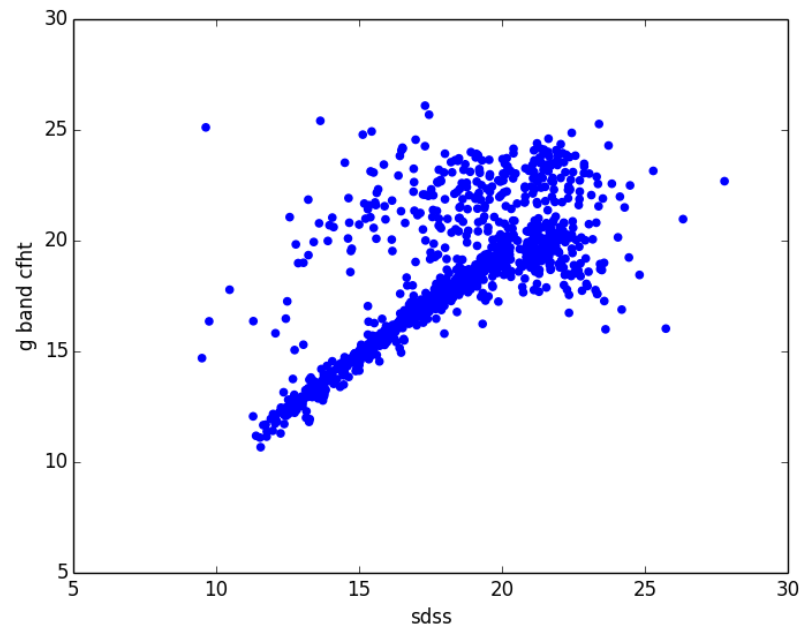


FIGURE 4.15 The SDSS data release 9 g-band magnitudes plotted against the CFHT g-band magnitudes. The y axis shows the values measured from the NGVS data.

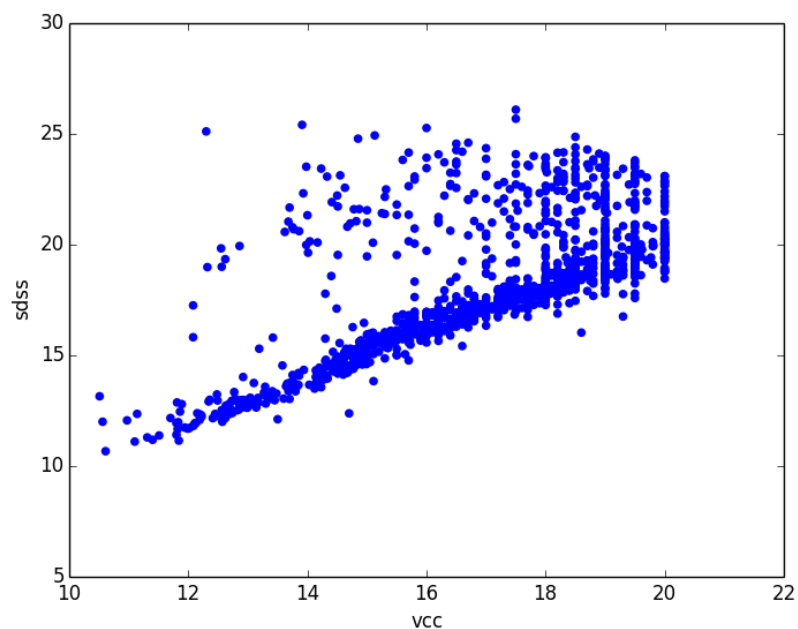


FIGURE 4.16 The VCC magnitudes from Binggeli et al. (1985) plotted against those from the SDSS data release 9.

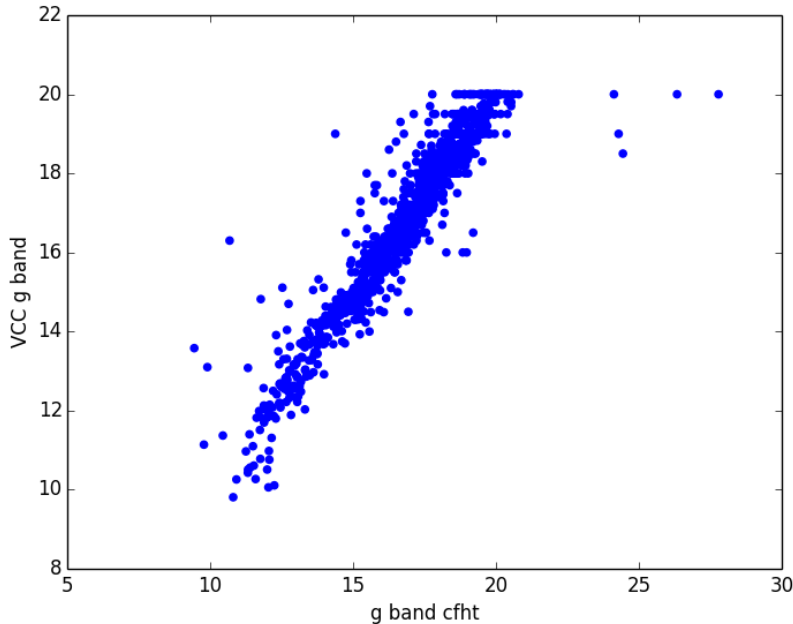


FIGURE 4.17 The VCC magnitudes from Binggeli et al. (1985) plotted against our g band $28 \text{ mag arcsec}^{-2}$ isophotal magnitudes. The x axis shows the values measured from the NGVS data.

replaced with the non star removed frames - this resolved the magnitude difference for all but 7 of these galaxies. Of these we found our magnitude to be correct in 4 cases, and in the other 3 cases the frames had to be removed due to bright stars affecting the photometry of the galaxy.

Many issues found on the frames could only be identified by eye so it was decided that all of the galaxy frames should be checked for defects. This was done in the g band first and the results inspected. Overall 127 galaxies were removed from the sample after this check: 15 of these had badly fitted together edge frames, and the remaining frames were removed because of over subtraction of stellar light due to stars lying very close to the target galaxy. This greatly improved results, and they were used to choose an aperture size for the VCC galaxies in order to obtain colours. As for the LSBVCC galaxies, the $28 \text{ mag arcsec}^{-2}$ isophotes will be used as these trace the galaxies well to the lowest detectable surface brightnesses. The results of the $28 \text{ mag arcsec}^{-2}$ isophotal magnitudes are plotted against the VCC magnitudes from Binggeli et al. (1985) in figure 4.17.

In checking remaining outliers it was discovered that a handful of the lower surface brightness VCC galaxies were being affected by the same issue that was found with many of the LSBVCC galaxies: the galaxies were so flocculent that the

isophotal measurements were being affected by the ‘clumpyness’ of the profile. The effect can be seen in the spread of our magnitudes at the faint magnitude end of figure 4.17. Again, we chose to smooth the sample and compare the smoothed and un-smoothed results, to see which were more accurate.

The photometry was re-run on the smoothed g band frames in order to compare these results with the un-smoothed run. We found that for the entire VCC sample this actually caused many more problems. The frames are generally a lot busier than the LSBVCC frames and contain many background galaxies, stars and stellar halos. In far too many instances these were being smoothed into the central galaxy and causing the photometry code to then over-measure radii and fluxes. As all VCC galaxies have apparent magnitudes which are brighter than 20 in the B band (Binggeli et al. 1985) only a few sources were affected by the original problem. Therefore it was decided to do photometry on un-smoothed frames for the VCC and afterwards remove unreliable results.

The results from the u, i and z bands were also then checked against those from the SDSS. Again, there was good agreement between the magnitudes for the VCC galaxies. Therefore, it was decided that galaxy sizes would be measured out to the 28 mag arcsec⁻² isophote in the g band, and this aperture would be used to calculate magnitudes for colours in all other bands.

4.7 PHOTOMETRIC ERRORS

We have incorporated both calibration and photometric errors. These have been added in quadrature to produce the final magnitude errors on tables 7.1 and 7.4.

Photometric errors have been calculated using the formula:

$$\sigma_{tot}^2 = \frac{1}{g} \sum_{i=1}^N \frac{(S_i - \bar{B})}{N_i} + (N + k \frac{N^2}{N_B}) \sigma_{B/pix}^2 \quad (4.1)$$

where σ_{tot}^2 is the noise variance in the flux of the source, g is the gain (this is given as 1.62 on the Canada France Hawaii Telescope website), N is the number of pixels in the source aperture, N_B is the number of pixels in the background annulus, N_i is the depth of coverage at pixel i (this is taken to be one as the frames aren’t co-adds), S_i is the signal in pixel i, \bar{B} is the median background per pixel, $k = \pi/2$ as we are using the median background, and $\sigma_{B/pix}^2$ is the variance in the background annulus.

SDSS band	uncertainty (%)
u	1.3
g	0.8
i	0.7
z	0.8

TABLE 4.2 The SDSS band calibration uncertainties.

The first term gives the noise-variance in a background subtracted source flux, and the second term comes from the variance in the mean sky background per pixel.²

Regarding the calibration uncertainties, Ferrarese et al. (2012) state that calibration of the NGVS data is accurate to within 1% of the SDSS. The most recent SDSS calibration uncertainties are given by Padmanabhan et al. (2008). Table 4.2 has these listed for the four bands we use. Therefore the total calibration uncertainty is taken to be the quadrature sum of both of these.

The radii quoted in tables 7.3 and 7.6 are subject to an error of ± 0.5 arcseconds as this is the width of the annuli that was iterated over to measure radial sizes.

As can be seen from the data tables in the appendix, the errors on our photometric measurements are very small, with the largest errors being of the order of $\sim 2\%$. These errors are smaller than those on similar data sets, such as the SDSS, due to the fact that the NGVS frames are processed so that the background sky level is the same in all frames (Ferrarese et al. 2012), this is not possible for larger surveys such as the SDSS as it covers a much greater area of sky. Therefore, they are included in that data tables but are not visible on plots.

4.8 SERENDIPITOUS DISCOVERIES

Through the course of carrying out the photometry some discoveries were made incidentally. This was due to the fact that when unexpected magnitude results were obtained for a galaxy then the cut-out image was inspected visually to look for clues as to why. This led to finding some interesting artefacts in the frames.

² A full derivation can be found at <http://wise2.ipac.caltech.edu/staff/fmasci/ApPhotUncert.pdf>.

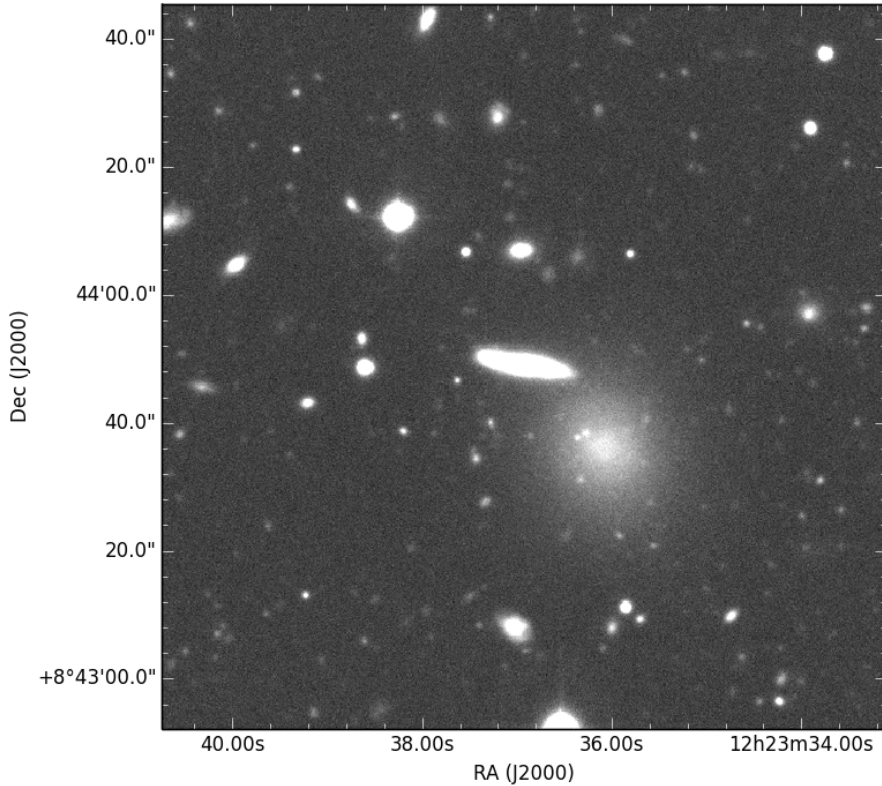


FIGURE 4.18 VCC 652 and it's companion.

4.8.1 VCC 652'S COMPANION

Initially, very faint magnitude values were obtained for VCC 652 compared to its SDSS magnitude, and that given in the VCC. When the cut-out was inspected a large LSB companion was found at coordinates: 185.90073, 8.72669. The term companion is used loosely, as we are unaware whether these two galaxies are physically related to one another. When these coordinates were searched in the SDSS DR13 it was discovered that their photometry had split this LSB companion into two objects. Figure 4.18 shows VCC652 and its companion.

The magnitude values from the two SDSS objects that the companion galaxy has been split into are shown in table 4.3.

Photometry was carried out on the CFHT image by hand in DS9, to ensure that VCC652 itself was not included in the background counts and subtracted. Additionally, we attain a mean surface brightness value for this source in the g band of $25.20 \text{ mags arcsec}^{-2}$.

This shows that when classed as one object the companion of VCC652 is

SDSS band	magnitude object a	magnitude object b
u	24.64	24.30
g	24.02	21.39
r	20.75	21.05
i	20.45	20.74
z	20.82	20.42

TABLE 4.3 The SDSS magnitudes of the two objects that the companion of VC652 is split into.

SDSS band	magnitude
u	19.30
g	18.08
i	17.25
z	17.07

TABLE 4.4 Our values for the SDSS-band magnitudes for the companion of VCC652, as calculated from photometry carried out on the CFHT images.

significantly brighter than it is measured to be in the SDSS, and can clearly be seen to be a dwarf elliptical galaxy. This also highlights problems with how the SDSS deals with low surface brightness objects. It is notoriously poor at measuring them as it often splits them into multiple objects. This can also affect the LSB outskirts of bright galaxies. This highlights the need for better detection software as survey data gets deeper.

This chapter has highlighted the various issues and challenges involved in carrying out automated photometry on a large data set. Having compared our results to those of others, and removed any frames on which photometry could not be carried out, we are left with the final sample for analysis. This consists of 620 VCC galaxies in all 4 bands and 232 LSBVCC galaxies all 4 bands.

4.9 PHOTOMETRY RESULTS

This chapter has highlighted the various issues and challenges involved in carrying out automated photometry on a large data set. Having compared our results to those of others, and removed any frames on which photometry could not be carried out, we are left with the final sample for analysis. This consists of 620 VCC galaxies in all 4 bands and 232 LSBVCC galaxies all 4 bands. This sample is superior to previous work as it covers more galaxies, in more bands, to lower surface brightness levels. For comparison, Davies et al. (2016) have measured a sample of 443 galaxies in the g band down to a surface brightness of 27.9 mags

arcsec^{-2} , Sabatini et al. (2003) and Sabatini et al. (2005) have 231 Virgo LSB dwarfs in the B and I bands to a surface brightness of 26 mag arcsec^{-2} , Lisker et al. (2007) use a sample of 413 Virgo dwarfs from the SDSS (their noise limit is 24.2 mag arcsec^{-2} in the u band, 24.7 in g, 24.4 in r, 23.9 in i, and 22.4 in z), and Roediger et al. (2017) present 404 Virgo galaxies from the NGVS data in four bands (they quote a limiting surface brightness of 26.9 mag arcsec^{-2}).

The results tables for the photometry of the Virgo cluster galaxies are given in the appendix. Tables 7.1, 7.2 and 7.3 include all data for the 620 VCC galaxies, and tables 7.4, 7.5 and 7.6 contain data for the LSBVCC sample. As explained above, the given magnitudes were measured within the g-band 28th magnitude arcsec^{-2} isophote. The magnitude results from this isophotal radius correlated well with both results from Binggeli et al. (1985) and Davies et al. (2016). A full explanation is given earlier in this chapter. The same size aperture was then used across all four bands, to ensure consistency. Magnitudes are given as apparent magnitudes in each band. This is due to the large range in distances of Virgo galaxies: without direct measurements the exact distance to each galaxy is not known, therefore if apparent magnitudes are converted to absolute magnitudes using one set distance then additional errors will be introduced. The Virgo cluster is made up of two main subclusters, A and B, at different distances. Mei et al. (2007) give the distances of the these as 16.7 ± 0.2 Mpc and 16.4 ± 0.2 Mpc respectively, whereas Gavazzi et al. (1999) gives the distance to subcluster A as 14.7 Mpc and B at 23.33 Mpc. We focus on subclusters A and B as this is the extent of the NGVS data, the full structure of the Virgo cluster is a lot more complex. Mei et al. (2007) gives the total distance range within subcluster A to be 2.4 Mpc, with Solanes et al. (2002) quoting a distance range for gas associated with Virgo cluster galaxies of 16 to 22 Mpc. This means that, for a Virgo galaxy with an apparent magnitude of 16 (which is quite typical for the sample discussed here), this distance range could introduce an additional error of ± 0.69 magnitudes on the absolute magnitude. As colour and surface brightness are both independent of distance in the local universe then these measurements are not affected.

CHAPTER 5

VIRGO CLUSTER RESULTS AND ANALYSIS

'Life is like a box of sardines and we are all looking for the key'

ALAN BENNETT

In Chapter 4 I described the method by which photometry was performed on the VCC and LSBVCC galaxies. This has provided a sample of 852 galaxies with photometry in all four bands (620 from the VCC and an additional 232 from the LS-BVCC). I have chosen to only include those galaxies with photometry in four bands in order to ensure that the sample being analysed is consistent. In this chapter I will use the results of my photometric analysis to explore the properties of Virgo cluster galaxies, with the aim of exploring whether these properties can be used to select for dwarf galaxies. I will then compare these results with a background field population. This will allow me to investigate whether dwarf galaxies in the Virgo cluster, and dwarfs in general, can be identified using their photometric properties alone.

5.0.1 VIRGO CLUSTER LUMINOSITY FUNCTION

In Davies et al. (2016) data is used from the new LSBVCC, as well as the VCC (Binggeli et al. 1985) and the EVCC (Kim et al. 2014) to produce a luminosity function for the Virgo cluster. Figure 5.1 shows our new luminosity function. The blue line is for the VCC galaxies, whereas the red line is the total luminosity

function including the VCC, EVCC and LSBVCC. It can be seen that the LSBVCC contributes significantly at the faint end of the function, but there are insufficient detected galaxies beyond $m_g \sim 18$ to maintain the slope. This means that either a significant number of faint galaxies have been missed (around a factor of 20 more galaxies at $m_g \sim 20$), or the slope drops off sharply after $m_g \sim 18$. Due to the fact that these faint galaxies are notoriously hard to find (as evidenced by chapter 3), it is most likely that a large population of faint galaxies have not been detected. A Schechter function has been fit to the data, only including sources with a magnitude brighter than $m_g = 18$, and a faint end slope (α value) of -1.35 ± 0.03 has been obtained. This is a slight improvement on the VCC α value of -1.30 ± 0.03 in comparison to predicted values from simulations. However, if more of the faint galaxies could be detected, this should further improve the faint end slope for the cluster. Later in this chapter I will explore the multi-band photometric properties of Virgo galaxies to investigate potential ways of doing this.

As mentioned previously throughout this thesis, the faint end slope of the Schechter function predicted by the majority of simulations does not currently match the observed faint end slope. We have presented here the most complete luminosity function to date for the Virgo cluster, with a faint end slope of -1.35 ± 0.03 . Guo et al. (2016a) compare the results from the EAGLE hydrodynamical simulations to those from two semi-analytical models, L-GALAXIES and GALFORM. The semi-analytical models have been applied to merger trees resulting from the EAGLE dark matter only simulations (EAGLEDMO). Both the EAGLE and EAGLEDMO simulations use a box size of 100 Mpc. EAGLEDMO uses a dark matter particle mass of $1.5 \times 10^7 M_\odot$, whereas EAGLE uses a dark matter particle mass of $9.70 \times 10^6 M_\odot$ and a gas particle mass of $1.81 \times 10^6 M_\odot$. As the work on Virgo is concerned with the local universe, we will compare our results with those from the zero redshift simulations. EAGLE, L-GALAXIES and GALFORM acquire faint end slope values of $\alpha = -1.43$, $\alpha = -1.34$, and $\alpha = -1.44$ respectively. The L-GALAXIES faint end slope value is comparable to that obtained in Davies et al. (2016), however, this is from a dark matter only simulation and the particle mass does not probe the mass scales of the smaller faint galaxies. The Illustris simulations (Vogelsberger et al. 2014b) modelled a volume of 106 Mpc³ and included both dark matter and baryons at a redshift of zero. They have a dark matter mass resolution of $6.26 \times 10^6 M_\odot$ and a baryonic mass resolution of $1.26 \times 10^6 M_\odot$. They claim their luminosity function matches the SDSS g,r,i and z luminosity functions well, however do not plot them against each other or provide a value for their faint end slope. Again, the Illustris particle masses do not probe the region of the smallest dwarf galaxies.

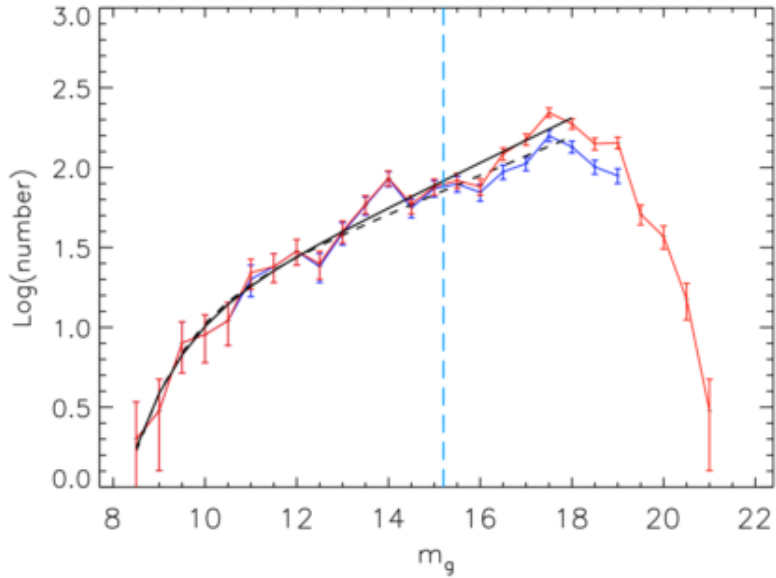


FIGURE 5.1 A luminosity function for the Virgo galaxies. The dark blue line shows the function for the VCC galaxies, and the red line for the combined VCC, EVCC and LSBVCC galaxies. Poisson error bars are shown. The black line shows the Schechter function fit to the combined data, yielding a faint end slope of -1.35 ± 0.03 . The light blue line marks the extent of the Montero-Dorta & Prada (2009) SDSS g band luminosity function data. From Davies et al. (2016).

This demonstrates that although simulations are improving, with respect to the amount of physics incorporated within them and the mass scales they probe, they still can't be reliably compared to observational data. The observations currently reach lower masses than simulations, and attain luminosity functions with less negative alpha values. However, to be able to compare them completely we need to know that our sample of dwarf galaxies is complete down to some magnitude limit. The work presented in the rest of this chapter aims to find a way of doing this by using the photometric properties of dwarf galaxies to separate them from contaminating background galaxies, which may otherwise end up in dwarf samples.

5.1 COMPARISON WITH COLOURS OF LOCAL GROUP DWARFS

I now have accurate colour values for 852 Virgo cluster galaxies. In order to explore the dwarf population of Virgo these colour values will be used, in combination with other photometric properties. However, before doing this it will be

Colour	Johnson et al. (2013) median	LSBVCC median	LSBVCC and VCC dE median
$u - g$	0.78 ± 0.21	1.06 ± 0.12	1.09 ± 0.15
$u - i$	1.16 ± 0.26	1.84 ± 0.22	1.88 ± 0.22
$u - z$	1.16 ± 0.31	1.91 ± 0.27	1.99 ± 0.26
$g - i$	0.41 ± 0.18	0.76 ± 0.16	0.79 ± 0.13
$g - z$	0.51 ± 0.24	0.85 ± 0.23	0.89 ± 0.19
$i - z$	0.08 ± 0.21	0.09 ± 0.14	0.10 ± 0.13

TABLE 5.1 Median colours for local dwarfs as well as the Virgo dwarfs. Column 1. gives the colour, 2. Johnson et al. (2013) median colour, 3. LSBVCC median colour and 4. median colour for the LSBVCC and dwarf elliptical VCC galaxies. Errors are given from the 1σ confidence interval on the median.

useful to explore how ‘typical’ these dwarf galaxies appear in terms of colour when compared to more local dwarfs.

We wanted to do a colour comparison between the Virgo cluster dwarf galaxies and the dwarf galaxies in our Local Group, however, colour information for Local Group dwarfs is extremely hard to come by. As the Local Group dwarfs are resolved there is generally information on the colours of members of their resolved stellar population, but little to no information on their global colours. Johnson et al. (2013) give SDSS u , g , i and z colours for a small sample of dwarf galaxies within the local void. They analyse galaxies from the ACS Nearby Galaxy Survey Treasury (ANGST, Dalcanton et al. 2009), which come from a diverse range of environments including pairs, groups, filaments and isolated regions. We have used the data for all galaxies in table 2 of Johnson et al. (2013) which had magnitudes in the u , g , i and z bands, this was a total of 21 galaxies.

We have used colour values for the LSBVCC galaxies and the dwarf elliptical galaxies from the VCC. To test whether the void galaxies are more or less similar to the LSBVCC galaxies than the general cluster dwarf population we have presented 2 separate medians: one is the median colour for just the LSBVCC galaxies, and the other is the median colour for the combined LSBVCC and VCC dwarf ellipticals (dE galaxies). We have a sample of 503 dwarf elliptical Virgo galaxies, and an additional 232 LSBVCC galaxies.

In table 5.1 we present the colour information from Johnson et al. (2013), as well as that from the Virgo cluster photometry. Column 1. gives the colour band, 2. Johnson et al. (2013) median colour. 3. LSBVCC median colour, and 4. the median colour from the combined LSBVCC sample and the VCC dwarf ellipticals. Errors are given from the 1σ confidence interval on the median.

From this small sample of data it appears that generally the Virgo dwarf population appears marginally redder than the local void dwarf galaxies. Others have also previously noted that Virgo galaxies generally appear redder than background populations (e.g. Taylor et al. 2012). This is interesting as it suggests that cluster dwarfs have redder stellar populations, or higher metallicities, than more isolated dwarf galaxies, which would imply that their stellar populations are older. This is perhaps to be expected as, due to the cluster environment, the dwarfs in the cluster are more likely to have lost gas through methods such as ram pressure stripping (e.g. Hester 2006, Ebeling et al. 2014), or to have not been able to retain gas after supernova explosions (e.g. Arimoto & Yoshii 1987, Larson 1974). This would mean they have a smaller gas reservoir for star formation and hence, fewer young, blue stellar populations. However, due to the small size of the local dwarf sample any results must be treated with caution. If a larger sample of global colours for local dwarfs could be obtained in the future then this would be an extremely interesting comparison to revisit.

5.2 EXPLORING VIRGO CLUSTER GALAXY PROPERTIES

The main aim of carrying out this photometry is to ascertain whether it is possible to identify cluster dwarfs solely by their observable traits, and thus separate them from background objects without direct distance measurements.

To investigate this I have used the data derived from the photometric analysis to determine whether dwarf galaxies can be identified using their photometric properties. Later, these results will be compared to those from a background field. As these plots explore relationships involving colour and magnitude I have chosen to only use the 852 galaxies for which there is photometry results in all four bands. This therefore provides a consistent sample which is the same across all analyses.

5.2.1 COLOUR-COLOUR PLOTS

Bower et al. (1992b) (published in Bower et al. 1992b and Bower et al. 1992a) carry out precision photometry on Virgo cluster early type galaxies, with the aim of exploring the colour-magnitude relation (discussed in section 5.2.2). However, their work only covers early type galaxies, and there is no published catalogue of colours for the entire Virgo cluster. Additionally, the relationship between different galactic colours in the cluster has not been explored.

In the hierarchical structure formation model, dwarf galaxies were the first to form and were the first sites of star formation (e.g. Grebel & Gallagher 2004). This means that their stellar populations are generally old and red (Gallagher & Wyse 1994). As dwarf galaxies do not have a large gas reservoir for further star formation and easily lose gas from events such as supernovae explosions (e.g. Ari-moto & Yoshii 1987, Larson 1974) they have little new or ongoing star formation. However, due to the same effects they are also relatively metal poor, when compared to larger early type galaxies. Therefore, we expect dwarf galaxies to have red colours, but not be as red as larger early type galaxies.

We will explore whether these features of dwarf galaxies can be used to aid in the identification of dwarf galaxies on colour-colour plots. Figure 5.2 shows the colour-colour diagrams for the combined VCC and LSBVCC data sets. The plots are coloured according to galaxy type, which have been taken from the original VCC. The LSBVCC galaxies are denoted by ‘lsb sample’. Dwarf early type galaxies are shown by yellow crosses, early type galaxies by red diamonds, late types galaxies by blue triangles, LSBVCC galaxies by green stars, dwarf late type galaxies by pink squares, blue compact dwarfs by pale blue circles and irregular galaxies by purple triangles.

In colour-colour space there does not appear to be any clear split between galaxy types. However, the LSBVCC galaxies and the dwarf ellipticals from the VCC do appear to have a smaller range of colours than other types: there is a lot less spread in the colours of the LSB and dwarf elliptical populations. Generally, the dwarf early type galaxies and LSBVCC galaxies seem to be clustered quite centrally within these diagrams. The LSBVCC galaxies cluster more tightly than the dwarf ellipticals in general. This means that if we have colour values for a galaxy we could compare them to the colours of the dwarfs presented here. Therefore, these colour-colour plots are able to define the region of the plot where dwarf galaxies might be found, so could exclude sample galaxies that are found elsewhere in the plot. However, it must be noted that even within the region dwarfs exist, there is a lot of confusion with other galactic types. Further methods must therefore be used to analyse the galaxies within this region.

5.2.2 COLOUR-MAGNITUDE RELATION

A colour-magnitude diagram shows the relationship between the luminosity of a galaxy, and its colour. We wanted to explore whether the lower luminosity dwarf galaxies fall on a different position on the diagrams to higher luminosity

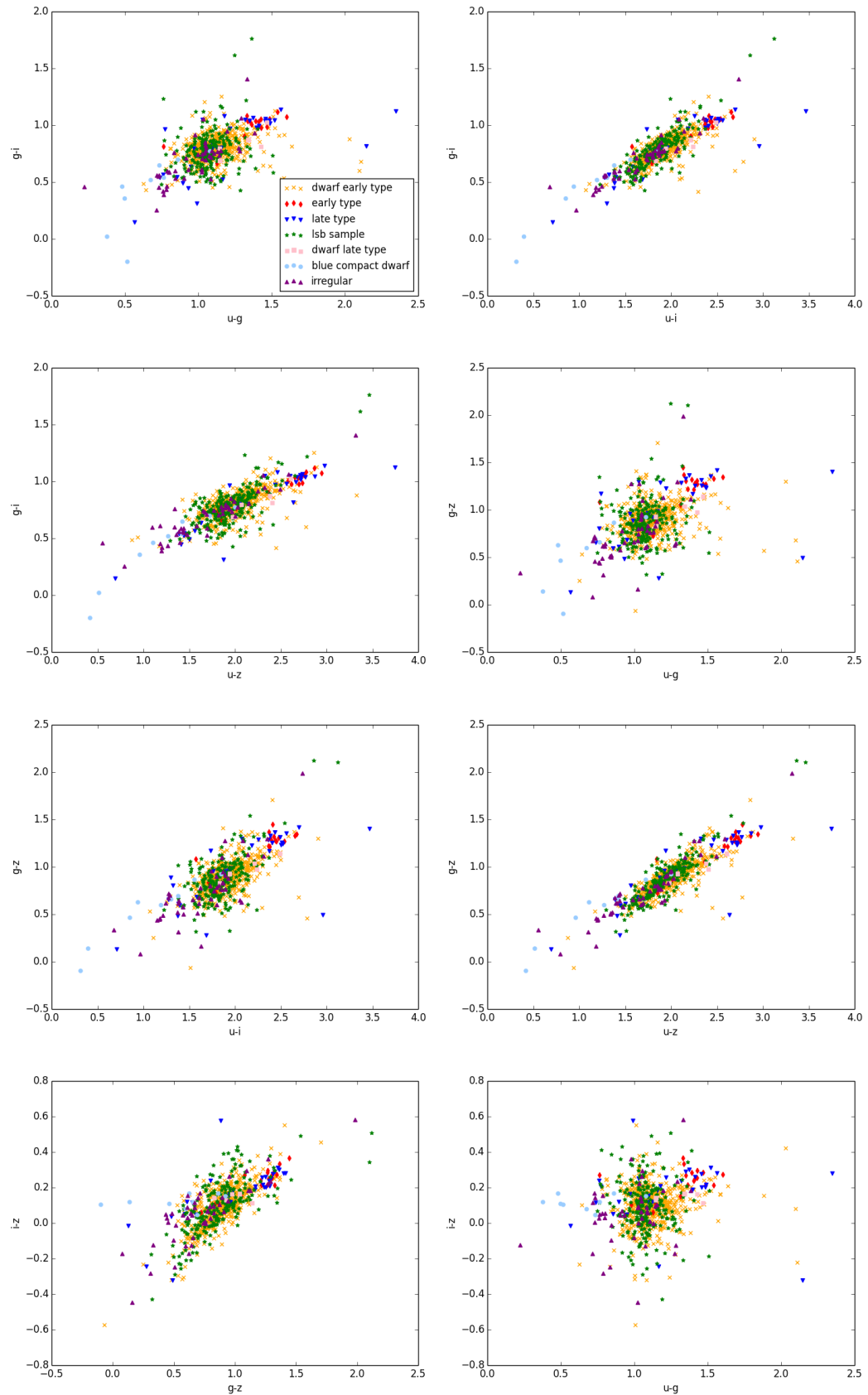


FIGURE 5.2 Colour-colour diagrams showing all colour combinations of the Virgo photometric data.

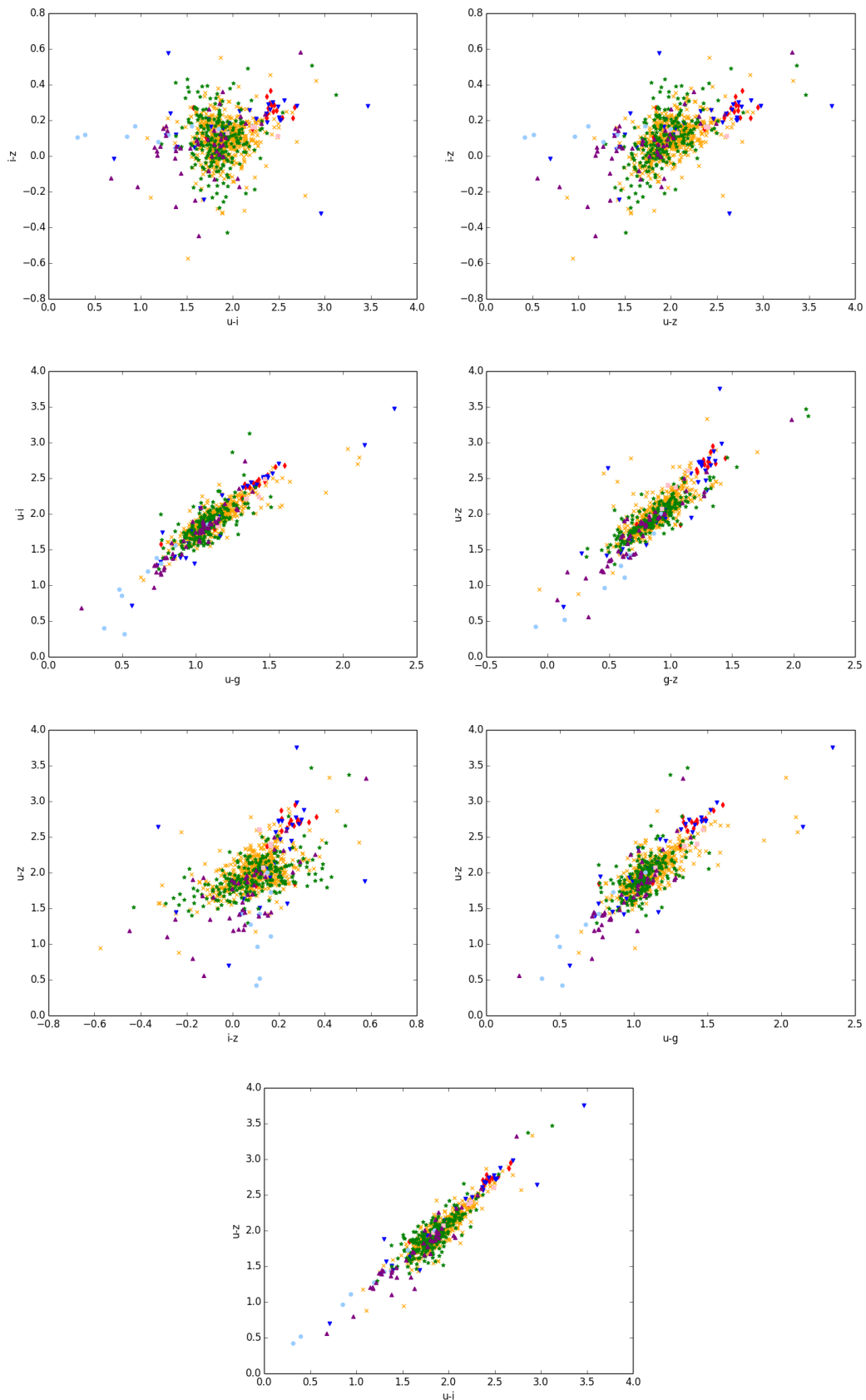


FIGURE 5.2 Continued. Colour-colour diagrams showing all colour combinations of the Virgo photometric data.

galaxies.

The colour-magnitude relation is the progressive reddening of the colours of galaxies as they get brighter (e.g. Faber 1973, Bower et al. 1992b, Bower et al. 1992a, Terlevich et al. 2001). The slope of the colour-magnitude relation has been described as a mass-metallicity relationship, with more massive galaxies having redder colours than less massive ones due to them being more metal rich (e.g. Dressler 1984). The higher metallicity of these more massive galaxies can be explained by the fact that they can retain ejected material from supernova explosions for longer periods than smaller galaxies, and therefore more of this gas can be processed in subsequent episodes of star formation before it leaves the galaxy (e.g. Arimoto & Yoshii 1987, Larson 1974). This means that as part of the supernova feedback process, metals are expelled from lower mass galaxies. Metals in stellar atmospheres absorb bluer wavelengths of light, so only the redder wavelengths are emitted. Therefore the colours of low mass galaxies remain bluer than those of their higher mass counterparts.

Odell et al. (2002) investigate the colour-magnitude relation in the Coma cluster. They use a narrowband, modified Strömgren, filter system with a wavelength of 5500 angstroms to measure their magnitudes. They find a linear colour-magnitude relation over an absolute magnitude range of -13 to -22. We have fit our Virgo colour-magnitude relation over the same range, to ascertain whether we see the same linearity. To make our results comparable we have fitted all galaxies brighter than an apparent magnitude of 18, which corresponds to an absolute magnitude of ~ -13 , taking the Virgo distance to be 16.5 Mpc (e.g. Mei et al. 2007, Blakeslee et al. 2009). Figure 5.3 shows the u-g, g colour magnitude relation for the Virgo cluster using our photometry. A least squares polynomial fit to the data is shown, over the range discussed in Odell et al. (2002). The line has an equation of $y = -0.056x + 2.057$. As can be seen, we also observe a linear colour-magnitude relation for the bright end galaxies of the Virgo cluster. Bower et al. (1992a) investigate the universality of the colour-magnitude relation by looking at both the Virgo and Coma clusters: they find that the relation has the same form in both clusters.

Figure 5.4 shows the full g-band colour-magnitude diagrams for the Virgo galaxies. There is a clear separation by type, however this is clearly largely along the magnitude axis. The brightest galaxies sit at the red end of the relation, whereas the fainter galaxies are less red. This is the red sequence which is discussed in section 5.4. There is a population of bright galaxies sitting below the red sequence. It can be seen in figure 5.3 that these consist of late type, blue compact dwarf, and irregular galaxies, which all have ongoing star formation. These diagrams

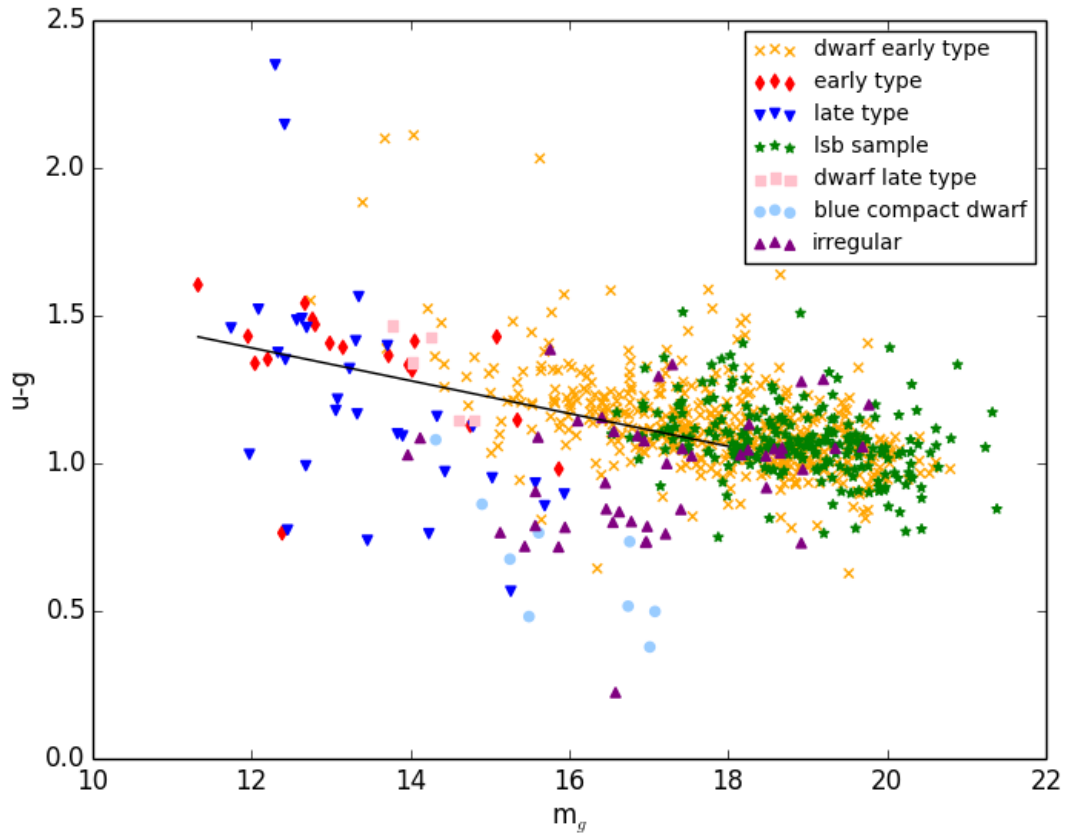


FIGURE 5.3 A $u-g, g$ colour-magnitude diagram for the Virgo cluster. A linear relationship can be seen at the bright end of the diagram.

could be helpful in narrowing down a search for dwarf-type galaxies in the typical cluster environment. Specifically, the dwarf early type galaxies on these plots tend to have faint magnitudes, although they can reach apparent magnitudes of ~ 14 . The LSBVCC galaxies are all very faint, with apparent magnitudes of 17 or fainter. These are also the bluest early type galaxies on the relation, meaning that they have the youngest stellar populations or are the most metal poor.

5.2.3 COLOUR-SURFACE BRIGHTNESS PLOTS

Whereas apparent magnitude is distance dependant, and absolute magnitude requires an accurate distance to be known, surface brightness is a distance independent measure of a galaxy's brightness (at least in the local universe). This means that we can calculate surface brightness for a galaxy in our Local Group in the same way as calculating it for a galaxy in the Virgo cluster and there is no need to take distance into account. The dwarf galaxies that we are interested in have

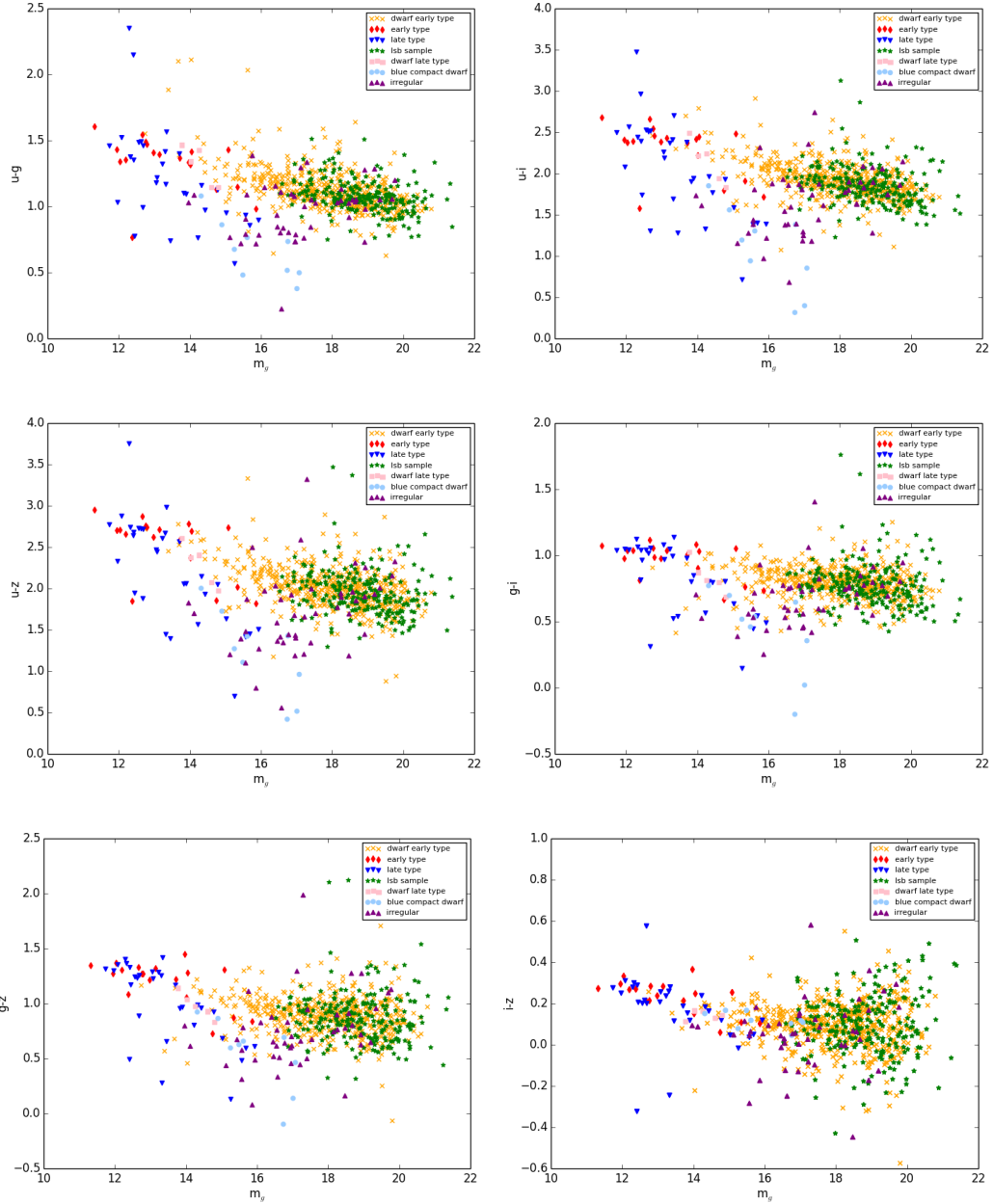


FIGURE 5.4 Colour-magnitude diagrams showing all of our Virgo colours against g-band magnitude. Colour key is the same as for previous plots.

low surface brightnesses. We have produced colour- surface brightness diagrams to explore whether we can use these attributes in combination to differentiate between galactic types.

Figure 5.5 shows plots of g-band surface brightness against colour. The surface brightnesses are the mean values within the g-band 28th mag arcsec⁻² isophotal radius. Again, a similar trend can be seen to the colour-magnitude diagrams. For the colour-magnitude diagrams generally, the fainter magnitude a galaxy has, the bluer it is. For the colour-surface brightness plots, on average the lower surface brightness galaxies are slightly bluer than their more luminous counterparts. We observe a surface brightness-colour relation, where early type galaxies all lie on one relation, and late types do not. At the higher surface brightness end the late type, blue compact dwarf and irregular galaxies fall below this relation in the bluer region of the plot.

Again, the dwarf early type galaxies have quite a large spread in their surface brightnesses with some having as high a value as 23 mags arcsec⁻², but the LSBVCC galaxies are more closely clustered at the low surface brightness end, with values ranging from 24 to near 28 mags arcsec⁻².

5.2.4 SURFACE BRIGHTNESS - MAGNITUDE RELATION

There has been much work done on the surface brightness-magnitude relation for galaxy populations (e.g. Ferguson & Sandage 1988, Ferguson & Binggeli 1994, Karick et al. 2003). There exists a clear relation on which galaxies belonging to a particular cluster lie. The physical explanation for this relation is not currently understood, and some have suggested that it may come from bias introduced from galaxy sample selection (e.g. Phillipps et al. 1987, Phillipps et al. 1988). Bothun et al. (1991) explore the surface brightness-magnitude relation for dwarf galaxies in the Fornax cluster. Karick et al. (2003) extend this work by constructing a surface brightness-magnitude relation for 190 Fornax cluster member galaxies, including all morphological types. They find a tight relation for all galactic morphologies, although they find that Ultra Compact Dwarfs do not sit on the relation as well as other types. Binggeli & Cameron (1991) explored the photometric properties of a sample of 225 Virgo cluster galaxies. Again, they find a surface brightness-magnitude relation with faint magnitude galaxies having lower surface brightnesses and vice-versa.

We have greatly extended this work on the surface brightness-magnitude relation for the Virgo cluster. Our sample of 852 Virgo galaxies is much bigger

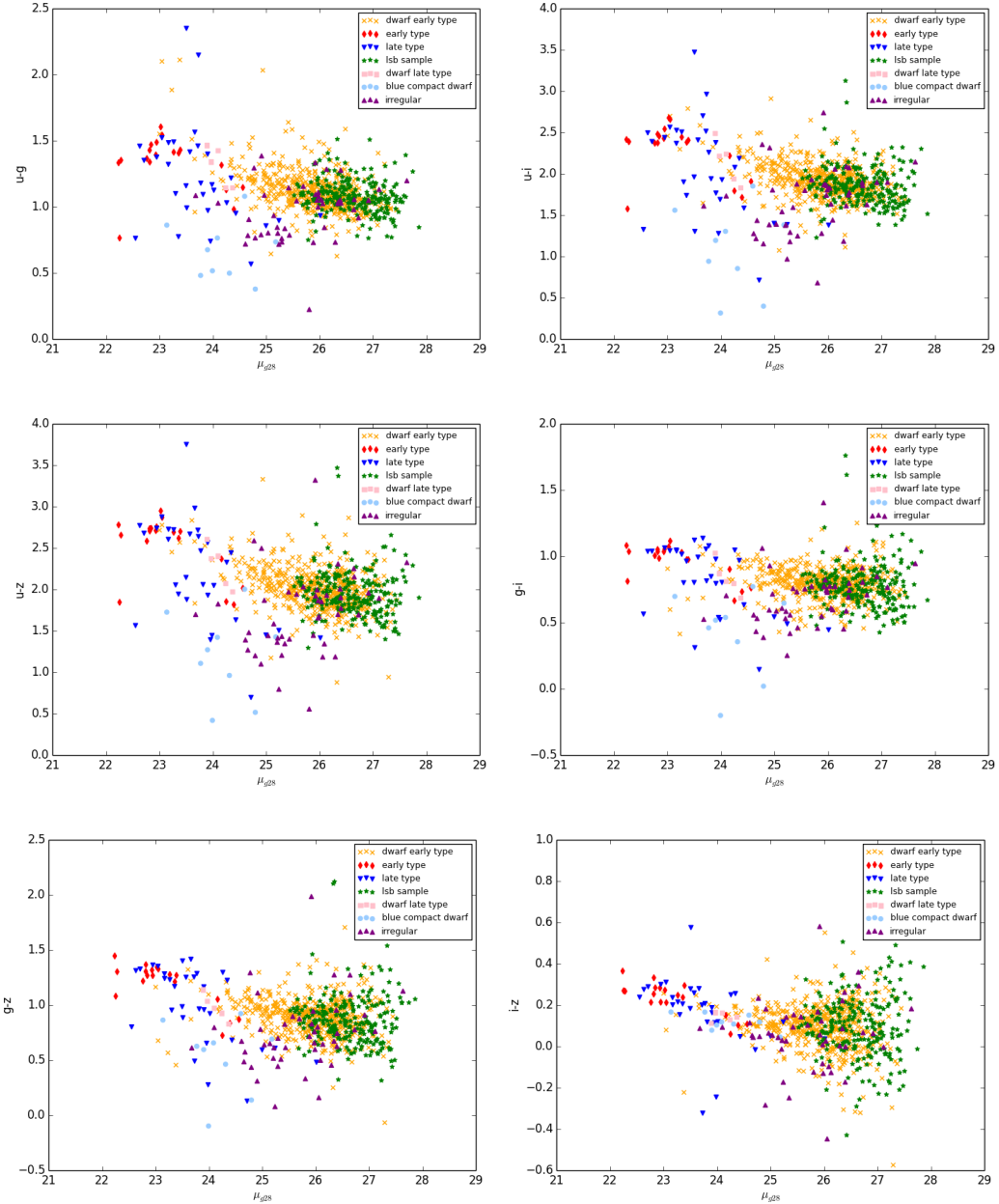


FIGURE 5.5 Colours are plotted against the g-band mean surface brightness within the 28th magnitude arcsec^{-2} isophotal radius. Colour key is the same as for previous plots.

than that of Binggeli & Cameron (1991), and includes the new population of LSB galaxies from Davies et al. (2016).

The VCC and LSBVCC galaxies appear to lie on a clear surface brightness - magnitude relation in all four bands. We have used a least squares polynomial fit to generate the lines in figure 5.6. Again, we observe the same surface brightness - magnitude relation as observed in previous studies of cluster galaxies (e.g. Binggeli & Cameron (1991), Ferguson & Binggeli 1994, Karick et al. 2003). The early and late type galaxies fall on the high magnitude, high surface brightness end of this relation, whereas the dwarf galaxies and LSBVCC sample are at the faint magnitude, low surface brightness end. This relation is extremely consistent across all bands, as can be seen in figure 5.6. This is particularly useful as it means than for a galaxy in the Virgo cluster if one of the magnitude and surface brightness were known, the other could be predicted. It is also useful as if an observed galaxy falls on this relation then it could be assumed to be a member of the Virgo cluster. To explore whether this relation could help identify cluster dwarf galaxies from background field galaxies, galaxies from a background field will later be added to this plot (see section 5.4.3).

5.2.5 SURFACE BRIGHTNESS - RADIUS RELATION

Perhaps unsurprisingly, figure 5.7 shows that smaller galaxies tend to have lower surface brightnesses. The radii appear to have a harsh cut-off at the small radii end due to the annulus size that was integrated over to measure the galaxies. However, it can also be seen that the higher surface brightness a galaxy has, the larger a spread in radii it can have. This data could be used to apply some size constraints when trying to select for dwarf galaxies, however additional analysis will be needed to definitively select dwarf galaxies. The plot shows us that the dwarf early type galaxies all have g-band 28th magnitude isophotal radii of less than 100 arcseconds (~ 8 kpc at a virgo cluster distance of 16.5 Mpc, Mei et al. 2007) , and the LSBVCC galaxies are more constrained, all having radii of around 50 arcseconds or less (~ 4 kpc or less at the Virgo distance). A radii cut could certainly be used as a measure to determine whether a galaxy was a dwarf or not within the cluster population. For a large data set this would be particularly useful as it would allow us to narrow down the initial sample to select for potentially interesting sources.

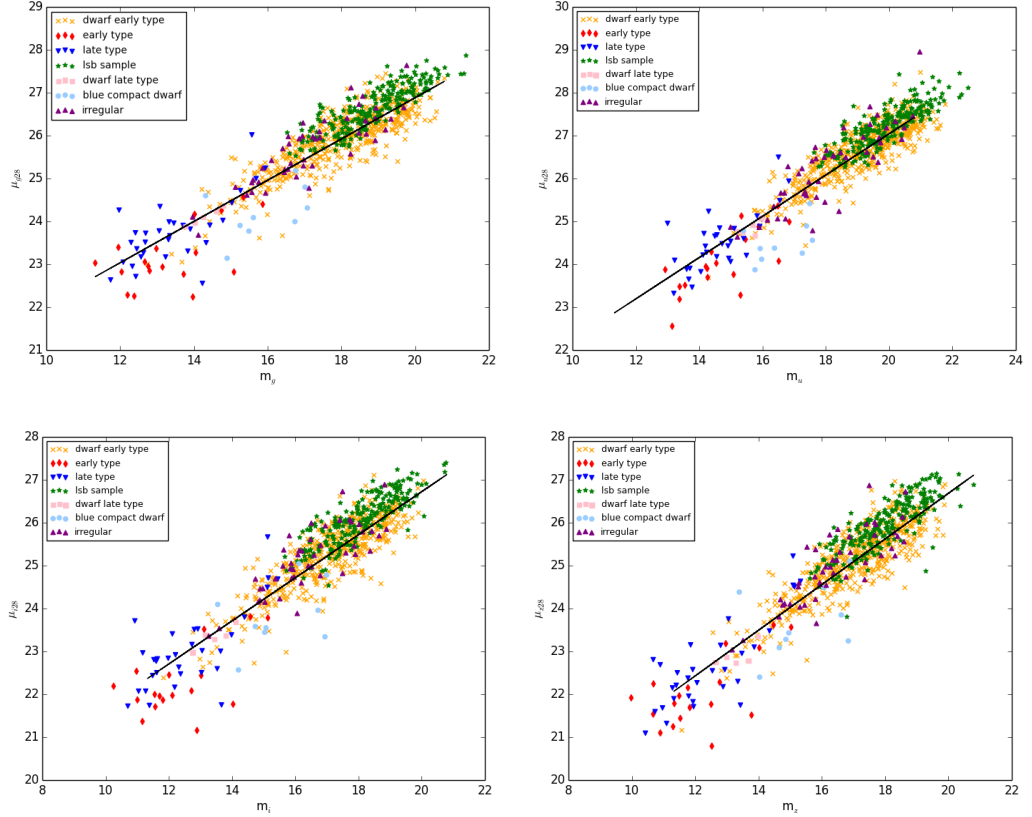


FIGURE 5.6 Surface brightness - magnitude plots of all the Virgo galaxies in four bands. The black lines shows the fitted surface brightness - magnitude relation. The equation of these lines in each band are; g band: $y = 0.48x + 17.26$, u band: $y = 0.48x + 17.42$, i band: $y = 0.50x + 16.68$, and z band: $y = 0.53x + 16.04$.

5.3 COMPARISON WITH BACKGROUND FIELD POPULATION

The NGVS released four background (off-cluster) fields (Ferrarese et al. 2012), each covering 1 square degree of sky. These can be used to compare the properties of the Virgo galaxies with a general background population, which may be detected in any pointing. I have used their background field one in the u, g, i and z bands to attain properties for a sample of background galaxies. These can then be compared to those in the cluster. To do this SExtractor was used to select objects. To exclude objects which occur due to background noise fluctuations the detection threshold was set at 5 sigma and the minimum object size at 100 pixels. These values were used to ensure a sensible sample size and exclude spurious detections. At the edge of the frames sometimes large regions were designated as

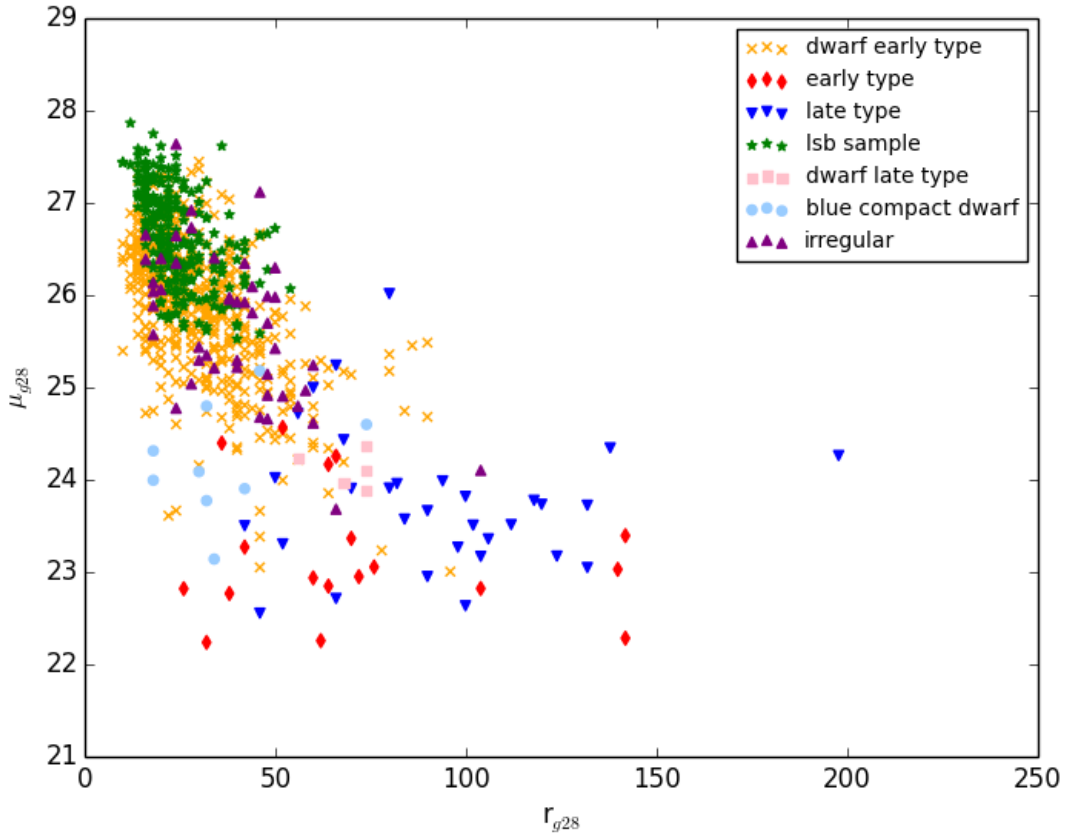


FIGURE 5.7 Surface Brightness- radius plot for the VCC and LSBVCC galaxies. The mean surface brightness within the 28th magnitude arcsec^{-2} isophotal radii is plotted against the 28th magnitude arcsec^{-2} isophotal radii.

object, so anything with a size greater than 20,000 pixels was excluded. Additionally, SExtractor has a parameter named ‘class’ which can be used to distinguish between point-like stellar objects and extended sources. On inspection of the frame the majority of stars had been assigned class values of 0.84 or above, so all objects with a class value of 0.8 or above were removed from the sample. To be included in this analysis the object must have been detected in all four bands. To further ensure that only galaxies were included the sources were matched to the SDSS DR13. Only those that are in the SDSS and classed as an extended source were then included. SExtractor photometry has the known issue of often separating a source into more than one object, or merging multiple sources into one object. To combat this the magnitudes obtained using SExtractor were plotted against those from the SDSS. The correlation between the two was extremely strong, but to ensure no errors were included the handful of sources where the SExtractor magnitudes and the SDSS magnitudes differed by one magnitude or more were

removed. This left a sample of 1426 background galaxies of which the properties could be explored.

5.3.1 COLOUR-COLOUR DIAGRAMS

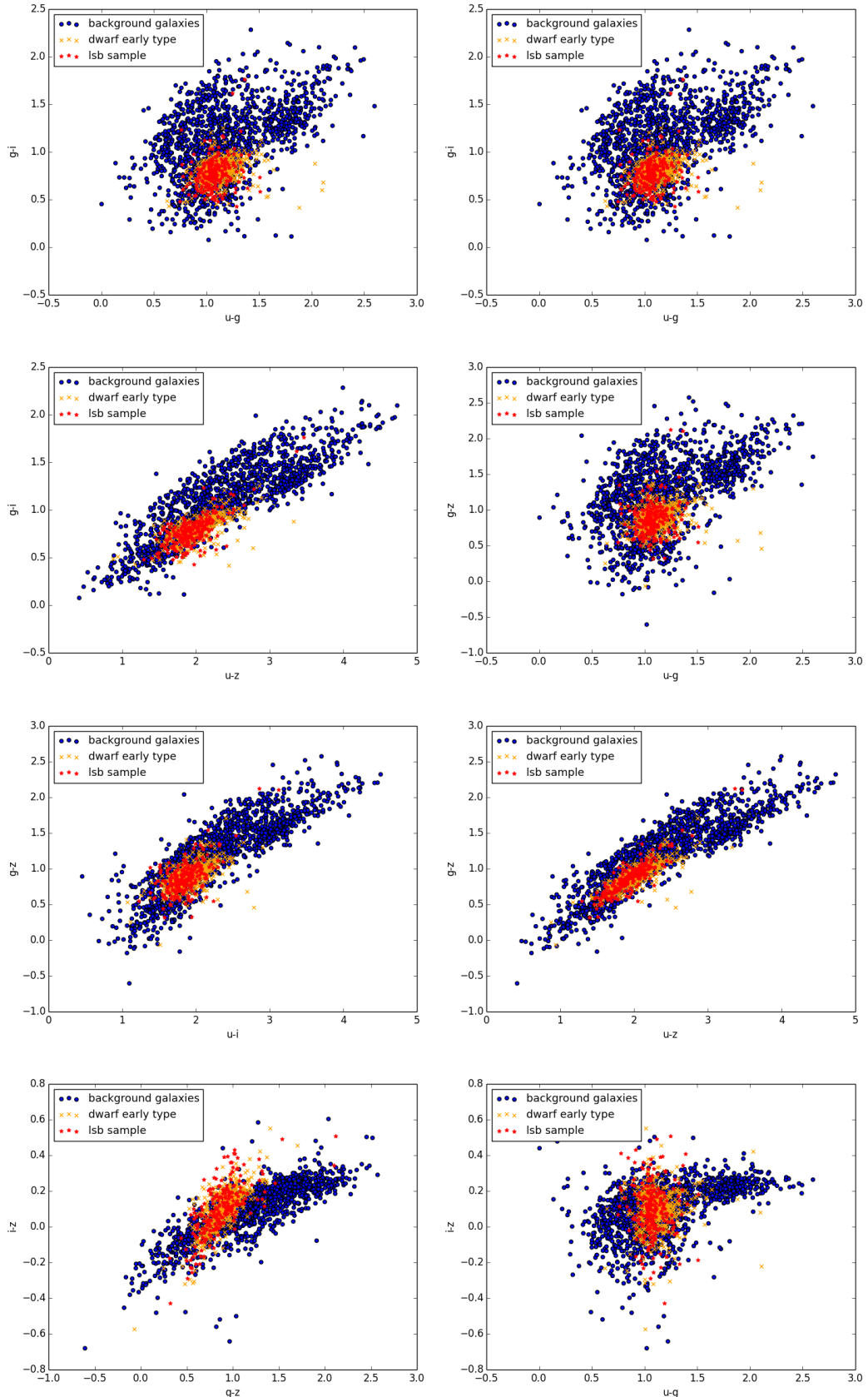


FIGURE 5.8 Colour-colour diagrams showing the cluster dwarf ellipticals and LSBVCC sample, as well as the background field galaxies.

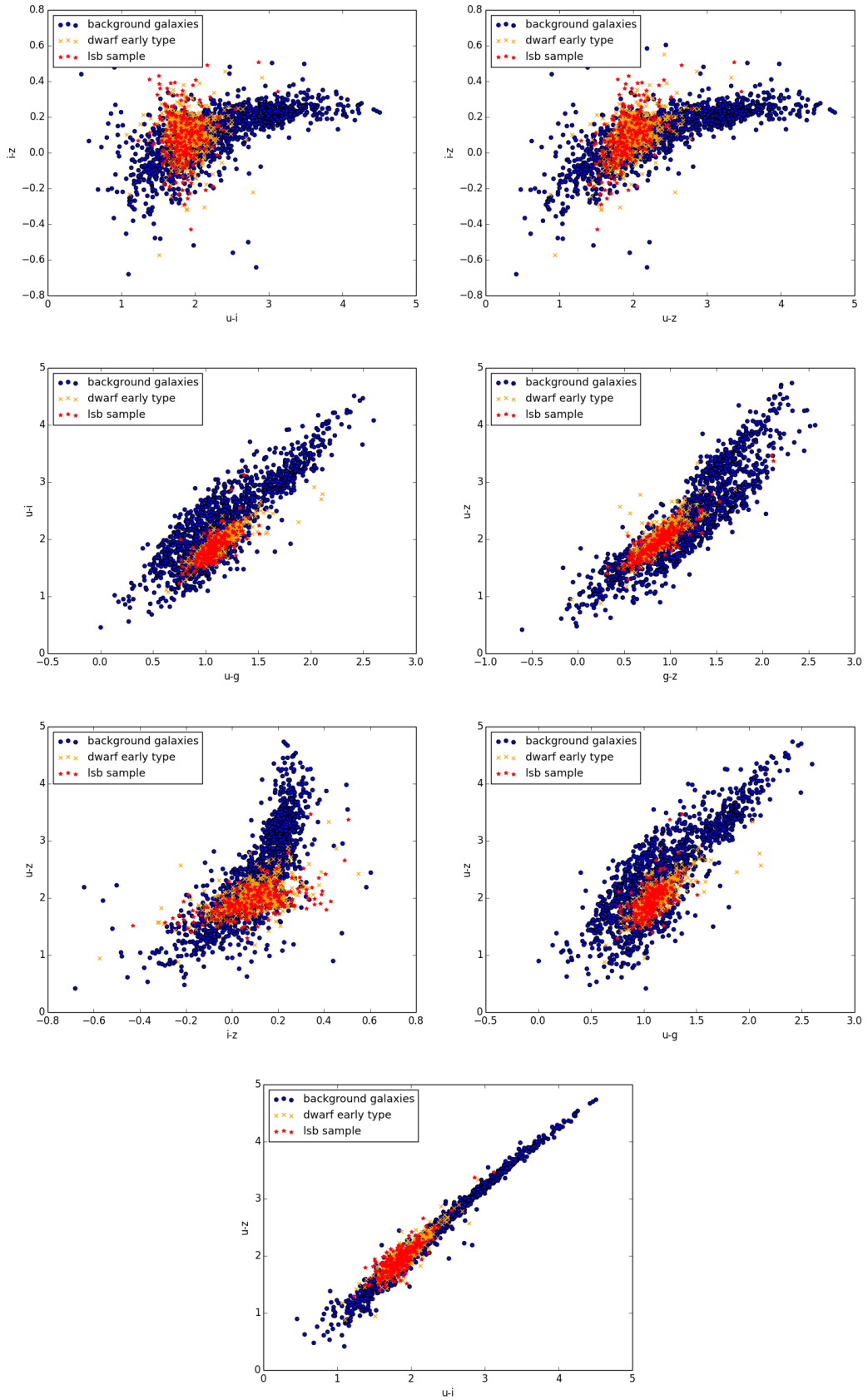


FIGURE 5.8 Continued. Colour-colour diagrams showing the cluster dwarf ellipticals and LSBVCC sample, as well as the background field galaxies.

To explore whether colour can be used to separate cluster galaxies from background field galaxies colour - colour diagrams have been plotted. In figure 5.8 the LSBVCC galaxies are denoted by red stars, dwarf early types by orange crosses and background field galaxies by navy points. As the plots show, although the dwarf galaxies do inhabit a specific region of the colour-colour plane, it is within the space that the background galaxies reside. This implies that the foreground dwarf galaxies, and background galaxies, have similar stellar populations. The colour of a galaxy can tell what age the stars residing within it are. As both galaxy samples cover the same range of colours, it is likely that the age of their stellar populations are similar, although this may also be due to metallicity. Therefore, these diagrams are helpful in so far that we can define areas of colour-colour space where dwarf galaxies are likely to reside, and so can rule out many background sources as dwarf candidates. However, there is still a lot of confusion with background sources within this region so further analysis would also be needed to identify dwarfs within this reduced sample.

5.3.2 COLOUR-MAGNITUDE DIAGRAMS

In figure 5.9 we show colour-magnitude diagrams for background galaxies, Virgo cluster dwarf ellipticals and the LSBVCC. The LSBVCC sample are shown in red, the dwarf elliptical galaxies from the VCC in orange and the background field galaxies in navy. It can be seen that the background and cluster populations have some quite clear separation, especially at the brighter magnitude end of the diagram. The dwarf elliptical and LSBVCC galaxies trace out the Virgo cluster red sequence (e.g. Roediger et al. 2017, discussed in section 5.5). This means that as their magnitude becomes fainter, the galaxies become slightly bluer. This relationship is not observed for the background galaxies, which appear at the faint magnitude end of this plot but cover a large range of colours. The brighter Virgo dwarfs are clearly separated from the background sample. However, the faintest dwarf galaxies become confused with the background population. Therefore, these diagrams are helpful in highlighting regions of colour magnitude space in which dwarfs are most likely to reside. Additionally, assuming that we might search for fainter dwarf galaxies at the faint magnitude end of the red sequence, we can use these plots to constrain the colours these galaxies are likely to have. If we find galaxies that do not sit on this extended red sequence then we can confidently determine them to be background galaxies, whereas those that do might be cluster members though they can't be ruled out as background objects.

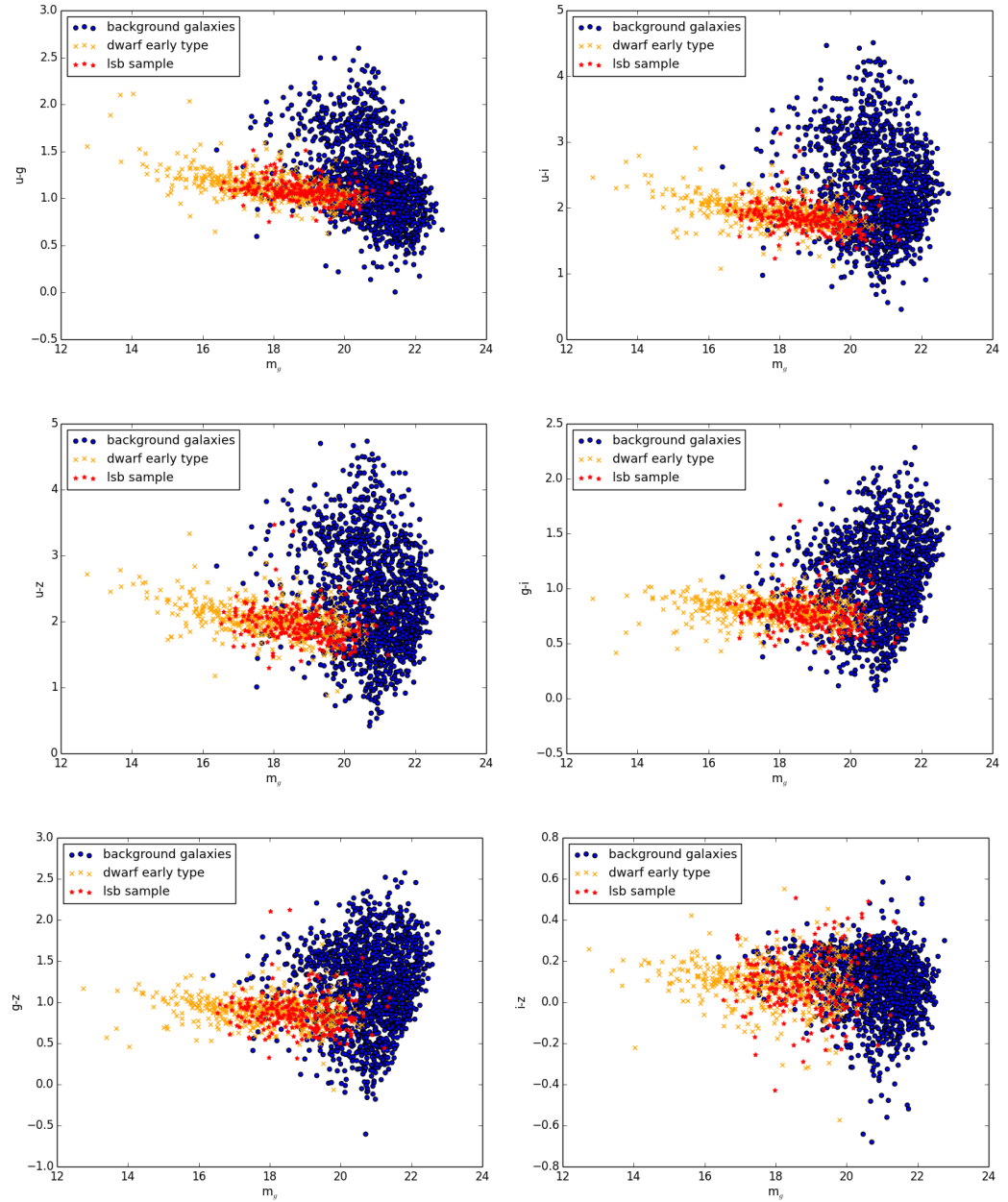


FIGURE 5.9 Colour-magnitude diagrams for the Virgo dwarfs and the background field. Magnitudes are in the g -band. The blue points denote field galaxies, orange crosses dwarf early types and red stars the LSBVCC sample.

5.3.3 SURFACE BRIGHTNESS

In figure 5.10 we have plotted the 25th magnitude isophotal radii surface brightnesses against the background field values from SExtractor. To do our SExtractor object detection and analysis we used a 5σ detection and analysis threshold - which is equivalent to a surface brightness of $25.25 \text{ mag arcsec}^{-2}$ on the NGVS frame, therefore our detection methods are comparable. As mentioned in chapter 4, for very low surface brightness sources the 25th magnitude isophote struggled to fit the galaxy well - due to the flocculent nature of LSB sources, therefore at the faint end of our surface brightness- magnitude relation there is some scatter caused by this. In surface brightness - magnitude space the faint magnitude galaxy populations are very well separated. L* type galaxies in the background field will generally appear to have much fainter apparent magnitudes than those in a nearby cluster, and without accurate distances this cannot be corrected to an absolute magnitude. However, as surface brightness is distance independent in the nearby universe it can be used as an absolute measure of a galaxy's brightness, regardless of magnitude. As the field galaxies are much further away than those in the cluster we only detect large (non dwarf) galaxies which sit at the higher end of the surface brightness scale, but due to their faint magnitudes they do not fall on the same surface-brightness magnitude relation as the Virgo galaxies. This means that by using the surface brightnesses and apparent magnitudes of galaxies we see a clear separation between those in a cluster and those in the background field.

Figure 5.10 also implies that there are no field LSB galaxies at a similar distance to the Virgo cluster in the region we have looked at. However, LSB galaxies are rare even within the Virgo cluster. As the background field only spans 1° of sky, whereas the NGVS Virgo fields cover 100° we must treat any conclusions with caution. The lack of LSB galaxies may hint towards an interesting dichotomy between field and cluster galaxy populations, with LSB galaxies perhaps being ubiquitous to a cluster environment.

However, there is potential that there is a bias in figure 5.10 due to selection effects. By selecting only sources which are classified as extended sources in the SDSS, and hence likely to be galaxies, we may be removing any sources uncatalogued by the SDSS. To check for this the full SExtractor output background population has been plotted, minus those with a SExtractor class value of 0.8 or above. This means that there are now 6850 sources in the background population. The plot is shown in figure 5.11. It can be seen that this has no significant effect on the relationship observed in figure 5.10. A collection of points appear at brighter

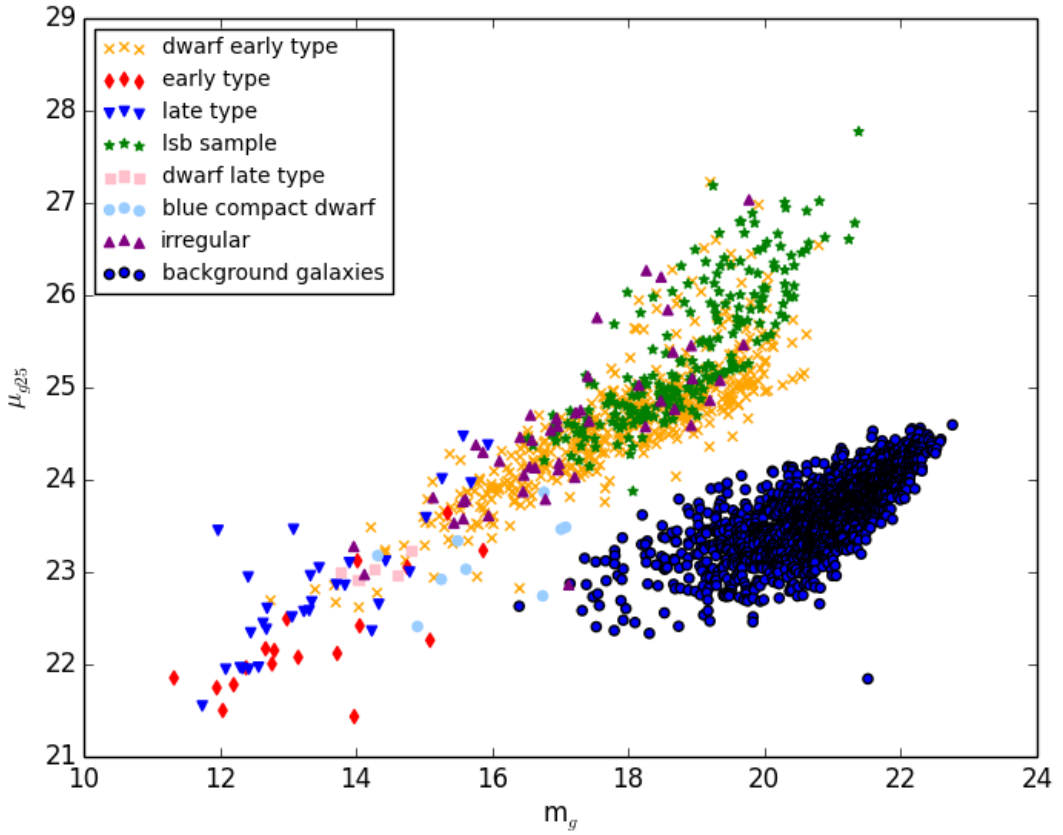


FIGURE 5.10 Surface Brightness - magnitude plot for the Virgo galaxies and the background field. The g-band magnitude is plotted against the mean surface brightness within the 25th magnitude arcsec^{-2} isophotal radii.

magnitudes and surface brightness, but these are due to contamination from stellar objects. This means that using surface brightness and magnitude does seem to be an effective method for separating foreground dwarf galaxies from the background population. If one can obtain a surface brightness-magnitude relation for a particular cluster then it is possible to determine cluster membership based on whether a galaxy lies on this relation or not. This is extremely useful as it makes photometric redshift information less important in ascertaining a galaxy's cluster membership.

5.4 THE VIRGO RED SEQUENCE

Having used the Virgo cluster photometry data to explore the possibility of identifying dwarf galaxies based on their physical properties, we can explore

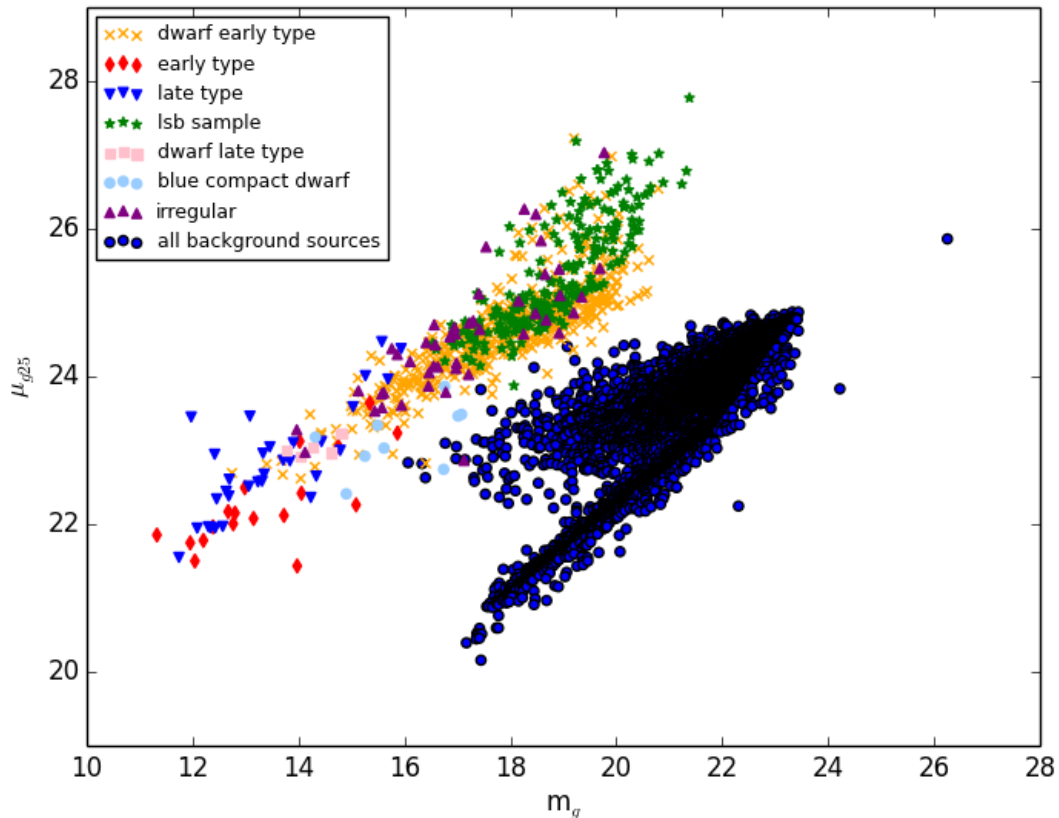


FIGURE 5.11 Surface Brightness - magnitude plot for the Virgo galaxies and all of the sources in the background field. The g -band magnitude is plotted against the mean surface brightness within the 25th magnitude arcsec^{-2} isophotal radii.

other uses that this data can be put to. There has been some work done recently by Roediger et al. (2017) on the red sequence in the centre of the Virgo cluster. I will use the Virgo data from this thesis to further explore the red sequence, both inside and outside of the cluster core.

Roediger et al. (2017) explore the red sequence in the central region of the Virgo cluster, using all five bands of the NGVS. They find that the red sequence slope flattens in all colours at fainter magnitudes, starting at absolute magnitudes between -14 and -13. Roediger et al. (2017) suggest that this could be explained by a constant mean age and metallicity for the lowest mass galaxies in the cluster core. To explore whether this is true for the whole cluster, and as an additional test of the photometry, I have followed their method to explore the red sequence. Due to the extremely restricted coverage of the cluster in the r band it has been excluded from the photometry, therefore I have six colours whereas Roediger et al. (2017) presents ten colour analysis of the core of the cluster. Following Roediger et al.

(2017) magnitudes have been converted to absolute magnitudes using a uniform distance of 16.5 Mpc (e.g. Mei et al. 2007, Blakeslee et al. 2009). A reddening correction has been applied using a Schlafly and Finkbeiner extinction law (Schlafly & Finkbeiner 2011). Figure 5.12 shows the red sequence in all colours produced by Roediger et al. (2017).

Roediger et al. (2017) fit the data using a non-parametric fitting method. They ran the Locally Weighted Scatterplot Smoothing Algorithm (LOWESS, Cleveland 1979). I have used the PYTHON function *lowess* in order to fit my data in the same way. The LOWESS algorithm is a parametric regression model that combines multiple linear regression models with k-nearest neighbour based algorithms. This means that it fits simple models to local data subsets and uses these to build up a function which describes the variation in the data.

Roediger et al. (2017) select red sequence galaxies by visual inspection of their sample. They remove galaxies which they believe to be clearly star forming, as well as those below their completeness limit, those with contaminated imaging, and those which they believe to be candidate remnants of tidal stripping. In order to select red sequence galaxies I have included all galaxies which are classified by Binggeli et al. (1985) as elliptical or dwarf elliptical, as well as all of those from the LSBVCC (Davies et al. 2016).

Roediger et al. (2017) have carried out an analysis of the Virgo red sequence in the cluster core. I have expanded on that to include VCC galaxies from the entirety of the cluster and the LSBVCC sample. As my work includes galaxies from both the core and non-core regions it has greatly expanded the sample of Virgo galaxies being analysed.

As can be seen from figure 5.13 my red sequence plots show the same faint end flattening as Roediger et al. (2017), as well as reproducing the shape of their fits extremely accurately. The *lowess* fits to my data are shown by the black lines. I have tried to reproduce the Roediger et al. (2017) fits in blue, by estimating points on their line on their plot and then using *lowess* again to fit these points. As can be seen from the figures we also observe a red sequence faint end flattening when taking the whole cluster into account.

Roediger et al. (2017) have only used data from the cluster core. Using data from the entire cluster it is possible to compare the red sequence for core and non-core galaxies. Previously no work has been done to investigate whether the Virgo red sequence persists outside of the cluster core. Figure 5.14 contains data for both cluster core and non-core galaxies. The cluster core galaxies are shown by the red points, again the black line shows the *lowess* fit to this data. Roediger et al. (2017)

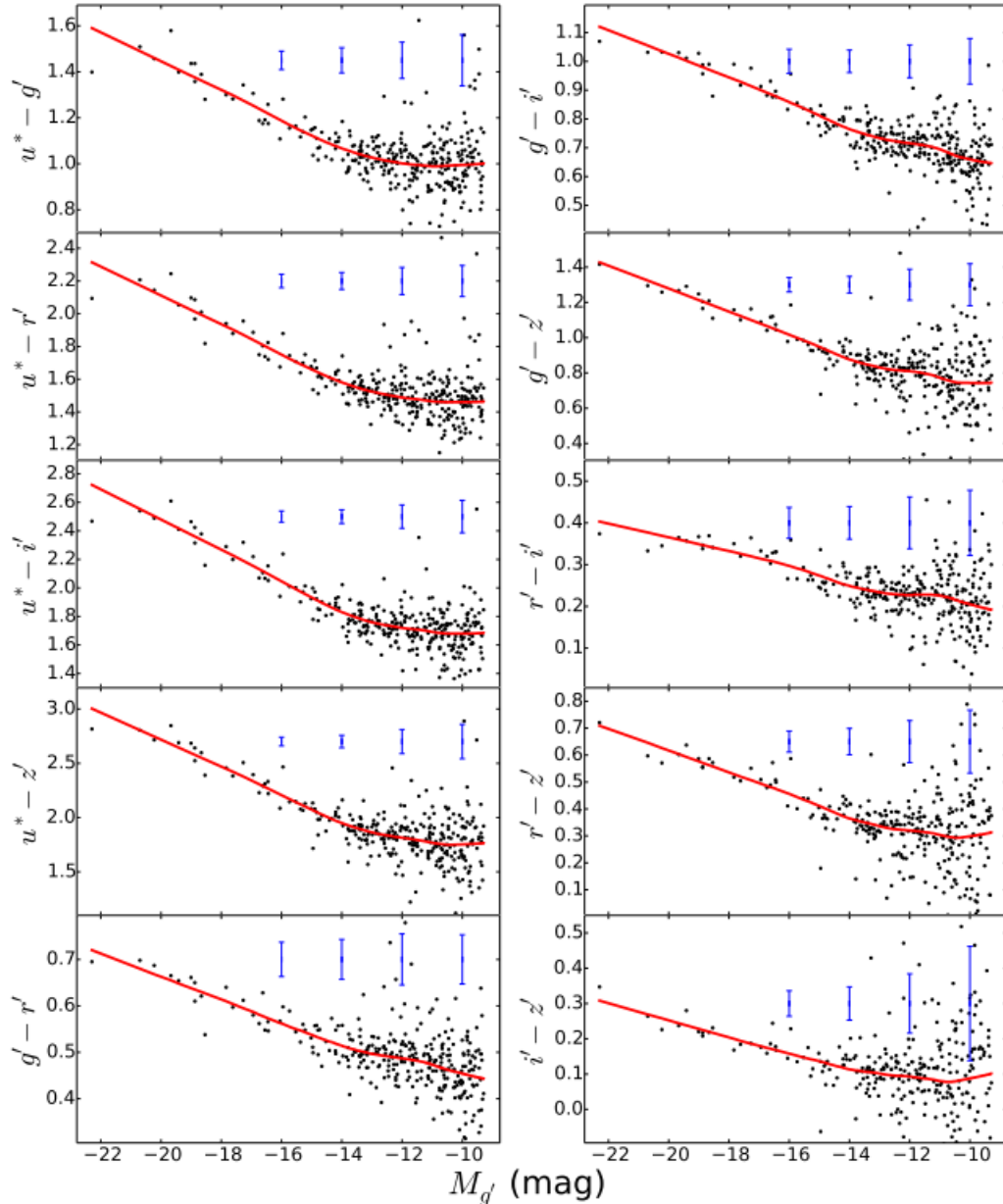


FIGURE 5.12 The red sequence plots from Roediger et al. (2017). A flattening can be seen at the faint end. Black points represent individual galaxies and the red lines show non-parametric fits to the data.

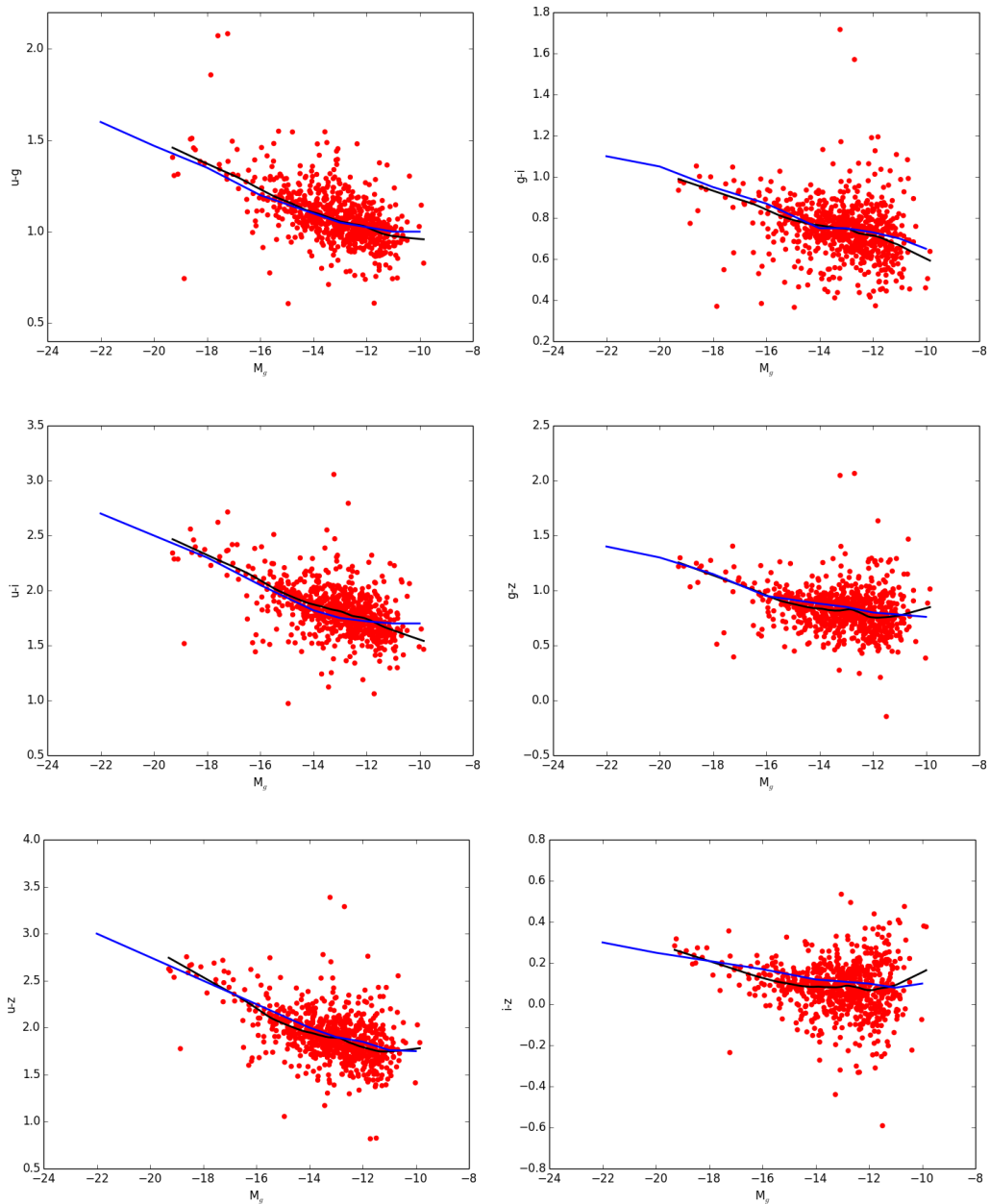


FIGURE 5.13 The red sequence plots using my Virgo photometry data. The black lines show the *lowess* fits to the data, as discussed in the text. In blue we have attempted to recreate the lines fit by Roediger et al. (2017) using data from their plot.

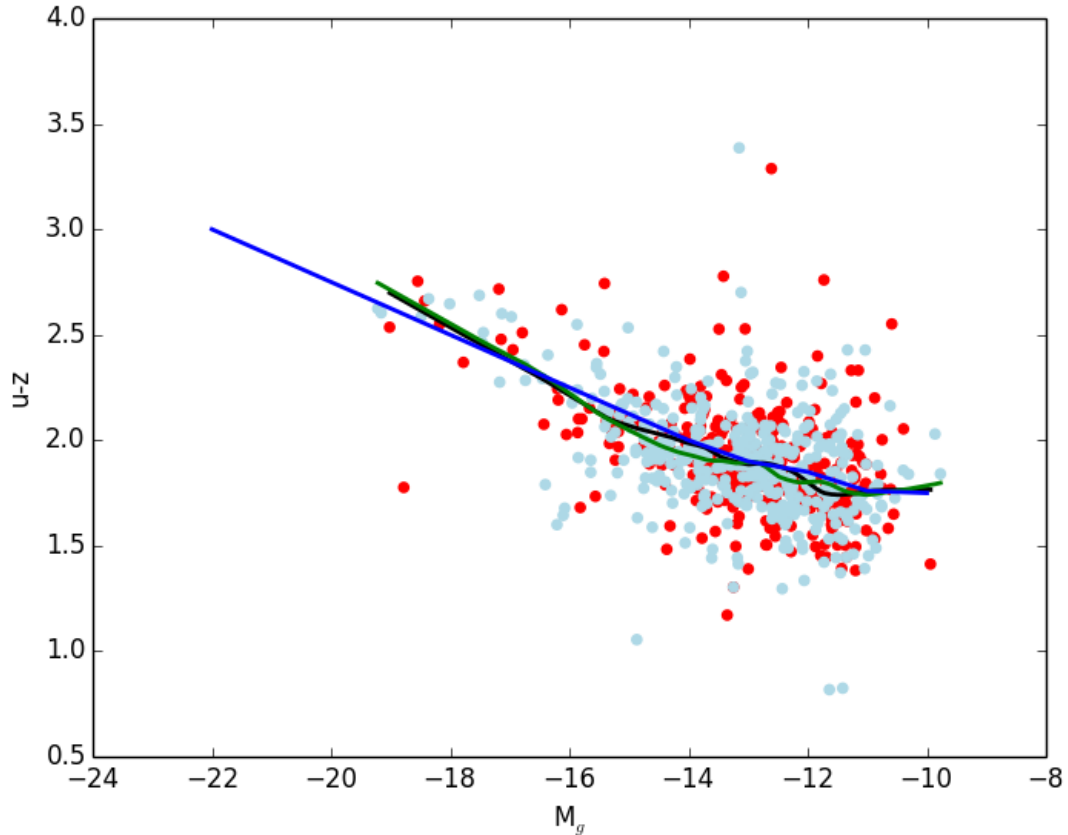


FIGURE 5.14 The red sequence of the Virgo cluster separated by core and non-core galaxies. The red points show core galaxies, and the black line shows the *lowess* fit to these points. The pale blue points show non-core galaxies, and the green line is the *lowess* fit to these. The blue line is the recreated fit from Roediger et al. (2017).

say their galaxies come from a 3.71 deg^2 area centred on M87; we have defined core galaxies within the same region as Roediger et al. (2017) (within a circle centred on M87 with a radius of 1.09 degrees). The galaxies that do not reside in the cluster core are shown by the pale blue points. We find that 339 of the combined VCC and LSBVCC galaxies reside in the core, and 436 outside of the core, therefore we analyse a total of 775 galaxies. The *lowess* fit to the non-core galaxies is shown by the green line. As in figure 5.13, the blue line shows the fit from Roediger et al. (2017).

As can be seen from figure 5.14 the faint end flattening is seen for both cluster core and non-core populations. This implies that the Virgo red sequence is consistent throughout the cluster, and does not depend on the environment within the cluster.

5.5 CAN WE IDENTIFY DWARFS BASED ON THEIR PROPERTIES?

The aim of this work was to investigate whether it is possible to distinguish cluster dwarf galaxies from background field galaxies based solely on their photometric properties. In order to do this photometry was carried out on 852 VCC and LSBVCC galaxies from within the NGVS 100° squared Virgo cluster data (Ferrarese et al. 2012). Additionally, we used a 1° squared NGVS background field to collect photometric information for a sample of background field galaxies. Using this data we have unveiled some new methods by which dwarf galaxies in clusters can be separated from background field galaxies. The results of photometry on 852 VCC and LSBVCC galaxies have been presented, along with analysis of their photometric properties. Photometry was also carried out on a background off-cluster field so that the properties of the two samples could be compared. The key methods that can be used to separate cluster dwarfs from background field galaxies involve using combinations of surface brightness, magnitude and colour.

In colour-magnitude diagrams, shown in figure 5.9, most dwarfs inhabit a distinctly different region to the galaxies in the field. They form a clear red sequence which can be separated from the field population for all but the faintest magnitudes. Field galaxies have a much larger range in colour, but, due to their distances, generally have fainter apparent magnitudes. This means that, even at the faintest magnitudes, we could discount galaxies which lay off this red-sequence as field galaxies, and concentrate our efforts on those that do. Therefore, we can use colour and magnitude information to select dwarf galaxy candidates from the background field.

Additionally, we have extended previous work by Binggeli & Cameron (1991) on the surface brightness- magnitude relation of the Virgo cluster, and have explored it in comparison to the field population. As shown by figure 5.10, the cluster dwarfs inhabit an extremely distinct region when compared to field galaxies in surface brightness-magnitude space. This means that if we are able to define a surface brightness-magnitude relation for our cluster galaxies then we can use this to test whether galaxies belong to this population or not.

A combination of these techniques would be the most effective in enabling classification of cluster dwarf galaxies.

CHAPTER 6

CONCLUSION

'Happiness can be found, even in the darkest of times, if one remembers to turn on the light.'

ALBUS PERCIVAL WULFRIC BRIAN
DUMBLEDORE

As explained in Chapter 1, the major motivation behind this work is the dwarf galaxy problem (e.g. Bullock 2010). This problem arises from the lack of observed dwarf galaxies when compared to results from numerical simulations. In this thesis I have investigated two different ways in which this problem could be addressed: dark galaxies and the LSB universe.

Initially, I used AGES H α data to search for gas clouds in the halo of M33 (published in Keenan et al. 2016). I found a population of 32 clouds, 11 of which were new detections. Although we found no strong evidence that these were gravitationally bound, and had no other features similar to that of dwarf galaxies, we did find one extremely interesting object. This cloud, named AGESM33-31, is a massive ring-shaped structure which is a similar size to M33 itself, if at the same distance. It has no associated stars, and also doesn't fit with any other proposed formation scenario, so could be a potential dark galaxy candidate.

The second part of my thesis has focused on using optical Next Generation Virgo Survey (Ferrarese et al. 2012) data to analyse features of dwarf galaxies which could be used to separate them from background populations. I attained magnitudes, colours, surface brightnesses and radii for a sample of 852 galaxies in four bands. Additionally, I collected data on the background population from one of the NGVS background fields. I found that the foreground dwarf population separated

quite nicely from the background field galaxies on colour-magnitude diagrams, however, they get confused at the low luminosity end. Additionally, the two populations separated extremely well on surface brightness - magnitude plots. This is the first time consistent photometry has been performed on such a large sample of Virgo cluster galaxies, and it has extended all previous work into studying their photometric properties. The use of these two findings together could greatly aid the discovery of future dwarf galaxies, and allow cluster membership to be confirmed without needing spectroscopic redshift measurements.

6.1 THE GAS CLOUD POPULATION OF M33

M33 is the third largest galaxy in our Local Group, after the Milky Way and Andromeda. However, it currently has no confirmed dwarf satellites. This is particularly surprising as we would expect a galaxy in a halo of its size to have around 25 subhalos with velocity widths of 9 km s^{-1} or greater (Sternberg et al. 2002). This highlights the dwarf galaxy problem on the scale of a single galaxy, and begs the question whether these subhalos do exist but aren't populated by stars.

In an attempt to address this question, in Keenan et al. (2016) we use data from the Arecibo telescope, as part of the Arecibo Galaxy Environment Survey, to search for neutral hydrogen gas in the halo of M33. One of the aims of this work was to look for clouds of gas which could potentially be starless dwarf galaxies, or 'dark galaxies'.

We observed a total of 32 clouds, 22 of which were discrete and not connected to M33's H I disk. This was extremely intriguing as the number of clouds we observed was very similar to the number of subhalos predicted by the equation from Sternberg et al. (2002). However, looking at the velocity maps of the clouds we generally saw no evidence for ordered rotation, which may have been indicative of them being gravitationally bound. Many of the clouds were also very patchy or flocculent in appearance, again making it less likely that they are stably bound.

However, we did find one particularly interesting cloud. AGESM33-31 is a giant ring-shaped cloud of H I which appears to be larger than M33 itself, if at the same distance.

6.2 AGESM33-31

This large ring-shaped cloud had been previously observed, but had never been resolved into one ring like structure. Thilker et al. (2002) previously detected the cloud, however it was unresolved in their survey. Additionally, Grossi et al. (2008) detect sections of the ring cloud, and designate them as two separate smaller clouds. The superior sensitivity of our data has subsequently allowed us to resolve the ring-like structure of AGESM33-31. AGESM33-31 is extremely spatially extended, similar to Wright's cloud, which can also be seen in our data. It has been suggested that Wright's cloud is associated with the Magellanic stream - they are at similar velocities and Wright's cloud has an extended component in the stream direction, although it is around 50 kpc away from the main structure of the stream (Nidever et al. 2010). AGESM33-31 is also at a similar velocity to Wright's cloud, so it is a possibility that they are both related to the Magellanic stream. However, at this point in the sky the stream appears extremely flocculent, so having one large cloud associated with it there seems incongruent, let alone two.

If at the same distance as M33, AGESM33-31 has a large size of \sim 18 kpc, which is bigger than M33, but a low H I mass of around 1% of that of M33. These features are extremely like those of the large 'failed' galaxies which have been proposed. However, AGESM33-31 may be closer to our galaxy, and could be a galactic HVC projected along the line of sight. In this case it would be much closer to our Milky Way, so its size would reduce to something much more akin to a HVC. These are all possibilities which can't be ruled out.

If one is to assume a location near M33, we can explore the plausibility that AGESM33-31 could be a dark galaxy. AGESM33-31 has a very low measured velocity width of 18 km s^{-1} , which is similar to the velocity dispersion of gas in a disk galaxy. This raises the possibility that AGESM33-31 may be a face-on disk of H I. Additionally, AGESM33-31 has a velocity gradient across it of 30 km s^{-1} , however it is unclear whether this is due to rotation. These ideas were also reached by Thilker et al. (2002), who describe AGESM33-31 as a 'dark companion' to M33.

However, this does not address the hole in the centre of the cloud. We have explored the idea that it may have been formed by stellar winds or a supernova explosion, but it appears around ten times bigger than we would expect if this were the case. Additionally, we have looked into whether the cloud could be a collisional ring galaxy, but find no characteristic disturbance of gas in the direction of the collision. There are no stars catalogued in the area, but with future data releases from surveys such as PAndAS CUBS (e.g. Martin et al. 2009) this can be

investigated further. There is the added complication that much of the cloud may lie behind M33 in the line of sight, making it impossible to detect associated stars.

We are left with a range of options for the origin of AGESM33-31, but can make no firm conclusions here. It has many of the properties of a disk type galaxy and has no currently detected stellar population. However, if it is not at the distance of M33 then it may be a galactic HVC. Alternatively, it may have a Magellanic stream origin, as Wright's cloud is proposed to have.

6.2.1 POTENTIAL FURTHER OBSERVATIONS

To further the debate about AGESM33-31 additional observations would be extremely advantageous. Further H I observations would allow us to explore whether AGESM33-31 has any further structure, which may give away clues to its origin. This would also allow us to search for any very low column density material which may connect it to M33, or otherwise. Additionally, further observations of any stellar population in the region may help determine whether the cloud has any associated stars, however, as mentioned above, this is made more difficult due to its position in relation to M33 itself.

6.3 THE LSB POPULATION OF THE VIRGO CLUSTER

The aim when embarking on the work on the Virgo cluster was to establish whether there was a method which would allow identification of dwarf galaxies based on their photometric properties. This will then allow the identification of dwarf galaxies more easily when looking at extremely large datasets, and will remove confusion with background objects. To do this Next Generation Virgo Survey data (Ferrarese et al. 2012) was used to carry out photometry on all confirmed Virgo cluster member galaxies, as well as the galaxies from Davies et al. (2016). Having removed frames with defects and unreliable results I collected full photometry for a total of 852 Virgo galaxies in four bands. This allowed analysis of six colours, as well as magnitudes, surface brightnesses and radii. It is the first time a consistent set of photometry has been collected for such a large sample of Virgo cluster galaxies, and has allowed thorough analysis of the Virgo galaxy population.

6.3.1 WHAT DID WE FIND?

The primary interest was to explore whether colour could be used to separate foreground cluster dwarfs from background field galaxies. The colour-colour analysis of the cluster and field populations proved unfruitful: the two populations thoroughly overlapped in colour-colour space, although the region the dwarfs inhabited was more constrained than the region inhabited by the background population. I then went on to explore colour magnitude space. This proved significantly more successful when looking for separation between the populations. The dwarf elliptical and LSBVCC galaxies lie on the Virgo cluster red sequence, so fall across a wide magnitude range but narrow colour range. The background galaxies have magnitudes at the fainter end of the scale, but a much broader range of colours. This means that the majority of the currently observed dwarf galaxies could be quite easily separated from background galaxies on a colour-magnitude plot. However, confusion occurs for the faint magnitude end of the population. This effectively limits the detection of dwarf galaxies by this method.

After doing this surface brightness-magnitude space was explored. This proved to be an extremely effective separator of the cluster and background populations. The Virgo cluster galaxies lie on a clear surface brightness-magnitude relation. The background galaxies, however, do not have the same relationship. In the local universe surface brightness is independent of distance, therefore although the background galaxies get fainter due to being further away from us, their surface brightnesses have the same value as if they were local galaxies. This means that although the Virgo dwarfs and the background galaxies inhabit a similar magnitude range, they are well separated in surface brightness. Therefore, if one can ascertain the surface brightness-magnitude relation for a cluster, then cluster sources can be identified from the background population.

The Virgo cluster photometry has shown that although colour alone is not enough to separate foreground dwarf galaxies from the background field population, when used in conjunction with magnitude and surface brightness information one has a very powerful set of parameters.

6.3.2 HOW COULD THIS BE USED IN THE FUTURE?

Surveys such as the NGVS cover vast regions of sky, and this will become increasing common with more modern survey telescopes, such as the LSST. These

telescopes will produce vast amounts of optical data so an efficient method will be needed to search for dwarf galaxies within the data. This will require both reliable automated source detection methods, and robust criteria with which to identify sources of interest.

For his PhD Daniel Prole is working on developing such a method, and implementing machine learning techniques so that dwarf galaxies can be identified in vast amounts of data without the need for checking the data by eye. The relationships discovered which separate cluster dwarfs from background galaxies is being used to train this software in dwarf detection, as will be discussed in Prole, Davies and Keenan. 2017, in prep. This will hopefully lead to the successful detection of many more dwarf galaxy populations.

6.4 COMMENTS ON HOW MY WORK COULD IMPACT THE DWARF GALAXY PROBLEM

6.4.1 DARK GALAXIES

The AGES work on the M33 region presented in this thesis has proved that if dark galaxies exist then we are able to detect them. We have detected a cloud population around M33, which matches in number the expected satellite population of a galaxy with its mass. Although there is no evidence that the majority of these clouds are anything other than transient formations, we have proved that we can detect cloud populations with masses similar to local dwarf galaxies.

Our detection of AGESM33-31 is particularly interesting. It has many features similar to a disk type galaxy, and we cannot rule out the possibility that it is a dark galaxy. However, as there are many other possibilities for its origin we cannot comment more at the current time without further observations. It is undeniable that AGESM33-31 is a mysterious and fascinating object.

With the next generation of radio telescopes, such as the square kilometre array (SKA), it will be possible to push work in this field forward. The SKA is a multi dish radio interferometer currently being built in Australia and South Africa, with an effective area of one square kilometre. It is scheduled to make its first observations in 2020. In H I astronomy it will push the distance over which resolved observations can be made to a redshift of around 1, whereas current radio telescopes can only reach a redshift of around 0.2. This will allow us to probe the H I content of the universe over a much larger sample of galaxies, and search

for signs of dark galaxies (Davies et al. 2006). So far the numbers of dark galaxy candidates have fallen far short of the number that would be needed to solve the dwarf galaxy problem. If the next generation of telescopes do not unveil any more then we may have to accept that gas rich dark galaxies are not the smoking gun which will solve the dwarf galaxy problem, but any detections we do make will help towards unveiling the hidden dwarf galaxy population.

6.4.2 THE LSB UNIVERSE

The aim of my work on the Virgo cluster was not to find new dwarf galaxies, but to come up with a method of identifying them from background sources. I have discovered that if colour information is used alongside magnitude and surface brightness information then this can be done relatively easily. Many new dwarf populations are being discovered as data quality improves (e.g. Davies et al. 2016, Mihos et al. 2015, van Dokkum et al. 2015a), and this number will only increase with new survey telescopes. The methods discussed in this thesis will aid in the confirmation of dwarf cluster membership, and therefore help in the identification of new dwarf populations. As we enter the age of big data astronomy it will be vital to use automated detection methods, along with strict identification criteria, to identify dwarf galaxy populations effectively, and hence harness the full power of the new generation of data.

This will directly contribute to helping solve the dwarf galaxy problem, as the number of identified dwarfs will increase. However, we may find that we end up extending the Schechter function to fainter mass bins, and not discovering new dwarfs at the current faint end of this function. This could mean that the slope of the Schechter function will not change by the amount required to solve the dwarf galaxy problem. It may be that a multi-pronged approach is needed to bring observations and simulations together: some new detections coupled with improvements in how accurate a version of our universe we can create in simulations.

BIBLIOGRAPHY

Ahn C. P. et al., 2012, *ApJS*, 203, 21

Arimoto N., Yoshii Y., 1987, *A&A*, 173, 23

Astropy Collaboration et al., 2013, *A&A*, 558, A33

Auld R. et al., 2006, *MNRAS*, 371, 1617

Barnes D. G. et al., 2001, *MNRAS*, 322, 486

Bekki K., 2008, *MNRAS*, 390, L24

Bekki K., Couch W. J., Drinkwater M. J., Shiota Y., 2003, *MNRAS*, 344, 399

Binggeli B., Cameron L. M., 1991, *A&A*, 252, 27

Binggeli B., Sandage A., Tammann G. A., 1985, *AJ*, 90, 1681

Blakeslee J. P. et al., 2009, *ApJ*, 694, 556

Blitz L., Robishaw T., 2000, *ApJ*, 541, 675

Blitz L., Spergel D. N., Teuben P. J., Hartmann D., 2004, in *Astrophysics and Space Science Library*, Vol. 312, *High Velocity Clouds*, van Woerden H., Wakker B. P., Schwarz U. J., de Boer K. S., eds., p. 297

Blitz L., Spergel D. N., Teuben P. J., Hartmann D., Burton W. B., 1999, *ApJ*, 514, 818

Boggess N. W. et al., 1992, *ApJ*, 397, 420

Boselli A., Boissier S., Cortese L., Gavazzi G., 2008, *ApJ*, 674, 742

Boselli A., Gavazzi G., Donas J., Scodéglio M., 2001, *AJ*, 121, 753

Bothun G. D., Impey C. D., Malin D. F., 1991, *ApJ*, 376, 404

- Bower R. G., Lucey J. R., Ellis R. S., 1992a, MNRAS, 254, 601
- Bower R. G., Lucey J. R., Ellis R. S., 1992b, MNRAS, 254, 589
- Boylan-Kolchin M., Springel V., White S. D. M., Jenkins A., Lemson G., 2009, MNRAS, 398, 1150
- Braun R., Thilker D. A., 2004, A&A, 417, 421
- Bullock J. S., 2010, Local Group Cosmology
- Camps P., Baes M., 2015, Astronomy and Computing, 9, 20
- Chapman S. C. et al., 2013, MNRAS, 430, 37
- Christian C. A., Tully R. B., 1983, AJ, 88, 934
- Clark C. J. R., 2015, PhD thesis, Cardiff University, School of Physics and Astronomy, Cardiff
- Cleveland W. S., 1979, Robust locally weighted regression and smoothing scatter-plots
- Cooray A., Milosavljević M., 2005, ApJ, 627, L89
- Corbelli E., 2003, MNRAS, 342, 199
- Dalcanton J. J. et al., 2009, ApJS, 183, 67
- Davé R., Hernquist L., Katz N., Weinberg D. H., 1999, ApJ, 511, 521
- Davé R., Spergel D. N., Steinhardt P. J., Wandelt B. D., 2001, ApJ, 547, 574
- Davies J. et al., 2004, MNRAS, 349, 922
- Davies J. I., Davies L. J. M., Keenan O. C., 2016, MNRAS, 456, 1607
- Davies J. I., Disney M. J., Minchin R. F., Auld R., Smith R., 2006, MNRAS, 368, 1479
- Dickel J. R., Rood H. J., 1978, ApJ, 223, 391
- Dressler A., 1984, ApJ, 281, 512
- Drinkwater M. J., Jones J. B., Gregg M. D., Phillipps S., 2000, PASA, 17, 227
- Drlica-Wagner A. et al., 2015, ApJ, 813, 109

- Duc P.-A., Bournaud F., 2008, *ApJ*, 673, 787
- Ebeling H., Stephenson L. N., Edge A. C., 2014, *ApJ*, 781, L40
- Efstathiou G., Ellis R. S., Peterson B. A., 1988, *MNRAS*, 232, 431
- Eggen O. J., Lynden-Bell D., Sandage A. R., 1962, *ApJ*, 136, 748
- Faber S. M., 1973, *ApJ*, 179, 731
- Ferguson H. C., Binggeli B., 1994, *A&A Rev.*, 6, 67
- Ferguson H. C., Sandage A., 1988, *AJ*, 96, 1520
- Ferrarese L. et al., 2012, *ApJS*, 200, 4
- Ferrarese L. et al., 2016, *ApJ*, 824, 10
- Freedman W. L., Wilson C. D., Madore B. F., 1991, *ApJ*, 372, 455
- Fu H. et al., 2013, *Nature*, 498, 338
- Gallagher, III J. S., Wyse R. F. G., 1994, *PASP*, 106, 1225
- Gavazzi G., Boselli A., Scodéglio M., Pierini D., Belsole E., 1999, *MNRAS*, 304, 595
- Grebel E. K., Gallagher, III J. S., 2004, *ApJ*, 610, L89
- Grossi M., Giovanardi C., Corbelli E., Giovanelli R., Haynes M. P., Martin A. M., Saintonge A., Dowell J. D., 2008, *A&A*, 487, 161
- Grossi M., Hwang N., Corbelli E., Giovanardi C., Okamoto S., Arimoto N., 2011, VizieR Online Data Catalog, 353, 39091
- Guo Q. et al., 2016a, *MNRAS*, 461, 3457
- Guo R., Hao C.-N., Xia X. Y., Mao S., Shi Y., 2016b, *ApJ*, 826, 30
- Hartmann D., Burton W. B., 1997, *Atlas of Galactic Neutral Hydrogen*
- Hester J. A., 2006, *ApJ*, 647, 910
- Hinshaw G. et al., 2013, *ApJS*, 208, 19
- Hosking J. R., Wallis J. R., 1987, *Technometrics*, 29, 339

- Huxor A., Ferguson A. M. N., Barker M. K., Tanvir N. R., Irwin M. J., Chapman S. C., Ibata R., Lewis G., 2009, *ApJ*, 698, L77
- Ivezic Z. et al., 2008, *Serbian Astronomical Journal*, 176, 1
- Johnson B. D. et al., 2013, *ApJ*, 772, 8
- Juneau S. et al., 2005, *ApJ*, 619, L135
- Karick A. M., Drinkwater M. J., Gregg M. D., 2003, *MNRAS*, 344, 188
- Keenan O. C., Davies J. I., Taylor R., Minchin R. F., 2016, *MNRAS*, 456, 951
- Kim S. et al., 2014, *ApJS*, 215, 22
- Klypin A., Kravtsov A. V., Valenzuela O., Prada F., 1999a, *ApJ*, 522, 82
- Klypin A., Kravtsov A. V., Valenzuela O., Prada F., 1999b, *ApJ*, 522, 82
- Koda J., Yagi M., Yamanoi H., Komiyama Y., 2015, *ApJ*, 807, L2
- Kravtsov A. V., Klypin A. A., Khokhlov A. M., 1997, *ApJS*, 111, 73
- Kriek M. et al., 2007, *ApJ*, 669, 776
- Lacey C., Cole S., 1993, *MNRAS*, 262, 627
- Larson R. B., 1974, *MNRAS*, 169, 229
- Lavery R. J., Remijan A., Charmandaris V., Hayes R. D., Ring A. A., 2004, *ApJ*, 612, 679
- Lemson G., Virgo Consortium t., 2006, ArXiv Astrophysics e-prints
- Licquia T., Newman J., 2014, in American Astronomical Society Meeting Abstracts, Vol. 223, American Astronomical Society Meeting Abstracts #223, p. 336.04
- Lin H., Kirshner R. P., Shectman S. A., Landy S. D., Oemler A., Tucker D. L., Schechter P. L., 1996, *ApJ*, 464, 60
- Lisker T., Grebel E. K., Binggeli B., Glatt K., 2007, *ApJ*, 660, 1186
- Lockman F. J., Benjamin R. A., Heroux A. J., Langston G. I., 2008, *ApJ*, 679, L21
- Loveday J., Peterson B. A., Efstathiou G., Maddox S. J., 1992, *ApJ*, 390, 338
- Martin N. F. et al., 2009, *ApJ*, 705, 758

- Marzke R. O., Huchra J. P., Geller M. J., 1994, *ApJ*, 428, 43
- McConnachie A. W., 2012a, *AJ*, 144, 4
- McConnachie A. W., 2012b, *AJ*, 144, 4
- Mei S. et al., 2007, *ApJ*, 655, 144
- Merritt A., van Dokkum P., Abraham R., 2014, *ApJ*, 787, L37
- Mihos J. C. et al., 2015, *ApJ*, 809, L21
- Minchin R. et al., 2005, *ApJ*, 622, L21
- Minchin R. et al., 2007a, a Dark Galaxy in the Virgo Cluster Imaged at 21-CM, DE JONG R. S., ed., p. 101
- Minchin R. F. et al., 2007b, in IAU Symposium, Vol. 235, IAU Symposium, Combes F., Palouš J., eds., pp. 227–229
- Minchin R. F. et al., 2016, *MNRAS*, 455, 3430
- Montero-Dorta A. D., Prada F., 2009, *MNRAS*, 399, 1106
- Moore B., Ghigna S., Governato F., Lake G., Quinn T., Stadel J., Tozzi P., 1999, *ApJ*, 524, L19
- Muñoz R. P. et al., 2015, *ApJ*, 813, L15
- Neistein E., van den Bosch F. C., Dekel A., 2006, *MNRAS*, 372, 933
- Nidever D. L., Majewski S. R., Butler Burton W., Nigra L., 2010, *ApJ*, 723, 1618
- Odell A. P., Schombert J., Rakos K., 2002, *AJ*, 124, 3061
- Oey M. S., Groves B., Staveley-Smith L., Smith R. C., 2002, *AJ*, 123, 255
- Padmanabhan N. et al., 2008, *ApJ*, 674, 1217
- Peng E. W., Lim S., 2016, *ApJ*, 822, L31
- Phillipps S., Davies J. I., Disney M. J., 1988, *MNRAS*, 233, 485
- Phillipps S., Disney M. J., Kibblewhite E. J., Cawson M. G. M., 1987, *MNRAS*, 229, 505
- Planck Collaboration et al., 2014, *A&A*, 571, A1

- Planck Collaboration et al., 2016, A&A, 594, A13
- Putman M. E. et al., 2009, ApJ, 703, 1486
- Ratcliffe A., Shanks T., Parker Q. A., Fong R., 1998, MNRAS, 293, 197
- Riess A. G. et al., 1998, AJ, 116, 1009
- Rigby E. E., Best P. N., Brookes M. H., Peacock J. A., Dunlop J. S., Röttgering H. J. A., Wall J. V., Ker L., 2011, MNRAS, 416, 1900
- Roediger J. C. et al., 2017, ApJ, 836, 120
- Rong Y., Guo Q., Gao L., Liao S., Xie L., Puzia T. H., Sun S., Pan J., 2017, ArXiv e-prints
- Sabatini S., Davies J., Scaramella R., Smith R., Baes M., Linder S. M., Roberts S., Testa V., 2003, MNRAS, 341, 981
- Sabatini S., Davies J., van Driel W., Baes M., Roberts S., Smith R., Linder S., O'Neil K., 2005, MNRAS, 357, 819
- Sandage A., 1975, Classification and Stellar Content of Galaxies Obtained from Direct Photography, Sandage A., Sandage M., Kristian J., eds., the University of Chicago Press, p. 1
- Sarajedini A., Barker M. K., Geisler D., Harding P., Schommer R., 2006, AJ, 132, 1361
- Sault R. J., Teuben P. J., Wright M. C. H., 1995a, in Astronomical Society of the Pacific Conference Series, Vol. 77, Astronomical Data Analysis Software and Systems IV, Shaw R. A., Payne H. E., Hayes J. J. E., eds., p. 433
- Sault R. J., Teuben P. J., Wright M. C. H., 1995b, in Astronomical Society of the Pacific Conference Series, Vol. 77, Astronomical Data Analysis Software and Systems IV, Shaw R. A., Payne H. E., Hayes J. J. E., eds., p. 433
- Sawala T. et al., 2016, MNRAS, 457, 1931
- Schawinski K. et al., 2014, MNRAS, 440, 889
- Schaye J. et al., 2015, MNRAS, 446, 521
- Schlafly E. F., Finkbeiner D. P., 2011, ApJ, 737, 103

- Searle L., Zinn R., 1978, *ApJ*, 225, 357
- Simon J. D., 2005, PhD thesis, University of California, Berkeley
- Smith G. P., 1963, *Bull. Astron. Inst. Netherlands*, 17, 203
- Smith R. J., Lucey J. R., Hudson M. J., Allanson S. P., Bridges T. J., Hornschemeier A. E., Marzke R. O., Miller N. A., 2009, *MNRAS*, 392, 1265
- Solanes J. M., Sanchis T., Salvador-Solé E., Giovanelli R., Haynes M. P., 2002, *AJ*, 124, 2440
- Stadel J., Potter D., Moore B., Diemand J., Madau P., Zemp M., Kuhlen M., Quilis V., 2009, *MNRAS*, 398, L21
- Sternberg A., McKee C. F., Wolfire M. G., 2002, *ApJS*, 143, 419
- Taylor R., Davies J. I., Auld R., Minchin R. F., 2012, *MNRAS*, 423, 787
- Taylor R., Davies J. I., Auld R., Minchin R. F., Smith R., 2013, *MNRAS*, 428, 459
- Taylor R., Davies J. I., Jáchym P., Keenan O., Minchin R. F., Palouš J., Smith R., Wünsch R., 2016, *MNRAS*, 461, 3001
- Taylor R., Minchin R. F., Herbst H., Davies J. I., Rodriguez R., Vazquez C., 2014, *MNRAS*, 443, 2634
- Terlevich A. I., Caldwell N., Bower R. G., 2001, *MNRAS*, 326, 1547
- Thilker D. A., Braun R., Walterbos R. A. M., 2002, in *Astronomical Society of the Pacific Conference Series*, Vol. 276, *Seeing Through the Dust: The Detection of HI and the Exploration of the ISM in Galaxies*, Taylor A. R., Landecker T. L., Willis A. G., eds., p. 370
- van Dokkum P. G., Abraham R., Merritt A., Zhang J., Geha M., Conroy C., 2015a, *ApJ*, 798, L45
- van Dokkum P. G. et al., 2015b, *ApJ*, 804, L26
- Vogelsberger M. et al., 2014a, *Nature*, 509, 177
- Vogelsberger M. et al., 2014b, *MNRAS*, 444, 1518
- Wakker B. P., 1991, *A&A*, 250, 499

- Westmeier T., Braun R., Thilker D., 2005, A&A, 436, 101
- Willman B. et al., 2005, ApJ, 626, L85
- Wolfe S. A., Pisano D. J., Lockman F. J., McGaugh S. S., Shaya E. J., 2013, Nature, 497, 224
- Wright M. C. H., 1979, ApJ, 233, 35
- Zehavi I. et al., 2011, ApJ, 736, 59
- Zucker D. B. et al., 2006, ApJ, 643, L103

APPENDIX

'This morning I found a book in my brother's bookcase. It's in English and deals with time and the universe and everything. I flipped through the pages, but started sweating and had to put it down. It was too much for me.'

ERLEND LOE, NAIIVE. SUPER

7.1 PHOTOMETRY DATA TABLES

Tables 1-6 below give the results from the photometry of the Virgo cluster galaxies.

Table 1 presents, in column order, 1. the galaxy's VCC number 2. RA 3. Dec 4. u band magnitude 5. u band magnitude error 6. g band magnitude 7. g band magnitude error 8. i band magnitude 9. i band magnitude error 10. z band magnitude 11. z band magnitude error.

Table 2 presents, in column order, 1. the VCC number 2. $u - g$ colour 3. $u - g$ error 4. $u - i$ colour 5. $u - i$ colour 6. $u - z$ colour 7. $u - z$ error 8. $g - i$ colour 9. $g - i$ colour error 10. $g - z$ colour 11. $g - z$ colour error 12. $i - z$ colour 13. $i - z$ colour error.

Table 3 presents, in column order, 1. the VCC number 2. the radius measured at the 28 mag arcsec⁻² isophote in the g band 3. u band mean surface brightness within this radius 4. u band surface brightness error 5. g band mean surface brightness within this radius 6. g band surface brightness error 7. i band mean

surface brightness within this radius 8. i band surface brightness error 9. z band mean surface brightness within this radius 10. z band surface brightness error.

Table 4 presents, in column order, 1. the galaxy's LSBVCC number 2. RA 3. Dec 4. u band magnitude 5. u band magnitude error 6. g band magnitude 7. g band magnitude error 8. i band magnitude 9. i band magnitude error 10. z band magnitude 11. z band magnitude error.

Table 5 presents, in column order, 1. the LSBVCC number 2. $u - g$ colour 3. $u - g$ error 4. $u - i$ colour 5. $u - i$ colour 6. $u - z$ colour 7. $u - z$ error 8. $g - i$ colour 9. $g - i$ colour error 10. $g - z$ colour 11. $g - z$ colour error 12. $i - z$ colour 13. $i - z$ colour error.

Table 6 presents, in column order, 1. the LSBVCC number 2. the radius measured at the 28 mag arcsec $^{-2}$ isophote in the g band 3. u band mean surface brightness within this radius 4. u band surface brightness error 5. g band mean surface brightness within this radius 6. g band surface brightness error 7. i band mean surface brightness within this radius 8. i band surface brightness error 9. z band mean surface brightness within this radius 10. z band surface brightness error.

TABLE 7.1 The VCC number, RA, Dec, magnitudes in the u, g, i and z bands with errors.

VCC	RA (deg)	Dec (deg)	u	u_err	g	g_err	i	i_err	z	z_err
299	184.6662	13.5982	18.29	0.02	17.19	0.01	16.43	0.01	16.26	0.02
306	184.7015	8.9884	19.71	0.03	18.73	0.02	18.06	0.02	18.02	0.03
309	184.7138	12.5984	17.27	0.02	16.51	0.01	16.03	0.01	16.05	0.02
310	184.7238	12.1939	19.84	0.03	18.77	0.02	18.00	0.02	18.05	0.03
319	184.7583	13.9824	16.22	0.02	15.12	0.01	14.67	0.01	14.45	0.02
322	184.7715	13.9805	16.05	0.02	15.02	0.01	14.42	0.01	14.33	0.01
328	184.7970	12.8836	16.99	0.02	16.35	0.01	15.92	0.01	15.82	0.01
330	184.8019	12.8519	17.85	0.02	16.77	0.01	15.89	0.01	15.81	0.02
333	184.8104	13.7957	19.78	0.03	18.85	0.02	18.24	0.02	18.06	0.03
334	184.8093	13.8824	16.38	0.02	15.61	0.01	15.08	0.01	14.96	0.01
350	184.8579	13.3109	17.69	0.02	16.96	0.01	16.51	0.02	16.51	0.02
353	184.8778	12.2089	19.57	0.03	18.52	0.02	17.63	0.02	17.54	0.02
354	184.8754	13.9907	17.60	0.02	16.53	0.01	15.72	0.01	15.58	0.02
355	184.8774	14.8777	13.71	0.02	12.33	0.01	11.27	0.01	10.97	0.01
361	184.9044	15.1622	18.28	0.02	17.18	0.01	16.35	0.01	16.23	0.02
364	184.9351	12.2826	18.63	0.02	17.30	0.01	15.89	0.01	15.31	0.01
369	184.9385	12.7983	14.65	0.02	12.30	0.01	11.18	0.01	10.90	0.01
372	184.9487	14.7063	19.65	0.03	18.21	0.02	17.22	0.02	17.10	0.02
389	185.0138	14.9615	15.37	0.02	14.03	0.01	13.16	0.01	12.99	0.01
391	185.0123	13.7962	19.08	0.03	18.04	0.04	17.21	0.03	16.91	0.03
394	185.0359	9.4681	18.53	0.02	17.42	0.01	16.62	0.01	16.49	0.02
401	185.0608	12.8652	18.86	0.02	18.00	0.01	17.49	0.02	17.41	0.02
407	185.0783	9.5454	15.87	0.02	14.58	0.01	13.70	0.01	13.56	0.01
410	185.0908	12.1878	17.58	0.02	17.08	0.01	16.72	0.01	16.61	0.02
414	185.1015	14.6908	18.61	0.02	17.42	0.01	16.62	0.01	16.58	0.02
418	185.1119	14.7853	18.59	0.02	17.46	0.01	16.69	0.01	16.52	0.02
421	185.1280	13.5192	18.80	0.02	17.54	0.01	16.77	0.01	16.71	0.02
425	185.1489	8.2011	19.18	0.03	18.15	0.02	17.41	0.02	17.41	0.03
426	185.1513	12.8848	19.42	0.03	18.39	0.02	17.48	0.02	17.36	0.02
428	185.1678	13.8896	17.39	0.02	17.01	0.01	16.99	0.02	16.87	0.02
431	185.1933	12.7578	19.40	0.03	18.38	0.02	17.55	0.02	17.41	0.02
444	185.2276	14.9889	18.64	0.02	17.46	0.01	16.69	0.01	16.81	0.02
447	185.2454	8.8662	20.53	0.06	19.63	0.02	18.96	0.04	19.03	0.06
452	185.2700	11.7546	17.07	0.02	15.82	0.01	15.02	0.01	14.89	0.01
455	185.2868	9.7096	18.86	0.02	17.66	0.01	16.91	0.01	16.81	0.02
456	185.2878	12.2992	19.51	0.03	18.52	0.02	17.73	0.02	17.62	0.02
458	185.3031	8.9632	17.87	0.02	16.74	0.01	15.86	0.01	15.80	0.01
461	185.3126	13.3465	17.81	0.02	16.60	0.01	15.68	0.01	15.58	0.01
471	185.3535	9.6203	19.65	0.02	18.92	0.02	18.37	0.02	18.20	0.03
477	185.3629	15.0200	18.25	0.02	17.40	0.01	16.81	0.02	16.90	0.02
493	185.4377	13.1932	18.64	0.02	17.65	0.01	16.87	0.01	16.68	0.02

VCC	RA (deg)	Dec (deg)	u	u_err	g	g_err	i	i_err	z	z_err
494	185.4235	15.0749	18.12	0.02	16.77	0.02	15.94	0.01	15.87	0.02
496	185.4282	9.3555	19.94	0.03	19.01	0.02	18.19	0.02	18.14	0.03
498	185.4304	10.2341	19.98	0.03	18.91	0.02	18.11	0.02	17.98	0.03
501	185.4500	12.8266	18.16	0.02	17.07	0.01	16.21	0.01	16.08	0.02
502	185.4533	11.8519	20.30	0.04	19.23	0.02	18.28	0.02	18.08	0.03
503	185.4597	8.5418	18.41	0.02	17.35	0.01	16.39	0.01	16.54	0.02
504	185.4586	9.7391	17.68	0.02	16.63	0.01	15.96	0.01	15.80	0.01
511	185.4828	8.3457	19.93	0.04	18.84	0.02	18.10	0.02	18.07	0.03
512	185.4816	11.9668	16.83	0.02	15.94	0.01	15.45	0.01	15.33	0.01
519	185.5036	14.1366	19.88	0.04	18.90	0.02	18.19	0.03	18.12	0.04
529	185.5358	9.8944	19.13	0.03	18.07	0.02	17.14	0.02	17.00	0.02
532	185.5435	11.6418	19.75	0.03	18.63	0.02	17.89	0.02	17.79	0.03
537	185.5533	12.6967	19.76	0.04	18.60	0.02	17.69	0.02	17.57	0.03
539	185.5617	14.1423	18.07	0.02	16.76	0.01	15.97	0.01	16.02	0.02
540	185.5704	10.9533	20.96	0.05	19.64	0.02	18.79	0.02	18.60	0.03
544	185.5843	9.0340	17.58	0.02	16.78	0.01	16.19	0.01	16.14	0.02
547	185.5871	15.1598	20.00	0.03	18.92	0.02	18.21	0.02	18.22	0.03
556	185.6171	13.1628	20.62	0.04	19.49	0.02	18.56	0.03	18.50	0.03
560	185.6319	11.8026	18.13	0.02	17.01	0.02	16.08	0.02	15.81	0.04
561	185.6488	8.8119	18.86	0.02	17.79	0.01	17.02	0.01	17.05	0.02
562	185.6496	12.1580	15.97	0.02	15.49	0.01	15.03	0.01	14.87	0.01
564	185.6517	11.2975	21.38	0.06	20.42	0.03	19.66	0.04	19.62	0.07
574	185.6762	8.8295	18.56	0.03	17.44	0.02	16.73	0.02	16.69	0.02
575	185.6804	8.1983	15.09	0.02	13.72	0.01	12.72	0.01	12.51	0.01
582	185.6968	8.4372	20.81	0.07	19.74	0.03	18.96	0.04	18.85	0.07
584	185.7012	7.9135	17.95	0.02	16.86	0.01	16.09	0.01	16.03	0.02
585	185.6957	11.3444	18.57	0.02	17.54	0.01	16.95	0.02	16.87	0.02
592	185.7119	13.5929	17.44	0.02	16.26	0.01	15.35	0.01	15.18	0.01
594	185.7131	15.2752	18.38	0.02	17.22	0.01	16.41	0.01	16.52	0.02
603	185.7467	13.7569	20.51	0.04	19.39	0.02	18.56	0.02	18.44	0.03
605	185.7583	13.5590	20.59	0.04	19.47	0.02	18.59	0.03	18.46	0.03
607	185.7601	13.9145	20.70	0.05	19.62	0.02	18.51	0.02	18.25	0.03
611	185.7702	8.3332	17.63	0.02	16.42	0.01	15.70	0.01	15.55	0.01
615	185.7697	12.0157	19.97	0.04	18.64	0.02	17.88	0.03	17.61	0.03
622	185.7955	9.0287	19.13	0.02	18.12	0.02	17.39	0.02	17.37	0.02
624	185.7983	13.4184	19.67	0.03	18.72	0.02	17.88	0.02	17.84	0.02
625	185.7967	14.8623	18.68	0.02	17.56	0.01	16.71	0.01	16.60	0.02
628	185.8173	7.6869	19.92	0.04	18.94	0.02	18.03	0.02	17.67	0.03
632	185.8333	7.0681	18.06	0.02	17.18	0.01	16.49	0.01	16.42	0.02
640	185.8640	7.8015	20.13	0.05	19.11	0.02	18.33	0.03	18.24	0.04
643	185.8723	14.8893	19.95	0.03	18.77	0.02	18.02	0.02	17.80	0.02
645	185.8818	11.2704	19.19	0.02	18.15	0.02	17.36	0.02	17.19	0.02

VCC	RA (deg)	Dec (deg)	u	u_err	g	g_err	i	i_err	z	z_err
651	185.8943	9.5149	18.37	0.02	17.55	0.01	17.07	0.02	16.86	0.02
658	185.9139	10.0308	20.09	0.03	19.01	0.02	18.09	0.02	18.00	0.02
659	185.9106	12.6277	19.18	0.02	18.15	0.02	17.30	0.02	17.15	0.02
660	185.9148	13.8336	18.42	0.02	17.12	0.01	16.06	0.01	15.83	0.01
668	185.9461	15.1253	18.71	0.02	17.43	0.01	16.57	0.01	16.48	0.02
673	185.9692	10.7600	20.81	0.04	19.80	0.02	18.99	0.03	18.77	0.03
674	185.9693	13.8825	18.77	0.02	17.42	0.01	16.54	0.02	16.45	0.02
678	185.9706	12.7730	19.46	0.03	18.41	0.02	17.36	0.02	17.21	0.02
684	185.9905	12.8871	17.30	0.02	16.07	0.01	15.12	0.01	14.94	0.01
686	185.9998	9.4940	20.06	0.04	19.08	0.02	18.50	0.03	18.51	0.05
687	185.9905	11.8923	19.37	0.02	18.16	0.02	17.39	0.02	17.40	0.02
688	186.0011	7.7852	14.94	0.02	13.84	0.01	13.04	0.01	12.88	0.01
691	186.0028	11.8593	20.91	0.05	19.96	0.02	19.36	0.05	19.14	0.04
692	186.0063	12.2048	14.50	0.02	13.33	0.01	12.81	0.01	13.05	0.01
698	186.0209	11.2181	14.73	0.02	13.31	0.01	12.32	0.01	12.06	0.01
701	186.0344	11.1458	20.59	0.05	19.69	0.03	18.98	0.03	18.97	0.05
702	186.0377	8.5136	20.21	0.04	19.19	0.02	18.39	0.03	18.22	0.03
703	186.0435	9.2362	17.15	0.02	15.76	0.01	14.83	0.01	14.65	0.01
704	186.0469	13.3734	19.60	0.03	18.59	0.02	17.88	0.02	17.69	0.02
705	186.0457	11.9466	18.22	0.02	17.18	0.01	16.40	0.02	16.21	0.02
706	186.0520	11.5294	18.63	0.02	17.56	0.01	16.80	0.01	16.67	0.02
708	186.0557	13.6326	19.66	0.03	18.55	0.02	17.69	0.02	17.54	0.02
709	186.0530	14.4933	19.75	0.03	18.75	0.02	18.01	0.02	17.79	0.03
711	186.0578	7.1751	17.68	0.02	16.54	0.01	15.68	0.01	15.80	0.02
719	186.0782	12.9126	19.73	0.03	18.65	0.02	17.83	0.02	17.68	0.02
725	186.1008	15.0745	17.51	0.02	15.93	0.01	15.41	0.01	15.40	0.01
731	186.1178	7.3177	12.93	0.02	11.33	0.01	10.25	0.01	9.98	0.01
732	186.1290	11.8114	19.67	0.03	18.67	0.02	18.05	0.03	17.98	0.03
733	186.1335	8.6375	18.78	0.02	17.72	0.01	16.90	0.01	16.80	0.02
743	186.1771	11.4822	21.21	0.06	20.16	0.03	19.40	0.04	19.33	0.06
745	186.1959	7.3530	16.17	0.02	14.81	0.01	13.88	0.01	13.69	0.01
746	186.1987	8.4391	19.19	0.03	17.98	0.02	17.18	0.02	17.14	0.03
747	186.1990	8.9914	18.36	0.02	17.13	0.01	16.36	0.01	16.50	0.02
748	186.1982	14.5764	18.58	0.02	17.24	0.01	16.36	0.01	16.23	0.02
752	186.1996	11.8183	20.66	0.04	19.53	0.02	18.90	0.04	18.81	0.04
753	186.2151	13.1112	17.67	0.02	16.45	0.01	15.64	0.01	15.51	0.01
754	186.2108	15.0110	20.02	0.03	18.94	0.02	18.15	0.02	18.26	0.03
755	186.2253	7.5569	18.13	0.02	16.75	0.01	15.77	0.01	15.64	0.02
756	186.2214	9.4937	17.95	0.02	16.90	0.01	16.32	0.01	16.17	0.02
757	186.2213	14.6553	19.38	0.03	18.27	0.02	17.43	0.02	17.36	0.02
758	186.2288	7.4449	14.91	0.02	13.35	0.01	12.21	0.01	11.93	0.01
760	186.2339	11.8321	18.46	0.02	17.33	0.01	16.51	0.02	16.40	0.02

VCC	RA (deg)	Dec (deg)	u	u_err	g	g_err	i	i_err	z	z_err
762	186.2624	7.5038	17.06	0.02	15.69	0.01	14.76	0.01	14.68	0.01
765	186.2645	13.2447	16.46	0.02	15.65	0.01	14.85	0.01	14.61	0.01
774	186.2919	10.4567	19.89	0.03	18.90	0.02	18.23	0.02	17.99	0.03
775	186.2903	12.3825	19.21	0.03	18.14	0.02	17.48	0.02	17.29	0.02
778	186.3014	14.7622	13.78	0.02	12.43	0.01	11.39	0.01	11.10	0.01
779	186.3046	13.0254	18.60	0.02	17.40	0.01	16.52	0.02	16.43	0.02
780	186.3050	14.8452	19.07	0.03	17.99	0.02	17.16	0.02	17.05	0.02
781	186.3133	12.7146	15.75	0.02	14.61	0.01	13.81	0.01	13.68	0.01
788	186.3201	11.6053	17.22	0.02	16.02	0.01	15.13	0.01	14.99	0.01
789	186.3287	13.2578	19.44	0.03	18.19	0.02	17.31	0.02	17.61	0.02
790	186.3231	14.1726	17.02	0.02	15.80	0.01	14.96	0.01	14.73	0.01
792	186.3424	10.0168	14.30	0.02	13.08	0.01	12.11	0.01	11.86	0.01
793	186.3400	13.0717	17.35	0.02	16.55	0.01	15.96	0.01	15.93	0.02
796	186.3485	12.6752	20.98	0.06	19.94	0.03	19.24	0.05	19.02	0.05
800	186.3610	12.6769	19.71	0.03	18.59	0.02	17.75	0.02	17.58	0.02
802	186.3710	13.4981	17.49	0.02	16.76	0.01	16.11	0.01	16.07	0.01
803	186.3700	12.4936	19.93	0.03	18.92	0.02	18.04	0.02	18.35	0.03
804	186.3769	12.9771	20.51	0.05	19.51	0.02	18.67	0.04	18.97	0.06
807	186.3883	7.8080	20.00	0.04	18.95	0.02	18.23	0.02	18.25	0.03
808	186.3815	14.1526	18.18	0.02	16.99	0.01	16.31	0.01	16.00	0.02
809	186.3880	12.2603	15.41	0.02	14.43	0.01	13.64	0.01	13.48	0.01
810	186.3897	13.2272	17.77	0.02	16.52	0.01	15.64	0.01	15.47	0.01
811	186.4093	10.2500	20.18	0.04	19.20	0.02	18.49	0.03	18.31	0.04
812	186.3952	15.1944	17.86	0.02	16.63	0.01	15.72	0.01	15.62	0.01
815	186.4050	13.1437	17.02	0.02	15.96	0.01	15.14	0.01	15.02	0.01
821	186.4120	7.7581	20.75	0.06	19.69	0.02	18.89	0.03	18.59	0.05
823	186.4122	12.3137	16.97	0.02	15.53	0.01	14.88	0.01	14.73	0.01
824	186.4115	14.1507	18.53	0.02	17.50	0.02	16.68	0.02	16.46	0.02
828	186.4237	12.8105	14.25	0.02	12.77	0.01	11.71	0.01	11.50	0.01
833	186.4360	13.0221	18.52	0.02	17.21	0.01	16.24	0.01	16.04	0.01
838	186.4462	12.7604	18.47	0.02	17.42	0.01	16.61	0.02	16.47	0.02
839	186.4468	10.0936	18.77	0.02	17.79	0.02	17.12	0.02	16.91	0.02
840	186.4455	11.6631	19.14	0.02	18.01	0.02	17.16	0.02	17.12	0.02
843	186.4543	12.8045	19.78	0.03	18.82	0.02	18.05	0.02	17.86	0.02
845	186.4505	13.8542	19.63	0.03	18.50	0.02	17.78	0.02	17.45	0.02
846	186.4605	13.1976	17.57	0.02	16.25	0.01	15.36	0.01	15.26	0.01
849	186.4611	10.4591	14.20	0.02	13.46	0.01	12.92	0.01	12.80	0.01
850	186.4693	13.1915	20.48	0.06	19.20	0.03	18.43	0.04	18.55	0.05
851	186.4754	7.5548	14.99	0.02	13.90	0.01	13.05	0.01	12.94	0.01
853	186.4823	11.8011	21.16	0.06	20.13	0.03	19.48	0.06	19.30	0.06
854	186.4821	12.7697	18.42	0.02	17.32	0.01	16.74	0.01	16.61	0.02
855	186.4838	7.2347	18.29	0.02	17.17	0.01	16.38	0.01	16.26	0.02

VCC	RA (deg)	Dec (deg)	u	u_err	g	g_err	i	i_err	z	z_err
856	186.4914	10.0538	15.69	0.02	14.43	0.01	13.52	0.01	13.33	0.01
861	186.4955	15.2772	18.47	0.02	17.47	0.01	16.71	0.01	16.54	0.02
863	186.4989	14.0396	19.25	0.03	18.09	0.02	17.27	0.02	17.15	0.02
867	186.5058	8.1931	19.73	0.04	18.68	0.02	17.90	0.02	17.88	0.03
868	186.5268	10.9583	20.77	0.05	19.82	0.03	19.16	0.04	19.17	0.05
869	186.5246	8.9674	17.67	0.02	16.56	0.01	15.81	0.01	15.80	0.02
870	186.5222	11.8122	15.95	0.02	14.80	0.01	14.12	0.01	13.98	0.01
871	186.5235	12.5596	17.02	0.02	15.82	0.01	14.96	0.01	14.83	0.01
872	186.5279	12.8610	18.03	0.02	16.78	0.01	15.85	0.01	15.68	0.01
876	186.5402	12.3952	19.81	0.03	18.74	0.02	17.96	0.02	17.76	0.02
877	186.5397	13.6731	18.69	0.02	17.60	0.01	16.80	0.02	16.57	0.02
883	186.5646	7.7563	20.10	0.03	18.93	0.02	18.15	0.02	18.08	0.03
884	186.5653	13.1430	20.21	0.04	19.07	0.02	18.19	0.03	18.10	0.03
886	186.5637	13.3409	21.56	0.05	20.58	0.03	19.90	0.10	19.71	0.06
891	186.5880	6.7901	21.04	0.06	20.00	0.03	19.21	0.03	18.94	0.06
892	186.5835	12.5101	19.36	0.02	18.30	0.02	17.46	0.02	17.43	0.02
893	186.5898	7.7778	20.63	0.05	19.54	0.02	18.79	0.03	18.57	0.04
894	186.5855	8.5580	20.87	0.06	19.73	0.02	19.18	0.04	18.84	0.05
895	186.6040	10.5819	18.57	0.03	17.47	0.02	16.97	0.02	16.73	0.02
896	186.5942	12.7866	18.80	0.02	17.69	0.01	16.89	0.01	16.82	0.02
897	186.5915	13.7571	20.24	0.03	19.21	0.02	18.46	0.03	18.28	0.03
900	186.6083	13.7383	19.49	0.03	18.45	0.02	17.67	0.02	17.60	0.02
902	186.6194	8.7953	19.90	0.03	18.77	0.02	17.95	0.02	17.88	0.03
903	186.6170	12.9206	19.78	0.03	18.85	0.02	18.11	0.02	18.09	0.03
906	186.6244	9.9789	20.11	0.04	19.00	0.02	18.09	0.02	17.91	0.03
914	186.6430	8.9931	19.96	0.03	18.89	0.02	18.15	0.02	18.15	0.04
915	186.6414	11.2848	19.18	0.03	18.22	0.02	17.34	0.02	17.15	0.02
916	186.6384	12.7430	17.29	0.02	15.78	0.01	14.70	0.01	14.45	0.01
917	186.6350	13.5788	16.28	0.02	15.14	0.01	14.32	0.01	14.16	0.01
922	186.6541	10.2078	20.69	0.05	19.76	0.03	19.03	0.03	19.08	0.06
923	186.6514	12.8028	20.11	0.03	18.96	0.02	18.38	0.02	18.21	0.03
925	186.6586	15.0853	19.64	0.04	18.70	0.02	17.86	0.02	17.64	0.03
926	186.6663	9.5004	17.78	0.02	16.77	0.01	16.01	0.01	15.91	0.02
927	186.6609	13.0783	20.99	0.05	19.91	0.03	18.84	0.03	18.57	0.03
928	186.6659	12.5135	17.20	0.02	16.01	0.01	15.16	0.01	15.06	0.01
929	186.6687	8.4357	15.09	0.02	13.70	0.01	12.77	0.01	12.56	0.01
931	186.6834	10.9048	16.32	0.02	15.38	0.01	14.70	0.01	14.54	0.01
932	186.6816	10.9568	19.12	0.02	18.11	0.02	17.32	0.02	17.22	0.02
933	186.6848	8.8237	17.79	0.02	16.60	0.01	15.75	0.01	15.75	0.02
935	186.6871	11.0022	20.21	0.04	19.21	0.02	18.29	0.02	18.03	0.03
936	186.6851	11.3797	17.11	0.02	15.99	0.01	15.12	0.01	14.90	0.01
937	186.6942	13.2668	20.31	0.04	19.36	0.02	18.64	0.03	18.53	0.04

VCC	RA (deg)	Dec (deg)	u	u_err	g	g_err	i	i_err	z	z_err
940	186.6961	12.4540	16.29	0.02	14.99	0.01	14.02	0.01	13.96	0.01
941	186.6995	13.3791	19.69	0.02	18.70	0.02	17.91	0.02	17.81	0.02
942	186.7017	12.4001	20.43	0.04	19.58	0.02	18.83	0.02	18.75	0.05
943	186.6983	13.6797	19.48	0.02	18.66	0.02	17.99	0.02	17.83	0.03
945	186.7131	13.1757	15.83	0.02	15.26	0.01	15.12	0.01	15.13	0.01
948	186.7220	7.7525	20.50	0.04	19.53	0.02	18.82	0.03	18.89	0.05
949	186.7273	10.6659	16.95	0.02	15.64	0.01	14.73	0.01	14.52	0.01
951	186.7264	11.6640	15.68	0.02	14.38	0.01	13.71	0.01	13.63	0.01
956	186.7351	12.9615	19.75	0.03	18.72	0.02	17.96	0.02	17.82	0.03
959	186.7401	12.4207	21.41	0.08	20.40	0.03	19.55	0.04	19.49	0.08
960	186.7452	6.8012	20.78	0.05	19.71	0.02	18.81	0.03	18.59	0.04
963	186.7465	14.7824	17.77	0.02	16.98	0.01	16.52	0.01	16.37	0.02
964	186.7579	14.1087	19.37	0.02	18.22	0.02	17.37	0.02	17.21	0.02
965	186.7628	12.5608	16.60	0.02	15.39	0.01	14.42	0.01	14.41	0.01
968	186.7753	13.3237	19.44	0.03	18.47	0.03	17.79	0.03	17.74	0.04
970	186.7832	7.8164	20.82	0.05	19.79	0.02	18.98	0.03	18.60	0.04
972	186.7851	13.3358	18.39	0.02	17.15	0.01	16.33	0.01	16.25	0.02
974	186.7913	8.3899	17.56	0.02	16.42	0.01	15.52	0.01	15.43	0.01
976	186.7997	8.8401	18.68	0.02	17.66	0.01	16.95	0.02	16.88	0.02
978	186.7970	12.1145	18.99	0.03	18.03	0.02	17.19	0.02	17.27	0.03
983	186.8132	9.6261	19.88	0.05	18.71	0.02	17.60	0.02	17.55	0.04
984	186.8055	12.7347	14.12	0.02	12.63	0.01	11.62	0.01	11.40	0.01
986	186.8192	10.6984	20.55	0.04	19.65	0.02	18.86	0.03	18.61	0.03
988	186.8236	6.7672	20.90	0.08	19.91	0.03	19.02	0.03	19.01	0.09
991	186.8239	14.1468	14.29	0.02	12.74	0.01	11.84	0.01	11.58	0.01
992	186.8279	8.2129	17.61	0.02	16.43	0.01	15.58	0.01	15.41	0.01
996	186.8378	13.1115	19.00	0.02	17.87	0.01	17.09	0.02	17.04	0.02
997	186.8424	12.0687	18.82	0.02	17.85	0.01	16.95	0.01	16.90	0.02
998	186.8479	12.3315	19.02	0.02	17.99	0.02	17.16	0.02	17.11	0.02
1000	186.8528	11.2381	19.94	0.03	18.79	0.02	17.92	0.02	17.76	0.02
1001	186.8521	13.7160	17.71	0.02	16.97	0.01	16.41	0.01	16.27	0.02
1004	186.8538	13.4063	19.94	0.04	18.89	0.02	18.16	0.03	18.28	0.04
1005	186.8560	13.7508	17.40	0.02	16.25	0.01	15.35	0.01	15.20	0.01
1006	186.8552	14.4336	19.59	0.03	18.26	0.02	17.44	0.02	17.43	0.02
1008	186.8624	11.9426	21.21	0.05	20.26	0.02	19.57	0.03	19.60	0.09
1009	186.8628	8.3523	20.06	0.03	19.07	0.02	18.24	0.02	18.14	0.03
1010	186.8641	12.2903	15.25	0.02	13.78	0.01	12.75	0.01	12.64	0.01
1011	186.8713	7.6435	15.98	0.02	15.03	0.01	14.39	0.01	14.35	0.01
1012	186.8688	8.3912	20.80	0.04	19.83	0.02	19.05	0.03	19.12	0.06
1013	186.8757	9.3411	17.46	0.02	16.63	0.01	15.87	0.01	16.12	0.02
1014	186.8740	12.2519	19.98	0.04	19.00	0.02	18.17	0.02	18.16	0.05
1015	186.8732	12.2689	21.50	0.08	20.53	0.03	19.79	0.05	19.83	0.12

VCC	RA (deg)	Dec (deg)	u	u_err	g	g_err	i	i_err	z	z_err
1020	186.8833	11.6152	18.27	0.02	17.15	0.01	16.28	0.01	16.18	0.02
1021	186.8895	10.0038	16.69	0.02	15.61	0.01	14.89	0.01	14.83	0.01
1022	186.8874	11.5323	20.71	0.05	19.80	0.02	18.92	0.03	18.95	0.05
1023	186.8933	12.8040	21.03	0.06	20.03	0.03	19.19	0.04	18.96	0.05
1025	186.9028	8.1543	14.27	0.02	12.80	0.01	11.82	0.01	11.53	0.01
1026	186.9008	14.8398	19.26	0.03	18.25	0.02	17.39	0.02	16.84	0.02
1027	186.9135	12.8799	19.32	0.03	18.01	0.02	17.32	0.02	17.36	0.02
1029	186.9123	14.5420	19.61	0.03	18.62	0.02	17.84	0.02	17.81	0.03
1030	186.9187	13.0789	13.20	0.02	11.74	0.01	10.70	0.01	10.43	0.01
1036	186.9218	12.3159	15.28	0.02	13.40	0.01	12.98	0.01	12.83	0.01
1037	186.9236	12.4877	20.76	0.04	19.76	0.02	19.10	0.03	18.97	0.04
1039	186.9345	11.2146	18.27	0.02	17.18	0.01	16.30	0.01	16.18	0.02
1040	186.9355	12.9836	18.42	0.02	17.14	0.02	16.17	0.01	16.10	0.02
1044	186.9428	11.4351	17.99	0.02	16.95	0.01	16.11	0.01	16.01	0.01
1045	186.9568	7.0258	19.63	0.04	18.58	0.02	17.73	0.02	17.67	0.04
1046	186.9562	12.4996	21.06	0.07	20.03	0.03	19.23	0.04	19.22	0.06
1047	186.9732	12.2933	14.15	0.02	12.69	0.01	11.64	0.01	11.44	0.01
1049	186.9785	8.0904	15.91	0.02	14.79	0.01	13.98	0.01	13.86	0.01
1052	186.9810	12.3710	20.07	0.04	18.97	0.02	18.23	0.02	18.31	0.06
1053	186.9783	13.8208	20.91	0.05	19.78	0.02	19.13	0.03	18.90	0.04
1056	186.9893	14.4706	19.72	0.04	18.60	0.02	17.88	0.02	17.74	0.03
1057	186.9974	8.1163	20.54	0.05	19.63	0.02	18.80	0.03	18.87	0.05
1059	187.0019	11.9498	18.62	0.02	17.54	0.01	16.67	0.01	16.57	0.02
1063	187.0188	11.6044	20.65	0.05	19.61	0.02	18.83	0.03	18.81	0.06
1064	187.0205	13.6120	18.38	0.02	17.27	0.01	16.53	0.01	16.45	0.02
1069	187.0272	12.8982	17.55	0.02	16.32	0.01	15.51	0.01	15.42	0.01
1070	187.0282	12.9786	20.36	0.04	19.15	0.02	18.69	0.03	18.57	0.05
1071	187.0307	8.8148	19.52	0.03	18.24	0.02	17.25	0.02	17.13	0.02
1073	187.0359	12.0933	15.87	0.02	14.39	0.01	13.38	0.01	13.27	0.01
1074	187.0422	8.4440	20.20	0.05	19.14	0.02	18.43	0.03	18.43	0.08
1075	187.0513	10.2977	16.43	0.02	15.22	0.01	14.29	0.01	14.18	0.01
1076	187.0535	10.5261	18.30	0.02	17.16	0.01	16.36	0.01	16.31	0.02
1079	187.0501	10.3653	18.09	0.02	17.01	0.01	16.23	0.01	16.16	0.02
1081	187.0536	13.0152	20.15	0.03	19.07	0.02	18.29	0.02	18.36	0.03
1083	187.0508	11.9702	20.57	0.04	19.49	0.02	18.76	0.02	18.80	0.06
1086	187.0664	9.4362	14.55	0.02	13.23	0.01	12.19	0.01	11.95	0.01
1088	187.0653	14.1549	20.99	0.06	19.91	0.03	19.19	0.05	18.93	0.05
1089	187.0735	10.8683	19.67	0.03	18.41	0.02	17.68	0.02	17.54	0.02
1093	187.0781	11.7003	17.92	0.02	16.75	0.01	15.90	0.01	15.79	0.02
1095	187.0864	8.0117	19.58	0.03	18.80	0.02	18.18	0.02	17.99	0.03
1096	187.0900	11.2434	21.03	0.07	19.96	0.03	19.12	0.04	19.00	0.05
1098	187.0933	8.7281	19.50	0.05	18.47	0.02	17.87	0.02	18.31	0.06

VCC	RA (deg)	Dec (deg)	u	u_err	g	g_err	i	i_err	z	z_err
1100	187.0979	11.5795	18.89	0.02	17.93	0.01	17.16	0.02	16.99	0.02
1101	187.0987	13.1957	17.32	0.02	15.99	0.01	15.23	0.01	15.29	0.01
1103	187.1095	12.3459	21.62	0.09	20.62	0.04	19.88	0.05	19.89	0.13
1104	187.1169	12.8237	16.51	0.02	15.30	0.01	14.52	0.01	14.41	0.01
1105	187.1144	14.1554	18.04	0.02	16.93	0.01	16.32	0.02	16.31	0.02
1106	187.1311	10.5186	18.47	0.02	17.42	0.01	16.60	0.01	16.48	0.02
1107	187.1270	7.3248	17.02	0.02	15.81	0.01	14.94	0.01	14.83	0.01
1108	187.1241	8.5378	20.75	0.04	19.53	0.02	18.71	0.02	18.62	0.03
1109	187.1295	6.9044	18.94	0.03	18.03	0.02	17.40	0.02	17.13	0.02
1113	187.1419	7.5714	20.03	0.04	19.02	0.02	18.33	0.03	18.41	0.05
1115	187.1355	11.7447	18.86	0.02	17.85	0.01	17.03	0.02	16.83	0.02
1118	187.1690	9.2588	13.67	0.02	12.68	0.01	12.37	0.01	11.80	0.01
1119	187.1729	9.7318	18.04	0.02	16.86	0.01	16.05	0.01	16.08	0.02
1120	187.1730	7.8042	18.14	0.02	17.02	0.01	16.24	0.01	16.17	0.02
1122	187.1738	12.9159	15.92	0.02	14.73	0.01	13.92	0.01	13.79	0.01
1123	187.1778	12.5498	18.11	0.02	16.94	0.01	16.15	0.01	16.02	0.02
1124	187.1836	10.8655	18.74	0.02	17.67	0.01	16.91	0.02	16.95	0.02
1125	187.1805	11.7550	14.05	0.02	12.57	0.01	11.53	0.01	11.33	0.01
1126	187.1803	14.9995	14.24	0.02	13.06	0.01	11.98	0.01	11.77	0.01
1127	187.1855	9.0260	19.59	0.03	18.41	0.02	17.55	0.02	17.59	0.03
1128	187.1871	9.0543	18.02	0.02	16.94	0.01	16.22	0.01	16.35	0.02
1129	187.1872	12.8098	18.67	0.02	17.66	0.01	16.90	0.01	16.78	0.02
1131	187.1917	12.0222	18.99	0.03	17.97	0.02	17.31	0.02	17.41	0.03
1135	187.2066	10.9210	20.03	0.03	19.03	0.02	18.23	0.02	18.16	0.03
1136	187.2043	12.1328	19.37	0.03	18.31	0.02	17.48	0.02	17.48	0.03
1137	187.2070	14.1572	19.11	0.03	17.82	0.02	17.13	0.02	16.92	0.02
1140	187.2196	14.3943	19.90	0.03	18.83	0.02	18.12	0.02	18.14	0.03
1143	187.2315	12.7068	19.72	0.03	18.72	0.02	17.90	0.02	17.76	0.03
1144	187.2385	14.7453	20.81	0.07	19.81	0.03	19.30	0.05	19.87	0.14
1146	187.2399	13.2419	14.39	0.02	12.98	0.01	12.01	0.01	11.77	0.01
1147	187.2403	11.9557	21.11	0.06	20.05	0.03	19.25	0.03	19.11	0.07
1149	187.2463	12.9083	19.02	0.03	18.15	0.02	17.41	0.02	17.57	0.03
1151	187.2469	7.5265	18.11	0.02	16.91	0.01	15.97	0.01	15.93	0.02
1158	187.2625	13.1838	13.61	0.02	12.09	0.01	11.04	0.01	10.73	0.01
1160	187.2677	8.4560	19.30	0.03	18.25	0.02	17.50	0.02	17.35	0.03
1161	187.2727	12.0306	20.10	0.04	19.07	0.02	18.19	0.02	18.02	0.04
1162	187.2715	12.1537	21.02	0.06	19.99	0.03	19.06	0.03	18.76	0.06
1163	187.2769	14.0049	17.74	0.02	16.58	0.01	15.65	0.01	15.72	0.02
1164	187.2840	9.4439	17.76	0.02	16.66	0.01	15.85	0.01	15.87	0.02
1165	187.2930	9.2674	19.51	0.03	18.52	0.02	17.74	0.02	17.71	0.03
1167	187.3110	7.8775	17.66	0.02	15.63	0.01	14.75	0.01	14.33	0.01
1170	187.3043	10.9906	20.83	0.05	19.80	0.02	19.10	0.03	19.03	0.04

VCC	RA (deg)	Dec (deg)	u	u_err	g	g_err	i	i_err	z	z_err
1172	187.3137	8.8145	16.73	0.02	15.53	0.01	14.63	0.01	14.48	0.01
1173	187.3119	12.9782	17.19	0.02	15.97	0.01	15.15	0.01	15.04	0.01
1175	187.3258	10.1358	16.85	0.02	15.87	0.01	15.13	0.01	15.03	0.01
1177	187.3302	12.3770	19.11	0.03	18.03	0.02	17.06	0.02	16.84	0.02
1178	187.3387	8.1566	14.54	0.02	13.15	0.01	12.12	0.01	11.83	0.01
1179	187.3444	9.9890	16.16	0.02	15.44	0.01	14.88	0.01	14.77	0.01
1183	187.3438	11.4339	15.69	0.02	14.26	0.01	13.45	0.01	13.29	0.01
1184	187.3507	9.9509	20.08	0.04	19.15	0.02	18.39	0.02	18.22	0.03
1185	187.3480	12.4508	17.15	0.02	15.74	0.01	14.85	0.01	14.66	0.01
1186	187.3585	10.2488	19.14	0.03	17.96	0.02	17.14	0.02	17.04	0.02
1187	187.3653	8.9401	20.42	0.05	19.43	0.02	18.76	0.03	18.94	0.08
1191	187.3695	12.4962	18.65	0.02	17.54	0.01	16.78	0.01	16.65	0.02
1193	187.3774	7.6964	14.99	0.02	14.23	0.01	13.67	0.01	13.43	0.01
1194	187.3718	14.1694	19.89	0.03	18.75	0.02	17.90	0.02	17.80	0.03
1195	187.3830	7.8217	19.78	0.03	18.79	0.02	17.99	0.02	18.05	0.03
1196	187.3788	14.0491	15.11	0.02	13.71	0.01	12.73	0.01	12.54	0.01
1197	187.3897	9.6143	20.54	0.05	19.70	0.02	18.86	0.03	19.11	0.07
1200	187.3957	10.7931	15.90	0.02	15.13	0.01	14.74	0.01	14.69	0.01
1204	187.4080	7.1065	17.46	0.02	16.22	0.01	15.41	0.01	15.29	0.01
1207	187.4083	9.5209	18.38	0.02	17.33	0.01	16.51	0.01	16.43	0.02
1209	187.4192	10.3849	18.11	0.02	17.05	0.01	16.26	0.02	16.17	0.02
1210	187.4104	11.2990	18.49	0.02	17.31	0.01	16.36	0.01	16.40	0.02
1211	187.4150	9.4636	19.51	0.03	18.44	0.02	17.59	0.02	17.42	0.03
1212	187.4126	11.6333	18.61	0.02	17.51	0.01	16.70	0.02	16.82	0.03
1213	187.4135	12.5483	17.62	0.02	16.41	0.01	15.62	0.01	15.47	0.01
1216	187.4223	12.0465	19.52	0.03	18.28	0.02	17.59	0.02	17.47	0.03
1217	187.4330	11.4047	16.51	0.02	15.57	0.01	15.13	0.01	15.09	0.01
1219	187.4337	12.8055	19.27	0.02	18.25	0.02	17.56	0.02	17.38	0.02
1222	187.4357	15.0248	17.31	0.02	16.10	0.01	15.20	0.01	15.04	0.01
1223	187.4332	15.1193	18.04	0.02	16.76	0.01	16.00	0.01	15.87	0.02
1225	187.4472	6.9653	18.36	0.02	17.30	0.01	16.51	0.01	16.34	0.02
1227	187.4458	11.1700	19.00	0.02	17.77	0.02	17.05	0.02	16.86	0.02
1230	187.4562	7.2836	19.69	0.03	18.65	0.02	17.60	0.02	17.38	0.02
1235	187.4563	14.2196	18.97	0.02	17.72	0.01	16.83	0.02	16.76	0.02
1240	187.4780	7.1382	18.36	0.02	17.32	0.01	16.54	0.01	16.45	0.02
1241	187.4745	13.9571	20.26	0.04	19.30	0.02	18.55	0.03	18.59	0.04
1245	187.4934	10.7805	19.54	0.03	18.12	0.02	17.26	0.02	17.18	0.02
1246	187.4975	10.8563	19.02	0.03	17.87	0.02	17.07	0.02	17.10	0.02
1247	187.4928	13.2724	19.57	0.03	18.54	0.02	17.83	0.02	17.92	0.03
1251	187.5045	13.1177	21.50	0.06	20.41	0.03	19.70	0.04	19.66	0.05
1252	187.5083	9.4739	19.34	0.02	18.27	0.02	17.45	0.02	17.44	0.03
1254	187.5211	8.0733	16.77	0.02	15.29	0.01	14.32	0.01	14.16	0.01

VCC	RA (deg)	Dec (deg)	u	u_err	g	g_err	i	i_err	z	z_err
1256	187.5173	13.9135	20.51	0.03	19.51	0.02	18.85	0.03	18.69	0.03
1259	187.5255	12.3773	18.95	0.02	17.78	0.02	17.23	0.02	17.16	0.02
1264	187.5454	12.1955	17.97	0.02	16.93	0.01	16.17	0.01	16.02	0.02
1265	187.5482	13.6911	19.95	0.03	18.73	0.02	17.80	0.02	17.71	0.02
1271	187.5641	12.5158	20.34	0.04	19.18	0.02	18.42	0.03	18.38	0.04
1281	187.5783	7.9053	19.60	0.03	18.47	0.02	17.84	0.02	17.69	0.03
1285	187.5850	14.1402	19.63	0.03	18.16	0.02	17.24	0.02	17.00	0.02
1287	187.6025	13.9816	19.39	0.03	18.26	0.02	17.50	0.02	17.50	0.03
1291	187.6083	11.4372	19.86	0.03	18.59	0.02	17.87	0.02	17.76	0.02
1292	187.6130	8.1852	19.92	0.03	18.87	0.02	18.14	0.02	18.06	0.03
1297	187.6332	12.4902	15.31	0.02	13.97	0.01	12.89	0.01	12.53	0.01
1299	187.6534	7.9849	20.67	0.05	19.49	0.02	18.89	0.03	18.90	0.06
1300	187.6443	12.4582	19.78	0.03	18.85	0.02	18.12	0.02	17.95	0.02
1301	187.6593	13.6196	20.65	0.05	19.47	0.02	18.89	0.03	18.68	0.04
1306	187.6912	9.0117	20.45	0.05	19.48	0.03	18.63	0.04	18.59	0.05
1307	187.6859	13.7994	19.06	0.02	17.96	0.01	17.14	0.01	16.96	0.02
1308	187.6913	11.3432	16.59	0.02	15.36	0.01	14.45	0.01	14.39	0.01
1309	187.7002	10.1398	20.38	0.05	19.45	0.02	18.62	0.03	18.62	0.05
1311	187.6970	7.6054	17.55	0.02	16.28	0.01	15.42	0.01	15.32	0.01
1312	187.6963	11.5382	19.92	0.04	18.89	0.02	18.13	0.02	17.97	0.03
1313	187.7022	12.0450	17.26	0.02	16.74	0.01	16.94	0.01	16.84	0.02
1315	187.7045	13.5089	20.97	0.08	19.77	0.03	18.83	0.04	18.64	0.05
1319	187.7181	13.8584	20.60	0.03	19.76	0.02	19.04	0.03	18.97	0.04
1327	187.7405	12.2704	13.15	0.02	12.38	0.01	11.57	0.01	11.30	0.01
1328	187.7392	13.6200	19.99	0.05	18.75	0.02	17.74	0.02	17.55	0.03
1330	187.7488	8.0779	14.56	0.02	12.42	0.01	11.60	0.01	11.92	0.01
1331	187.7442	11.7079	18.81	0.02	17.65	0.01	16.79	0.01	16.65	0.02
1333	187.7547	7.7232	17.89	0.02	16.84	0.01	16.01	0.01	15.90	0.02
1335	187.7637	12.0780	20.86	0.05	19.84	0.02	19.17	0.03	19.09	0.04
1336	187.7665	11.8364	18.68	0.02	17.45	0.01	16.54	0.01	16.46	0.02
1345	187.8160	9.3589	20.41	0.04	19.31	0.02	18.61	0.03	18.34	0.04
1348	187.8155	12.3318	16.73	0.02	15.42	0.01	14.40	0.01	14.21	0.01
1349	187.8230	7.8611	19.78	0.03	18.68	0.02	17.91	0.02	17.78	0.02
1356	187.8456	11.4924	15.93	0.02	15.25	0.01	14.73	0.01	14.66	0.01
1357	187.8517	9.4744	20.20	0.04	18.92	0.02	18.12	0.02	18.30	0.04
1360	187.8579	8.3340	19.97	0.04	18.91	0.02	18.19	0.02	18.07	0.03
1361	187.8633	9.7333	18.82	0.03	17.63	0.02	16.87	0.02	16.90	0.03
1363	187.8646	10.9357	20.30	0.03	18.66	0.02	17.84	0.02	17.64	0.02
1365	187.8781	10.0054	19.84	0.04	18.80	0.02	18.06	0.02	17.83	0.03
1366	187.8820	11.6030	19.02	0.03	17.84	0.02	16.98	0.02	16.93	0.02
1367	187.8879	8.9678	19.40	0.03	18.48	0.02	17.77	0.02	17.70	0.04
1369	187.8890	12.0638	17.91	0.02	16.79	0.01	16.00	0.01	16.04	0.02

VCC	RA (deg)	Dec (deg)	u	u_err	g	g_err	i	i_err	z	z_err
1370	187.9039	11.0078	18.94	0.02	17.50	0.01	16.73	0.01	16.64	0.02
1371	187.8991	13.8242	19.38	0.03	18.42	0.02	17.33	0.02	17.17	0.02
1377	187.9125	10.8407	17.56	0.02	16.41	0.01	15.64	0.01	15.53	0.02
1387	187.9605	13.6807	19.85	0.03	18.72	0.02	17.82	0.02	17.78	0.02
1389	187.9667	12.4818	17.03	0.02	15.89	0.01	14.91	0.01	14.91	0.01
1392	187.9830	12.1740	16.52	0.02	15.17	0.01	14.28	0.01	14.13	0.01
1394	187.9805	7.8690	19.41	0.03	18.21	0.02	17.40	0.02	17.27	0.02
1396	187.9849	11.9727	18.61	0.02	17.23	0.01	16.25	0.01	16.30	0.02
1402	188.0011	11.0232	19.34	0.03	18.05	0.02	17.18	0.02	17.36	0.03
1404	188.0064	8.6697	19.01	0.02	17.86	0.01	17.08	0.02	17.07	0.02
1405	188.0002	11.3026	20.64	0.06	19.43	0.02	18.62	0.03	18.65	0.06
1406	188.0115	8.0750	19.90	0.03	18.87	0.02	18.10	0.02	18.09	0.03
1407	188.0114	11.8901	16.25	0.02	15.01	0.01	14.05	0.01	13.96	0.01
1408	188.0187	7.9440	19.22	0.03	18.10	0.02	17.31	0.02	17.16	0.02
1411	188.0237	11.8179	16.48	0.02	15.57	0.01	15.04	0.01	15.00	0.01
1413	188.0323	12.4341	18.93	0.02	17.81	0.01	17.09	0.01	17.07	0.02
1415	188.0368	8.0394	19.04	0.03	17.88	0.02	16.96	0.02	16.87	0.02
1420	188.0510	12.0616	17.50	0.02	16.32	0.01	15.37	0.01	15.33	0.01
1422	188.0592	10.2515	15.34	0.02	14.02	0.01	13.12	0.01	12.97	0.01
1425	188.0867	10.0574	20.31	0.04	19.22	0.02	18.52	0.02	18.45	0.04
1426	188.0979	11.8933	17.25	0.02	16.11	0.01	15.37	0.01	15.28	0.01
1431	188.0975	11.2630	15.67	0.02	14.31	0.01	13.29	0.01	13.09	0.01
1432	188.1232	10.0188	18.26	0.02	17.08	0.01	16.30	0.01	16.29	0.02
1436	188.1324	13.8504	19.28	0.02	18.23	0.02	17.38	0.02	17.27	0.02
1437	188.1396	9.1737	15.76	0.02	14.90	0.01	14.20	0.01	14.04	0.01
1439	188.1465	8.6364	20.56	0.04	19.39	0.02	18.67	0.02	18.75	0.04
1441	188.1493	8.0924	17.20	0.02	15.99	0.01	15.17	0.01	15.03	0.01
1444	188.1495	9.8863	17.17	0.02	15.86	0.01	15.13	0.01	15.09	0.01
1446	188.1625	10.0921	17.29	0.02	16.04	0.01	15.16	0.01	15.05	0.01
1454	188.1871	10.9495	19.73	0.03	18.59	0.02	17.86	0.02	17.67	0.03
1455	188.1949	7.7990	17.39	0.02	16.45	0.01	15.84	0.01	15.80	0.02
1461	188.2135	11.2959	20.34	0.06	19.29	0.03	18.47	0.03	18.39	0.07
1464	188.2245	11.1913	18.71	0.02	17.62	0.01	16.85	0.02	16.85	0.02
1470	188.2517	10.1284	20.79	0.04	19.73	0.02	19.11	0.03	19.06	0.05
1472	188.2714	9.9864	19.22	0.03	18.14	0.02	17.41	0.02	17.47	0.03
1481	188.2874	10.8362	18.94	0.02	17.86	0.01	17.08	0.02	16.90	0.02
1485	188.2968	9.1116	20.37	0.04	19.37	0.02	18.58	0.03	18.68	0.05
1487	188.3012	8.3775	20.72	0.05	19.68	0.02	18.85	0.03	18.65	0.04
1488	188.3060	9.3974	15.88	0.02	14.75	0.01	14.09	0.01	14.03	0.01
1489	188.3079	10.9285	16.99	0.02	15.87	0.01	15.08	0.01	14.91	0.01
1494	188.3205	12.2824	20.68	0.06	19.63	0.02	18.86	0.03	18.79	0.05
1496	188.3283	9.1205	19.02	0.02	17.92	0.01	17.18	0.02	17.24	0.02

VCC	RA (deg)	Dec (deg)	u	u_err	g	g_err	i	i_err	z	z_err
1498	188.3370	7.8545	17.36	0.02	16.40	0.01	15.72	0.01	15.53	0.01
1500	188.3434	11.6419	20.50	0.04	19.38	0.02	18.62	0.02	18.47	0.03
1506	188.3665	7.8548	20.15	0.03	19.52	0.02	19.03	0.03	19.27	0.05
1511	188.3884	13.4767	19.15	0.03	18.08	0.02	17.26	0.02	17.23	0.02
1512	188.3944	11.2619	16.87	0.02	15.71	0.01	14.89	0.01	14.71	0.01
1518	188.4198	12.3824	19.67	0.03	18.60	0.02	17.87	0.02	17.85	0.02
1519	188.4261	7.7831	18.65	0.02	17.49	0.01	16.58	0.01	16.31	0.02
1520	188.4260	10.7878	21.19	0.06	20.10	0.03	19.42	0.04	19.22	0.07
1522	188.4460	11.7817	19.83	0.04	18.69	0.02	17.76	0.02	17.59	0.03
1531	188.4835	10.5781	18.60	0.02	17.51	0.01	16.69	0.01	16.57	0.02
1538	188.5250	11.0540	20.39	0.04	19.33	0.02	18.58	0.03	18.58	0.05
1546	188.5461	13.5725	20.64	0.05	19.48	0.02	18.23	0.02	17.77	0.02
1549	188.5617	11.0715	16.15	0.02	14.04	0.01	13.36	0.01	13.58	0.01
1551	188.5641	11.4671	20.40	0.05	19.28	0.02	18.38	0.03	18.24	0.04
1558	188.5891	11.4159	20.40	0.04	19.35	0.02	18.65	0.02	18.39	0.03
1561	188.6042	12.9046	17.86	0.02	16.69	0.01	15.85	0.01	15.77	0.02
1563	188.6085	11.9170	17.65	0.02	16.46	0.01	15.68	0.01	15.56	0.01
1565	188.6268	11.7344	18.42	0.02	17.16	0.01	16.45	0.02	16.15	0.02
1569	188.6325	13.5037	16.55	0.02	15.69	0.01	15.15	0.01	15.10	0.01
1573	188.6357	10.5482	17.67	0.02	16.49	0.01	15.75	0.01	15.64	0.01
1578	188.6737	11.1428	20.61	0.04	19.65	0.02	18.83	0.02	18.67	0.03
1582	188.6772	14.2231	18.23	0.02	17.23	0.01	16.49	0.01	16.57	0.02
1586	188.6938	14.2922	20.40	0.03	19.35	0.02	18.28	0.02	18.02	0.02
1591	188.7380	10.0628	19.88	0.03	18.83	0.02	18.19	0.02	18.03	0.03
1594	188.7503	11.3440	19.57	0.02	18.51	0.02	17.73	0.02	17.58	0.02
1599	188.7780	11.9009	18.94	0.03	17.77	0.02	16.85	0.02	16.73	0.02
1601	188.7837	12.9658	19.15	0.03	17.85	0.02	16.89	0.01	16.76	0.02
1602	188.7840	13.4853	18.56	0.02	17.44	0.01	16.57	0.01	16.48	0.02
1603	188.7824	13.5644	18.50	0.02	17.35	0.01	16.58	0.01	16.41	0.02
1604	188.7934	13.9862	17.98	0.02	16.74	0.01	16.03	0.01	15.95	0.01
1606	188.8112	12.2374	18.36	0.02	17.26	0.01	16.40	0.01	16.35	0.02
1609	188.8346	11.6359	18.61	0.02	17.46	0.01	16.63	0.01	16.51	0.02
1612	188.8518	13.7660	19.26	0.02	18.24	0.02	17.50	0.02	17.36	0.02
1613	188.8621	12.5282	19.88	0.03	18.82	0.02	18.00	0.02	18.00	0.03
1614	188.8635	12.7503	15.49	0.02	14.33	0.01	13.53	0.01	13.35	0.01
1616	188.8668	14.2613	17.97	0.02	16.76	0.01	15.92	0.01	15.81	0.01
1619	188.8774	12.2208	13.56	0.02	12.20	0.01	11.17	0.01	10.90	0.01
1621	188.8915	11.7859	19.79	0.03	18.78	0.02	17.93	0.02	17.87	0.03
1625	188.8955	11.6200	19.96	0.04	18.73	0.02	17.73	0.02	17.70	0.02
1626	188.8958	11.9581	19.72	0.03	18.68	0.02	17.84	0.02	17.52	0.02
1627	188.9052	12.3820	16.51	0.02	15.09	0.01	14.04	0.01	13.78	0.01
1630	188.9081	12.2640	14.21	0.02	12.67	0.01	11.56	0.01	11.34	0.01

VCC	RA (deg)	Dec (deg)	u	u_err	g	g_err	i	i_err	z	z_err
1631	188.9105	12.3415	21.13	0.05	20.10	0.02	19.44	0.03	19.28	0.04
1634	188.9244	12.2068	21.07	0.06	20.05	0.03	19.37	0.04	19.02	0.05
1635	188.9201	12.2354	21.08	0.07	20.01	0.03	19.20	0.04	19.12	0.06
1637	188.9397	12.1814	19.03	0.02	18.05	0.02	17.27	0.02	17.29	0.02
1642	188.9714	11.6819	18.49	0.02	17.37	0.01	16.81	0.02	16.61	0.02
1644	188.9660	13.8592	17.97	0.02	17.21	0.01	16.79	0.01	16.77	0.02
1647	188.9860	10.9363	17.18	0.02	16.09	0.01	15.25	0.01	15.20	0.01
1650	189.0130	13.4859	18.61	0.02	17.66	0.01	17.05	0.02	16.94	0.02
1654	189.0440	9.9226	16.73	0.02	15.94	0.01	15.51	0.01	15.46	0.01
1658	189.0740	13.5756	18.02	0.02	16.92	0.01	16.07	0.01	15.96	0.02
1661	189.1033	10.3847	17.45	0.02	16.14	0.01	15.19	0.01	14.85	0.01
1662	189.1056	13.4912	20.72	0.05	19.68	0.02	18.87	0.03	18.89	0.05
1663	189.1132	11.8881	19.34	0.03	17.75	0.02	16.84	0.02	16.68	0.02
1669	189.1276	13.6383	17.47	0.02	16.27	0.01	15.38	0.01	15.29	0.01
1670	189.1258	13.9447	20.86	0.05	19.90	0.03	19.04	0.03	19.07	0.05
1672	189.1358	12.5183	20.27	0.04	19.19	0.02	18.36	0.02	18.38	0.03
1673	189.1363	11.2580	13.00	0.02	11.97	0.01	10.93	0.01	10.68	0.01
1674	189.1349	13.7484	17.51	0.02	16.22	0.01	15.26	0.01	15.18	0.01
1677	189.1449	13.5993	18.11	0.02	16.52	0.01	15.99	0.01	15.82	0.02
1680	189.1528	10.9912	20.68	0.04	19.62	0.02	18.89	0.03	18.87	0.04
1681	189.1559	11.1536	19.49	0.03	18.32	0.02	17.55	0.02	17.42	0.02
1682	189.1530	14.2259	18.49	0.02	17.32	0.01	16.37	0.01	16.18	0.01
1684	189.1642	11.1019	16.16	0.02	15.10	0.01	14.49	0.01	14.40	0.01
1689	189.2140	12.3688	18.48	0.02	17.44	0.01	16.23	0.01	16.09	0.01
1691	189.2130	12.9588	18.70	0.02	17.58	0.01	16.69	0.01	16.65	0.02
1693	189.2192	13.2834	20.24	0.04	19.01	0.02	18.25	0.02	18.19	0.03
1694	189.2188	13.7676	19.73	0.03	18.60	0.02	17.76	0.02	17.60	0.02
1700	189.2640	11.4788	20.41	0.04	19.43	0.02	18.52	0.02	18.60	0.04
1702	189.2790	13.9817	19.14	0.03	18.09	0.02	17.17	0.02	17.11	0.02
1704	189.2904	10.2723	17.48	0.02	16.27	0.01	15.55	0.01	15.47	0.01
1706	189.2971	12.4461	20.58	0.04	19.47	0.02	18.62	0.02	18.62	0.03
1707	189.3134	10.7206	19.91	0.03	19.12	0.02	18.65	0.03	18.49	0.04
1711	189.3423	12.2870	17.44	0.02	16.18	0.01	15.31	0.01	15.22	0.01
1714	189.3539	14.3126	18.53	0.02	17.50	0.01	16.82	0.02	16.74	0.02
1717	189.3706	12.3532	18.04	0.02	16.78	0.01	15.99	0.01	16.03	0.01
1728	189.4393	9.9851	17.31	0.02	16.46	0.01	15.93	0.01	15.95	0.02
1729	189.4422	10.9852	19.38	0.02	18.30	0.02	17.55	0.02	17.40	0.02
1731	189.4546	13.4400	20.22	0.03	19.06	0.02	18.18	0.02	18.09	0.03
1736	189.4799	11.1490	19.97	0.04	18.94	0.02	18.15	0.02	18.19	0.04
1740	189.5015	14.1788	18.65	0.02	17.52	0.02	16.67	0.02	16.62	0.02
1746	189.5493	12.0583	19.33	0.03	17.80	0.01	16.68	0.01	16.43	0.02
1747	189.5402	13.5808	18.92	0.02	17.65	0.01	16.80	0.01	16.82	0.02

VCC	RA (deg)	Dec (deg)	u	u_err	g	g_err	i	i_err	z	z_err
1749	189.5507	10.7018	19.57	0.03	18.66	0.02	17.95	0.02	17.75	0.03
1754	189.5714	11.1811	19.93	0.04	18.85	0.02	18.04	0.02	18.37	0.04
1767	189.6565	9.6751	17.69	0.02	16.61	0.01	15.79	0.01	15.70	0.01
1775	189.7210	12.9833	20.65	0.04	19.62	0.02	18.68	0.02	18.67	0.03
1778	189.7673	13.3635	15.21	0.02	14.12	0.01	13.60	0.01	13.51	0.01
1783	189.8061	12.1007	18.94	0.02	17.80	0.01	16.97	0.02	16.93	0.02
1785	189.8154	11.2698	19.08	0.03	17.93	0.02	17.15	0.02	17.06	0.02
1786	189.8180	12.9708	19.30	0.03	18.16	0.02	17.35	0.02	17.29	0.02
1787	189.8266	12.2558	20.25	0.05	19.10	0.02	18.34	0.03	18.25	0.03
1792	189.8583	12.9281	19.71	0.04	18.22	0.02	17.58	0.02	17.41	0.02
1796	189.8752	12.6809	17.65	0.02	16.50	0.01	15.85	0.01	15.70	0.02
1798	189.8803	11.4540	20.10	0.05	19.11	0.02	18.42	0.03	18.50	0.05
1803	189.9071	10.9758	17.60	0.02	16.43	0.01	15.61	0.01	15.46	0.01
1812	189.9814	11.8579	18.39	0.02	17.40	0.01	16.64	0.01	16.47	0.02
1815	189.9846	11.9046	18.59	0.02	17.60	0.01	17.00	0.02	17.01	0.02
1816	189.9937	13.7814	16.81	0.02	16.58	0.01	16.12	0.01	16.25	0.02
1818	190.0064	13.6540	19.76	0.04	18.47	0.02	17.65	0.02	17.59	0.03
1823	190.0371	12.7919	19.43	0.03	18.45	0.02	17.75	0.02	17.64	0.02
1828	190.0558	12.8748	16.62	0.02	15.34	0.01	14.46	0.01	14.27	0.01
1831	190.0763	10.9964	19.39	0.03	18.23	0.02	17.56	0.02	17.49	0.02
1841	190.1127	12.1992	20.25	0.04	19.17	0.02	18.18	0.02	17.80	0.02
1843	190.1147	10.8389	18.52	0.02	17.35	0.01	16.49	0.01	16.41	0.02
1861	190.2440	11.1845	15.76	0.02	14.42	0.01	13.51	0.01	13.32	0.01
1870	190.3138	11.2986	17.15	0.02	15.99	0.01	15.29	0.01	15.22	0.01
1871	190.3155	11.3873	15.47	0.02	14.05	0.01	13.02	0.01	12.78	0.01
1879	190.3641	11.1459	18.38	0.02	17.29	0.01	16.49	0.01	16.36	0.02
1880	190.3671	12.4278	19.34	0.02	18.28	0.02	17.48	0.02	17.34	0.02
1881	190.3726	10.7630	17.35	0.02	16.03	0.01	15.20	0.01	15.13	0.01
1882	190.3784	11.6821	21.16	0.08	19.76	0.03	19.16	0.05	19.04	0.06
1886	190.4142	12.2474	16.49	0.02	15.35	0.01	14.58	0.01	14.48	0.01
1888	190.4322	13.6691	20.95	0.06	20.01	0.02	19.26	0.03	19.18	0.05
1891	190.4539	11.1914	17.98	0.02	16.88	0.01	16.04	0.01	15.90	0.01
1904	190.5115	10.9537	19.75	0.03	18.70	0.02	17.88	0.02	17.72	0.03
1909	190.5308	11.8281	17.43	0.02	16.30	0.01	15.48	0.01	15.39	0.01
1910	190.5361	11.7543	15.78	0.02	13.68	0.01	13.08	0.01	13.00	0.01
1915	190.5565	12.5451	18.17	0.02	16.94	0.01	15.93	0.01	16.05	0.02
1921	190.6105	11.7403	16.98	0.02	15.65	0.01	14.73	0.01	14.52	0.01
1925	190.6426	11.8203	20.55	0.05	19.51	0.02	18.79	0.03	18.50	0.05
1928	190.6577	13.6056	18.60	0.02	17.34	0.01	16.53	0.01	16.49	0.02
1931	190.6698	13.2669	16.36	0.02	15.57	0.01	14.98	0.01	15.26	0.01
1938	190.6976	11.4425	13.38	0.02	11.95	0.01	10.98	0.01	10.68	0.01
1943	190.7183	13.2574	13.23	0.02	12.45	0.01	11.49	0.01	11.28	0.01

VCC	RA (deg)	Dec (deg)	u	u_err	g	g_err	i	i_err	z	z_err
1946	190.7247	12.5379	21.77	0.10	20.79	0.04	20.06	0.06	19.83	0.08
1948	190.7418	10.6818	16.64	0.02	15.53	0.01	14.77	0.01	14.66	0.01
1949	190.7407	12.2870	15.74	0.02	14.22	0.01	13.24	0.01	13.06	0.01
1951	190.7593	11.6981	18.31	0.02	16.98	0.01	16.06	0.01	15.87	0.02
1955	190.7819	12.0512	15.40	0.02	14.32	0.01	13.55	0.01	13.40	0.01
1958	190.7931	11.0370	17.88	0.02	16.71	0.01	15.92	0.01	15.82	0.01
1963	190.8252	11.4751	20.75	0.06	19.66	0.03	18.75	0.03	18.66	0.05
1968	190.8634	10.9560	20.56	0.05	19.50	0.02	18.78	0.03	18.70	0.04
1971	190.8788	11.0471	17.65	0.02	16.43	0.01	15.62	0.01	15.52	0.01
1975	190.8979	10.7559	19.13	0.02	18.08	0.02	17.28	0.02	17.08	0.02
1976	190.8989	13.2512	19.52	0.03	18.45	0.02	17.63	0.02	17.54	0.03
1982	190.9628	11.4670	16.92	0.02	15.76	0.01	14.96	0.01	14.79	0.01
1983	190.9721	10.7457	17.55	0.02	16.56	0.01	15.97	0.01	15.89	0.01
1985	190.9818	10.6118	20.01	0.03	18.90	0.02	18.17	0.02	18.26	0.03
1986	190.9908	11.8808	19.60	0.03	18.47	0.02	17.57	0.02	17.57	0.03
1989	191.0185	13.2508	18.97	0.02	17.90	0.02	17.06	0.02	16.99	0.02
1990	191.0284	12.6844	20.54	0.06	19.73	0.03	18.93	0.03	18.69	0.04
1991	191.0390	11.1766	17.11	0.02	15.79	0.01	14.90	0.01	14.77	0.01
1992	191.0394	12.1165	16.58	0.02	15.86	0.01	15.61	0.01	15.79	0.02
2000	191.1333	11.1905	13.38	0.02	12.04	0.01	11.01	0.01	10.68	0.01
2001	191.1405	11.7953	19.49	0.03	18.25	0.02	17.41	0.02	17.35	0.03
2002	191.1431	11.2037	19.97	0.04	18.83	0.02	18.08	0.02	17.91	0.03
2003	191.1727	11.5203	19.39	0.03	18.17	0.02	17.37	0.02	17.20	0.02
2006	191.1916	12.3514	14.99	0.02	13.97	0.01	13.26	0.01	13.17	0.01
2008	191.1978	12.0643	16.73	0.02	15.53	0.01	14.81	0.01	14.80	0.01
2010	191.2206	12.1826	19.63	0.03	18.64	0.02	17.88	0.02	17.81	0.02
2011	191.2676	12.3511	18.30	0.02	17.22	0.01	16.46	0.01	16.44	0.02
2012	191.2736	10.9009	16.37	0.02	15.05	0.01	14.18	0.01	14.04	0.01
2014	191.2904	10.6304	18.67	0.02	17.41	0.01	16.49	0.01	16.45	0.02
2019	191.3351	13.6927	16.00	0.02	14.71	0.01	13.80	0.01	13.64	0.01
2025	191.3974	11.5521	19.50	0.03	18.40	0.02	17.59	0.02	17.55	0.02
2028	191.4061	13.3282	17.33	0.02	16.33	0.01	15.72	0.01	15.61	0.01

TABLE 7.2 The VCC number, all colours and errors on colours.

VCC	$u - g$	$u - g$ error	$u - i$	$u - i$ error	$u - z$	$u - z$ error	$g - i$	$g - i$ error	$g - z$	$g - z$ error	$i - z$	$i - z$ error
299	1.10	0.03	1.86	0.03	2.03	0.03	0.76	0.02	0.93	0.02	0.17	0.02
306	0.97	0.04	1.65	0.04	1.69	0.04	0.67	0.03	0.71	0.03	0.04	0.03
309	0.76	0.02	1.23	0.02	1.22	0.02	0.48	0.02	0.46	0.02	-0.02	0.02
310	1.06	0.04	1.84	0.04	1.79	0.04	0.77	0.03	0.72	0.03	-0.05	0.04
319	1.10	0.02	1.55	0.02	1.77	0.03	0.45	0.02	0.67	0.02	0.22	0.02
322	1.04	0.02	1.63	0.02	1.72	0.02	0.60	0.02	0.69	0.02	0.09	0.02
328	0.64	0.02	1.07	0.02	1.17	0.02	0.43	0.02	0.53	0.02	0.10	0.02
330	1.08	0.02	1.96	0.02	2.04	0.02	0.88	0.02	0.96	0.02	0.08	0.02
333	0.93	0.03	1.54	0.04	1.73	0.04	0.61	0.03	0.80	0.03	0.18	0.04
334	0.76	0.02	1.30	0.02	1.42	0.02	0.54	0.02	0.66	0.02	0.12	0.02
350	0.73	0.02	1.18	0.03	1.19	0.03	0.45	0.02	0.45	0.02	0.00	0.03
353	1.05	0.03	1.94	0.03	2.03	0.03	0.89	0.02	0.98	0.03	0.09	0.03
354	1.08	0.02	1.88	0.02	2.02	0.02	0.81	0.02	0.94	0.02	0.14	0.02
355	1.38	0.02	2.44	0.02	2.74	0.02	1.06	0.02	1.36	0.02	0.30	0.02
361	1.10	0.02	1.93	0.02	2.05	0.02	0.82	0.02	0.94	0.02	0.12	0.02
364	1.33	0.03	2.74	0.03	3.32	0.03	1.40	0.02	1.99	0.02	0.58	0.02
369	2.35	0.02	3.47	0.02	3.75	0.02	1.12	0.02	1.40	0.02	0.28	0.02
372	1.43	0.04	2.43	0.04	2.55	0.04	0.99	0.02	1.11	0.03	0.12	0.03
389	1.34	0.02	2.21	0.02	2.38	0.02	0.87	0.02	1.04	0.02	0.16	0.02
391	1.03	0.05	1.87	0.04	2.17	0.04	0.83	0.05	1.14	0.05	0.30	0.04
394	1.11	0.03	1.91	0.03	2.04	0.03	0.80	0.02	0.93	0.02	0.13	0.02
401	0.86	0.03	1.37	0.03	1.45	0.03	0.51	0.02	0.59	0.02	0.07	0.03
407	1.29	0.02	2.17	0.02	2.31	0.02	0.88	0.02	1.02	0.02	0.14	0.02
410	0.50	0.02	0.85	0.02	0.96	0.02	0.36	0.02	0.46	0.02	0.11	0.02
414	1.20	0.03	1.99	0.03	2.03	0.03	0.79	0.02	0.83	0.02	0.04	0.02
418	1.13	0.03	1.90	0.03	2.07	0.03	0.77	0.02	0.94	0.02	0.17	0.02
421	1.26	0.03	2.03	0.03	2.09	0.03	0.77	0.02	0.83	0.02	0.06	0.02
425	1.03	0.03	1.77	0.04	1.77	0.04	0.74	0.03	0.74	0.03	0.00	0.03
426	1.04	0.03	1.94	0.03	2.07	0.04	0.91	0.02	1.03	0.03	0.12	0.03
428	0.38	0.02	0.40	0.02	0.52	0.03	0.02	0.02	0.14	0.02	0.12	0.02
431	1.02	0.03	1.86	0.03	1.99	0.04	0.83	0.02	0.97	0.03	0.13	0.03
444	1.18	0.03	1.95	0.03	1.84	0.03	0.77	0.02	0.65	0.02	-0.11	0.02
447	0.90	0.06	1.57	0.07	1.50	0.08	0.66	0.05	0.60	0.07	-0.07	0.07
452	1.25	0.02	2.05	0.02	2.18	0.02	0.80	0.02	0.93	0.02	0.13	0.02
455	1.21	0.03	1.96	0.03	2.05	0.03	0.75	0.02	0.85	0.02	0.10	0.02
456	0.98	0.03	1.78	0.04	1.89	0.04	0.80	0.03	0.90	0.03	0.11	0.03
458	1.13	0.02	2.01	0.02	2.07	0.02	0.88	0.02	0.94	0.02	0.06	0.02
461	1.21	0.02	2.13	0.02	2.23	0.02	0.92	0.02	1.02	0.02	0.10	0.02
471	0.73	0.03	1.28	0.03	1.45	0.04	0.55	0.03	0.72	0.03	0.17	0.03
477	0.84	0.03	1.44	0.03	1.34	0.03	0.60	0.02	0.50	0.03	-0.10	0.03

VCC	$u - g$	$u - g$ error	$u - i$	$u - i$ error	$u - z$	$u - z$ error	$g - i$	$g - i$ error	$g - z$	$g - z$ error	$i - z$	$i - z$ error
493	0.98	0.02	1.77	0.02	1.96	0.03	0.78	0.02	0.97	0.02	0.19	0.02
494	1.35	0.03	2.18	0.02	2.25	0.03	0.83	0.02	0.90	0.02	0.07	0.02
496	0.93	0.04	1.75	0.04	1.80	0.04	0.82	0.03	0.87	0.03	0.05	0.04
498	1.07	0.04	1.87	0.04	2.01	0.04	0.80	0.03	0.93	0.03	0.13	0.03
501	1.09	0.02	1.95	0.02	2.08	0.03	0.86	0.02	0.99	0.02	0.13	0.02
502	1.08	0.05	2.03	0.05	2.23	0.05	0.95	0.03	1.15	0.03	0.20	0.04
503	1.06	0.03	2.02	0.03	1.87	0.03	0.96	0.02	0.81	0.02	-0.14	0.02
504	1.04	0.02	1.72	0.02	1.88	0.02	0.67	0.02	0.83	0.02	0.16	0.02
511	1.08	0.04	1.82	0.05	1.86	0.05	0.74	0.03	0.77	0.04	0.04	0.04
512	0.90	0.02	1.39	0.02	1.50	0.02	0.49	0.02	0.61	0.02	0.12	0.02
519	0.98	0.04	1.69	0.05	1.76	0.06	0.71	0.03	0.78	0.04	0.07	0.05
529	1.06	0.03	1.99	0.03	2.13	0.03	0.92	0.02	1.07	0.03	0.14	0.03
532	1.12	0.04	1.86	0.04	1.96	0.04	0.73	0.03	0.84	0.03	0.10	0.03
537	1.15	0.05	2.07	0.05	2.19	0.05	0.91	0.03	1.04	0.03	0.12	0.04
539	1.31	0.02	2.10	0.02	2.05	0.03	0.79	0.02	0.74	0.02	-0.05	0.02
540	1.32	0.06	2.17	0.06	2.36	0.06	0.85	0.03	1.03	0.04	0.18	0.04
544	0.80	0.02	1.39	0.02	1.44	0.02	0.59	0.02	0.64	0.02	0.05	0.02
547	1.07	0.04	1.79	0.04	1.78	0.05	0.71	0.03	0.71	0.04	-0.01	0.04
556	1.13	0.05	2.06	0.05	2.12	0.05	0.93	0.04	1.00	0.04	0.06	0.05
560	1.12	0.03	2.05	0.03	2.32	0.05	0.93	0.02	1.20	0.04	0.28	0.04
561	1.06	0.03	1.84	0.03	1.81	0.03	0.77	0.02	0.75	0.02	-0.03	0.02
562	0.48	0.02	0.94	0.02	1.11	0.02	0.46	0.02	0.63	0.02	0.17	0.02
564	0.97	0.07	1.72	0.07	1.76	0.09	0.76	0.05	0.80	0.08	0.04	0.08
574	1.12	0.03	1.83	0.03	1.87	0.03	0.71	0.02	0.75	0.03	0.04	0.03
575	1.37	0.02	2.37	0.02	2.58	0.02	1.00	0.02	1.22	0.02	0.21	0.02
582	1.07	0.07	1.85	0.08	1.96	0.10	0.78	0.04	0.89	0.07	0.10	0.08
584	1.09	0.03	1.87	0.03	1.92	0.03	0.77	0.02	0.83	0.02	0.06	0.02
585	1.03	0.03	1.61	0.03	1.70	0.03	0.59	0.02	0.67	0.02	0.09	0.03
592	1.18	0.02	2.08	0.02	2.25	0.02	0.91	0.02	1.08	0.02	0.17	0.02
594	1.16	0.03	1.97	0.02	1.86	0.03	0.80	0.02	0.70	0.02	-0.11	0.02
603	1.12	0.04	1.95	0.04	2.07	0.05	0.83	0.03	0.95	0.03	0.12	0.04
605	1.12	0.05	2.00	0.05	2.13	0.05	0.87	0.03	1.01	0.04	0.14	0.04
607	1.08	0.05	2.19	0.05	2.45	0.05	1.11	0.03	1.37	0.03	0.26	0.04
611	1.21	0.02	1.93	0.02	2.07	0.02	0.72	0.02	0.87	0.02	0.15	0.02
615	1.32	0.05	2.08	0.05	2.35	0.05	0.76	0.03	1.03	0.03	0.27	0.04
622	1.01	0.03	1.74	0.03	1.77	0.03	0.73	0.02	0.75	0.03	0.02	0.03
624	0.96	0.03	1.79	0.04	1.83	0.04	0.84	0.03	0.87	0.03	0.04	0.03
625	1.12	0.03	1.96	0.03	2.07	0.03	0.84	0.02	0.95	0.02	0.11	0.02
628	0.98	0.05	1.89	0.05	2.25	0.05	0.91	0.03	1.27	0.04	0.36	0.04
632	0.89	0.03	1.57	0.03	1.65	0.03	0.69	0.02	0.76	0.02	0.07	0.02
640	1.03	0.05	1.81	0.05	1.89	0.06	0.78	0.03	0.86	0.05	0.08	0.05

VCC	$u - g$	$u - g$ error	$u - i$	$u - i$ error	$u - z$	$u - z$ error	$g - i$	$g - i$ error	$g - z$	$g - z$ error	$i - z$	$i - z$ error
643	1.18	0.03	1.93	0.04	2.15	0.04	0.75	0.02	0.97	0.03	0.22	0.03
645	1.04	0.03	1.83	0.03	2.00	0.03	0.79	0.02	0.96	0.02	0.17	0.03
651	0.82	0.03	1.30	0.03	1.51	0.03	0.48	0.02	0.69	0.03	0.21	0.03
658	1.09	0.04	2.00	0.04	2.10	0.04	0.92	0.03	1.01	0.03	0.09	0.03
659	1.03	0.03	1.88	0.03	2.03	0.03	0.85	0.02	1.00	0.02	0.15	0.02
660	1.29	0.02	2.35	0.02	2.59	0.02	1.06	0.02	1.29	0.02	0.23	0.02
668	1.28	0.03	2.14	0.03	2.23	0.03	0.86	0.02	0.96	0.02	0.09	0.02
673	1.02	0.05	1.82	0.05	2.04	0.06	0.81	0.04	1.03	0.04	0.22	0.05
674	1.35	0.03	2.23	0.03	2.32	0.03	0.88	0.02	0.97	0.02	0.09	0.02
678	1.05	0.04	2.09	0.04	2.25	0.04	1.05	0.03	1.20	0.03	0.15	0.03
684	1.23	0.02	2.18	0.02	2.37	0.02	0.95	0.02	1.13	0.02	0.18	0.02
686	0.98	0.04	1.56	0.04	1.55	0.06	0.57	0.03	0.57	0.05	-0.01	0.05
687	1.21	0.03	1.98	0.03	1.97	0.03	0.77	0.02	0.76	0.02	-0.01	0.03
688	1.10	0.02	1.90	0.02	2.05	0.02	0.80	0.02	0.95	0.02	0.15	0.02
691	0.95	0.06	1.55	0.07	1.77	0.07	0.60	0.05	0.82	0.05	0.22	0.06
692	1.17	0.02	1.69	0.02	1.44	0.02	0.52	0.02	0.28	0.02	-0.25	0.02
698	1.42	0.02	2.41	0.02	2.67	0.02	0.99	0.02	1.25	0.02	0.26	0.02
701	0.90	0.05	1.62	0.06	1.62	0.07	0.72	0.04	0.72	0.06	0.01	0.06
702	1.02	0.04	1.81	0.05	1.99	0.05	0.80	0.03	0.97	0.04	0.17	0.04
703	1.39	0.02	2.32	0.02	2.50	0.02	0.93	0.02	1.11	0.02	0.18	0.02
704	1.01	0.03	1.72	0.04	1.91	0.04	0.71	0.03	0.90	0.03	0.19	0.03
705	1.04	0.03	1.82	0.03	2.01	0.03	0.78	0.02	0.97	0.02	0.18	0.02
706	1.07	0.03	1.83	0.03	1.96	0.03	0.76	0.02	0.89	0.02	0.13	0.02
708	1.11	0.04	1.97	0.04	2.12	0.04	0.86	0.03	1.02	0.03	0.15	0.03
709	1.00	0.04	1.74	0.04	1.96	0.04	0.74	0.03	0.96	0.03	0.22	0.03
711	1.13	0.02	2.00	0.02	1.88	0.03	0.87	0.02	0.75	0.02	-0.12	0.02
719	1.08	0.03	1.90	0.04	2.04	0.04	0.82	0.03	0.97	0.03	0.14	0.03
725	1.57	0.02	2.10	0.02	2.11	0.02	0.52	0.02	0.54	0.02	0.01	0.02
731	1.60	0.02	2.68	0.02	2.95	0.02	1.07	0.02	1.34	0.02	0.27	0.02
732	1.01	0.03	1.62	0.04	1.69	0.04	0.61	0.03	0.69	0.03	0.07	0.04
733	1.06	0.03	1.88	0.03	1.98	0.03	0.82	0.02	0.92	0.02	0.10	0.02
743	1.05	0.07	1.81	0.07	1.88	0.08	0.76	0.05	0.83	0.06	0.07	0.07
745	1.36	0.02	2.28	0.02	2.48	0.02	0.92	0.02	1.12	0.02	0.19	0.02
746	1.21	0.04	2.01	0.04	2.06	0.04	0.80	0.02	0.85	0.03	0.05	0.03
747	1.23	0.03	2.00	0.03	1.86	0.03	0.77	0.02	0.63	0.02	-0.14	0.02
748	1.33	0.03	2.22	0.03	2.34	0.03	0.89	0.02	1.01	0.02	0.12	0.02
752	1.13	0.05	1.76	0.06	1.85	0.06	0.64	0.04	0.73	0.05	0.09	0.06
753	1.23	0.02	2.04	0.02	2.16	0.02	0.81	0.02	0.93	0.02	0.12	0.02
754	1.09	0.04	1.87	0.04	1.76	0.04	0.78	0.03	0.68	0.03	-0.11	0.04
755	1.38	0.03	2.35	0.02	2.49	0.03	0.97	0.02	1.11	0.02	0.13	0.02
756	1.05	0.02	1.63	0.02	1.77	0.03	0.58	0.02	0.73	0.02	0.14	0.02

VCC	$u - g$	$u - g$ error	$u - i$	$u - i$ error	$u - z$	$u - z$ error	$g - i$	$g - i$ error	$g - z$	$g - z$ error	$i - z$	$i - z$ error
757	1.11	0.03	1.95	0.03	2.02	0.03	0.84	0.02	0.91	0.02	0.07	0.02
758	1.56	0.02	2.70	0.02	2.98	0.02	1.14	0.02	1.42	0.02	0.28	0.02
760	1.13	0.03	1.95	0.03	2.06	0.03	0.82	0.02	0.93	0.02	0.11	0.02
762	1.38	0.02	2.31	0.02	2.38	0.02	0.93	0.02	1.00	0.02	0.08	0.02
765	0.81	0.02	1.60	0.02	1.85	0.02	0.79	0.02	1.04	0.02	0.24	0.02
774	0.99	0.04	1.66	0.04	1.90	0.04	0.68	0.03	0.91	0.03	0.24	0.04
775	1.07	0.03	1.72	0.04	1.91	0.04	0.66	0.03	0.84	0.03	0.19	0.03
778	1.35	0.02	2.39	0.02	2.68	0.02	1.04	0.02	1.33	0.02	0.29	0.02
779	1.20	0.03	2.08	0.03	2.17	0.03	0.88	0.02	0.97	0.02	0.09	0.02
780	1.08	0.03	1.91	0.03	2.02	0.03	0.83	0.02	0.94	0.02	0.11	0.03
781	1.15	0.02	1.94	0.02	2.07	0.02	0.80	0.02	0.93	0.02	0.13	0.02
788	1.20	0.02	2.09	0.02	2.22	0.02	0.89	0.02	1.02	0.02	0.13	0.02
789	1.24	0.03	2.13	0.03	1.82	0.04	0.89	0.02	0.58	0.03	-0.31	0.03
790	1.22	0.02	2.06	0.02	2.29	0.02	0.84	0.02	1.07	0.02	0.22	0.02
792	1.22	0.02	2.19	0.02	2.44	0.02	0.97	0.02	1.22	0.02	0.26	0.02
793	0.80	0.02	1.38	0.02	1.41	0.02	0.58	0.02	0.61	0.02	0.03	0.02
796	1.04	0.06	1.75	0.08	1.96	0.07	0.71	0.06	0.92	0.06	0.21	0.07
800	1.12	0.03	1.96	0.04	2.13	0.04	0.84	0.03	1.01	0.03	0.17	0.03
802	0.73	0.02	1.38	0.02	1.43	0.02	0.65	0.02	0.69	0.02	0.05	0.02
803	1.00	0.03	1.89	0.04	1.57	0.04	0.89	0.03	0.57	0.04	-0.32	0.04
804	1.01	0.06	1.84	0.07	1.54	0.08	0.83	0.05	0.54	0.07	-0.30	0.08
807	1.05	0.04	1.77	0.04	1.75	0.05	0.72	0.03	0.70	0.04	-0.02	0.04
808	1.19	0.02	1.87	0.02	2.18	0.03	0.68	0.02	0.99	0.02	0.31	0.02
809	0.97	0.02	1.77	0.02	1.93	0.02	0.79	0.02	0.96	0.02	0.16	0.02
810	1.24	0.02	2.13	0.02	2.29	0.02	0.89	0.02	1.05	0.02	0.16	0.02
811	0.97	0.05	1.69	0.05	1.87	0.05	0.71	0.04	0.90	0.04	0.18	0.05
812	1.23	0.02	2.14	0.02	2.25	0.02	0.91	0.02	1.01	0.02	0.10	0.02
815	1.06	0.02	1.88	0.02	1.99	0.02	0.82	0.02	0.93	0.02	0.11	0.02
821	1.06	0.07	1.86	0.07	2.15	0.08	0.80	0.04	1.10	0.05	0.29	0.06
823	1.44	0.02	2.09	0.02	2.24	0.02	0.64	0.02	0.80	0.02	0.15	0.02
824	1.04	0.03	1.85	0.03	2.07	0.03	0.82	0.02	1.03	0.02	0.22	0.02
828	1.49	0.02	2.54	0.02	2.76	0.02	1.05	0.02	1.27	0.02	0.21	0.02
833	1.30	0.02	2.27	0.02	2.48	0.02	0.97	0.02	1.17	0.02	0.20	0.02
838	1.05	0.03	1.86	0.03	2.00	0.03	0.81	0.02	0.95	0.02	0.14	0.02
839	0.98	0.03	1.65	0.03	1.85	0.03	0.66	0.02	0.87	0.03	0.21	0.03
840	1.13	0.03	1.98	0.03	2.02	0.03	0.85	0.02	0.89	0.02	0.04	0.03
843	0.96	0.03	1.73	0.03	1.92	0.03	0.77	0.03	0.97	0.03	0.20	0.03
845	1.12	0.03	1.85	0.03	2.18	0.03	0.72	0.02	1.06	0.03	0.33	0.03
846	1.32	0.02	2.20	0.02	2.30	0.02	0.89	0.02	0.98	0.02	0.10	0.02
849	0.74	0.02	1.28	0.02	1.39	0.02	0.54	0.02	0.65	0.02	0.11	0.02
850	1.28	0.07	2.06	0.08	1.93	0.08	0.77	0.05	0.65	0.06	-0.13	0.07

VCC	$u - g$	$u - g$ error	$u - i$	$u - i$ error	$u - z$	$u - z$ error	$g - i$	$g - i$ error	$g - z$	$g - z$ error	$i - z$	$i - z$ error
851	1.09	0.02	1.94	0.02	2.06	0.02	0.85	0.02	0.97	0.02	0.12	0.02
853	1.03	0.07	1.68	0.08	1.86	0.09	0.65	0.06	0.83	0.07	0.18	0.08
854	1.10	0.02	1.68	0.02	1.81	0.02	0.58	0.02	0.71	0.02	0.13	0.02
855	1.12	0.03	1.90	0.03	2.03	0.03	0.78	0.02	0.91	0.02	0.12	0.02
856	1.26	0.02	2.16	0.02	2.35	0.02	0.90	0.02	1.10	0.02	0.19	0.02
861	0.99	0.03	1.76	0.03	1.92	0.03	0.76	0.02	0.93	0.02	0.17	0.02
863	1.16	0.03	1.97	0.03	2.09	0.03	0.81	0.02	0.93	0.03	0.12	0.03
867	1.05	0.04	1.83	0.04	1.85	0.05	0.77	0.03	0.80	0.04	0.03	0.04
868	0.95	0.05	1.61	0.06	1.59	0.07	0.66	0.04	0.64	0.06	-0.01	0.07
869	1.11	0.02	1.86	0.02	1.87	0.03	0.75	0.02	0.76	0.02	0.01	0.02
870	1.15	0.02	1.83	0.02	1.98	0.02	0.69	0.02	0.83	0.02	0.14	0.02
871	1.20	0.02	2.06	0.02	2.19	0.02	0.86	0.02	0.98	0.02	0.13	0.02
872	1.25	0.02	2.18	0.02	2.35	0.02	0.93	0.02	1.10	0.02	0.17	0.02
876	1.07	0.03	1.86	0.03	2.06	0.03	0.78	0.03	0.99	0.03	0.20	0.03
877	1.08	0.03	1.89	0.03	2.12	0.03	0.80	0.02	1.04	0.02	0.23	0.02
883	1.16	0.04	1.95	0.04	2.02	0.04	0.79	0.03	0.85	0.03	0.07	0.03
884	1.14	0.04	2.01	0.05	2.10	0.05	0.87	0.03	0.96	0.04	0.09	0.04
886	0.98	0.06	1.67	0.11	1.86	0.08	0.68	0.11	0.87	0.07	0.19	0.12
891	1.03	0.07	1.83	0.07	2.09	0.08	0.80	0.04	1.06	0.06	0.26	0.06
892	1.06	0.03	1.90	0.03	1.93	0.03	0.84	0.02	0.87	0.03	0.03	0.03
893	1.09	0.06	1.84	0.06	2.05	0.07	0.75	0.04	0.96	0.05	0.21	0.05
894	1.14	0.07	1.70	0.07	2.03	0.08	0.56	0.05	0.89	0.06	0.33	0.06
895	1.10	0.03	1.60	0.03	1.84	0.04	0.51	0.03	0.74	0.03	0.24	0.03
896	1.11	0.03	1.91	0.03	1.98	0.03	0.80	0.02	0.87	0.02	0.07	0.02
897	1.04	0.04	1.78	0.05	1.97	0.05	0.74	0.04	0.93	0.04	0.18	0.04
900	1.05	0.03	1.83	0.03	1.89	0.04	0.78	0.03	0.85	0.03	0.07	0.03
902	1.13	0.04	1.95	0.04	2.02	0.04	0.83	0.03	0.89	0.03	0.07	0.04
903	0.94	0.03	1.67	0.03	1.69	0.04	0.74	0.03	0.75	0.03	0.02	0.03
906	1.11	0.04	2.02	0.04	2.20	0.05	0.91	0.03	1.09	0.03	0.18	0.04
914	1.08	0.04	1.81	0.04	1.81	0.05	0.74	0.03	0.74	0.04	0.00	0.05
915	0.96	0.03	1.84	0.03	2.02	0.04	0.89	0.03	1.07	0.03	0.18	0.03
916	1.51	0.02	2.59	0.02	2.83	0.02	1.07	0.02	1.32	0.02	0.25	0.02
917	1.14	0.02	1.96	0.02	2.12	0.02	0.82	0.02	0.98	0.02	0.16	0.02
922	0.93	0.05	1.65	0.06	1.61	0.08	0.73	0.04	0.68	0.06	-0.05	0.07
923	1.16	0.04	1.73	0.04	1.90	0.04	0.57	0.03	0.75	0.03	0.18	0.04
925	0.93	0.04	1.77	0.04	1.99	0.05	0.84	0.03	1.06	0.04	0.22	0.04
926	1.00	0.02	1.77	0.02	1.87	0.03	0.76	0.02	0.87	0.02	0.10	0.02
927	1.08	0.06	2.15	0.06	2.41	0.06	1.07	0.04	1.34	0.04	0.26	0.04
928	1.19	0.02	2.04	0.02	2.14	0.02	0.85	0.02	0.95	0.02	0.10	0.02
929	1.39	0.02	2.32	0.02	2.53	0.02	0.93	0.02	1.14	0.02	0.20	0.02
931	0.94	0.02	1.62	0.02	1.78	0.02	0.68	0.02	0.83	0.02	0.16	0.02

VCC	$u - g$	$u - g$ error	$u - i$	$u - i$ error	$u - z$	$u - z$ error	$g - i$	$g - i$ error	$g - z$	$g - z$ error	$i - z$	$i - z$ error
932	1.01	0.03	1.80	0.03	1.90	0.03	0.78	0.02	0.89	0.03	0.11	0.03
933	1.19	0.02	2.03	0.02	2.04	0.03	0.85	0.02	0.85	0.02	0.01	0.02
935	1.00	0.04	1.91	0.05	2.18	0.05	0.91	0.03	1.17	0.03	0.26	0.04
936	1.11	0.02	1.99	0.02	2.20	0.02	0.88	0.02	1.09	0.02	0.21	0.02
937	0.94	0.04	1.67	0.04	1.78	0.05	0.72	0.03	0.84	0.04	0.11	0.05
940	1.30	0.02	2.28	0.02	2.33	0.02	0.97	0.02	1.03	0.02	0.06	0.02
941	1.00	0.03	1.79	0.03	1.88	0.03	0.79	0.02	0.88	0.02	0.09	0.02
942	0.85	0.04	1.60	0.04	1.68	0.06	0.75	0.03	0.83	0.05	0.08	0.05
943	0.82	0.03	1.49	0.03	1.65	0.04	0.67	0.03	0.83	0.03	0.16	0.03
945	0.57	0.02	0.71	0.02	0.70	0.02	0.15	0.02	0.13	0.02	-0.02	0.02
948	0.97	0.05	1.68	0.05	1.61	0.07	0.71	0.04	0.64	0.06	-0.08	0.06
949	1.31	0.02	2.22	0.02	2.44	0.02	0.91	0.02	1.12	0.02	0.21	0.02
951	1.31	0.02	1.98	0.02	2.05	0.02	0.67	0.02	0.74	0.02	0.07	0.02
956	1.03	0.03	1.79	0.04	1.93	0.04	0.76	0.03	0.89	0.03	0.14	0.03
959	1.01	0.08	1.86	0.09	1.92	0.12	0.86	0.05	0.91	0.09	0.06	0.09
960	1.07	0.06	1.97	0.06	2.19	0.06	0.89	0.04	1.12	0.04	0.22	0.05
963	0.79	0.02	1.25	0.02	1.40	0.02	0.46	0.02	0.61	0.02	0.15	0.02
964	1.15	0.03	2.00	0.03	2.17	0.03	0.85	0.02	1.02	0.02	0.17	0.02
965	1.21	0.02	2.18	0.02	2.19	0.02	0.98	0.02	0.98	0.02	0.00	0.02
968	0.97	0.04	1.65	0.04	1.70	0.05	0.68	0.04	0.73	0.05	0.05	0.05
970	1.04	0.06	1.84	0.06	2.22	0.07	0.81	0.04	1.19	0.05	0.38	0.05
972	1.24	0.02	2.06	0.02	2.14	0.03	0.82	0.02	0.90	0.02	0.08	0.02
974	1.14	0.02	2.04	0.02	2.14	0.02	0.90	0.02	0.99	0.02	0.10	0.02
976	1.02	0.03	1.73	0.03	1.79	0.03	0.71	0.02	0.77	0.03	0.07	0.03
978	0.97	0.03	1.80	0.03	1.72	0.04	0.84	0.02	0.76	0.03	-0.08	0.03
983	1.17	0.05	2.28	0.06	2.33	0.07	1.10	0.03	1.16	0.05	0.06	0.05
984	1.49	0.02	2.51	0.02	2.72	0.02	1.02	0.02	1.23	0.02	0.22	0.02
986	0.89	0.05	1.69	0.05	1.94	0.05	0.79	0.04	1.05	0.04	0.25	0.05
988	0.99	0.08	1.87	0.08	1.89	0.11	0.89	0.05	0.90	0.09	0.01	0.09
991	1.55	0.02	2.46	0.02	2.72	0.02	0.91	0.02	1.16	0.02	0.26	0.02
992	1.18	0.02	2.04	0.02	2.21	0.02	0.86	0.02	1.03	0.02	0.17	0.02
996	1.13	0.03	1.91	0.03	1.96	0.03	0.78	0.02	0.83	0.02	0.05	0.02
997	0.97	0.03	1.86	0.03	1.92	0.03	0.90	0.02	0.95	0.02	0.05	0.02
998	1.03	0.03	1.85	0.03	1.91	0.04	0.82	0.02	0.88	0.03	0.05	0.03
1000	1.15	0.03	2.02	0.03	2.18	0.04	0.86	0.02	1.03	0.03	0.16	0.03
1001	0.73	0.02	1.29	0.02	1.43	0.02	0.56	0.02	0.70	0.02	0.14	0.02
1004	1.05	0.04	1.78	0.05	1.67	0.06	0.73	0.03	0.61	0.05	-0.11	0.05
1005	1.15	0.02	2.05	0.02	2.20	0.02	0.90	0.02	1.05	0.02	0.14	0.02
1006	1.32	0.03	2.15	0.03	2.16	0.04	0.83	0.02	0.83	0.03	0.01	0.03
1008	0.94	0.06	1.64	0.06	1.61	0.10	0.69	0.04	0.66	0.09	-0.03	0.09
1009	1.00	0.04	1.82	0.04	1.92	0.05	0.83	0.03	0.92	0.04	0.10	0.04

VCC	$u - g$	$u - g$ error	$u - i$	$u - i$ error	$u - z$	$u - z$ error	$g - i$	$g - i$ error	$g - z$	$g - z$ error	$i - z$	$i - z$ error
1010	1.47	0.02	2.49	0.02	2.61	0.02	1.03	0.02	1.14	0.02	0.11	0.02
1011	0.95	0.02	1.58	0.02	1.63	0.02	0.63	0.02	0.68	0.02	0.05	0.02
1012	0.96	0.05	1.74	0.05	1.68	0.07	0.78	0.04	0.71	0.06	-0.07	0.06
1013	0.84	0.02	1.59	0.02	1.34	0.03	0.76	0.02	0.51	0.02	-0.25	0.02
1014	0.99	0.04	1.81	0.05	1.82	0.07	0.83	0.03	0.83	0.06	0.01	0.06
1015	0.97	0.08	1.71	0.09	1.67	0.14	0.74	0.06	0.70	0.12	-0.04	0.13
1020	1.12	0.02	1.99	0.02	2.09	0.03	0.87	0.02	0.97	0.02	0.11	0.02
1021	1.09	0.02	1.80	0.02	1.87	0.02	0.72	0.02	0.78	0.02	0.06	0.02
1022	0.92	0.05	1.80	0.06	1.76	0.07	0.88	0.04	0.84	0.05	-0.04	0.06
1023	1.00	0.07	1.84	0.08	2.07	0.08	0.84	0.05	1.07	0.06	0.22	0.07
1025	1.47	0.02	2.45	0.02	2.74	0.02	0.98	0.02	1.27	0.02	0.28	0.02
1026	1.01	0.03	1.87	0.03	2.42	0.03	0.86	0.02	1.41	0.02	0.55	0.02
1027	1.32	0.03	2.01	0.03	1.96	0.04	0.69	0.02	0.64	0.03	-0.05	0.03
1029	0.99	0.03	1.77	0.03	1.80	0.04	0.78	0.02	0.81	0.03	0.03	0.03
1030	1.46	0.02	2.50	0.02	2.77	0.02	1.04	0.02	1.31	0.02	0.28	0.02
1036	1.88	0.02	2.30	0.02	2.45	0.02	0.41	0.02	0.57	0.02	0.15	0.02
1037	0.99	0.05	1.65	0.05	1.78	0.06	0.66	0.04	0.79	0.04	0.13	0.05
1039	1.10	0.03	1.97	0.02	2.10	0.03	0.88	0.02	1.00	0.02	0.12	0.02
1040	1.28	0.03	2.25	0.03	2.32	0.03	0.97	0.02	1.04	0.02	0.07	0.02
1044	1.04	0.02	1.88	0.02	1.98	0.02	0.84	0.02	0.94	0.02	0.10	0.02
1045	1.05	0.04	1.90	0.05	1.96	0.05	0.85	0.03	0.91	0.04	0.06	0.04
1046	1.03	0.08	1.83	0.08	1.84	0.09	0.80	0.05	0.81	0.07	0.01	0.07
1047	1.46	0.02	2.51	0.02	2.72	0.02	1.05	0.02	1.26	0.02	0.20	0.02
1049	1.13	0.02	1.93	0.02	2.05	0.02	0.80	0.02	0.92	0.02	0.12	0.02
1052	1.09	0.05	1.84	0.05	1.76	0.07	0.75	0.03	0.66	0.06	-0.08	0.06
1053	1.13	0.06	1.79	0.06	2.01	0.07	0.65	0.04	0.88	0.05	0.22	0.05
1056	1.12	0.04	1.85	0.04	1.99	0.05	0.72	0.03	0.86	0.03	0.14	0.04
1057	0.90	0.05	1.73	0.05	1.67	0.07	0.83	0.04	0.77	0.05	-0.06	0.06
1059	1.08	0.02	1.95	0.02	2.04	0.03	0.87	0.02	0.96	0.02	0.10	0.02
1063	1.03	0.05	1.81	0.06	1.84	0.08	0.78	0.03	0.80	0.07	0.02	0.07
1064	1.11	0.02	1.85	0.03	1.93	0.03	0.74	0.02	0.83	0.02	0.08	0.02
1069	1.23	0.02	2.05	0.02	2.14	0.02	0.81	0.02	0.90	0.02	0.09	0.02
1070	1.21	0.05	1.67	0.06	1.79	0.06	0.46	0.04	0.58	0.05	0.13	0.06
1071	1.28	0.03	2.27	0.03	2.39	0.04	0.99	0.02	1.10	0.03	0.12	0.03
1073	1.48	0.02	2.49	0.02	2.59	0.02	1.01	0.02	1.12	0.02	0.10	0.02
1074	1.06	0.05	1.77	0.05	1.77	0.10	0.71	0.04	0.71	0.09	0.00	0.09
1075	1.21	0.02	2.14	0.02	2.26	0.02	0.93	0.02	1.05	0.02	0.11	0.02
1076	1.15	0.03	1.94	0.03	2.00	0.03	0.79	0.02	0.85	0.02	0.05	0.02
1079	1.08	0.03	1.86	0.03	1.93	0.03	0.78	0.02	0.85	0.02	0.07	0.02
1081	1.09	0.04	1.86	0.04	1.79	0.05	0.78	0.03	0.71	0.04	-0.07	0.04
1083	1.08	0.04	1.80	0.05	1.77	0.07	0.73	0.03	0.69	0.06	-0.03	0.06

VCC	$u - g$	$u - g$ error	$u - i$	$u - i$ error	$u - z$	$u - z$ error	$g - i$	$g - i$ error	$g - z$	$g - z$ error	$i - z$	$i - z$ error
1086	1.32	0.02	2.37	0.02	2.60	0.02	1.05	0.02	1.28	0.02	0.24	0.02
1088	1.08	0.07	1.80	0.08	2.07	0.08	0.72	0.05	0.98	0.06	0.27	0.07
1089	1.26	0.04	1.99	0.04	2.13	0.04	0.73	0.03	0.87	0.03	0.14	0.03
1093	1.16	0.02	2.02	0.02	2.12	0.03	0.85	0.02	0.96	0.02	0.11	0.02
1095	0.78	0.03	1.40	0.04	1.59	0.04	0.62	0.03	0.81	0.03	0.19	0.04
1096	1.07	0.07	1.91	0.08	2.03	0.08	0.84	0.05	0.96	0.06	0.12	0.06
1098	1.02	0.05	1.63	0.05	1.19	0.08	0.61	0.02	0.16	0.06	-0.45	0.06
1100	0.95	0.03	1.73	0.03	1.89	0.03	0.77	0.02	0.94	0.03	0.17	0.03
1101	1.34	0.02	2.10	0.02	2.04	0.02	0.76	0.02	0.70	0.02	-0.06	0.02
1103	1.00	0.10	1.74	0.11	1.73	0.16	0.73	0.07	0.72	0.14	-0.01	0.15
1104	1.21	0.02	1.99	0.02	2.10	0.02	0.78	0.02	0.89	0.02	0.10	0.02
1105	1.11	0.02	1.72	0.03	1.73	0.03	0.61	0.02	0.62	0.02	0.01	0.02
1106	1.05	0.03	1.87	0.03	1.99	0.03	0.82	0.02	0.94	0.02	0.12	0.02
1107	1.21	0.02	2.08	0.02	2.19	0.02	0.87	0.02	0.99	0.02	0.12	0.02
1108	1.22	0.05	2.04	0.05	2.13	0.05	0.82	0.03	0.91	0.04	0.09	0.04
1109	0.91	0.03	1.54	0.03	1.81	0.04	0.63	0.03	0.90	0.03	0.27	0.03
1113	1.02	0.05	1.71	0.05	1.62	0.07	0.69	0.04	0.60	0.06	-0.09	0.06
1115	1.01	0.03	1.83	0.03	2.03	0.03	0.82	0.02	1.02	0.03	0.20	0.03
1118	0.99	0.02	1.30	0.02	1.88	0.02	0.31	0.02	0.89	0.02	0.58	0.02
1119	1.18	0.02	1.99	0.02	1.95	0.03	0.81	0.02	0.78	0.02	-0.03	0.02
1120	1.12	0.02	1.90	0.02	1.97	0.03	0.78	0.02	0.85	0.02	0.07	0.02
1122	1.20	0.02	2.00	0.02	2.14	0.02	0.81	0.02	0.94	0.02	0.13	0.02
1123	1.17	0.02	1.96	0.02	2.09	0.02	0.80	0.02	0.92	0.02	0.13	0.02
1124	1.07	0.03	1.83	0.03	1.79	0.03	0.76	0.02	0.72	0.02	-0.04	0.02
1125	1.49	0.02	2.53	0.02	2.73	0.02	1.04	0.02	1.24	0.02	0.20	0.02
1126	1.18	0.02	2.26	0.02	2.47	0.02	1.08	0.02	1.29	0.02	0.21	0.02
1127	1.18	0.04	2.04	0.04	2.00	0.04	0.86	0.02	0.82	0.03	-0.04	0.04
1128	1.08	0.02	1.80	0.02	1.67	0.03	0.73	0.02	0.60	0.02	-0.13	0.02
1129	1.01	0.03	1.77	0.03	1.89	0.03	0.76	0.02	0.88	0.02	0.12	0.02
1131	1.02	0.03	1.68	0.03	1.58	0.04	0.66	0.02	0.56	0.04	-0.10	0.04
1135	1.00	0.04	1.80	0.04	1.87	0.04	0.79	0.03	0.86	0.03	0.07	0.04
1136	1.06	0.03	1.89	0.03	1.90	0.04	0.83	0.02	0.84	0.03	0.01	0.04
1137	1.28	0.03	1.97	0.04	2.18	0.04	0.69	0.03	0.90	0.03	0.21	0.03
1140	1.06	0.03	1.77	0.04	1.76	0.04	0.71	0.03	0.70	0.03	-0.01	0.03
1143	1.00	0.04	1.82	0.04	1.96	0.04	0.82	0.03	0.96	0.03	0.14	0.03
1144	1.01	0.08	1.52	0.09	0.94	0.16	0.51	0.06	-0.07	0.15	-0.57	0.15
1146	1.41	0.02	2.38	0.02	2.62	0.02	0.97	0.02	1.21	0.02	0.24	0.02
1147	1.06	0.06	1.86	0.07	2.00	0.09	0.79	0.04	0.94	0.07	0.14	0.08
1149	0.86	0.03	1.60	0.03	1.45	0.04	0.74	0.03	0.59	0.04	-0.15	0.04
1151	1.20	0.03	2.14	0.03	2.17	0.03	0.94	0.02	0.97	0.02	0.04	0.02
1158	1.52	0.02	2.56	0.02	2.87	0.02	1.04	0.02	1.35	0.02	0.31	0.02

VCC	$u - g$	$u - g$ error	$u - i$	$u - i$ error	$u - z$	$u - z$ error	$g - i$	$g - i$ error	$g - z$	$g - z$ error	$i - z$	$i - z$ error
1160	1.04	0.03	1.80	0.03	1.94	0.04	0.75	0.02	0.90	0.03	0.14	0.03
1161	1.03	0.04	1.91	0.04	2.08	0.05	0.88	0.03	1.05	0.04	0.17	0.04
1162	1.03	0.07	1.96	0.07	2.26	0.09	0.93	0.04	1.23	0.07	0.30	0.07
1163	1.16	0.02	2.09	0.02	2.02	0.02	0.94	0.02	0.87	0.02	-0.07	0.02
1164	1.10	0.02	1.91	0.02	1.89	0.03	0.82	0.02	0.80	0.02	-0.02	0.02
1165	1.00	0.03	1.77	0.04	1.81	0.04	0.78	0.03	0.81	0.04	0.03	0.04
1167	2.03	0.02	2.91	0.02	3.33	0.02	0.88	0.02	1.30	0.02	0.42	0.02
1170	1.03	0.06	1.73	0.06	1.80	0.07	0.70	0.04	0.77	0.05	0.07	0.05
1172	1.20	0.02	2.11	0.02	2.26	0.02	0.90	0.02	1.05	0.02	0.15	0.02
1173	1.22	0.02	2.04	0.02	2.15	0.02	0.82	0.02	0.93	0.02	0.11	0.02
1175	0.98	0.02	1.71	0.02	1.82	0.02	0.73	0.02	0.83	0.02	0.10	0.02
1177	1.08	0.03	2.04	0.03	2.26	0.03	0.97	0.02	1.19	0.03	0.22	0.03
1178	1.39	0.02	2.43	0.02	2.71	0.02	1.03	0.02	1.32	0.02	0.28	0.02
1179	0.72	0.02	1.28	0.02	1.39	0.02	0.56	0.02	0.67	0.02	0.11	0.02
1183	1.43	0.02	2.24	0.02	2.40	0.02	0.81	0.02	0.98	0.02	0.16	0.02
1184	0.93	0.04	1.69	0.04	1.86	0.05	0.76	0.03	0.93	0.04	0.17	0.04
1185	1.41	0.02	2.30	0.02	2.49	0.02	0.89	0.02	1.08	0.02	0.19	0.02
1186	1.19	0.03	2.00	0.03	2.10	0.03	0.82	0.02	0.92	0.02	0.10	0.03
1187	0.99	0.05	1.66	0.05	1.48	0.09	0.67	0.04	0.49	0.08	-0.18	0.08
1191	1.11	0.02	1.87	0.02	2.00	0.03	0.76	0.02	0.89	0.02	0.12	0.02
1193	0.76	0.02	1.33	0.02	1.56	0.02	0.56	0.02	0.80	0.02	0.24	0.02
1194	1.15	0.04	1.99	0.04	2.09	0.04	0.84	0.03	0.95	0.03	0.10	0.04
1195	0.99	0.04	1.79	0.04	1.73	0.05	0.80	0.03	0.74	0.04	-0.06	0.04
1196	1.40	0.02	2.38	0.02	2.56	0.02	0.98	0.02	1.17	0.02	0.19	0.02
1197	0.84	0.05	1.67	0.06	1.43	0.08	0.84	0.04	0.59	0.07	-0.25	0.08
1200	0.77	0.02	1.15	0.02	1.20	0.02	0.39	0.02	0.44	0.02	0.05	0.02
1204	1.25	0.02	2.05	0.02	2.17	0.02	0.80	0.02	0.92	0.02	0.12	0.02
1207	1.06	0.03	1.87	0.03	1.95	0.03	0.82	0.02	0.90	0.02	0.08	0.02
1209	1.06	0.03	1.85	0.03	1.94	0.03	0.79	0.02	0.88	0.02	0.09	0.02
1210	1.18	0.03	2.13	0.03	2.10	0.03	0.95	0.02	0.91	0.02	-0.03	0.02
1211	1.07	0.04	1.93	0.04	2.10	0.04	0.86	0.03	1.03	0.03	0.17	0.03
1212	1.09	0.03	1.91	0.03	1.78	0.03	0.82	0.02	0.69	0.03	-0.13	0.03
1213	1.21	0.02	2.00	0.02	2.14	0.02	0.79	0.02	0.94	0.02	0.14	0.02
1216	1.24	0.03	1.93	0.03	2.05	0.04	0.69	0.02	0.81	0.04	0.11	0.04
1217	0.93	0.02	1.38	0.02	1.41	0.02	0.44	0.02	0.48	0.02	0.04	0.02
1219	1.02	0.03	1.71	0.03	1.89	0.03	0.69	0.02	0.88	0.03	0.18	0.03
1222	1.21	0.02	2.11	0.02	2.27	0.02	0.89	0.02	1.05	0.02	0.16	0.02
1223	1.29	0.03	2.05	0.03	2.17	0.03	0.76	0.02	0.88	0.02	0.13	0.02
1225	1.06	0.02	1.85	0.02	2.02	0.02	0.79	0.02	0.96	0.02	0.17	0.02
1227	1.23	0.03	1.95	0.03	2.14	0.03	0.71	0.02	0.91	0.02	0.20	0.02
1230	1.03	0.04	2.09	0.04	2.31	0.04	1.05	0.03	1.27	0.03	0.22	0.03

VCC	$u - g$	$u - g$ error	$u - i$	$u - i$ error	$u - z$	$u - z$ error	$g - i$	$g - i$ error	$g - z$	$g - z$ error	$i - z$	$i - z$ error
1235	1.25	0.03	2.14	0.03	2.21	0.03	0.89	0.02	0.96	0.02	0.07	0.02
1240	1.05	0.02	1.82	0.02	1.91	0.03	0.77	0.02	0.86	0.02	0.09	0.02
1241	0.96	0.05	1.71	0.05	1.67	0.06	0.76	0.04	0.71	0.05	-0.05	0.05
1245	1.42	0.04	2.27	0.04	2.35	0.04	0.85	0.02	0.93	0.03	0.08	0.03
1246	1.15	0.03	1.95	0.03	1.92	0.03	0.80	0.02	0.78	0.03	-0.03	0.03
1247	1.04	0.03	1.74	0.03	1.66	0.04	0.71	0.02	0.62	0.03	-0.09	0.03
1251	1.09	0.06	1.80	0.07	1.84	0.08	0.71	0.05	0.75	0.06	0.03	0.06
1252	1.07	0.03	1.89	0.03	1.90	0.04	0.82	0.02	0.82	0.03	0.01	0.03
1254	1.48	0.02	2.45	0.02	2.61	0.02	0.97	0.02	1.13	0.02	0.16	0.02
1256	1.00	0.04	1.66	0.04	1.82	0.05	0.65	0.03	0.81	0.04	0.16	0.04
1259	1.17	0.03	1.72	0.03	1.79	0.03	0.55	0.02	0.63	0.03	0.07	0.03
1264	1.04	0.02	1.80	0.02	1.95	0.03	0.76	0.02	0.91	0.02	0.15	0.02
1265	1.22	0.04	2.15	0.04	2.23	0.04	0.93	0.03	1.01	0.03	0.08	0.03
1271	1.16	0.05	1.91	0.05	1.95	0.06	0.75	0.04	0.80	0.05	0.04	0.05
1281	1.13	0.03	1.76	0.04	1.92	0.04	0.63	0.03	0.78	0.03	0.15	0.03
1285	1.48	0.04	2.40	0.04	2.64	0.04	0.92	0.02	1.16	0.03	0.24	0.03
1287	1.13	0.03	1.90	0.04	1.89	0.04	0.77	0.03	0.76	0.03	0.00	0.03
1291	1.27	0.03	1.99	0.03	2.10	0.04	0.72	0.02	0.83	0.03	0.10	0.03
1292	1.05	0.04	1.78	0.04	1.86	0.05	0.73	0.03	0.81	0.04	0.08	0.04
1297	1.33	0.02	2.41	0.02	2.78	0.02	1.08	0.02	1.45	0.02	0.36	0.02
1299	1.18	0.06	1.78	0.06	1.77	0.08	0.60	0.04	0.59	0.06	-0.01	0.07
1300	0.93	0.03	1.66	0.03	1.83	0.03	0.73	0.02	0.90	0.03	0.17	0.03
1301	1.19	0.05	1.76	0.06	1.98	0.06	0.57	0.04	0.79	0.05	0.22	0.05
1306	0.97	0.06	1.82	0.06	1.86	0.07	0.85	0.05	0.89	0.06	0.04	0.07
1307	1.10	0.03	1.92	0.03	2.10	0.03	0.82	0.02	1.00	0.02	0.17	0.02
1308	1.24	0.02	2.15	0.02	2.21	0.02	0.91	0.02	0.97	0.02	0.06	0.02
1309	0.93	0.05	1.76	0.06	1.76	0.07	0.83	0.04	0.83	0.06	0.00	0.06
1311	1.27	0.02	2.13	0.02	2.24	0.02	0.85	0.02	0.96	0.02	0.11	0.02
1312	1.03	0.04	1.79	0.04	1.95	0.04	0.75	0.03	0.92	0.03	0.17	0.03
1313	0.52	0.02	0.32	0.02	0.42	0.02	-0.20	0.02	-0.10	0.02	0.10	0.02
1315	1.20	0.08	2.14	0.09	2.33	0.09	0.95	0.05	1.13	0.06	0.18	0.06
1319	0.84	0.04	1.56	0.04	1.63	0.05	0.72	0.03	0.79	0.04	0.07	0.04
1327	0.76	0.02	1.58	0.02	1.85	0.02	0.81	0.02	1.08	0.02	0.27	0.02
1328	1.25	0.06	2.25	0.06	2.44	0.06	1.01	0.03	1.19	0.04	0.19	0.04
1330	2.15	0.02	2.96	0.02	2.64	0.02	0.81	0.02	0.49	0.02	-0.32	0.02
1331	1.16	0.03	2.02	0.03	2.16	0.03	0.86	0.02	1.00	0.02	0.14	0.02
1333	1.05	0.02	1.88	0.02	1.99	0.02	0.82	0.02	0.94	0.02	0.12	0.02
1335	1.02	0.05	1.69	0.06	1.78	0.07	0.67	0.04	0.75	0.05	0.08	0.05
1336	1.24	0.03	2.14	0.03	2.23	0.03	0.91	0.02	0.99	0.02	0.08	0.02
1345	1.10	0.05	1.79	0.05	2.07	0.06	0.69	0.03	0.97	0.04	0.28	0.05
1348	1.31	0.02	2.32	0.02	2.52	0.02	1.01	0.02	1.21	0.02	0.20	0.02

VCC	$u - g$	$u - g$ error	$u - i$	$u - i$ error	$u - z$	$u - z$ error	$g - i$	$g - i$ error	$g - z$	$g - z$ error	$i - z$	$i - z$ error
1349	1.10	0.03	1.87	0.03	2.00	0.04	0.77	0.02	0.90	0.03	0.13	0.03
1356	0.68	0.02	1.19	0.02	1.27	0.02	0.52	0.02	0.60	0.02	0.08	0.02
1357	1.28	0.04	2.07	0.04	1.90	0.06	0.80	0.03	0.62	0.04	-0.17	0.04
1360	1.06	0.04	1.78	0.04	1.90	0.05	0.72	0.03	0.84	0.04	0.12	0.04
1361	1.19	0.03	1.95	0.03	1.93	0.04	0.76	0.02	0.73	0.03	-0.03	0.03
1363	1.64	0.04	2.45	0.04	2.66	0.04	0.81	0.02	1.02	0.03	0.21	0.03
1365	1.04	0.04	1.78	0.04	2.01	0.05	0.74	0.03	0.97	0.04	0.23	0.04
1366	1.18	0.03	2.04	0.03	2.09	0.04	0.85	0.03	0.91	0.03	0.05	0.03
1367	0.92	0.04	1.63	0.04	1.69	0.05	0.71	0.03	0.78	0.04	0.07	0.04
1369	1.12	0.02	1.91	0.02	1.87	0.03	0.79	0.02	0.75	0.02	-0.03	0.02
1370	1.45	0.03	2.21	0.03	2.30	0.03	0.77	0.02	0.85	0.02	0.09	0.02
1371	0.96	0.04	2.04	0.04	2.20	0.04	1.08	0.03	1.24	0.03	0.16	0.03
1377	1.15	0.02	1.93	0.02	2.03	0.02	0.77	0.02	0.88	0.02	0.10	0.02
1387	1.13	0.03	2.03	0.03	2.07	0.04	0.90	0.02	0.93	0.03	0.04	0.03
1389	1.14	0.02	2.12	0.02	2.12	0.02	0.98	0.02	0.98	0.02	-0.01	0.02
1392	1.34	0.02	2.24	0.02	2.39	0.02	0.89	0.02	1.05	0.02	0.15	0.02
1394	1.20	0.03	2.00	0.03	2.14	0.03	0.81	0.02	0.94	0.03	0.13	0.03
1396	1.38	0.03	2.36	0.03	2.31	0.03	0.98	0.02	0.92	0.02	-0.06	0.02
1402	1.28	0.03	2.15	0.03	1.97	0.04	0.87	0.02	0.69	0.03	-0.18	0.03
1404	1.15	0.03	1.92	0.03	1.93	0.03	0.77	0.02	0.78	0.03	0.01	0.03
1405	1.21	0.06	2.02	0.07	1.99	0.09	0.81	0.04	0.78	0.07	-0.03	0.07
1406	1.03	0.03	1.80	0.04	1.81	0.04	0.77	0.02	0.78	0.03	0.01	0.03
1407	1.24	0.02	2.20	0.02	2.29	0.02	0.96	0.02	1.05	0.02	0.09	0.02
1408	1.12	0.03	1.91	0.04	2.06	0.04	0.79	0.02	0.94	0.03	0.15	0.03
1411	0.90	0.02	1.44	0.02	1.48	0.02	0.53	0.02	0.57	0.02	0.04	0.02
1413	1.12	0.03	1.84	0.03	1.86	0.03	0.72	0.02	0.74	0.02	0.02	0.02
1415	1.17	0.03	2.09	0.03	2.17	0.03	0.92	0.02	1.00	0.03	0.08	0.03
1420	1.18	0.02	2.13	0.02	2.17	0.02	0.96	0.02	0.99	0.02	0.03	0.02
1422	1.32	0.02	2.22	0.02	2.37	0.02	0.90	0.02	1.05	0.02	0.15	0.02
1425	1.08	0.04	1.78	0.04	1.86	0.05	0.70	0.03	0.77	0.04	0.08	0.04
1426	1.14	0.02	1.88	0.02	1.97	0.02	0.73	0.02	0.83	0.02	0.09	0.02
1431	1.36	0.02	2.38	0.02	2.58	0.02	1.02	0.02	1.22	0.02	0.20	0.02
1432	1.17	0.02	1.96	0.02	1.97	0.03	0.79	0.02	0.79	0.02	0.01	0.02
1436	1.05	0.03	1.89	0.03	2.01	0.03	0.85	0.02	0.96	0.02	0.12	0.02
1437	0.86	0.02	1.56	0.02	1.73	0.02	0.70	0.02	0.86	0.02	0.17	0.02
1439	1.17	0.04	1.89	0.04	1.81	0.06	0.72	0.03	0.64	0.04	-0.09	0.05
1441	1.21	0.02	2.03	0.02	2.17	0.02	0.83	0.02	0.97	0.02	0.14	0.02
1444	1.32	0.02	2.04	0.02	2.08	0.02	0.73	0.02	0.76	0.02	0.03	0.02
1446	1.25	0.02	2.13	0.02	2.24	0.02	0.88	0.02	1.00	0.02	0.11	0.02
1454	1.14	0.04	1.87	0.04	2.06	0.04	0.73	0.03	0.92	0.03	0.19	0.04
1455	0.93	0.02	1.54	0.02	1.58	0.02	0.61	0.02	0.65	0.02	0.04	0.02

VCC	$u - g$	$u - g$ error	$u - i$	$u - i$ error	$u - z$	$u - z$ error	$g - i$	$g - i$ error	$g - z$	$g - z$ error	$i - z$	$i - z$ error
1461	1.06	0.06	1.88	0.07	1.95	0.09	0.82	0.04	0.89	0.07	0.07	0.07
1464	1.08	0.03	1.86	0.03	1.86	0.03	0.78	0.02	0.78	0.03	0.00	0.03
1470	1.07	0.05	1.68	0.05	1.74	0.07	0.62	0.04	0.67	0.05	0.05	0.06
1472	1.09	0.03	1.82	0.03	1.76	0.04	0.73	0.02	0.67	0.03	-0.06	0.03
1481	1.09	0.03	1.86	0.03	2.04	0.03	0.77	0.02	0.96	0.02	0.19	0.02
1485	1.00	0.04	1.79	0.05	1.70	0.06	0.79	0.03	0.69	0.05	-0.10	0.06
1487	1.03	0.05	1.87	0.06	2.07	0.06	0.84	0.04	1.03	0.05	0.20	0.05
1488	1.13	0.02	1.79	0.02	1.85	0.02	0.66	0.02	0.72	0.02	0.06	0.02
1489	1.12	0.02	1.92	0.02	2.09	0.02	0.80	0.02	0.97	0.02	0.17	0.02
1494	1.05	0.06	1.82	0.06	1.89	0.08	0.76	0.04	0.83	0.06	0.07	0.06
1496	1.11	0.03	1.84	0.03	1.78	0.03	0.74	0.02	0.68	0.03	-0.06	0.03
1498	0.96	0.02	1.65	0.02	1.83	0.02	0.69	0.02	0.87	0.02	0.19	0.02
1500	1.12	0.04	1.88	0.04	2.03	0.05	0.76	0.03	0.91	0.03	0.15	0.04
1506	0.63	0.03	1.11	0.04	0.88	0.06	0.48	0.03	0.25	0.05	-0.23	0.06
1511	1.07	0.03	1.89	0.03	1.92	0.03	0.82	0.02	0.85	0.03	0.03	0.03
1512	1.16	0.02	1.97	0.02	2.16	0.02	0.81	0.02	1.00	0.02	0.19	0.02
1518	1.07	0.03	1.80	0.03	1.82	0.04	0.73	0.02	0.76	0.03	0.03	0.03
1519	1.17	0.03	2.08	0.03	2.34	0.03	0.91	0.02	1.17	0.02	0.27	0.02
1520	1.09	0.07	1.78	0.07	1.98	0.09	0.69	0.05	0.89	0.07	0.20	0.08
1522	1.14	0.04	2.06	0.04	2.23	0.05	0.93	0.03	1.10	0.03	0.17	0.03
1531	1.09	0.03	1.90	0.03	2.03	0.03	0.82	0.02	0.94	0.02	0.12	0.02
1538	1.06	0.05	1.81	0.05	1.81	0.06	0.76	0.03	0.75	0.05	-0.01	0.06
1546	1.16	0.05	2.41	0.05	2.86	0.05	1.25	0.03	1.71	0.03	0.45	0.03
1549	2.11	0.02	2.79	0.02	2.57	0.02	0.68	0.02	0.46	0.02	-0.22	0.02
1551	1.11	0.05	2.02	0.06	2.16	0.06	0.90	0.04	1.05	0.04	0.15	0.05
1558	1.05	0.04	1.74	0.04	2.01	0.05	0.69	0.03	0.95	0.04	0.26	0.04
1561	1.17	0.02	2.01	0.02	2.09	0.02	0.84	0.02	0.92	0.02	0.08	0.02
1563	1.19	0.02	1.97	0.02	2.09	0.02	0.78	0.02	0.90	0.02	0.12	0.02
1565	1.26	0.03	1.96	0.03	2.27	0.03	0.70	0.02	1.01	0.02	0.31	0.02
1569	0.86	0.02	1.40	0.02	1.45	0.02	0.54	0.02	0.59	0.02	0.05	0.02
1573	1.18	0.02	1.92	0.02	2.04	0.02	0.74	0.02	0.85	0.02	0.12	0.02
1578	0.96	0.05	1.78	0.05	1.94	0.05	0.82	0.03	0.98	0.04	0.15	0.04
1582	1.00	0.02	1.74	0.02	1.66	0.03	0.74	0.02	0.66	0.02	-0.08	0.02
1586	1.05	0.04	2.12	0.04	2.38	0.04	1.06	0.03	1.33	0.03	0.26	0.03
1591	1.05	0.04	1.69	0.04	1.84	0.05	0.64	0.03	0.79	0.04	0.16	0.04
1594	1.06	0.03	1.84	0.03	1.98	0.03	0.78	0.02	0.93	0.03	0.15	0.03
1599	1.16	0.03	2.09	0.03	2.20	0.03	0.93	0.02	1.04	0.02	0.12	0.02
1601	1.31	0.03	2.26	0.03	2.39	0.03	0.95	0.02	1.09	0.02	0.14	0.02
1602	1.12	0.03	2.00	0.03	2.08	0.03	0.87	0.02	0.96	0.02	0.08	0.02
1603	1.15	0.02	1.92	0.02	2.09	0.03	0.76	0.02	0.93	0.02	0.17	0.02
1604	1.24	0.02	1.95	0.02	2.03	0.02	0.71	0.02	0.79	0.02	0.08	0.02

VCC	$u - g$	$u - g$ error	$u - i$	$u - i$ error	$u - z$	$u - z$ error	$g - i$	$g - i$ error	$g - z$	$g - z$ error	$i - z$	$i - z$ error
1606	1.09	0.02	1.96	0.02	2.01	0.03	0.86	0.02	0.91	0.02	0.05	0.02
1609	1.15	0.03	1.98	0.03	2.10	0.03	0.82	0.02	0.95	0.02	0.12	0.02
1612	1.01	0.03	1.76	0.03	1.90	0.03	0.75	0.02	0.89	0.02	0.14	0.02
1613	1.06	0.04	1.88	0.04	1.88	0.05	0.82	0.03	0.82	0.04	0.00	0.04
1614	1.16	0.02	1.96	0.02	2.14	0.02	0.80	0.02	0.99	0.02	0.18	0.02
1616	1.21	0.02	2.05	0.02	2.16	0.02	0.84	0.02	0.95	0.02	0.11	0.02
1619	1.35	0.02	2.39	0.02	2.66	0.02	1.04	0.02	1.30	0.02	0.27	0.02
1621	1.01	0.03	1.86	0.03	1.92	0.04	0.85	0.02	0.91	0.03	0.06	0.03
1625	1.24	0.04	2.23	0.04	2.26	0.04	1.00	0.03	1.02	0.03	0.03	0.03
1626	1.03	0.03	1.88	0.03	2.19	0.03	0.85	0.02	1.16	0.03	0.31	0.03
1627	1.43	0.02	2.48	0.02	2.73	0.02	1.05	0.02	1.31	0.02	0.25	0.02
1630	1.54	0.02	2.66	0.02	2.87	0.02	1.12	0.02	1.33	0.02	0.21	0.02
1631	1.03	0.05	1.69	0.06	1.85	0.06	0.66	0.04	0.82	0.05	0.17	0.05
1634	1.02	0.07	1.70	0.08	2.06	0.08	0.68	0.05	1.04	0.05	0.35	0.06
1635	1.06	0.07	1.88	0.08	1.95	0.09	0.82	0.05	0.89	0.07	0.07	0.07
1637	0.98	0.03	1.76	0.03	1.73	0.03	0.78	0.02	0.75	0.03	-0.03	0.03
1642	1.11	0.03	1.68	0.03	1.88	0.03	0.57	0.02	0.77	0.02	0.20	0.02
1644	0.76	0.02	1.18	0.02	1.21	0.03	0.42	0.02	0.44	0.02	0.03	0.02
1647	1.09	0.02	1.93	0.02	1.99	0.02	0.83	0.02	0.89	0.02	0.06	0.02
1650	0.96	0.03	1.57	0.03	1.67	0.03	0.61	0.02	0.71	0.02	0.11	0.02
1654	0.78	0.02	1.22	0.02	1.27	0.02	0.43	0.02	0.49	0.02	0.05	0.02
1658	1.11	0.03	1.95	0.03	2.06	0.03	0.84	0.02	0.96	0.02	0.11	0.02
1661	1.31	0.02	2.26	0.02	2.59	0.02	0.95	0.02	1.29	0.02	0.33	0.02
1662	1.04	0.05	1.84	0.06	1.82	0.07	0.80	0.04	0.78	0.05	-0.02	0.06
1663	1.59	0.03	2.50	0.03	2.66	0.03	0.91	0.02	1.07	0.02	0.16	0.02
1669	1.20	0.02	2.09	0.02	2.19	0.02	0.88	0.02	0.98	0.02	0.10	0.02
1670	0.97	0.06	1.82	0.06	1.79	0.07	0.85	0.04	0.82	0.06	-0.03	0.06
1672	1.08	0.04	1.92	0.04	1.89	0.05	0.83	0.03	0.81	0.04	-0.03	0.04
1673	1.03	0.02	2.08	0.02	2.33	0.02	1.05	0.02	1.30	0.02	0.25	0.02
1674	1.29	0.02	2.26	0.02	2.33	0.02	0.97	0.02	1.04	0.02	0.07	0.02
1677	1.59	0.02	2.12	0.02	2.28	0.03	0.53	0.02	0.70	0.02	0.16	0.02
1680	1.06	0.05	1.79	0.05	1.81	0.06	0.73	0.03	0.75	0.05	0.02	0.05
1681	1.17	0.03	1.94	0.03	2.08	0.04	0.77	0.02	0.90	0.03	0.13	0.03
1682	1.17	0.02	2.13	0.02	2.31	0.02	0.95	0.02	1.14	0.02	0.18	0.02
1684	1.06	0.02	1.67	0.02	1.76	0.02	0.61	0.02	0.70	0.02	0.09	0.02
1689	1.04	0.02	2.25	0.02	2.39	0.03	1.20	0.02	1.34	0.02	0.14	0.02
1691	1.12	0.02	2.01	0.02	2.05	0.03	0.89	0.02	0.93	0.02	0.04	0.02
1693	1.23	0.04	1.98	0.04	2.05	0.05	0.75	0.03	0.82	0.04	0.07	0.04
1694	1.13	0.03	1.97	0.04	2.14	0.04	0.84	0.03	1.00	0.03	0.16	0.03
1700	0.97	0.04	1.89	0.05	1.80	0.05	0.92	0.03	0.83	0.04	-0.09	0.04
1702	1.05	0.03	1.97	0.03	2.03	0.03	0.92	0.02	0.98	0.03	0.07	0.03

VCC	$u - g$	$u - g$ error	$u - i$	$u - i$ error	$u - z$	$u - z$ error	$g - i$	$g - i$ error	$g - z$	$g - z$ error	$i - z$	$i - z$ error
1704	1.20	0.02	1.92	0.02	2.00	0.02	0.72	0.02	0.80	0.02	0.08	0.02
1706	1.11	0.04	1.96	0.05	1.95	0.05	0.85	0.03	0.85	0.04	0.00	0.04
1707	0.79	0.04	1.26	0.04	1.42	0.05	0.47	0.04	0.63	0.04	0.16	0.05
1711	1.25	0.02	2.13	0.02	2.21	0.02	0.87	0.02	0.96	0.02	0.09	0.02
1714	1.03	0.03	1.71	0.03	1.79	0.03	0.68	0.02	0.76	0.02	0.08	0.02
1717	1.26	0.02	2.05	0.02	2.01	0.02	0.79	0.02	0.75	0.02	-0.04	0.02
1728	0.85	0.02	1.38	0.02	1.36	0.02	0.53	0.02	0.52	0.02	-0.01	0.02
1729	1.08	0.03	1.83	0.03	1.98	0.03	0.75	0.02	0.90	0.03	0.15	0.03
1731	1.16	0.04	2.04	0.04	2.13	0.04	0.88	0.03	0.97	0.03	0.09	0.03
1736	1.03	0.04	1.83	0.04	1.78	0.05	0.79	0.03	0.75	0.04	-0.05	0.04
1740	1.13	0.03	1.98	0.03	2.04	0.03	0.85	0.02	0.90	0.02	0.06	0.03
1746	1.52	0.03	2.65	0.03	2.89	0.03	1.12	0.02	1.37	0.02	0.24	0.02
1747	1.27	0.03	2.12	0.03	2.10	0.03	0.85	0.02	0.83	0.02	-0.02	0.02
1749	0.91	0.04	1.62	0.04	1.82	0.04	0.71	0.03	0.91	0.03	0.20	0.03
1754	1.08	0.04	1.89	0.04	1.57	0.05	0.80	0.03	0.48	0.04	-0.32	0.04
1767	1.08	0.02	1.90	0.02	1.99	0.02	0.82	0.02	0.92	0.02	0.09	0.02
1775	1.03	0.05	1.97	0.05	1.98	0.05	0.94	0.03	0.95	0.04	0.01	0.04
1778	1.09	0.02	1.61	0.02	1.70	0.02	0.52	0.02	0.61	0.02	0.09	0.02
1783	1.14	0.03	1.97	0.03	2.01	0.03	0.83	0.02	0.87	0.02	0.04	0.02
1785	1.15	0.03	1.93	0.03	2.01	0.03	0.78	0.02	0.86	0.03	0.08	0.03
1786	1.14	0.04	1.94	0.04	2.01	0.04	0.81	0.02	0.87	0.03	0.06	0.03
1787	1.15	0.05	1.91	0.05	2.00	0.06	0.76	0.03	0.85	0.04	0.10	0.04
1792	1.49	0.04	2.13	0.04	2.30	0.04	0.64	0.02	0.81	0.03	0.17	0.03
1796	1.14	0.02	1.80	0.02	1.94	0.02	0.66	0.02	0.80	0.02	0.15	0.02
1798	0.99	0.05	1.68	0.06	1.61	0.07	0.69	0.04	0.62	0.06	-0.07	0.06
1803	1.17	0.02	1.98	0.02	2.14	0.02	0.82	0.02	0.97	0.02	0.16	0.02
1812	0.98	0.02	1.75	0.02	1.92	0.02	0.76	0.02	0.93	0.02	0.17	0.02
1815	0.99	0.03	1.60	0.03	1.58	0.03	0.60	0.02	0.59	0.02	-0.02	0.02
1816	0.22	0.02	0.68	0.02	0.56	0.03	0.46	0.02	0.33	0.02	-0.12	0.02
1818	1.28	0.05	2.11	0.05	2.17	0.05	0.82	0.03	0.88	0.03	0.06	0.03
1823	0.99	0.03	1.68	0.03	1.80	0.03	0.70	0.02	0.81	0.03	0.11	0.03
1828	1.27	0.02	2.15	0.02	2.35	0.02	0.88	0.02	1.07	0.02	0.19	0.02
1831	1.16	0.03	1.83	0.03	1.90	0.03	0.67	0.02	0.74	0.03	0.07	0.03
1841	1.08	0.04	2.07	0.04	2.45	0.04	0.98	0.03	1.37	0.03	0.39	0.03
1843	1.17	0.03	2.02	0.03	2.11	0.03	0.86	0.02	0.94	0.02	0.09	0.02
1861	1.34	0.02	2.25	0.02	2.44	0.02	0.92	0.02	1.11	0.02	0.19	0.02
1870	1.16	0.02	1.85	0.02	1.93	0.02	0.69	0.02	0.77	0.02	0.08	0.02
1871	1.41	0.02	2.44	0.02	2.69	0.02	1.03	0.02	1.28	0.02	0.25	0.02
1879	1.09	0.03	1.89	0.02	2.02	0.03	0.80	0.02	0.93	0.02	0.12	0.02
1880	1.06	0.03	1.86	0.03	2.00	0.03	0.80	0.02	0.94	0.02	0.14	0.03
1881	1.33	0.02	2.15	0.02	2.23	0.02	0.83	0.02	0.90	0.02	0.07	0.02

VCC	$u - g$	$u - g$ error	$u - i$	$u - i$ error	$u - z$	$u - z$ error	$g - i$	$g - i$ error	$g - z$	$g - z$ error	$i - z$	$i - z$ error
1882	1.41	0.09	2.00	0.09	2.12	0.10	0.60	0.05	0.72	0.07	0.12	0.08
1886	1.15	0.02	1.91	0.02	2.02	0.02	0.76	0.02	0.87	0.02	0.11	0.02
1888	0.95	0.06	1.70	0.06	1.78	0.08	0.75	0.04	0.83	0.06	0.08	0.06
1891	1.10	0.02	1.94	0.02	2.08	0.02	0.84	0.02	0.98	0.02	0.14	0.02
1904	1.05	0.04	1.87	0.04	2.03	0.04	0.82	0.03	0.97	0.03	0.15	0.04
1909	1.14	0.02	1.95	0.02	2.04	0.02	0.82	0.02	0.90	0.02	0.09	0.02
1910	2.10	0.02	2.70	0.02	2.78	0.02	0.60	0.02	0.68	0.02	0.08	0.02
1915	1.23	0.03	2.24	0.03	2.12	0.03	1.01	0.02	0.89	0.02	-0.12	0.02
1921	1.33	0.02	2.25	0.02	2.45	0.02	0.92	0.02	1.12	0.02	0.20	0.02
1925	1.03	0.06	1.76	0.06	2.04	0.07	0.73	0.04	1.01	0.05	0.28	0.06
1928	1.26	0.03	2.07	0.03	2.12	0.03	0.81	0.02	0.86	0.02	0.05	0.02
1931	0.79	0.02	1.38	0.02	1.10	0.02	0.59	0.02	0.31	0.02	-0.28	0.02
1938	1.43	0.02	2.41	0.02	2.70	0.02	0.98	0.02	1.27	0.02	0.29	0.02
1943	0.77	0.02	1.74	0.02	1.94	0.02	0.96	0.02	1.17	0.02	0.21	0.02
1946	0.98	0.11	1.71	0.11	1.95	0.13	0.73	0.07	0.97	0.09	0.24	0.10
1948	1.11	0.02	1.88	0.02	1.98	0.02	0.76	0.02	0.87	0.02	0.10	0.02
1949	1.52	0.02	2.50	0.02	2.68	0.02	0.97	0.02	1.15	0.02	0.18	0.02
1951	1.33	0.03	2.25	0.03	2.43	0.03	0.92	0.02	1.10	0.02	0.19	0.02
1955	1.08	0.02	1.85	0.02	2.00	0.02	0.77	0.02	0.92	0.02	0.15	0.02
1958	1.17	0.02	1.96	0.02	2.07	0.02	0.79	0.02	0.90	0.02	0.10	0.02
1963	1.09	0.06	2.01	0.07	2.09	0.08	0.91	0.04	1.00	0.06	0.08	0.06
1968	1.06	0.05	1.79	0.05	1.86	0.06	0.73	0.03	0.81	0.05	0.08	0.05
1971	1.22	0.02	2.03	0.02	2.13	0.02	0.80	0.02	0.91	0.02	0.11	0.02
1975	1.05	0.03	1.85	0.03	2.05	0.03	0.80	0.02	1.00	0.02	0.20	0.02
1976	1.07	0.04	1.89	0.04	1.98	0.04	0.82	0.02	0.91	0.03	0.09	0.03
1982	1.16	0.02	1.97	0.02	2.14	0.02	0.81	0.02	0.98	0.02	0.17	0.02
1983	0.99	0.02	1.59	0.02	1.66	0.02	0.59	0.02	0.67	0.02	0.07	0.02
1985	1.11	0.04	1.84	0.04	1.75	0.04	0.73	0.03	0.65	0.04	-0.09	0.04
1986	1.13	0.04	2.02	0.04	2.02	0.04	0.90	0.02	0.90	0.03	0.00	0.03
1989	1.08	0.03	1.92	0.03	1.98	0.03	0.84	0.02	0.91	0.02	0.07	0.02
1990	0.81	0.06	1.61	0.07	1.85	0.07	0.79	0.04	1.04	0.05	0.25	0.06
1991	1.32	0.02	2.21	0.02	2.34	0.02	0.89	0.02	1.02	0.02	0.13	0.02
1992	0.72	0.02	0.97	0.02	0.80	0.02	0.25	0.02	0.08	0.02	-0.17	0.02
2000	1.34	0.02	2.37	0.02	2.71	0.02	1.03	0.02	1.37	0.02	0.33	0.02
2001	1.23	0.03	2.08	0.03	2.14	0.04	0.85	0.02	0.91	0.03	0.06	0.03
2002	1.14	0.04	1.89	0.04	2.06	0.05	0.75	0.03	0.92	0.04	0.17	0.04
2003	1.21	0.03	2.02	0.03	2.19	0.03	0.80	0.02	0.98	0.03	0.17	0.03
2006	1.03	0.02	1.73	0.02	1.82	0.02	0.70	0.02	0.80	0.02	0.09	0.02
2008	1.20	0.02	1.92	0.02	1.93	0.02	0.72	0.02	0.73	0.02	0.01	0.02
2010	0.99	0.03	1.75	0.03	1.83	0.04	0.75	0.02	0.83	0.03	0.08	0.03
2011	1.08	0.02	1.84	0.02	1.86	0.03	0.76	0.02	0.79	0.02	0.02	0.02

VCC	$u - g$	$u - g$ error	$u - i$	$u - i$ error	$u - z$	$u - z$ error	$g - i$	$g - i$ error	$g - z$	$g - z$ error	$i - z$	$i - z$ error
2012	1.32	0.02	2.19	0.02	2.33	0.02	0.87	0.02	1.01	0.02	0.14	0.02
2014	1.25	0.03	2.18	0.03	2.21	0.03	0.92	0.02	0.96	0.02	0.04	0.02
2019	1.29	0.02	2.20	0.02	2.36	0.02	0.91	0.02	1.06	0.02	0.15	0.02
2025	1.09	0.03	1.91	0.03	1.95	0.03	0.82	0.02	0.85	0.03	0.04	0.03
2028	1.00	0.02	1.61	0.02	1.72	0.02	0.61	0.02	0.73	0.02	0.11	0.02

TABLE 7.3 The VCC number, radius measured at the 28 mag arcsec⁻² isophote in the g band, mean surface brightnesses within that radius in each band and errors on all surface brightnesses.

VCC	rad28 g	sb28 u	sb28 u error	sb28 g	sb28 g error	sb28 i	sb28 i error	sb28 z	sb28 z error
299	49.93	26.28	0.03	25.80	0.03	25.13	0.03	24.96	0.03
306	15.98	26.56	0.07	25.87	0.07	25.48	0.07	25.16	0.07
309	37.95	25.75	0.03	25.35	0.03	24.98	0.03	24.77	0.03
310	21.97	27.43	0.06	26.53	0.05	26.32	0.05	25.81	0.06
319	85.88	25.94	0.02	25.45	0.02	24.95	0.02	24.78	0.02
322	89.87	24.85	0.02	25.49	0.02	24.94	0.02	24.84	0.02
328	47.93	25.46	0.03	25.09	0.03	24.66	0.03	24.56	0.03
330	41.94	26.33	0.03	25.55	0.03	25.02	0.03	24.94	0.03
333	17.97	26.55	0.07	26.08	0.06	25.68	0.06	25.51	0.07
334	29.96	24.38	0.04	24.09	0.04	23.55	0.04	23.43	0.04
350	49.93	26.46	0.03	26.30	0.03	25.99	0.03	25.85	0.03
353	21.97	26.84	0.06	26.16	0.05	25.60	0.05	25.36	0.05
354	49.93	26.47	0.03	25.71	0.03	25.06	0.03	24.85	0.03
355	89.87	23.91	0.02	22.95	0.02	22.07	0.02	21.68	0.02
361	23.97	25.80	0.05	25.06	0.05	24.41	0.05	23.95	0.05
364	41.94	26.49	0.04	25.92	0.03	24.71	0.03	24.04	0.03
369	101.86	24.85	0.02	23.51	0.02	22.97	0.02	22.69	0.02
372	23.97	26.84	0.06	26.18	0.05	25.35	0.05	25.07	0.05
389	67.90	24.75	0.02	23.97	0.02	23.39	0.02	22.86	0.02
391	21.97	26.79	0.06	25.94	0.06	25.30	0.06	24.99	0.06
394	27.96	26.30	0.04	25.50	0.04	24.70	0.04	24.57	0.04
401	17.97	26.35	0.06	25.49	0.06	24.98	0.06	25.13	0.06
407	77.89	25.01	0.02	24.28	0.02	23.45	0.02	23.26	0.02
410	17.97	24.56	0.06	24.31	0.06	23.96	0.06	23.85	0.06
414	29.96	26.26	0.04	25.52	0.04	24.73	0.04	24.53	0.04
418	31.95	26.50	0.04	25.91	0.04	25.57	0.04	25.20	0.04
421	27.96	26.51	0.05	25.92	0.04	25.15	0.04	24.92	0.04
425	33.95	26.97	0.04	26.40	0.04	26.06	0.04	25.97	0.04
426	23.97	26.93	0.05	26.39	0.05	25.64	0.05	25.52	0.05
428	31.95	24.89	0.04	24.80	0.04	24.78	0.04	25.10	0.04
431	29.96	26.62	0.05	26.09	0.04	25.39	0.04	25.50	0.04
444	37.95	26.83	0.04	25.96	0.03	25.49	0.03	25.18	0.03
447	17.97	27.23	0.08	26.55	0.07	26.12	0.07	26.20	0.09
452	39.94	25.60	0.03	24.82	0.03	24.02	0.03	23.78	0.03
455	17.97	25.43	0.06	24.75	0.06	24.22	0.06	24.13	0.06
456	21.97	26.58	0.06	25.79	0.05	24.99	0.05	24.88	0.05
458	35.95	26.06	0.04	25.43	0.03	24.86	0.03	24.60	0.03
461	45.93	26.31	0.03	25.59	0.03	24.84	0.03	24.57	0.03

VCC	rad28 g	sb28 u	sb28 u	sb28 g	sb28 g	sb28 i	sb28 i	sb28 z	sb28 z
			error		error		error		error
471	17.97	26.38	0.07	25.89	0.06	25.34	0.06	25.40	0.07
477	43.94	26.53	0.03	26.09	0.03	25.47	0.03	25.31	0.03
493	15.98	25.71	0.07	24.72	0.07	23.94	0.07	24.00	0.07
494	33.95	26.41	0.04	25.61	0.04	24.78	0.04	24.71	0.04
496	21.97	26.73	0.06	26.12	0.05	25.64	0.05	25.59	0.06
498	17.97	26.23	0.07	25.67	0.06	24.87	0.06	24.74	0.07
501	33.95	25.93	0.04	25.22	0.04	24.49	0.03	24.35	0.04
502	15.98	26.99	0.08	26.38	0.07	25.87	0.07	25.47	0.07
503	29.96	26.47	0.04	25.85	0.04	25.26	0.04	24.72	0.04
504	39.94	25.75	0.03	25.03	0.03	24.47	0.03	24.62	0.03
511	19.97	27.03	0.07	26.37	0.06	25.63	0.06	25.59	0.06
512	65.91	25.94	0.02	25.24	0.02	24.69	0.02	24.63	0.02
519	21.97	27.01	0.06	26.39	0.05	25.87	0.06	25.61	0.06
529	25.96	26.55	0.05	25.80	0.04	25.15	0.04	24.89	0.05
532	27.96	26.71	0.05	26.33	0.04	25.85	0.05	25.84	0.05
537	23.97	27.11	0.06	26.45	0.05	25.83	0.05	25.58	0.05
539	31.95	25.97	0.04	25.26	0.04	24.71	0.04	24.37	0.04
540	13.98	27.13	0.09	26.52	0.08	26.29	0.08	26.28	0.08
544	27.96	24.79	0.04	25.04	0.04	24.60	0.04	24.54	0.04
547	21.97	26.78	0.06	26.45	0.05	25.93	0.05	25.74	0.06
556	15.98	27.12	0.08	26.54	0.07	25.85	0.07	25.80	0.08
560	27.96	26.23	0.04	25.43	0.04	24.78	0.04	24.91	0.06
561	21.97	26.03	0.05	25.16	0.05	24.58	0.05	24.60	0.05
562	31.95	24.12	0.04	23.77	0.04	23.44	0.04	23.28	0.04
564	11.98	27.55	0.11	26.89	0.10	26.46	0.10	26.09	0.11
574	39.94	27.11	0.04	26.27	0.03	25.83	0.03	25.79	0.04
575	37.95	23.76	0.03	22.77	0.03	22.08	0.03	21.77	0.03
582	13.98	26.76	0.10	26.37	0.08	25.59	0.09	25.48	0.10
584	39.94	26.50	0.03	25.93	0.03	25.25	0.03	24.85	0.03
585	41.94	27.18	0.03	26.35	0.03	25.93	0.03	25.67	0.03
592	45.93	25.54	0.03	24.75	0.03	24.10	0.03	23.94	0.03
594	39.94	26.45	0.03	25.78	0.03	25.16	0.03	24.97	0.03
603	13.98	27.15	0.09	26.31	0.08	25.98	0.08	25.86	0.08
605	17.97	27.04	0.07	26.60	0.06	25.95	0.07	25.81	0.07
607	23.97	27.46	0.07	26.90	0.05	26.53	0.05	26.40	0.05
611	53.92	26.21	0.03	25.58	0.02	25.01	0.02	25.05	0.03
615	31.95	27.72	0.06	27.22	0.04	26.46	0.04	26.47	0.04
622	25.96	26.22	0.05	25.71	0.04	25.13	0.04	24.79	0.05
624	21.97	27.09	0.06	26.48	0.05	25.96	0.05	26.06	0.05
625	33.95	26.35	0.04	25.73	0.04	25.11	0.04	24.77	0.04
628	23.97	27.18	0.06	26.64	0.05	25.96	0.05	25.71	0.06

VCC	rad28 g	sb28 u	sb28 u	sb28 g	sb28 g	sb28 i	sb28 i	sb28 z	sb28 z
			error		error		error		error
632	31.95	26.30	0.04	25.81	0.04	25.56	0.04	24.62	0.04
640	17.97	27.15	0.08	26.51	0.06	25.94	0.07	25.86	0.07
643	17.97	26.71	0.07	26.07	0.06	25.32	0.06	25.10	0.06
645	25.96	26.95	0.05	26.22	0.04	25.57	0.04	25.66	0.05
651	27.96	25.93	0.04	25.58	0.04	25.25	0.04	25.04	0.04
658	23.97	27.47	0.06	26.64	0.05	25.89	0.05	25.63	0.05
659	21.97	26.65	0.05	25.81	0.05	25.30	0.05	25.30	0.05
660	23.97	25.24	0.05	24.78	0.05	23.89	0.05	23.65	0.05
668	27.96	26.65	0.05	25.69	0.04	25.10	0.04	25.35	0.04
673	13.98	27.24	0.09	26.52	0.08	25.99	0.08	25.49	0.09
674	37.95	26.85	0.04	26.21	0.03	25.61	0.03	25.35	0.03
678	29.96	27.37	0.05	26.91	0.04	26.11	0.04	25.94	0.04
684	31.95	25.69	0.04	24.74	0.04	23.92	0.04	23.73	0.04
686	19.97	26.91	0.07	26.13	0.06	25.75	0.06	25.34	0.07
687	23.97	26.83	0.05	25.97	0.05	25.20	0.05	25.01	0.05
688	51.93	24.14	0.03	23.31	0.03	22.51	0.02	22.18	0.03
691	15.98	27.22	0.08	26.77	0.07	25.90	0.08	25.72	0.08
692	93.87	24.66	0.02	23.99	0.02	23.51	0.02	23.76	0.02
698	83.88	24.48	0.02	23.57	0.02	22.63	0.02	22.27	0.02
701	21.97	27.60	0.07	27.06	0.06	26.87	0.06	26.86	0.07
702	15.98	26.22	0.08	25.51	0.07	24.70	0.07	24.82	0.08
703	47.93	26.11	0.03	24.92	0.03	24.15	0.03	23.81	0.03
704	25.96	27.09	0.05	26.37	0.05	25.80	0.05	25.62	0.05
705	41.94	26.61	0.03	26.15	0.03	25.62	0.03	25.50	0.03
706	23.97	26.27	0.05	25.57	0.05	24.97	0.05	25.13	0.05
708	19.97	26.71	0.06	26.00	0.06	25.35	0.06	25.19	0.06
709	21.97	26.80	0.06	26.53	0.05	25.79	0.05	25.57	0.06
711	37.95	26.45	0.03	25.53	0.03	24.88	0.03	24.50	0.03
719	19.97	26.64	0.06	26.00	0.06	25.54	0.06	25.39	0.06
725	45.93	26.29	0.03	25.37	0.03	25.02	0.03	24.83	0.03
731	139.80	23.88	0.02	23.03	0.02	22.19	0.02	21.92	0.02
732	21.97	27.14	0.06	26.50	0.05	26.05	0.06	25.99	0.06
733	19.97	25.82	0.06	25.01	0.06	24.18	0.06	24.08	0.06
743	13.98	27.40	0.10	26.96	0.08	26.43	0.09	26.39	0.10
745	59.91	25.16	0.03	24.35	0.02	23.50	0.02	23.24	0.02
746	31.95	26.54	0.05	25.90	0.04	25.11	0.04	25.06	0.04
747	33.95	26.63	0.04	25.91	0.04	25.47	0.04	24.86	0.04
748	29.96	26.47	0.04	25.61	0.04	24.98	0.04	24.60	0.04
752	15.98	27.35	0.08	26.70	0.07	26.28	0.08	26.19	0.08
753	41.94	26.37	0.03	25.67	0.03	25.05	0.03	24.84	0.03
754	21.97	26.84	0.06	26.31	0.05	26.09	0.05	25.83	0.06

VCC	rad28 g	sb28 u	sb28 u	sb28 g	sb28 g	sb28 i	sb28 i	sb28 z	sb28 z
			error		error		error		error
755	37.95	26.10	0.04	25.31	0.03	24.55	0.03	24.31	0.03
756	35.95	26.10	0.04	25.43	0.03	24.84	0.03	24.70	0.03
757	21.97	26.36	0.06	25.67	0.05	25.32	0.05	24.94	0.05
758	89.87	24.43	0.02	23.67	0.02	22.92	0.02	21.83	0.02
760	27.96	26.58	0.04	25.59	0.04	25.04	0.04	24.94	0.04
762	37.95	25.43	0.03	24.56	0.03	23.74	0.03	23.18	0.03
765	39.94	25.17	0.03	24.78	0.03	23.56	0.03	23.85	0.03
774	19.97	26.90	0.06	26.49	0.06	26.03	0.06	25.77	0.06
775	37.95	27.15	0.04	26.58	0.03	26.02	0.04	25.84	0.04
778	65.91	23.46	0.02	22.71	0.02	21.74	0.02	21.32	0.02
779	31.95	26.79	0.04	25.96	0.04	25.21	0.04	25.13	0.04
780	31.95	26.81	0.04	26.16	0.04	25.45	0.04	25.22	0.04
781	55.92	24.66	0.03	24.24	0.02	23.36	0.02	22.78	0.02
788	53.92	25.48	0.03	24.79	0.02	24.12	0.02	23.84	0.02
789	29.96	27.12	0.05	26.37	0.04	25.62	0.04	25.79	0.04
790	35.95	25.52	0.04	24.68	0.03	23.83	0.03	23.61	0.03
792	137.80	25.23	0.02	24.35	0.02	23.41	0.02	23.15	0.02
793	39.94	25.69	0.03	25.22	0.03	24.74	0.03	24.61	0.03
796	13.98	27.46	0.10	26.70	0.08	26.43	0.09	26.22	0.09
800	21.97	26.87	0.06	26.14	0.05	25.47	0.05	25.30	0.05
802	45.93	25.42	0.03	25.18	0.03	25.05	0.03	24.49	0.03
803	25.96	27.30	0.05	26.59	0.05	26.07	0.05	25.83	0.05
804	21.97	27.70	0.07	27.27	0.06	26.71	0.06	26.73	0.08
807	15.98	26.92	0.08	26.13	0.07	25.41	0.07	25.43	0.08
808	39.94	26.72	0.03	25.75	0.03	25.07	0.03	24.76	0.03
809	79.89	24.60	0.02	23.91	0.02	23.00	0.02	22.95	0.02
810	31.95	25.96	0.04	24.99	0.04	24.24	0.04	23.94	0.04
811	29.96	28.20	0.05	27.45	0.04	27.11	0.05	26.96	0.05
812	41.94	26.10	0.03	25.41	0.03	24.69	0.03	24.07	0.03
815	41.94	25.95	0.03	25.20	0.03	24.57	0.03	24.45	0.03
821	15.98	27.45	0.09	26.65	0.07	25.85	0.08	25.56	0.08
823	41.94	25.83	0.03	24.70	0.03	24.05	0.03	23.90	0.03
824	35.95	26.65	0.04	25.95	0.03	25.25	0.03	25.04	0.03
828	71.90	23.90	0.02	22.95	0.02	21.96	0.02	21.96	0.02
833	23.97	26.26	0.05	25.32	0.05	24.35	0.05	24.48	0.05
838	23.97	26.34	0.05	25.49	0.05	24.68	0.05	24.54	0.05
839	29.96	27.02	0.04	26.29	0.04	25.62	0.04	25.65	0.04
840	35.95	26.99	0.04	26.26	0.03	26.03	0.04	25.37	0.04
843	17.97	26.84	0.07	25.88	0.06	25.34	0.06	25.15	0.06
845	25.96	27.06	0.05	26.37	0.04	25.93	0.05	25.59	0.05
846	37.95	25.77	0.03	25.10	0.03	24.60	0.03	24.00	0.03

VCC	rad28 g	sb28 u	sb28 u	sb28 g	sb28 g	sb28 i	sb28 i	sb28 z	sb28 z
			error		error		error		error
849	81.88	24.42	0.02	23.96	0.02	23.52	0.02	23.14	0.02
850	17.97	27.18	0.09	26.14	0.07	25.80	0.07	26.13	0.08
851	99.86	24.54	0.02	23.82	0.02	23.02	0.02	22.58	0.02
853	13.98	27.59	0.10	26.82	0.08	26.17	0.10	26.26	0.10
854	41.94	26.02	0.03	25.33	0.03	24.75	0.03	24.62	0.03
855	37.95	26.11	0.04	25.46	0.03	24.78	0.03	24.85	0.03
856	51.93	24.90	0.03	24.00	0.03	23.09	0.02	22.90	0.03
861	37.95	26.29	0.04	25.73	0.03	24.97	0.03	24.80	0.03
863	37.95	27.25	0.04	26.54	0.03	26.00	0.03	25.86	0.04
867	17.97	26.84	0.07	26.04	0.06	25.26	0.06	25.24	0.07
868	15.98	27.18	0.08	26.49	0.07	25.83	0.08	25.85	0.09
869	49.93	26.73	0.03	25.98	0.03	25.70	0.03	25.37	0.03
870	73.89	25.07	0.02	24.37	0.02	23.68	0.02	23.35	0.02
871	63.91	26.01	0.02	25.21	0.02	24.65	0.02	24.58	0.02
872	27.96	26.09	0.04	25.15	0.04	24.36	0.04	24.20	0.04
876	21.97	26.71	0.06	26.04	0.05	25.25	0.05	25.23	0.05
877	25.96	26.22	0.05	25.65	0.04	24.85	0.04	24.92	0.05
883	15.98	26.42	0.08	25.56	0.07	24.77	0.07	24.70	0.07
884	29.96	27.61	0.05	27.04	0.04	26.60	0.05	26.36	0.05
886	9.99	27.16	0.12	26.56	0.11	26.23	0.15	26.03	0.12
891	11.98	27.23	0.11	26.53	0.09	26.17	0.10	26.03	0.11
892	17.97	26.33	0.06	25.52	0.06	24.92	0.06	24.65	0.06
893	15.98	27.01	0.09	26.45	0.07	25.71	0.07	25.77	0.08
894	15.98	27.52	0.09	26.74	0.07	26.39	0.08	26.28	0.08
895	33.95	26.88	0.04	26.25	0.04	25.75	0.04	25.63	0.04
896	31.95	26.35	0.04	25.64	0.04	25.19	0.04	25.11	0.04
897	19.97	26.92	0.06	26.26	0.06	25.70	0.06	25.97	0.06
900	27.96	26.93	0.05	26.43	0.04	25.79	0.04	25.59	0.05
902	19.97	27.04	0.06	26.31	0.06	25.68	0.06	25.76	0.06
903	15.98	26.66	0.07	26.01	0.07	25.27	0.07	25.25	0.07
906	17.97	26.95	0.07	26.30	0.06	26.16	0.06	25.22	0.07
914	19.97	27.14	0.06	26.24	0.06	25.70	0.06	25.51	0.07
915	29.96	27.16	0.05	26.68	0.04	25.91	0.04	25.61	0.04
916	21.97	24.91	0.05	23.61	0.05	22.73	0.05	22.48	0.05
917	55.92	24.74	0.03	24.22	0.02	23.24	0.02	22.99	0.02
922	15.98	27.18	0.08	26.53	0.07	25.80	0.08	25.85	0.09
923	17.97	27.13	0.07	26.21	0.06	25.64	0.07	25.71	0.07
925	27.96	27.48	0.05	26.88	0.04	26.44	0.04	26.30	0.05
926	41.94	26.34	0.03	25.88	0.03	25.12	0.03	25.02	0.03
927	15.98	28.47	0.09	27.03	0.07	26.19	0.07	25.94	0.08
928	43.94	25.43	0.03	24.77	0.03	24.10	0.03	23.92	0.03

VCC	rad28 g	sb28 u	sb28 u	sb28 g	sb28 g	sb28 i	sb28 i	sb28 z	sb28 z
			error		error		error		error
929	63.91	24.73	0.02	23.85	0.02	23.45	0.02	23.44	0.02
931	67.90	26.15	0.02	25.17	0.02	24.50	0.02	24.34	0.02
932	23.97	26.62	0.05	25.96	0.05	25.37	0.05	25.22	0.05
933	45.93	26.42	0.03	25.51	0.03	24.66	0.03	24.56	0.03
935	19.97	27.07	0.07	26.29	0.06	25.38	0.06	25.11	0.06
936	41.94	25.76	0.03	24.96	0.03	24.18	0.03	23.97	0.03
937	19.97	27.51	0.07	26.92	0.06	26.38	0.06	26.77	0.07
940	51.93	25.35	0.03	24.50	0.03	23.76	0.02	23.29	0.03
941	15.98	26.13	0.07	25.39	0.07	24.85	0.07	24.75	0.07
942	13.98	26.80	0.09	26.24	0.08	25.76	0.08	25.69	0.09
943	17.97	26.41	0.07	25.84	0.06	25.16	0.06	25.00	0.07
945	55.92	25.13	0.03	24.72	0.02	24.49	0.02	24.51	0.02
948	15.98	26.79	0.08	26.37	0.07	25.89	0.07	25.74	0.09
949	59.91	25.90	0.03	25.11	0.02	24.57	0.02	24.18	0.02
951	71.90	25.23	0.02	24.38	0.02	23.71	0.02	23.45	0.02
956	25.96	26.84	0.05	26.28	0.05	25.52	0.05	25.39	0.05
959	13.98	27.31	0.11	26.88	0.08	26.02	0.09	26.32	0.11
960	15.98	27.14	0.08	26.63	0.07	25.98	0.07	25.76	0.08
963	29.96	25.93	0.04	25.44	0.04	24.98	0.04	24.82	0.04
964	17.97	26.21	0.06	25.29	0.06	24.67	0.06	24.50	0.06
965	59.91	25.49	0.03	24.66	0.02	23.89	0.02	23.68	0.02
968	23.97	26.34	0.06	25.92	0.05	25.35	0.05	25.25	0.06
970	15.98	27.31	0.09	26.81	0.07	26.24	0.08	26.07	0.08
972	35.95	26.55	0.04	25.81	0.03	25.21	0.03	24.78	0.03
974	37.95	25.60	0.03	24.93	0.03	24.43	0.03	23.94	0.03
976	27.96	26.13	0.04	25.43	0.04	24.72	0.04	24.49	0.04
978	41.94	26.80	0.04	26.38	0.03	25.73	0.03	25.32	0.04
983	37.95	27.51	0.06	27.04	0.04	25.93	0.04	26.18	0.05
984	97.86	24.22	0.02	23.27	0.02	22.50	0.02	22.21	0.02
986	15.98	27.04	0.08	26.65	0.07	26.11	0.07	25.86	0.08
988	17.97	27.43	0.10	27.19	0.07	26.30	0.07	26.28	0.10
991	95.86	23.69	0.02	23.01	0.02	22.38	0.02	21.16	0.02
992	33.95	26.17	0.04	25.24	0.03	24.51	0.03	24.22	0.04
996	25.96	26.55	0.05	25.91	0.04	25.28	0.04	25.07	0.05
997	19.97	26.29	0.06	25.33	0.06	24.52	0.06	24.77	0.06
998	33.95	26.64	0.04	26.09	0.04	25.38	0.04	25.33	0.04
1000	19.97	26.83	0.06	25.86	0.06	25.19	0.06	25.03	0.06
1001	29.96	25.56	0.04	25.30	0.04	24.99	0.04	24.97	0.04
1004	31.95	27.50	0.05	26.99	0.04	26.27	0.04	26.08	0.05
1005	45.93	26.04	0.03	25.37	0.03	24.72	0.03	24.41	0.03
1006	23.97	27.18	0.05	26.36	0.05	25.70	0.05	25.69	0.05

VCC	rad28 g	sb28 u	sb28 u error	sb28 g	sb28 g error	sb28 i	sb28 i error	sb28 z	sb28 z error
1008	9.99	26.89	0.12	26.36	0.11	25.67	0.11	25.70	0.14
1009	15.98	26.94	0.08	26.21	0.07	25.65	0.07	25.55	0.08
1010	73.89	24.77	0.02	23.89	0.02	22.98	0.02	22.75	0.02
1011	67.90	25.05	0.02	24.43	0.02	23.80	0.02	23.48	0.02
1012	11.98	27.38	0.10	26.42	0.09	26.02	0.10	26.12	0.11
1013	31.95	25.92	0.04	25.35	0.04	25.05	0.04	24.97	0.04
1014	21.97	27.28	0.06	26.60	0.05	25.95	0.05	26.09	0.07
1015	9.99	27.38	0.13	26.41	0.11	25.67	0.12	25.71	0.16
1020	29.96	26.06	0.04	25.08	0.04	24.21	0.04	24.25	0.04
1021	57.92	25.66	0.03	24.97	0.02	24.46	0.02	24.11	0.02
1022	17.97	27.54	0.08	26.82	0.07	26.14	0.07	26.18	0.08
1023	15.98	27.67	0.09	27.12	0.07	26.49	0.08	26.28	0.09
1025	63.91	23.69	0.02	22.85	0.02	21.86	0.02	21.44	0.02
1026	33.95	26.63	0.04	26.02	0.04	25.38	0.04	24.91	0.04
1027	29.96	27.11	0.05	26.31	0.04	26.14	0.04	25.66	0.04
1029	21.97	26.65	0.06	26.00	0.05	25.55	0.05	25.19	0.06
1030	99.86	23.32	0.02	22.64	0.02	21.72	0.02	21.09	0.02
1036	77.89	24.69	0.02	23.23	0.02	22.82	0.02	22.55	0.02
1037	13.98	27.21	0.09	26.47	0.08	26.08	0.08	26.16	0.09
1039	31.95	26.23	0.04	25.68	0.04	25.15	0.04	25.03	0.04
1040	23.97	25.47	0.05	24.60	0.05	24.86	0.05	25.48	0.05
1044	31.95	25.86	0.04	25.09	0.04	24.25	0.04	23.86	0.04
1045	27.96	27.48	0.06	26.92	0.04	26.07	0.05	26.01	0.05
1046	13.98	27.69	0.10	26.92	0.08	26.62	0.09	26.62	0.10
1047	131.81	24.72	0.02	23.72	0.02	22.83	0.02	22.50	0.02
1049	49.93	24.88	0.03	24.02	0.03	23.38	0.03	23.10	0.03
1052	29.96	27.43	0.06	27.37	0.04	26.86	0.04	26.71	0.07
1053	17.97	27.06	0.08	26.60	0.06	26.32	0.07	26.08	0.07
1056	23.97	27.43	0.06	26.67	0.05	26.23	0.05	26.11	0.05
1057	15.98	27.36	0.08	26.68	0.07	26.07	0.07	25.91	0.08
1059	25.96	25.78	0.05	25.04	0.04	24.18	0.04	24.08	0.04
1063	17.97	27.09	0.08	26.48	0.06	25.94	0.07	25.91	0.09
1064	33.95	26.13	0.04	25.40	0.04	24.79	0.04	24.70	0.04
1069	45.93	25.59	0.03	24.98	0.03	24.25	0.03	24.17	0.03
1070	19.97	27.37	0.07	26.67	0.06	26.22	0.06	26.30	0.07
1071	19.97	26.53	0.06	25.50	0.06	24.51	0.06	24.39	0.06
1073	89.87	25.23	0.02	24.68	0.02	23.72	0.02	22.90	0.02
1074	25.96	27.34	0.06	26.65	0.05	26.08	0.05	26.32	0.09
1075	59.91	25.56	0.03	24.79	0.02	24.00	0.02	23.68	0.02
1076	31.95	26.47	0.04	25.88	0.04	25.32	0.04	25.03	0.04
1079	39.94	26.77	0.03	25.98	0.03	25.76	0.03	25.13	0.03

VCC	rad28 g	sb28 u	sb28 u	sb28 g	sb28 g	sb28 i	sb28 i	sb28 z	sb28 z
			error		error		error		error
1081	19.97	26.97	0.06	26.28	0.06	25.71	0.06	25.57	0.06
1083	11.98	27.15	0.10	26.07	0.09	25.66	0.09	25.37	0.11
1086	103.85	24.18	0.02	23.17	0.02	22.16	0.02	21.71	0.02
1088	13.98	27.11	0.10	26.63	0.08	25.91	0.09	25.64	0.09
1089	27.96	27.22	0.05	26.37	0.04	25.77	0.04	25.50	0.04
1093	41.94	26.39	0.03	25.63	0.03	25.05	0.03	25.02	0.03
1095	15.98	26.33	0.07	25.86	0.07	25.24	0.07	25.05	0.07
1096	15.98	27.33	0.09	27.00	0.07	26.42	0.08	26.05	0.08
1098	19.97	26.50	0.08	26.06	0.06	25.45	0.06	25.23	0.08
1100	27.96	26.60	0.04	25.79	0.04	25.30	0.04	25.14	0.04
1101	57.92	25.81	0.03	25.26	0.02	24.88	0.02	24.24	0.02
1103	13.98	27.24	0.12	27.24	0.09	26.80	0.10	26.89	0.16
1104	47.93	25.36	0.03	24.53	0.03	23.75	0.03	23.55	0.03
1105	37.95	26.44	0.03	25.66	0.03	24.95	0.03	24.80	0.03
1106	37.95	26.61	0.04	25.95	0.03	25.24	0.03	25.12	0.03
1107	61.91	26.08	0.03	25.29	0.02	24.67	0.02	24.30	0.02
1108	9.99	26.62	0.12	25.40	0.11	24.58	0.11	24.49	0.11
1109	27.96	26.49	0.05	26.39	0.04	25.76	0.04	25.49	0.05
1113	21.97	27.18	0.07	26.87	0.05	26.37	0.06	26.46	0.07
1115	27.96	26.89	0.05	26.00	0.04	25.50	0.04	24.99	0.05
1118	111.84	23.65	0.02	23.52	0.02	22.47	0.02	21.96	0.02
1119	43.94	26.29	0.03	25.49	0.03	24.86	0.03	24.90	0.03
1120	33.95	26.17	0.04	25.43	0.03	24.77	0.03	24.70	0.04
1122	67.90	24.90	0.02	24.19	0.02	23.51	0.02	23.25	0.02
1123	37.95	26.61	0.03	25.88	0.03	25.37	0.03	25.25	0.03
1124	41.94	26.91	0.03	26.22	0.03	25.71	0.03	25.50	0.03
1125	123.82	23.83	0.02	23.17	0.02	22.81	0.02	21.90	0.02
1126	117.83	24.28	0.02	23.78	0.02	22.84	0.02	22.38	0.02
1127	29.96	26.26	0.05	25.69	0.04	24.83	0.04	24.57	0.05
1128	47.93	26.66	0.03	25.99	0.03	25.34	0.03	25.13	0.03
1129	23.97	26.30	0.05	25.47	0.05	24.71	0.05	24.59	0.05
1131	31.95	27.08	0.04	26.30	0.04	25.63	0.04	26.06	0.05
1135	19.97	27.29	0.06	26.64	0.06	26.18	0.06	26.36	0.06
1136	25.96	27.01	0.05	26.36	0.04	25.93	0.05	25.94	0.05
1137	33.95	27.09	0.04	26.41	0.04	25.73	0.04	25.52	0.04
1140	19.97	26.79	0.06	26.15	0.06	25.44	0.06	25.21	0.06
1143	17.97	26.94	0.07	26.17	0.06	25.56	0.06	25.43	0.07
1144	19.97	27.80	0.09	27.30	0.06	26.79	0.07	26.41	0.15
1146	69.90	24.29	0.02	23.36	0.02	22.45	0.02	22.15	0.02
1147	11.98	27.20	0.11	26.43	0.09	26.20	0.10	26.05	0.11
1149	35.95	27.65	0.04	27.09	0.03	26.62	0.04	26.76	0.04

VCC	rad28 g	sb28 u	sb28 u error	sb28 g	sb28 g error	sb28 i	sb28 i error	sb28 z	sb28 z error
1151	33.95	26.48	0.04	25.66	0.04	25.02	0.04	25.03	0.04
1158	131.81	23.89	0.02	23.05	0.02	22.07	0.02	21.60	0.02
1160	17.97	26.62	0.07	25.57	0.06	24.82	0.06	24.67	0.07
1161	19.97	27.02	0.07	26.39	0.06	25.71	0.06	25.54	0.07
1162	15.98	27.53	0.09	26.96	0.07	26.48	0.07	25.96	0.09
1163	31.95	25.98	0.04	25.11	0.04	24.30	0.04	23.85	0.04
1164	45.93	26.53	0.03	25.88	0.03	25.32	0.03	24.77	0.03
1165	23.97	26.81	0.05	26.16	0.05	25.54	0.05	25.58	0.06
1167	47.93	26.63	0.03	24.94	0.03	24.23	0.03	23.95	0.03
1170	13.98	27.34	0.09	26.57	0.08	26.33	0.08	26.05	0.09
1172	39.94	25.71	0.03	24.73	0.03	23.82	0.03	23.67	0.03
1173	39.94	25.57	0.03	24.69	0.03	24.07	0.03	23.96	0.03
1175	35.95	24.99	0.04	24.40	0.03	23.78	0.03	23.56	0.03
1177	37.95	26.85	0.04	26.42	0.03	25.73	0.03	25.12	0.04
1178	59.91	24.02	0.03	22.94	0.02	21.97	0.02	21.69	0.02
1179	59.91	25.03	0.03	24.61	0.02	24.19	0.02	24.08	0.02
1183	73.89	24.92	0.02	24.09	0.02	23.28	0.02	22.74	0.02
1184	17.97	26.55	0.07	26.10	0.06	25.34	0.07	25.17	0.07
1185	51.93	25.78	0.03	25.15	0.03	24.41	0.02	24.07	0.03
1186	25.96	26.76	0.05	26.10	0.04	25.43	0.04	25.34	0.05
1187	15.98	27.01	0.08	26.28	0.07	25.61	0.07	26.05	0.10
1191	31.95	26.34	0.04	25.78	0.04	25.36	0.04	25.24	0.04
1193	45.93	24.06	0.03	22.56	0.03	21.75	0.03	21.75	0.03
1194	21.97	27.10	0.06	26.43	0.05	25.76	0.05	26.25	0.06
1195	19.97	26.77	0.06	26.36	0.06	25.77	0.06	25.83	0.06
1196	69.90	24.83	0.02	23.91	0.02	23.16	0.02	22.55	0.02
1197	17.97	27.18	0.08	26.74	0.06	25.89	0.07	25.86	0.09
1200	55.92	24.86	0.03	24.80	0.02	24.69	0.02	24.21	0.02
1204	51.93	26.00	0.03	25.19	0.03	24.38	0.02	24.27	0.03
1207	27.96	26.51	0.04	25.60	0.04	25.06	0.04	25.11	0.04
1209	33.95	25.90	0.04	25.76	0.04	25.10	0.04	25.01	0.04
1210	27.96	26.28	0.04	25.59	0.04	25.04	0.04	24.82	0.04
1211	15.98	26.44	0.08	25.67	0.07	25.10	0.07	24.90	0.07
1212	43.94	27.26	0.03	26.56	0.03	26.05	0.03	25.87	0.04
1213	37.95	26.24	0.03	25.49	0.03	24.91	0.03	24.44	0.03
1216	31.95	27.03	0.05	26.56	0.04	26.00	0.04	25.88	0.05
1217	79.89	26.50	0.02	26.02	0.02	25.67	0.02	25.22	0.02
1219	17.97	26.25	0.06	25.47	0.06	25.00	0.06	26.05	0.06
1222	53.92	25.96	0.03	25.07	0.02	24.33	0.02	24.17	0.02
1223	51.93	26.38	0.03	25.77	0.03	25.36	0.03	24.89	0.03
1225	21.97	25.94	0.05	24.87	0.05	24.28	0.05	24.11	0.05

VCC	rad28 g	sb28 u	sb28 u	sb28 g	sb28 g	sb28 i	sb28 i	sb28 z	sb28 z
			error		error		error		error
1227	29.96	26.85	0.04	26.32	0.04	25.85	0.04	25.86	0.04
1230	23.97	26.95	0.06	26.35	0.05	25.30	0.05	25.07	0.05
1235	41.94	26.63	0.04	26.17	0.03	25.38	0.03	25.22	0.03
1240	33.95	26.24	0.04	25.44	0.04	24.90	0.04	24.91	0.04
1241	23.97	27.34	0.06	26.83	0.05	26.24	0.05	26.12	0.06
1245	23.97	27.41	0.06	25.85	0.05	25.00	0.05	24.92	0.05
1246	29.96	26.89	0.04	26.41	0.04	25.91	0.04	25.49	0.04
1247	21.97	26.81	0.06	26.35	0.05	25.83	0.05	25.52	0.06
1251	13.98	27.16	0.10	26.34	0.08	26.11	0.09	25.85	0.09
1252	19.97	26.60	0.06	25.93	0.06	25.48	0.06	24.89	0.06
1254	39.94	25.49	0.03	24.35	0.03	23.59	0.03	23.22	0.03
1256	13.98	26.74	0.08	26.05	0.08	25.67	0.08	25.51	0.08
1259	35.95	26.64	0.04	25.92	0.03	25.37	0.03	25.29	0.04
1264	35.95	26.57	0.04	25.75	0.03	25.10	0.03	24.84	0.03
1265	19.97	27.32	0.06	26.32	0.06	25.61	0.06	25.31	0.06
1271	19.97	27.20	0.07	26.69	0.06	26.15	0.06	25.90	0.07
1281	23.97	27.06	0.05	26.00	0.05	25.37	0.05	25.22	0.05
1285	23.97	27.41	0.06	26.08	0.05	25.35	0.05	25.46	0.05
1287	45.93	27.67	0.04	27.12	0.03	26.73	0.03	26.87	0.04
1291	23.97	26.96	0.05	26.41	0.05	26.11	0.05	25.75	0.05
1292	17.97	27.02	0.07	26.22	0.06	25.49	0.06	25.12	0.07
1297	31.95	23.28	0.04	22.24	0.04	21.16	0.04	20.79	0.04
1299	13.98	27.04	0.09	26.18	0.08	25.58	0.08	25.59	0.10
1300	13.98	26.50	0.08	25.57	0.08	24.84	0.08	24.96	0.08
1301	19.97	27.11	0.07	26.37	0.06	25.98	0.06	25.76	0.07
1306	15.98	27.24	0.08	26.71	0.07	26.20	0.08	26.10	0.09
1307	19.97	26.13	0.06	25.24	0.06	24.62	0.06	24.45	0.06
1308	49.93	25.15	0.03	24.50	0.03	24.25	0.03	23.35	0.03
1309	23.97	27.18	0.07	26.78	0.05	25.95	0.05	25.95	0.07
1311	39.94	26.20	0.03	25.26	0.03	24.69	0.03	24.29	0.03
1312	23.97	26.96	0.06	26.36	0.05	25.90	0.05	25.73	0.05
1313	17.97	24.26	0.06	24.00	0.06	23.34	0.06	23.24	0.06
1315	23.97	28.95	0.09	27.64	0.05	26.89	0.06	26.72	0.06
1319	11.98	26.96	0.10	26.12	0.09	26.37	0.09	25.33	0.10
1327	61.91	22.56	0.02	22.26	0.02	21.71	0.02	21.25	0.02
1328	21.97	27.09	0.07	26.52	0.05	25.52	0.05	25.34	0.06
1330	119.83	24.69	0.02	23.73	0.02	22.77	0.02	22.58	0.02
1331	37.95	27.08	0.04	26.41	0.03	25.83	0.03	25.71	0.03
1333	41.94	26.38	0.03	25.51	0.03	24.79	0.03	24.68	0.03
1335	13.98	27.18	0.09	26.45	0.08	25.78	0.08	25.70	0.09
1336	37.95	27.27	0.04	26.42	0.03	25.52	0.03	25.43	0.03

VCC	rad28 g	sb28 u	sb28 u	sb28 g	sb28 g	sb28 i	sb28 i	sb28 z	sb28 z
			error		error		error		error
1345	21.97	27.27	0.07	26.65	0.05	25.97	0.06	26.27	0.06
1348	39.94	25.30	0.03	24.33	0.03	23.51	0.03	23.32	0.03
1349	21.97	26.51	0.06	25.82	0.05	25.05	0.05	24.92	0.06
1356	41.94	24.37	0.03	23.90	0.03	23.58	0.03	23.09	0.03
1357	19.97	27.34	0.07	26.40	0.06	25.79	0.06	25.77	0.07
1360	19.97	27.09	0.07	26.44	0.06	25.72	0.06	25.60	0.06
1361	45.93	27.00	0.04	26.64	0.03	25.97	0.03	26.01	0.03
1363	15.98	26.80	0.08	25.42	0.07	24.86	0.07	24.64	0.07
1365	19.97	27.01	0.06	26.49	0.06	26.08	0.06	26.04	0.06
1366	25.96	26.72	0.05	25.84	0.05	25.54	0.05	24.93	0.05
1367	27.96	27.26	0.05	26.73	0.04	26.03	0.04	25.96	0.05
1369	37.95	26.21	0.03	25.56	0.03	25.27	0.03	24.56	0.03
1370	29.96	26.77	0.04	25.73	0.04	25.09	0.04	25.01	0.04
1371	33.95	27.47	0.05	26.87	0.04	25.99	0.04	25.84	0.04
1377	47.93	26.41	0.03	25.70	0.03	25.37	0.03	25.43	0.03
1387	17.97	26.49	0.07	25.87	0.06	25.68	0.06	24.93	0.06
1389	37.95	25.52	0.03	24.86	0.03	24.17	0.03	24.00	0.03
1392	57.92	25.74	0.03	24.96	0.02	24.63	0.02	23.92	0.02
1394	29.96	26.65	0.04	26.04	0.04	25.36	0.04	24.94	0.04
1396	39.94	26.92	0.04	26.10	0.03	25.46	0.03	25.17	0.03
1402	23.97	27.03	0.05	26.09	0.05	25.39	0.05	25.39	0.05
1404	29.96	26.50	0.04	25.94	0.04	25.60	0.04	25.52	0.04
1405	17.97	27.69	0.08	26.85	0.06	26.24	0.07	26.08	0.09
1406	15.98	26.37	0.07	25.65	0.07	24.88	0.07	24.88	0.07
1407	49.93	25.31	0.03	24.43	0.03	23.78	0.03	23.39	0.03
1408	27.96	26.98	0.05	26.27	0.04	25.61	0.04	25.60	0.05
1411	45.93	25.06	0.03	24.68	0.03	24.15	0.03	24.10	0.03
1413	31.95	27.07	0.04	26.07	0.04	25.47	0.04	25.46	0.04
1415	27.96	26.66	0.05	26.24	0.04	25.47	0.04	25.39	0.04
1420	45.93	25.90	0.03	25.21	0.03	24.56	0.03	24.31	0.03
1422	63.91	25.13	0.02	24.17	0.02	23.52	0.02	23.18	0.02
1425	13.98	26.53	0.09	25.76	0.08	25.35	0.08	25.28	0.09
1426	49.93	26.23	0.03	25.42	0.03	24.69	0.03	24.60	0.03
1431	45.93	24.61	0.03	23.66	0.03	22.74	0.03	22.54	0.03
1432	27.96	26.15	0.04	25.29	0.04	24.78	0.04	24.33	0.04
1436	21.97	26.39	0.05	25.75	0.05	25.24	0.05	25.13	0.05
1437	33.95	23.87	0.04	23.14	0.03	22.57	0.03	22.40	0.03
1439	13.98	27.00	0.09	26.13	0.08	25.41	0.08	25.13	0.09
1441	29.96	25.22	0.04	24.16	0.04	23.47	0.04	23.19	0.04
1444	63.91	25.74	0.03	25.03	0.02	24.36	0.02	23.96	0.02
1446	35.95	25.84	0.04	24.96	0.03	24.40	0.03	23.97	0.03

VCC	rad28 g	sb28 u	sb28 u	sb28 g	sb28 g	sb28 i	sb28 i	sb28 z	sb28 z
			error		error		error		error
1454	33.95	27.13	0.05	26.44	0.04	25.72	0.04	25.53	0.04
1455	47.93	25.61	0.03	25.14	0.03	24.93	0.03	24.22	0.03
1461	19.97	27.46	0.08	26.83	0.06	26.01	0.06	25.93	0.09
1464	35.95	26.55	0.04	26.03	0.03	25.47	0.03	25.69	0.04
1470	13.98	26.65	0.09	25.91	0.08	25.30	0.08	25.24	0.09
1472	23.97	26.61	0.05	26.07	0.05	25.51	0.05	25.18	0.05
1481	25.96	26.42	0.05	25.67	0.04	25.05	0.04	24.71	0.05
1485	15.98	26.89	0.08	26.16	0.07	25.60	0.07	25.19	0.08
1487	19.97	27.26	0.07	26.61	0.06	25.97	0.06	25.78	0.07
1488	65.91	24.88	0.02	24.26	0.02	23.72	0.02	23.08	0.02
1489	53.92	25.63	0.03	24.93	0.02	24.28	0.02	23.96	0.02
1494	17.97	27.41	0.08	26.77	0.07	26.21	0.07	25.93	0.08
1496	27.96	26.25	0.05	25.63	0.04	25.17	0.04	24.80	0.04
1498	23.97	24.44	0.05	23.67	0.05	22.98	0.05	22.79	0.05
1500	15.98	27.01	0.08	26.12	0.07	25.62	0.07	25.46	0.07
1506	13.98	26.95	0.08	26.33	0.08	26.36	0.08	26.07	0.09
1511	27.96	26.90	0.05	26.39	0.04	25.71	0.04	25.55	0.04
1512	47.93	25.58	0.03	24.79	0.03	24.06	0.03	23.88	0.03
1518	23.97	26.94	0.05	26.36	0.05	25.79	0.05	25.43	0.05
1519	31.95	26.63	0.04	25.86	0.04	25.40	0.04	25.22	0.04
1520	11.98	27.60	0.11	26.51	0.09	26.15	0.10	25.98	0.11
1522	21.97	27.11	0.06	26.48	0.05	26.13	0.05	25.56	0.06
1531	23.97	26.17	0.05	25.44	0.05	24.79	0.05	24.67	0.05
1538	19.97	27.23	0.07	26.73	0.06	26.17	0.06	26.16	0.07
1546	19.97	27.37	0.07	26.55	0.06	25.50	0.06	25.04	0.06
1549	45.93	25.10	0.03	23.38	0.03	22.97	0.03	23.11	0.03
1551	25.96	27.76	0.06	27.21	0.05	26.44	0.05	26.48	0.06
1558	15.98	26.91	0.08	26.39	0.07	25.70	0.07	25.68	0.07
1561	53.92	26.67	0.03	25.95	0.02	25.50	0.02	25.43	0.03
1563	49.93	26.30	0.03	25.54	0.03	24.93	0.03	24.65	0.03
1565	35.95	26.60	0.04	25.80	0.03	25.49	0.03	25.18	0.03
1569	59.91	25.48	0.03	25.00	0.02	24.71	0.02	24.54	0.02
1573	39.94	25.72	0.03	25.01	0.03	24.27	0.03	23.93	0.03
1578	15.98	27.25	0.08	26.29	0.07	25.94	0.07	25.80	0.08
1582	37.95	26.52	0.03	25.98	0.03	25.61	0.03	25.32	0.03
1586	15.98	27.04	0.08	26.38	0.07	25.86	0.07	25.60	0.07
1591	19.97	26.95	0.06	26.27	0.06	25.84	0.06	25.47	0.06
1594	19.97	26.26	0.06	25.42	0.06	24.84	0.06	24.83	0.06
1599	37.95	27.06	0.04	26.60	0.03	25.78	0.03	25.56	0.03
1601	23.97	26.16	0.05	25.62	0.05	24.84	0.05	24.70	0.05
1602	41.94	26.49	0.03	25.86	0.03	25.25	0.03	25.33	0.03

VCC	rad28 g	sb28 u	sb28 u error	sb28 g	sb28 g error	sb28 i	sb28 i error	sb28 z	sb28 z error
1603	35.95	25.94	0.04	25.32	0.03	24.77	0.03	24.38	0.03
1604	41.94	26.34	0.03	25.53	0.03	25.00	0.03	24.64	0.03
1606	33.95	26.30	0.04	25.57	0.04	25.13	0.04	24.89	0.04
1609	35.95	26.79	0.04	26.09	0.03	25.48	0.03	25.46	0.03
1612	17.97	26.00	0.06	25.49	0.06	24.96	0.06	24.83	0.06
1613	21.97	27.04	0.06	26.18	0.05	25.36	0.05	25.36	0.06
1614	41.94	24.21	0.03	23.50	0.03	22.60	0.03	22.30	0.03
1616	43.94	26.04	0.03	25.35	0.03	24.60	0.03	24.49	0.03
1619	141.80	23.51	0.02	22.28	0.02	21.37	0.02	21.10	0.02
1621	21.97	26.74	0.06	26.10	0.05	25.43	0.05	25.37	0.06
1625	25.96	27.59	0.05	26.99	0.05	26.13	0.05	25.97	0.05
1626	19.97	26.71	0.06	25.88	0.06	25.24	0.06	24.92	0.06
1627	25.96	24.07	0.05	22.82	0.04	21.77	0.04	21.51	0.04
1630	75.89	23.94	0.02	23.06	0.02	22.00	0.02	21.78	0.02
1631	11.98	27.37	0.10	26.66	0.09	26.01	0.10	25.84	0.10
1634	15.98	27.70	0.09	27.05	0.07	26.57	0.08	26.23	0.08
1635	13.98	27.26	0.10	26.78	0.08	26.26	0.09	26.19	0.10
1637	25.96	26.46	0.05	26.11	0.04	25.48	0.05	25.51	0.05
1642	33.95	26.74	0.04	25.86	0.04	25.51	0.04	25.30	0.04
1644	39.94	25.45	0.03	25.29	0.03	24.77	0.03	24.74	0.03
1647	43.94	25.95	0.03	25.15	0.03	24.58	0.03	24.06	0.03
1650	31.95	26.58	0.04	25.76	0.04	25.27	0.04	25.04	0.04
1654	47.93	25.06	0.03	24.66	0.03	24.23	0.03	24.08	0.03
1658	57.92	26.65	0.03	25.88	0.02	25.29	0.02	25.44	0.02
1661	43.94	26.49	0.03	25.49	0.03	24.54	0.03	24.30	0.03
1662	15.98	27.47	0.08	26.82	0.07	26.42	0.07	26.04	0.08
1663	37.95	27.23	0.04	26.49	0.03	25.77	0.03	25.53	0.03
1669	47.93	25.78	0.03	24.95	0.03	24.07	0.03	23.88	0.03
1670	13.98	27.25	0.09	26.59	0.08	26.03	0.08	25.77	0.09
1672	19.97	27.03	0.07	26.69	0.06	26.52	0.06	26.34	0.06
1673	197.72	24.95	0.02	24.26	0.01	23.71	0.01	22.81	0.01
1674	45.93	26.12	0.03	25.40	0.03	24.72	0.03	24.54	0.03
1677	39.94	26.50	0.03	25.49	0.03	24.85	0.03	24.69	0.03
1680	15.98	26.78	0.08	26.27	0.07	25.55	0.07	25.25	0.08
1681	23.97	27.02	0.05	26.02	0.05	25.41	0.05	25.28	0.05
1682	31.95	25.92	0.04	25.01	0.04	24.19	0.04	24.01	0.04
1684	53.92	24.98	0.03	24.45	0.02	23.84	0.02	23.75	0.02
1689	29.96	26.55	0.04	25.89	0.04	24.69	0.04	24.55	0.04
1691	35.95	26.02	0.04	25.28	0.03	24.60	0.03	24.45	0.03
1693	19.97	27.05	0.06	26.48	0.06	25.91	0.06	25.66	0.06
1694	23.97	26.73	0.05	26.33	0.05	25.49	0.05	25.33	0.05

VCC	rad28 g	sb28 u	sb28 u	sb28 g	sb28 g	sb28 i	sb28 i	sb28 z	sb28 z
			error		error		error		error
1700	17.97	27.56	0.07	26.79	0.06	26.16	0.06	25.96	0.07
1702	45.93	27.23	0.04	26.67	0.03	25.98	0.03	25.77	0.03
1704	35.95	25.58	0.04	25.07	0.03	24.46	0.03	24.27	0.03
1706	13.98	26.71	0.09	26.27	0.08	25.85	0.08	25.41	0.08
1707	15.98	26.85	0.07	26.32	0.07	26.09	0.07	25.93	0.08
1711	33.95	25.68	0.04	24.97	0.03	24.21	0.03	24.00	0.03
1714	33.95	26.39	0.04	25.87	0.04	25.31	0.04	25.11	0.04
1717	49.93	26.46	0.03	25.81	0.03	25.02	0.03	25.07	0.03
1728	33.95	25.64	0.04	25.21	0.03	24.91	0.03	24.56	0.04
1729	27.96	26.47	0.05	26.04	0.04	25.43	0.04	25.13	0.04
1731	25.96	26.89	0.05	26.38	0.05	25.79	0.05	25.56	0.05
1736	25.96	27.45	0.05	26.85	0.05	26.05	0.05	26.10	0.06
1740	35.95	26.65	0.04	26.11	0.03	25.38	0.03	25.21	0.04
1746	29.96	26.84	0.04	25.68	0.04	24.56	0.04	24.45	0.04
1747	41.94	26.55	0.04	25.92	0.03	25.25	0.03	25.09	0.03
1749	25.96	27.20	0.05	26.63	0.05	26.07	0.05	25.87	0.05
1754	21.97	27.39	0.06	26.68	0.05	26.19	0.05	25.94	0.06
1767	47.93	26.24	0.03	25.52	0.03	25.01	0.03	24.69	0.03
1775	11.98	26.93	0.10	26.22	0.09	25.59	0.09	25.27	0.10
1778	65.91	24.64	0.02	23.68	0.02	23.54	0.02	23.26	0.02
1783	37.95	26.71	0.04	26.24	0.03	25.50	0.03	25.56	0.03
1785	37.95	26.73	0.04	26.14	0.03	25.46	0.03	25.27	0.04
1786	41.94	26.97	0.04	26.52	0.03	25.81	0.03	25.45	0.04
1787	17.97	26.82	0.08	26.21	0.06	25.88	0.07	25.74	0.07
1792	25.96	27.06	0.06	25.99	0.04	25.35	0.05	25.18	0.05
1796	45.93	25.98	0.03	25.45	0.03	24.97	0.03	24.82	0.03
1798	27.96	27.84	0.06	27.33	0.04	26.76	0.05	26.72	0.06
1803	45.93	25.96	0.03	25.08	0.03	24.35	0.03	24.20	0.03
1812	25.96	26.05	0.05	25.22	0.04	24.62	0.04	24.45	0.04
1815	35.95	26.81	0.04	26.15	0.03	25.66	0.03	25.56	0.04
1816	43.94	26.28	0.03	25.81	0.03	25.35	0.03	25.72	0.03
1818	27.96	27.24	0.06	26.47	0.04	25.79	0.04	25.59	0.05
1823	21.97	26.31	0.06	25.72	0.05	25.36	0.05	24.91	0.05
1828	53.92	25.63	0.03	24.96	0.02	24.30	0.02	24.17	0.02
1831	21.97	26.83	0.06	26.07	0.05	25.58	0.05	25.33	0.05
1841	17.97	27.10	0.07	26.22	0.06	25.45	0.06	25.07	0.06
1843	35.95	26.46	0.04	25.78	0.03	25.14	0.03	24.45	0.03
1861	63.91	25.26	0.02	24.34	0.02	23.61	0.02	23.42	0.02
1870	79.89	25.90	0.02	25.18	0.02	24.68	0.02	24.24	0.02
1871	41.94	24.58	0.03	23.27	0.03	22.44	0.03	22.28	0.03
1879	33.95	26.44	0.04	25.73	0.04	25.34	0.03	24.80	0.04

VCC	rad28 g	sb28 u	sb28 u	sb28 g	sb28 g	sb28 i	sb28 i	sb28 z	sb28 z
			error		error		error		error
1880	21.97	26.54	0.05	25.86	0.05	25.24	0.05	25.10	0.05
1881	41.94	26.08	0.03	25.13	0.03	24.41	0.03	24.23	0.03
1882	23.97	27.56	0.09	27.10	0.05	26.50	0.06	26.38	0.08
1886	51.93	25.36	0.03	24.57	0.03	23.81	0.02	23.61	0.03
1888	13.98	26.93	0.10	26.28	0.08	26.00	0.08	25.45	0.09
1891	35.95	25.89	0.04	25.29	0.03	24.95	0.03	24.73	0.03
1904	23.97	26.67	0.06	26.67	0.05	26.13	0.05	26.10	0.05
1909	43.94	25.88	0.03	25.15	0.03	24.43	0.03	24.15	0.03
1910	45.93	24.72	0.03	23.05	0.03	22.63	0.03	22.37	0.03
1915	41.94	26.55	0.03	25.62	0.03	24.70	0.03	24.73	0.03
1921	69.90	25.88	0.02	25.14	0.02	24.28	0.02	24.08	0.02
1925	21.97	27.82	0.07	27.16	0.06	26.30	0.06	26.05	0.07
1928	31.95	26.30	0.04	25.65	0.04	24.96	0.04	24.48	0.04
1931	51.93	25.35	0.03	24.91	0.03	24.46	0.02	24.51	0.03
1938	141.80	23.48	0.02	23.39	0.02	22.54	0.02	22.24	0.02
1943	105.85	24.09	0.02	23.36	0.02	22.44	0.02	22.15	0.02
1946	13.98	27.73	0.13	27.33	0.09	26.98	0.10	26.84	0.11
1948	51.93	25.51	0.03	24.74	0.03	24.21	0.02	23.70	0.03
1949	83.88	25.26	0.02	24.75	0.02	23.87	0.02	23.69	0.02
1951	39.94	26.74	0.03	25.93	0.03	25.11	0.03	24.92	0.03
1955	73.89	24.79	0.02	24.60	0.02	24.09	0.02	24.38	0.02
1958	31.95	25.87	0.04	25.11	0.04	24.68	0.04	24.21	0.04
1963	17.97	27.91	0.08	27.05	0.07	26.13	0.07	26.05	0.08
1968	13.98	27.12	0.09	26.37	0.08	25.94	0.08	25.56	0.09
1971	37.95	25.77	0.03	25.03	0.03	24.44	0.03	24.52	0.03
1975	23.97	26.31	0.05	25.82	0.05	25.19	0.05	25.28	0.05
1976	23.97	26.93	0.06	26.22	0.05	25.83	0.05	25.61	0.05
1982	45.93	25.39	0.03	24.46	0.03	24.13	0.03	23.95	0.03
1983	31.95	25.46	0.04	25.07	0.04	24.72	0.04	24.12	0.04
1985	17.97	26.91	0.07	26.01	0.06	25.49	0.06	25.59	0.07
1986	27.96	27.35	0.05	26.50	0.04	25.74	0.04	25.60	0.05
1989	21.97	26.19	0.06	25.51	0.05	24.86	0.05	24.79	0.05
1990	13.98	27.36	0.10	26.55	0.08	26.23	0.08	26.21	0.09
1991	53.92	26.18	0.03	25.25	0.02	24.50	0.02	24.23	0.02
1992	59.91	25.66	0.03	25.24	0.02	24.99	0.02	24.74	0.02
2000	103.85	23.19	0.02	22.82	0.02	21.87	0.02	21.54	0.02
2001	19.97	26.71	0.06	25.91	0.06	25.28	0.06	25.22	0.06
2002	17.97	26.73	0.07	25.84	0.06	25.32	0.07	25.15	0.07
2003	31.95	26.92	0.04	26.10	0.04	25.03	0.04	24.88	0.04
2006	103.85	24.87	0.02	24.10	0.02	23.36	0.02	23.04	0.02
2008	79.89	26.06	0.02	25.36	0.02	25.15	0.02	24.35	0.02

VCC	rad28 g	sb28 u	sb28 u	sb28 g	sb28 g	sb28 i	sb28 i	sb28 z	sb28 z
			error		error		error		error
2010	21.97	26.77	0.06	26.11	0.05	25.54	0.05	25.47	0.06
2011	37.95	26.44	0.04	25.91	0.03	25.35	0.03	24.89	0.03
2012	53.92	26.04	0.03	24.87	0.02	24.29	0.02	24.08	0.02
2014	37.95	27.10	0.04	26.35	0.03	25.87	0.03	25.28	0.03
2019	59.91	25.24	0.03	24.40	0.02	23.69	0.02	23.48	0.02
2025	23.97	26.94	0.05	26.00	0.05	25.49	0.05	25.46	0.05
2028	41.94	25.47	0.03	24.81	0.03	24.20	0.03	23.97	0.03

TABLE 7.4 The LSBVCC number, RA, Dec, magnitudes in the u, g, i and z bands and errors.

LSBVCC	RA (deg)	Dec (deg)	u	u_err	g	g_err	i	i_err	z	z_err
001	187.8825	11.6030	19.04	0.02	17.82	0.01	16.98	0.01	16.96	0.01
002	187.7446	11.7081	18.54	0.02	17.49	0.01	16.64	0.01	16.45	0.01
003	188.4454	11.7821	19.52	0.02	18.36	0.01	17.60	0.01	17.44	0.01
005	187.7663	11.8355	18.59	0.02	17.42	0.01	16.52	0.01	16.39	0.01
006	187.9846	11.9725	18.55	0.02	17.19	0.01	16.47	0.01	16.26	0.01
007	188.4688	12.1177	20.87	0.02	20.02	0.02	19.24	0.02	19.26	0.02
008	187.5729	12.2409	19.54	0.02	18.45	0.01	17.78	0.01	17.75	0.01
009	188.4208	12.3826	19.64	0.02	18.58	0.01	17.86	0.01	17.76	0.01
010	188.0317	12.4349	18.80	0.02	17.76	0.01	17.03	0.01	16.93	0.01
024	188.3554	13.4164	20.42	0.02	18.91	0.01	18.18	0.01	18.36	0.02
025	187.7063	13.5051	20.45	0.02	19.30	0.02	18.42	0.01	18.22	0.01
026	188.2096	13.4976	20.71	0.02	19.61	0.02	18.66	0.02	18.58	0.02
027	187.7921	13.5119	20.67	0.02	19.68	0.02	19.09	0.01	19.08	0.02
029	187.7400	13.6198	19.27	0.02	18.17	0.01	17.26	0.01	17.12	0.01
030	188.3308	13.6202	21.73	0.03	20.62	0.02	19.57	0.02	19.08	0.02
031	187.9154	13.6482	20.66	0.02	19.38	0.02	18.95	0.02	18.69	0.02
032	187.8988	13.8242	19.22	0.02	18.18	0.01	17.27	0.01	17.14	0.01
033	188.1325	13.8508	19.23	0.02	18.21	0.01	17.35	0.01	17.25	0.01
038	188.2875	10.8362	18.93	0.02	17.84	0.01	17.08	0.01	16.88	0.01
039	187.7238	10.9117	20.97	0.02	19.93	0.02	19.21	0.02	18.89	0.02
040	188.1871	10.9491	19.34	0.02	18.06	0.01	17.44	0.01	17.44	0.02
041	187.9038	11.0076	18.36	0.02	17.24	0.01	16.27	0.01	16.08	0.01
042	188.0008	11.0234	19.29	0.02	18.03	0.01	17.17	0.01	17.10	0.01
043	187.9363	11.2329	20.60	0.03	19.53	0.02	18.71	0.02	18.69	0.02
045	188.2133	11.2957	20.07	0.02	18.99	0.01	18.21	0.01	17.98	0.02
046	188.0000	11.3016	20.55	0.02	19.32	0.02	18.60	0.01	18.63	0.02
047	187.6079	11.4371	19.67	0.02	18.54	0.01	17.83	0.01	17.65	0.01
048	188.0833	9.7723	20.37	0.02	19.26	0.02	18.78	0.01	18.69	0.02
049	188.2713	9.9863	19.18	0.02	18.13	0.01	17.40	0.01	17.41	0.01
050	187.8779	10.0055	19.91	0.02	18.78	0.01	18.10	0.01	17.81	0.01
051	187.7004	10.1396	19.97	0.02	18.91	0.02	18.28	0.01	18.13	0.02
053	188.8946	11.6204	19.86	0.02	18.64	0.01	17.68	0.01	17.62	0.01
054	188.6263	11.7345	18.13	0.02	16.93	0.01	16.24	0.01	15.93	0.01
055	188.5271	11.8372	19.27	0.02	17.92	0.01	17.12	0.01	17.06	0.01
056	189.1129	11.8890	19.13	0.02	17.79	0.01	16.83	0.01	16.68	0.01
057	188.7775	11.9007	18.95	0.02	17.74	0.01	16.87	0.01	16.73	0.01
058	188.9238	12.2077	20.82	0.02	19.80	0.02	19.09	0.01	18.98	0.02
059	188.9200	12.2353	20.75	0.02	19.76	0.02	19.02	0.01	19.11	0.02
060	188.6533	12.4311	21.89	0.03	20.80	0.02	19.86	0.02	19.74	0.02

LSBVCC	RA (deg)	Dec (deg)	u	u_err	g	g_err	i	i_err	z	z_err
061	189.1358	12.5178	19.90	0.02	18.87	0.02	17.99	0.01	17.97	0.01
062	188.8617	12.5282	19.49	0.02	18.51	0.01	17.66	0.01	17.87	0.01
063	188.9338	12.6095	20.06	0.02	18.87	0.01	17.95	0.01	17.76	0.01
064	189.3708	12.8751	21.17	0.02	20.24	0.02	19.51	0.02	19.44	0.02
065	189.4067	12.9099	20.16	0.02	19.06	0.01	18.36	0.01	18.15	0.01
066	189.2188	13.2839	20.18	0.02	18.95	0.01	18.25	0.01	18.23	0.02
067	189.1054	13.4911	20.70	0.02	19.62	0.02	18.87	0.01	18.96	0.02
068	189.3654	13.7923	20.55	0.02	19.64	0.02	19.03	0.01	18.67	0.02
069	188.9313	14.0790	20.68	0.02	19.64	0.02	18.72	0.02	18.84	0.02
070	188.6767	14.2230	18.07	0.02	17.15	0.01	16.38	0.01	16.45	0.01
071	188.6946	14.2923	20.13	0.02	19.10	0.02	18.07	0.01	17.77	0.01
072	189.3817	11.0370	20.87	0.02	19.96	0.02	19.26	0.02	19.22	0.02
073	188.5250	11.0544	20.32	0.02	19.23	0.02	18.50	0.01	18.56	0.02
074	189.1558	11.1534	18.63	0.02	17.42	0.01	16.68	0.01	16.85	0.01
076	188.5646	11.4675	20.04	0.02	18.98	0.02	18.10	0.01	17.99	0.02
077	189.2633	11.4785	20.28	0.02	19.28	0.02	18.39	0.01	18.44	0.01
079	189.6700	11.9785	20.81	0.02	19.66	0.02	19.14	0.02	18.75	0.02
080	190.3083	12.2491	21.00	0.02	20.16	0.02	19.61	0.02	19.50	0.02
081	190.3671	12.4280	19.24	0.02	18.20	0.01	17.42	0.01	17.30	0.01
082	189.5504	10.7019	19.55	0.02	18.57	0.01	17.82	0.01	17.82	0.01
083	190.2317	10.7030	20.98	0.02	19.93	0.02	19.21	0.02	19.25	0.02
084	190.0763	10.9967	19.26	0.02	18.20	0.01	17.51	0.01	17.45	0.01
085	189.5713	11.1807	19.84	0.02	18.78	0.01	17.98	0.01	18.27	0.02
086	189.8821	11.4543	19.86	0.02	18.78	0.01	18.28	0.01	18.46	0.02
087	190.0200	11.5711	19.80	0.02	18.65	0.01	17.91	0.01	17.72	0.01
088	186.8883	11.5317	20.57	0.02	19.59	0.02	18.74	0.01	18.91	0.02
089	187.4129	11.6329	18.52	0.02	17.43	0.01	16.62	0.01	16.88	0.01
090	187.2479	11.9236	20.94	0.03	19.98	0.02	19.29	0.02	19.48	0.02
091	186.9308	11.9679	21.03	0.02	19.98	0.02	19.41	0.02	19.31	0.02
092	187.4221	12.0459	19.43	0.02	18.23	0.01	17.54	0.01	17.37	0.01
093	187.2463	12.0417	21.30	0.03	20.30	0.02	19.62	0.02	19.69	0.03
094	187.2050	12.1323	19.27	0.02	18.22	0.01	17.36	0.01	17.37	0.02
095	187.2717	12.1542	20.47	0.02	19.40	0.02	18.50	0.01	18.12	0.02
099	186.8196	10.6988	20.44	0.02	19.54	0.02	18.83	0.01	18.57	0.01
100	186.7354	10.7981	22.22	0.05	20.89	0.03	20.08	0.02	20.29	0.03
101	187.4975	10.8563	18.97	0.02	17.84	0.01	17.03	0.01	17.05	0.01
102	187.2071	10.9208	19.96	0.02	18.94	0.01	18.14	0.01	18.11	0.02
103	187.3379	10.9942	20.79	0.02	19.70	0.02	19.08	0.02	19.09	0.02
104	187.3038	10.9907	20.53	0.02	19.57	0.02	18.75	0.01	18.81	0.02
105	186.9346	11.2147	18.27	0.02	17.16	0.01	16.29	0.01	16.18	0.01
106	186.6417	11.2850	19.08	0.02	17.97	0.01	17.26	0.01	17.27	0.01
107	187.4879	11.4010	20.68	0.02	19.77	0.02	19.23	0.02	19.18	0.02

LSBVCC	RA (deg)	Dec (deg)	u	u_err	g	g_err	i	i_err	z	z_err
108	187.0975	11.5796	18.87	0.02	17.93	0.01	17.15	0.01	17.02	0.01
109	190.0075	13.6546	19.63	0.02	18.45	0.01	17.62	0.01	17.50	0.01
110	190.0642	13.8789	21.21	0.02	20.43	0.02	19.83	0.02	19.42	0.02
111	189.5021	14.1776	18.70	0.02	17.58	0.01	16.74	0.01	16.64	0.01
117	190.6575	13.6063	18.45	0.02	17.30	0.01	16.50	0.01	16.36	0.01
118	190.7354	13.7654	20.67	0.02	19.64	0.02	18.66	0.02	18.50	0.02
129	189.5092	14.4149	21.24	0.03	20.27	0.02	19.70	0.02	19.63	0.02
151	186.8154	13.4499	20.49	0.02	19.34	0.02	18.17	0.01	18.01	0.02
152	186.6983	13.6804	19.33	0.02	18.52	0.01	17.88	0.01	17.72	0.01
153	187.5492	13.6911	19.84	0.02	18.70	0.01	17.78	0.01	17.66	0.01
154	187.4758	13.9564	20.11	0.02	19.17	0.02	18.39	0.01	18.21	0.02
156	187.1133	14.1556	17.89	0.02	16.88	0.01	16.33	0.01	16.27	0.01
157	187.0788	14.1377	20.72	0.02	19.66	0.02	18.97	0.02	18.77	0.02
158	187.2067	14.1578	18.95	0.02	17.68	0.01	17.10	0.01	16.89	0.01
159	187.3725	14.1697	19.86	0.02	18.64	0.01	17.80	0.01	17.73	0.01
161	187.2908	14.2278	20.90	0.02	19.98	0.02	19.16	0.02	19.33	0.02
167	185.9104	12.6278	19.15	0.02	18.09	0.01	17.06	0.01	16.80	0.01
168	186.3483	12.6753	20.25	0.02	19.24	0.02	18.52	0.02	18.35	0.02
169	186.3608	12.6769	19.71	0.02	18.59	0.02	17.76	0.01	17.60	0.01
170	185.9708	12.7726	19.48	0.02	18.36	0.01	17.37	0.01	17.24	0.01
171	186.4546	12.8044	19.62	0.02	18.65	0.01	17.96	0.01	17.80	0.01
172	186.0779	12.9126	19.61	0.02	18.53	0.01	17.73	0.01	17.58	0.01
173	186.3763	12.9770	20.40	0.02	19.41	0.02	18.62	0.01	18.85	0.02
174	186.5175	12.9879	21.32	0.03	20.44	0.02	19.46	0.02	19.23	0.02
175	186.3050	13.0254	18.59	0.02	17.39	0.01	16.52	0.01	16.45	0.01
176	186.4546	13.2832	21.43	0.03	20.03	0.02	19.42	0.02	19.01	0.02
177	186.1896	13.3403	18.62	0.02	17.87	0.01	17.40	0.01	17.33	0.01
178	186.0467	13.3735	19.45	0.02	18.46	0.01	17.74	0.01	17.52	0.01
179	185.6988	13.3533	21.37	0.03	20.29	0.02	19.56	0.02	19.51	0.02
180	186.1429	13.3735	20.56	0.02	19.52	0.02	18.81	0.01	18.93	0.02
181	185.7983	13.4188	19.68	0.02	18.70	0.01	17.87	0.01	17.86	0.01
182	186.0908	13.4185	19.43	0.02	18.27	0.01	17.37	0.01	17.29	0.01
183	186.4500	13.8545	19.56	0.02	18.50	0.01	17.72	0.01	17.37	0.01
184	186.3821	14.1521	18.01	0.02	16.92	0.01	16.19	0.01	15.87	0.01
185	186.4213	14.1920	20.58	0.02	19.27	0.02	18.59	0.01	18.62	0.02
186	186.0529	14.4936	19.78	0.02	18.75	0.01	18.04	0.01	17.84	0.01
187	186.4796	14.6414	20.11	0.02	19.12	0.02	18.00	0.01	17.85	0.02
188	186.2213	14.6551	19.32	0.02	18.21	0.01	17.39	0.01	17.34	0.01
189	186.2517	15.0937	20.39	0.02	19.32	0.02	18.63	0.01	18.60	0.02
190	186.1463	15.1642	19.94	0.02	18.91	0.01	18.26	0.01	18.20	0.02
195	185.5538	12.6965	19.66	0.02	18.52	0.01	17.67	0.01	17.68	0.01
196	185.3721	12.7982	20.07	0.02	19.01	0.01	18.29	0.01	18.29	0.02

LSBVCC	RA (deg)	Dec (deg)	u	u_err	g	g_err	i	i_err	z	z_err
197	184.8021	12.8518	17.85	0.02	16.76	0.01	15.91	0.01	15.81	0.01
198	185.1517	12.8850	19.39	0.02	18.37	0.01	17.49	0.01	17.37	0.01
200	184.6771	12.9451	21.46	0.03	20.39	0.02	19.87	0.02	19.59	0.02
201	185.6167	13.1629	20.40	0.02	19.29	0.02	18.42	0.02	18.49	0.02
202	185.3129	13.3462	17.77	0.02	16.60	0.01	15.73	0.01	15.63	0.01
208	191.0275	12.6841	20.38	0.02	19.60	0.02	18.86	0.01	18.66	0.02
225	185.6129	10.1662	21.33	0.02	20.30	0.02	19.53	0.02	19.48	0.02
226	185.0729	10.3204	19.18	0.02	17.99	0.01	17.23	0.01	17.66	0.01
227	184.9642	10.3071	20.87	0.02	19.82	0.02	19.23	0.02	19.16	0.02
228	185.3708	10.4859	18.85	0.02	17.83	0.01	17.23	0.01	17.16	0.01
231	185.1492	8.2016	19.12	0.02	18.10	0.01	17.38	0.01	17.36	0.01
232	185.4825	8.3459	19.82	0.02	18.72	0.01	18.01	0.01	17.93	0.01
233	185.4600	8.5418	18.38	0.02	17.30	0.01	16.48	0.01	16.54	0.01
234	184.7404	8.6444	19.81	0.02	18.55	0.01	17.57	0.01	17.54	0.01
235	185.6150	7.0978	19.32	0.02	18.30	0.01	17.47	0.01	17.49	0.01
240	191.2904	10.6282	18.57	0.02	17.37	0.01	16.48	0.01	16.38	0.01
247	184.6833	10.5484	21.05	0.02	19.85	0.02	18.85	0.01	18.54	0.02
274	186.6192	8.7951	19.83	0.02	18.68	0.01	18.17	0.01	18.09	0.02
277	187.5121	9.2397	18.87	0.02	17.98	0.01	17.45	0.01	17.40	0.01
278	187.2838	9.4436	17.63	0.02	16.53	0.01	15.67	0.01	15.66	0.01
279	187.4154	9.4636	19.11	0.02	18.06	0.01	17.37	0.01	17.22	0.01
280	187.5083	9.4740	19.34	0.02	18.26	0.01	17.47	0.01	17.45	0.02
281	187.4088	9.5209	18.17	0.02	17.08	0.01	16.30	0.01	16.37	0.01
282	186.4813	10.7211	20.21	0.02	19.14	0.02	18.41	0.01	18.44	0.02
284	185.8829	11.2708	19.17	0.02	18.12	0.01	17.36	0.01	17.19	0.01
285	186.0521	11.5294	18.60	0.02	17.52	0.01	16.75	0.01	16.69	0.01
286	186.2354	9.9268	21.58	0.03	20.54	0.02	19.43	0.02	19.35	0.02
287	185.8708	10.0226	21.06	0.02	20.09	0.02	19.32	0.02	19.24	0.02
288	185.8229	10.0568	21.63	0.03	20.65	0.02	20.15	0.02	19.82	0.02
289	186.4471	10.0927	18.78	0.02	17.74	0.01	17.19	0.01	16.93	0.01
290	185.8521	10.1569	21.31	0.03	20.15	0.02	18.99	0.02	18.80	0.02
291	186.0321	10.4141	19.39	0.02	18.03	0.01	16.27	0.01	15.92	0.01
292	186.3638	10.4197	22.50	0.04	21.33	0.02	20.77	0.02	20.38	0.02
293	186.2921	10.4567	19.95	0.02	18.94	0.01	18.30	0.01	18.08	0.01
294	186.1288	10.5258	21.27	0.02	20.32	0.02	19.74	0.02	19.55	0.02
295	186.6033	10.5817	18.94	0.02	17.43	0.01	16.85	0.01	16.67	0.01
296	185.7771	10.5901	21.55	0.03	20.37	0.02	19.56	0.02	19.57	0.02
297	186.4463	11.6623	19.12	0.02	18.05	0.01	17.28	0.01	17.09	0.01
298	186.4821	11.8010	20.33	0.02	19.42	0.02	18.77	0.02	18.59	0.02
299	186.1288	11.8117	19.69	0.02	18.64	0.01	18.07	0.01	17.95	0.02
300	186.2338	11.8323	18.38	0.02	17.28	0.01	16.46	0.01	16.35	0.01
301	186.1996	11.8185	20.64	0.02	19.51	0.02	18.97	0.01	18.76	0.02

LSBVCC	RA (deg)	Dec (deg)	u	u_err	g	g_err	i	i_err	z	z_err
302	185.9908	11.8922	19.12	0.02	18.02	0.01	17.18	0.01	17.09	0.02
303	185.9121	12.1839	19.82	0.02	18.57	0.01	16.96	0.01	16.45	0.01
304	185.7242	12.3889	20.52	0.02	19.49	0.02	18.67	0.01	18.67	0.02
305	188.0058	8.6697	18.87	0.02	17.76	0.01	17.01	0.01	17.00	0.01
306	187.6917	9.0126	20.18	0.03	19.32	0.02	18.42	0.02	18.33	0.03
307	188.4625	9.0793	22.23	0.04	21.38	0.03	20.71	0.02	20.33	0.03
308	187.8171	9.3592	20.14	0.02	19.10	0.02	18.28	0.01	18.02	0.02
309	187.5675	9.4621	21.25	0.03	20.30	0.02	19.66	0.02	19.71	0.03
310	187.8529	9.4745	20.20	0.02	19.21	0.02	18.58	0.01	18.22	0.02
311	191.2904	10.6303	18.62	0.02	17.37	0.01	16.48	0.01	16.46	0.01
312	190.8975	10.7557	19.10	0.02	18.07	0.01	17.27	0.01	17.08	0.01
313	191.3546	10.9239	20.16	0.02	19.00	0.02	18.25	0.01	18.41	0.02
314	191.2275	10.9616	20.59	0.02	19.50	0.02	18.97	0.02	18.77	0.02
315	190.5117	10.9537	19.51	0.02	18.22	0.01	17.43	0.01	17.47	0.01
316	191.2258	11.0189	20.39	0.02	19.19	0.02	18.54	0.01	18.51	0.02
318	191.1313	11.3984	21.23	0.03	20.19	0.02	19.58	0.02	19.70	0.03
319	190.9529	11.4253	20.83	0.02	19.89	0.02	19.16	0.02	19.12	0.02
320	190.8250	11.4743	19.86	0.02	18.82	0.01	17.98	0.01	17.99	0.02
321	191.3975	11.5521	19.45	0.02	18.41	0.01	17.60	0.01	17.56	0.01
322	190.7838	11.6213	20.63	0.02	19.54	0.02	18.87	0.01	18.93	0.02
323	190.7592	11.6978	18.27	0.02	16.95	0.01	16.06	0.01	15.89	0.01
324	190.5954	11.6853	20.83	0.02	19.75	0.02	18.96	0.02	18.92	0.02
325	191.1404	11.7953	19.07	0.02	17.80	0.01	16.95	0.01	16.93	0.01
326	191.1871	11.8011	20.31	0.02	19.13	0.02	18.29	0.01	18.24	0.02
327	190.9908	11.8807	19.31	0.02	18.23	0.01	17.37	0.01	17.48	0.01
328	191.2208	12.1830	19.54	0.02	18.56	0.01	17.82	0.01	17.71	0.01
329	191.4379	12.2356	18.99	0.02	18.00	0.01	17.27	0.01	17.21	0.01
330	191.2667	12.3515	18.26	0.02	17.21	0.01	16.45	0.01	16.40	0.01
331	190.5133	12.4805	19.38	0.02	18.36	0.01	17.61	0.01	17.55	0.02
357	185.3475	13.5834	21.35	0.03	20.43	0.02	19.84	0.02	19.41	0.02
358	185.5942	14.4303	21.09	0.02	20.14	0.02	19.33	0.02	19.29	0.02
359	184.9488	14.7065	19.59	0.02	18.19	0.01	17.22	0.01	17.09	0.01
360	185.1121	14.7854	18.45	0.02	17.33	0.01	16.48	0.01	16.29	0.01
361	185.5871	15.1600	19.96	0.02	18.88	0.01	18.19	0.01	18.11	0.02
390	190.0888	12.7191	20.39	0.02	19.35	0.02	18.56	0.01	18.69	0.02
394	187.3692	12.4963	18.56	0.02	17.51	0.01	16.75	0.01	16.62	0.01
395	186.9563	12.4996	21.00	0.03	19.85	0.02	19.08	0.02	19.31	0.02
397	187.5633	12.5157	20.12	0.02	19.04	0.02	18.40	0.01	18.23	0.02
398	187.1775	12.5500	18.12	0.02	16.94	0.01	16.16	0.01	16.04	0.01
399	186.7613	12.5805	20.80	0.03	19.90	0.02	19.19	0.02	18.96	0.02
401	186.8154	12.6601	20.32	0.02	19.24	0.02	18.46	0.01	18.22	0.02
402	187.1963	12.6419	20.98	0.02	19.95	0.02	19.32	0.02	19.10	0.02

LSBVCC	RA (deg)	Dec (deg)	u	u_err	g	g_err	i	i_err	z	z_err
403	186.7171	12.6524	21.18	0.03	20.15	0.02	19.31	0.02	19.22	0.02
404	187.2313	12.7069	19.73	0.02	18.68	0.01	17.89	0.01	17.77	0.01
405	186.6163	12.7643	21.58	0.03	20.31	0.02	19.28	0.02	19.29	0.02
406	186.6521	12.8033	19.27	0.02	18.28	0.01	17.62	0.01	17.45	0.01
407	186.8933	12.8039	20.48	0.02	19.50	0.02	18.62	0.01	18.38	0.02
409	186.8096	12.9025	21.00	0.02	20.23	0.02	19.37	0.02	19.15	0.02
411	187.0283	12.9786	19.97	0.02	19.20	0.02	17.97	0.01	17.86	0.01
412	186.6596	13.0797	20.11	0.02	19.05	0.02	18.13	0.01	18.06	0.01
413	186.6946	13.2674	20.26	0.02	19.31	0.02	18.70	0.01	18.68	0.03
414	187.0829	13.3597	21.68	0.03	20.62	0.02	20.00	0.02	19.74	0.02
415	187.3367	13.3700	22.29	0.04	21.24	0.02	20.73	0.02	20.80	0.03
416	186.8150	13.4128	20.82	0.02	19.90	0.02	19.21	0.01	19.23	0.02
429	187.4963	9.7967	20.43	0.02	19.33	0.02	18.73	0.01	18.76	0.02
431	187.3579	10.2492	19.06	0.02	17.92	0.01	17.12	0.01	16.92	0.01
432	187.5338	10.2646	21.03	0.02	20.01	0.02	19.35	0.02	19.22	0.02
433	187.0500	10.3646	17.98	0.02	16.89	0.01	16.14	0.01	16.14	0.01
434	187.3258	10.4968	19.39	0.02	18.07	0.01	16.85	0.01	16.61	0.01
435	187.1308	10.5190	18.45	0.02	17.41	0.01	16.58	0.01	16.46	0.01
436	187.0538	10.5259	18.28	0.02	17.11	0.01	16.35	0.01	16.28	0.01
438	185.5438	11.6417	19.71	0.02	18.61	0.01	17.90	0.01	17.81	0.01
439	185.4538	11.8524	20.27	0.02	19.20	0.02	18.40	0.01	18.11	0.02
440	184.7242	12.1943	19.83	0.02	18.76	0.01	17.98	0.01	18.06	0.01
441	184.8779	12.2088	19.55	0.02	18.50	0.01	17.63	0.01	17.55	0.01
442	185.2292	12.3292	20.09	0.02	19.11	0.02	18.44	0.01	18.11	0.02
443	185.3138	12.4068	19.96	0.02	18.89	0.01	18.16	0.01	18.03	0.01

TABLE 7.5 The LSBVCC number, all colours and errors on colours.

LSBVCC	$u - g$	$u - g$ error	$u - i$	$u - i$ error	$u - z$	$u - z$ error	$g - i$	$g - i$ error	$g - z$	$g - z$ error	$i - z$	$i - z$ error
001	1.22	0.03	2.05	0.02	2.08	0.03	0.83	0.02	0.86	0.02	0.03	0.02
002	1.04	0.02	1.90	0.02	2.09	0.02	0.86	0.02	1.04	0.02	0.19	0.02
003	1.16	0.02	1.92	0.02	2.08	0.02	0.76	0.02	0.92	0.02	0.16	0.02
005	1.17	0.02	2.07	0.02	2.20	0.02	0.90	0.02	1.04	0.02	0.13	0.02
006	1.36	0.02	2.09	0.02	2.29	0.02	0.73	0.02	0.93	0.02	0.21	0.02
007	0.85	0.03	1.63	0.03	1.61	0.03	0.78	0.02	0.75	0.03	-0.02	0.03
008	1.08	0.02	1.75	0.02	1.78	0.02	0.67	0.02	0.70	0.02	0.03	0.02
009	1.06	0.02	1.78	0.02	1.88	0.02	0.72	0.02	0.82	0.02	0.10	0.02
010	1.04	0.02	1.77	0.02	1.87	0.02	0.73	0.02	0.83	0.02	0.10	0.02
024	1.51	0.03	2.24	0.03	2.05	0.03	0.73	0.02	0.54	0.02	-0.19	0.02
025	1.15	0.03	2.04	0.03	2.23	0.03	0.89	0.02	1.08	0.02	0.20	0.02
026	1.10	0.03	2.05	0.03	2.13	0.03	0.95	0.02	1.03	0.02	0.08	0.02
027	0.99	0.03	1.58	0.03	1.59	0.03	0.59	0.02	0.60	0.02	0.01	0.02
029	1.10	0.02	2.00	0.02	2.15	0.02	0.91	0.02	1.05	0.02	0.14	0.02
030	1.12	0.04	2.17	0.03	2.66	0.03	1.05	0.03	1.54	0.03	0.49	0.02
031	1.29	0.03	1.71	0.03	1.98	0.03	0.43	0.02	0.69	0.02	0.26	0.02
032	1.04	0.02	1.95	0.02	2.08	0.02	0.91	0.02	1.04	0.02	0.13	0.02
033	1.03	0.02	1.88	0.02	1.98	0.02	0.85	0.02	0.96	0.02	0.10	0.02
038	1.09	0.02	1.85	0.02	2.05	0.02	0.76	0.02	0.96	0.02	0.20	0.02
039	1.04	0.03	1.76	0.03	2.08	0.03	0.72	0.02	1.04	0.02	0.32	0.02
040	1.28	0.02	1.90	0.02	1.90	0.03	0.62	0.02	0.62	0.02	0.00	0.02
041	1.12	0.02	2.09	0.02	2.28	0.02	0.97	0.02	1.16	0.02	0.19	0.02
042	1.26	0.02	2.12	0.02	2.18	0.02	0.86	0.02	0.93	0.02	0.06	0.02
043	1.07	0.03	1.89	0.03	1.91	0.03	0.82	0.02	0.85	0.03	0.03	0.02
045	1.08	0.03	1.86	0.02	2.09	0.03	0.78	0.02	1.01	0.02	0.23	0.02
046	1.23	0.03	1.95	0.03	1.92	0.03	0.72	0.02	0.69	0.02	-0.03	0.02
047	1.13	0.02	1.84	0.02	2.02	0.02	0.71	0.02	0.89	0.02	0.18	0.02
048	1.11	0.03	1.59	0.03	1.69	0.03	0.48	0.02	0.58	0.02	0.10	0.02
049	1.05	0.02	1.78	0.02	1.77	0.02	0.73	0.02	0.72	0.02	-0.01	0.02
050	1.13	0.02	1.81	0.02	2.10	0.02	0.68	0.02	0.97	0.02	0.29	0.02
051	1.06	0.03	1.69	0.02	1.84	0.03	0.63	0.02	0.78	0.02	0.15	0.02
053	1.21	0.02	2.18	0.02	2.24	0.02	0.97	0.02	1.02	0.02	0.05	0.02
054	1.20	0.02	1.89	0.02	2.20	0.02	0.69	0.02	1.00	0.02	0.31	0.02
055	1.35	0.02	2.15	0.02	2.21	0.02	0.79	0.02	0.86	0.02	0.07	0.02
056	1.33	0.02	2.30	0.02	2.45	0.02	0.97	0.02	1.11	0.02	0.15	0.02
057	1.21	0.02	2.07	0.02	2.22	0.02	0.86	0.02	1.01	0.02	0.14	0.02
058	1.02	0.03	1.73	0.03	1.84	0.03	0.71	0.02	0.82	0.02	0.11	0.02
059	0.99	0.03	1.73	0.03	1.64	0.03	0.74	0.02	0.65	0.02	-0.09	0.02
060	1.08	0.04	2.03	0.04	2.15	0.04	0.95	0.03	1.07	0.03	0.12	0.03
061	1.03	0.03	1.91	0.03	1.93	0.03	0.88	0.02	0.90	0.02	0.02	0.02

LSBVCC	$u - g$	$u - g$ error	$u - i$	$u - i$ error	$u - z$	$u - z$ error	$g - i$	$g - i$ error	$g - z$	$g - z$ error	$i - z$	$i - z$ error
062	0.98	0.02	1.83	0.02	1.62	0.02	0.85	0.02	0.64	0.02	-0.21	0.02
063	1.19	0.03	2.11	0.03	2.30	0.03	0.93	0.02	1.12	0.02	0.19	0.02
064	0.93	0.03	1.66	0.03	1.72	0.03	0.73	0.02	0.80	0.02	0.06	0.02
065	1.09	0.02	1.80	0.02	2.01	0.02	0.71	0.02	0.91	0.02	0.21	0.02
066	1.23	0.03	1.93	0.02	1.95	0.03	0.70	0.02	0.73	0.02	0.03	0.02
067	1.08	0.03	1.83	0.03	1.74	0.03	0.75	0.02	0.66	0.02	-0.09	0.02
068	0.91	0.03	1.53	0.03	1.89	0.03	0.62	0.02	0.98	0.02	0.36	0.02
069	1.04	0.03	1.95	0.03	1.83	0.03	0.91	0.02	0.80	0.02	-0.12	0.02
070	0.92	0.02	1.69	0.02	1.62	0.02	0.77	0.02	0.69	0.02	-0.07	0.02
071	1.03	0.03	2.06	0.02	2.36	0.03	1.03	0.02	1.33	0.02	0.30	0.02
072	0.91	0.03	1.61	0.03	1.65	0.03	0.70	0.02	0.74	0.03	0.04	0.02
073	1.09	0.03	1.83	0.03	1.77	0.03	0.74	0.02	0.67	0.02	-0.06	0.02
074	1.21	0.02	1.95	0.02	1.78	0.02	0.74	0.02	0.57	0.02	-0.17	0.02
076	1.06	0.03	1.94	0.02	2.05	0.03	0.88	0.02	0.99	0.02	0.11	0.02
077	1.00	0.03	1.89	0.02	1.85	0.03	0.89	0.02	0.84	0.02	-0.05	0.02
079	1.15	0.03	1.67	0.03	2.06	0.03	0.52	0.02	0.91	0.02	0.39	0.02
080	0.83	0.03	1.38	0.03	1.50	0.03	0.55	0.02	0.66	0.02	0.11	0.02
081	1.03	0.02	1.82	0.02	1.93	0.02	0.79	0.02	0.90	0.02	0.11	0.02
082	0.98	0.02	1.73	0.02	1.73	0.02	0.75	0.02	0.76	0.02	0.00	0.02
083	1.05	0.03	1.77	0.03	1.73	0.03	0.72	0.02	0.68	0.02	-0.04	0.02
084	1.06	0.02	1.75	0.02	1.81	0.02	0.69	0.02	0.75	0.02	0.06	0.02
085	1.06	0.02	1.86	0.02	1.57	0.02	0.80	0.02	0.51	0.02	-0.29	0.02
086	1.08	0.03	1.58	0.02	1.40	0.03	0.49	0.02	0.32	0.02	-0.18	0.02
087	1.15	0.02	1.89	0.02	2.08	0.02	0.74	0.02	0.92	0.02	0.19	0.02
088	0.98	0.03	1.83	0.03	1.67	0.03	0.85	0.02	0.69	0.02	-0.17	0.02
089	1.09	0.02	1.90	0.02	1.64	0.02	0.81	0.02	0.56	0.02	-0.26	0.02
090	0.96	0.03	1.65	0.03	1.46	0.04	0.69	0.02	0.50	0.03	-0.19	0.03
091	1.05	0.03	1.63	0.03	1.72	0.03	0.58	0.02	0.67	0.02	0.09	0.02
092	1.19	0.02	1.89	0.02	2.06	0.02	0.70	0.02	0.86	0.02	0.17	0.02
093	1.00	0.03	1.67	0.03	1.61	0.04	0.68	0.02	0.61	0.03	-0.06	0.03
094	1.05	0.02	1.91	0.02	1.90	0.03	0.86	0.02	0.85	0.02	-0.01	0.02
095	1.06	0.03	1.97	0.03	2.35	0.03	0.91	0.02	1.29	0.02	0.38	0.02
099	0.90	0.03	1.61	0.03	1.88	0.03	0.72	0.02	0.98	0.02	0.26	0.02
100	1.33	0.06	2.14	0.05	1.93	0.06	0.81	0.03	0.60	0.04	-0.21	0.04
101	1.13	0.02	1.94	0.02	1.92	0.02	0.81	0.02	0.79	0.02	-0.02	0.02
102	1.02	0.02	1.82	0.02	1.85	0.03	0.80	0.02	0.83	0.02	0.03	0.02
103	1.09	0.03	1.71	0.03	1.70	0.03	0.62	0.02	0.61	0.02	-0.01	0.02
104	0.95	0.03	1.77	0.03	1.72	0.03	0.82	0.02	0.76	0.02	-0.05	0.02
105	1.10	0.02	1.97	0.02	2.08	0.02	0.87	0.02	0.98	0.02	0.11	0.02
106	1.11	0.02	1.82	0.02	1.81	0.02	0.71	0.02	0.70	0.02	-0.01	0.02
107	0.90	0.03	1.45	0.03	1.50	0.03	0.54	0.02	0.59	0.03	0.05	0.02

LSBVCC	$u - g$	$u - g$ error	$u - i$	$u - i$ error	$u - z$	$u - z$ error	$g - i$	$g - i$ error	$g - z$	$g - z$ error	$i - z$	$i - z$ error
108	0.94	0.02	1.72	0.02	1.85	0.02	0.78	0.02	0.91	0.02	0.13	0.02
109	1.18	0.02	2.01	0.02	2.13	0.02	0.83	0.02	0.95	0.02	0.12	0.02
110	0.78	0.03	1.38	0.03	1.79	0.03	0.60	0.02	1.01	0.03	0.41	0.03
111	1.12	0.02	1.96	0.02	2.05	0.02	0.84	0.02	0.94	0.02	0.10	0.02
117	1.15	0.02	1.95	0.02	2.09	0.02	0.80	0.02	0.94	0.02	0.14	0.02
118	1.03	0.03	2.01	0.03	2.17	0.03	0.98	0.02	1.14	0.02	0.16	0.02
129	0.97	0.03	1.54	0.03	1.61	0.03	0.58	0.02	0.64	0.03	0.07	0.03
151	1.15	0.03	2.32	0.03	2.47	0.03	1.17	0.02	1.32	0.02	0.15	0.02
152	0.81	0.02	1.45	0.02	1.61	0.02	0.64	0.02	0.80	0.02	0.16	0.02
153	1.14	0.02	2.07	0.02	2.19	0.02	0.92	0.02	1.05	0.02	0.12	0.02
154	0.94	0.03	1.72	0.02	1.90	0.03	0.79	0.02	0.96	0.02	0.17	0.02
156	1.01	0.02	1.56	0.02	1.62	0.02	0.55	0.02	0.61	0.02	0.06	0.02
157	1.06	0.03	1.75	0.03	1.95	0.03	0.69	0.02	0.90	0.02	0.21	0.02
158	1.28	0.02	1.85	0.02	2.06	0.02	0.57	0.02	0.79	0.02	0.21	0.02
159	1.22	0.02	2.05	0.02	2.13	0.02	0.84	0.02	0.91	0.02	0.07	0.02
161	0.92	0.03	1.74	0.03	1.57	0.03	0.82	0.02	0.65	0.03	-0.17	0.03
167	1.06	0.02	2.09	0.02	2.35	0.02	1.03	0.02	1.29	0.02	0.26	0.02
168	1.01	0.03	1.73	0.03	1.89	0.03	0.72	0.02	0.88	0.02	0.16	0.02
169	1.12	0.02	1.94	0.02	2.11	0.02	0.82	0.02	0.99	0.02	0.17	0.02
170	1.11	0.02	2.11	0.02	2.24	0.02	1.00	0.02	1.13	0.02	0.13	0.02
171	0.96	0.02	1.66	0.02	1.82	0.02	0.70	0.02	0.86	0.02	0.16	0.02
172	1.07	0.02	1.88	0.02	2.03	0.02	0.80	0.02	0.96	0.02	0.16	0.02
173	0.99	0.03	1.78	0.03	1.55	0.03	0.79	0.02	0.56	0.02	-0.23	0.02
174	0.88	0.04	1.86	0.04	2.09	0.04	0.97	0.03	1.21	0.03	0.23	0.03
175	1.20	0.02	2.07	0.02	2.14	0.02	0.87	0.02	0.94	0.02	0.07	0.02
176	1.39	0.03	2.01	0.03	2.42	0.03	0.62	0.02	1.03	0.02	0.41	0.02
177	0.75	0.02	1.23	0.02	1.29	0.02	0.48	0.02	0.54	0.02	0.07	0.02
178	0.99	0.02	1.71	0.02	1.92	0.02	0.72	0.02	0.94	0.02	0.21	0.02
179	1.08	0.03	1.81	0.03	1.87	0.03	0.73	0.03	0.79	0.03	0.06	0.03
180	1.05	0.03	1.75	0.03	1.64	0.03	0.70	0.02	0.59	0.02	-0.11	0.02
181	0.97	0.02	1.81	0.02	1.82	0.02	0.83	0.02	0.85	0.02	0.02	0.02
182	1.16	0.02	2.06	0.02	2.14	0.02	0.90	0.02	0.98	0.02	0.09	0.02
183	1.06	0.02	1.83	0.02	2.18	0.02	0.77	0.02	1.12	0.02	0.35	0.02
184	1.09	0.02	1.82	0.02	2.14	0.02	0.73	0.02	1.05	0.02	0.32	0.02
185	1.31	0.03	1.99	0.03	1.96	0.03	0.68	0.02	0.65	0.02	-0.04	0.02
186	1.03	0.02	1.74	0.02	1.94	0.02	0.71	0.02	0.91	0.02	0.20	0.02
187	0.98	0.03	2.10	0.03	2.25	0.03	1.12	0.02	1.27	0.02	0.15	0.02
188	1.11	0.02	1.93	0.02	1.99	0.02	0.82	0.02	0.88	0.02	0.05	0.02
189	1.07	0.03	1.75	0.03	1.79	0.03	0.69	0.02	0.72	0.02	0.03	0.02
190	1.03	0.02	1.68	0.02	1.74	0.02	0.65	0.02	0.71	0.02	0.06	0.02
195	1.14	0.02	1.99	0.02	1.98	0.02	0.85	0.02	0.84	0.02	-0.01	0.02

LSBVCC	$u - g$	$u - g$ error	$u - i$	$u - i$ error	$u - z$	$u - z$ error	$g - i$	$g - i$ error	$g - z$	$g - z$ error	$i - z$	$i - z$ error
196	1.06	0.02	1.77	0.02	1.78	0.02	0.71	0.02	0.72	0.02	0.01	0.02
197	1.09	0.02	1.94	0.02	2.04	0.02	0.86	0.02	0.95	0.02	0.09	0.02
198	1.02	0.02	1.90	0.02	2.02	0.02	0.88	0.02	1.00	0.02	0.12	0.02
200	1.06	0.03	1.59	0.03	1.86	0.03	0.53	0.02	0.80	0.03	0.27	0.03
201	1.11	0.03	1.97	0.03	1.90	0.03	0.87	0.02	0.80	0.02	-0.07	0.02
202	1.17	0.02	2.04	0.02	2.14	0.02	0.87	0.02	0.97	0.02	0.10	0.02
208	0.78	0.03	1.52	0.03	1.73	0.03	0.74	0.02	0.95	0.02	0.20	0.02
225	1.04	0.03	1.80	0.03	1.86	0.03	0.76	0.02	0.82	0.02	0.05	0.02
226	1.19	0.02	1.94	0.02	1.51	0.02	0.75	0.02	0.32	0.02	-0.43	0.02
227	1.05	0.03	1.65	0.03	1.71	0.03	0.60	0.02	0.66	0.02	0.06	0.02
228	1.02	0.02	1.62	0.02	1.68	0.02	0.60	0.02	0.67	0.02	0.06	0.02
231	1.01	0.02	1.74	0.02	1.75	0.02	0.72	0.02	0.74	0.02	0.02	0.02
232	1.10	0.02	1.81	0.02	1.89	0.02	0.71	0.02	0.79	0.02	0.08	0.02
233	1.08	0.02	1.90	0.02	1.85	0.02	0.82	0.02	0.77	0.02	-0.05	0.02
234	1.26	0.03	2.24	0.02	2.27	0.02	0.98	0.02	1.01	0.02	0.03	0.02
235	1.03	0.02	1.86	0.02	1.84	0.02	0.83	0.02	0.81	0.02	-0.02	0.02
240	1.19	0.02	2.09	0.02	2.19	0.02	0.89	0.02	0.99	0.02	0.10	0.02
247	1.20	0.03	2.20	0.03	2.52	0.03	1.01	0.02	1.32	0.02	0.31	0.02
274	1.15	0.02	1.66	0.02	1.74	0.03	0.51	0.02	0.58	0.02	0.08	0.02
277	0.89	0.02	1.43	0.02	1.47	0.02	0.54	0.02	0.58	0.02	0.04	0.02
278	1.10	0.02	1.96	0.02	1.97	0.02	0.86	0.02	0.87	0.02	0.01	0.02
279	1.04	0.02	1.74	0.02	1.88	0.02	0.69	0.02	0.84	0.02	0.15	0.02
280	1.08	0.02	1.87	0.02	1.89	0.02	0.79	0.02	0.81	0.02	0.01	0.02
281	1.09	0.02	1.88	0.02	1.81	0.02	0.78	0.02	0.71	0.02	-0.07	0.02
282	1.07	0.03	1.79	0.02	1.76	0.03	0.73	0.02	0.69	0.02	-0.03	0.02
284	1.06	0.02	1.81	0.02	1.98	0.02	0.75	0.02	0.92	0.02	0.17	0.02
285	1.09	0.02	1.85	0.02	1.92	0.02	0.76	0.02	0.83	0.02	0.06	0.02
286	1.04	0.04	2.15	0.04	2.23	0.04	1.12	0.03	1.19	0.03	0.08	0.03
287	0.97	0.03	1.74	0.03	1.82	0.03	0.77	0.02	0.85	0.02	0.08	0.02
288	0.99	0.03	1.49	0.03	1.81	0.03	0.50	0.03	0.83	0.03	0.32	0.03
289	1.04	0.02	1.59	0.02	1.86	0.02	0.55	0.02	0.82	0.02	0.27	0.02
290	1.16	0.03	2.32	0.03	2.51	0.03	1.15	0.02	1.35	0.02	0.20	0.02
291	1.37	0.02	3.13	0.02	3.47	0.02	1.76	0.02	2.10	0.02	0.34	0.02
292	1.17	0.05	1.73	0.05	2.12	0.05	0.55	0.03	0.95	0.03	0.39	0.03
293	1.02	0.02	1.65	0.02	1.88	0.02	0.63	0.02	0.86	0.02	0.23	0.02
294	0.95	0.03	1.52	0.03	1.71	0.03	0.57	0.02	0.76	0.03	0.19	0.02
295	1.51	0.02	2.09	0.02	2.28	0.02	0.58	0.02	0.76	0.02	0.18	0.02
296	1.18	0.03	2.00	0.03	1.98	0.03	0.82	0.03	0.80	0.03	-0.01	0.03
297	1.07	0.02	1.84	0.02	2.03	0.02	0.77	0.02	0.96	0.02	0.19	0.02
298	0.90	0.03	1.55	0.03	1.74	0.03	0.65	0.02	0.83	0.03	0.18	0.03
299	1.05	0.02	1.62	0.02	1.74	0.02	0.56	0.02	0.69	0.02	0.13	0.02

LSBVCC	$u - g$	$u - g$ error	$u - i$	$u - i$ error	$u - z$	$u - z$ error	$g - i$	$g - i$ error	$g - z$	$g - z$ error	$i - z$	$i - z$ error
300	1.11	0.02	1.92	0.02	2.03	0.02	0.81	0.02	0.92	0.02	0.11	0.02
301	1.13	0.03	1.67	0.03	1.89	0.03	0.54	0.02	0.76	0.02	0.21	0.02
302	1.10	0.02	1.94	0.02	2.03	0.02	0.84	0.02	0.93	0.02	0.09	0.02
303	1.25	0.02	2.86	0.02	3.37	0.02	1.61	0.02	2.12	0.02	0.51	0.02
304	1.03	0.03	1.85	0.03	1.85	0.03	0.82	0.02	0.82	0.02	0.00	0.02
305	1.11	0.02	1.86	0.02	1.87	0.02	0.76	0.02	0.76	0.02	0.00	0.02
306	0.86	0.03	1.76	0.03	1.85	0.04	0.90	0.03	0.99	0.03	0.09	0.03
307	0.85	0.05	1.51	0.05	1.90	0.05	0.67	0.04	1.05	0.04	0.39	0.04
308	1.04	0.03	1.86	0.03	2.11	0.03	0.82	0.02	1.07	0.03	0.26	0.02
309	0.96	0.03	1.59	0.03	1.55	0.04	0.64	0.03	0.59	0.04	-0.05	0.04
310	0.99	0.03	1.62	0.02	1.98	0.03	0.63	0.02	0.99	0.02	0.36	0.02
311	1.26	0.02	2.14	0.02	2.16	0.02	0.89	0.02	0.91	0.02	0.02	0.02
312	1.03	0.02	1.83	0.02	2.02	0.02	0.80	0.02	0.99	0.02	0.19	0.02
313	1.15	0.03	1.90	0.03	1.75	0.03	0.75	0.02	0.60	0.02	-0.15	0.02
314	1.09	0.03	1.62	0.03	1.82	0.03	0.53	0.02	0.74	0.02	0.20	0.02
315	1.29	0.02	2.08	0.02	2.03	0.02	0.79	0.02	0.75	0.02	-0.04	0.02
316	1.19	0.03	1.84	0.03	1.88	0.03	0.65	0.02	0.68	0.02	0.03	0.02
318	1.04	0.03	1.66	0.03	1.53	0.04	0.62	0.02	0.49	0.03	-0.13	0.03
319	0.94	0.03	1.67	0.03	1.70	0.03	0.73	0.02	0.77	0.02	0.03	0.02
320	1.04	0.02	1.88	0.02	1.87	0.03	0.84	0.02	0.83	0.02	-0.01	0.02
321	1.05	0.02	1.85	0.02	1.89	0.02	0.81	0.02	0.84	0.02	0.04	0.02
322	1.09	0.03	1.75	0.03	1.70	0.03	0.66	0.02	0.61	0.02	-0.06	0.02
323	1.32	0.02	2.21	0.02	2.38	0.02	0.89	0.02	1.06	0.02	0.17	0.02
324	1.08	0.03	1.87	0.03	1.91	0.03	0.79	0.02	0.83	0.02	0.04	0.02
325	1.28	0.02	2.12	0.02	2.14	0.02	0.85	0.02	0.87	0.02	0.02	0.02
326	1.17	0.03	2.02	0.03	2.07	0.03	0.84	0.02	0.89	0.02	0.05	0.02
327	1.08	0.02	1.94	0.02	1.83	0.02	0.86	0.02	0.75	0.02	-0.10	0.02
328	0.98	0.02	1.72	0.02	1.83	0.02	0.74	0.02	0.86	0.02	0.12	0.02
329	0.99	0.02	1.72	0.02	1.78	0.02	0.73	0.02	0.79	0.02	0.06	0.02
330	1.05	0.02	1.81	0.02	1.86	0.02	0.76	0.02	0.81	0.02	0.05	0.02
331	1.02	0.03	1.77	0.03	1.83	0.03	0.75	0.02	0.80	0.02	0.06	0.02
357	0.92	0.03	1.51	0.03	1.94	0.03	0.59	0.02	1.02	0.03	0.43	0.02
358	0.95	0.03	1.76	0.03	1.80	0.03	0.81	0.02	0.85	0.02	0.04	0.02
359	1.41	0.02	2.37	0.02	2.50	0.02	0.97	0.02	1.09	0.02	0.13	0.02
360	1.12	0.02	1.98	0.02	2.16	0.02	0.86	0.02	1.04	0.02	0.18	0.02
361	1.08	0.03	1.76	0.02	1.85	0.03	0.68	0.02	0.77	0.02	0.09	0.02
390	1.03	0.03	1.83	0.03	1.69	0.03	0.79	0.02	0.66	0.02	-0.13	0.02
394	1.06	0.02	1.81	0.02	1.95	0.02	0.75	0.02	0.89	0.02	0.14	0.02
395	1.16	0.03	1.93	0.03	1.70	0.03	0.77	0.02	0.54	0.02	-0.23	0.02
397	1.09	0.03	1.73	0.03	1.90	0.03	0.64	0.02	0.81	0.02	0.17	0.02
398	1.19	0.02	1.96	0.02	2.09	0.02	0.77	0.02	0.90	0.02	0.13	0.02

LSBVCC	$u - g$	$u - g$ error	$u - i$	$u - i$ error	$u - z$	$u - z$ error	$g - i$	$g - i$ error	$g - z$	$g - z$ error	$i - z$	$i - z$ error
399	0.91	0.03	1.61	0.03	1.84	0.03	0.71	0.03	0.94	0.03	0.23	0.03
401	1.08	0.03	1.86	0.03	2.09	0.03	0.79	0.02	1.02	0.02	0.23	0.02
402	1.03	0.03	1.66	0.03	1.88	0.03	0.62	0.02	0.85	0.02	0.23	0.02
403	1.03	0.03	1.87	0.03	1.96	0.03	0.84	0.02	0.93	0.02	0.09	0.02
404	1.05	0.02	1.84	0.02	1.96	0.02	0.79	0.02	0.91	0.02	0.12	0.02
405	1.27	0.04	2.30	0.04	2.29	0.04	1.03	0.02	1.02	0.03	-0.01	0.03
406	1.00	0.02	1.66	0.02	1.82	0.02	0.66	0.02	0.83	0.02	0.17	0.02
407	0.98	0.03	1.86	0.03	2.10	0.03	0.88	0.02	1.12	0.02	0.24	0.02
409	0.77	0.03	1.63	0.03	1.85	0.03	0.87	0.02	1.08	0.02	0.22	0.02
411	0.76	0.03	1.99	0.02	2.11	0.02	1.23	0.02	1.35	0.02	0.11	0.02
412	1.06	0.03	1.99	0.02	2.06	0.03	0.93	0.02	1.00	0.02	0.07	0.02
413	0.95	0.03	1.56	0.03	1.58	0.03	0.61	0.02	0.63	0.03	0.01	0.03
414	1.06	0.03	1.68	0.03	1.94	0.03	0.62	0.03	0.88	0.03	0.26	0.03
415	1.05	0.04	1.56	0.04	1.49	0.05	0.50	0.03	0.44	0.04	-0.06	0.04
416	0.92	0.03	1.60	0.03	1.59	0.03	0.69	0.02	0.67	0.02	-0.01	0.02
429	1.10	0.03	1.71	0.03	1.67	0.03	0.60	0.02	0.57	0.02	-0.04	0.02
431	1.15	0.02	1.95	0.02	2.14	0.02	0.80	0.02	0.99	0.02	0.19	0.02
432	1.02	0.03	1.67	0.03	1.80	0.03	0.66	0.02	0.79	0.02	0.13	0.02
433	1.09	0.02	1.84	0.02	1.84	0.02	0.75	0.02	0.76	0.02	0.00	0.02
434	1.33	0.02	2.54	0.02	2.79	0.02	1.22	0.02	1.46	0.02	0.24	0.02
435	1.05	0.02	1.87	0.02	2.00	0.02	0.82	0.02	0.95	0.02	0.13	0.02
436	1.17	0.02	1.93	0.02	2.00	0.02	0.76	0.02	0.83	0.02	0.07	0.02
438	1.10	0.02	1.81	0.02	1.90	0.02	0.71	0.02	0.80	0.02	0.09	0.02
439	1.08	0.03	1.87	0.02	2.16	0.03	0.80	0.02	1.08	0.02	0.29	0.02
440	1.06	0.02	1.85	0.02	1.76	0.02	0.78	0.02	0.70	0.02	-0.09	0.02
441	1.05	0.02	1.92	0.02	1.99	0.02	0.87	0.02	0.94	0.02	0.07	0.02
442	0.98	0.03	1.65	0.03	1.98	0.03	0.67	0.02	1.00	0.02	0.33	0.02
443	1.07	0.03	1.81	0.02	1.93	0.03	0.73	0.02	0.86	0.02	0.12	0.02

TABLE 7.6 The LSBVCC number, radius measured at the 28 mag arcsec⁻² isophote in the g band, mean surface brightnesses within that radius in each band and errors on all surface brightnesses.

LSBVCC	rad28 g	sb28 u	sb28 u error	sb28 g	sb28 g error	sb28 i	sb28 i error	sb28 z	sb28 z error
001	27.96	26.73	0.04	25.97	0.04	25.56	0.04	24.95	0.04
002	45.93	27.05	0.03	26.65	0.03	25.92	0.03	25.67	0.03
003	25.96	27.34	0.05	26.58	0.04	26.07	0.04	25.79	0.04
005	39.94	27.33	0.03	26.53	0.03	25.62	0.03	25.58	0.03
006	41.94	26.89	0.03	26.18	0.03	25.35	0.03	25.51	0.03
007	17.97	27.79	0.06	27.42	0.06	26.59	0.06	26.43	0.06
008	27.96	27.28	0.04	26.57	0.04	26.01	0.04	25.86	0.04
009	23.97	27.07	0.05	26.36	0.05	25.79	0.05	25.55	0.05
010	33.95	26.84	0.04	26.15	0.03	25.68	0.03	25.60	0.03
024	23.97	27.69	0.05	26.94	0.05	26.33	0.05	26.39	0.05
025	21.97	27.64	0.05	26.98	0.05	26.44	0.05	26.30	0.05
026	21.97	27.64	0.06	27.37	0.05	26.41	0.05	26.33	0.05
027	17.97	27.38	0.06	26.84	0.06	26.24	0.06	26.00	0.06
029	25.96	27.22	0.05	26.30	0.04	26.00	0.04	25.86	0.04
030	13.98	27.81	0.08	27.34	0.08	26.52	0.08	26.04	0.08
031	19.97	27.37	0.06	26.97	0.06	26.36	0.06	26.53	0.06
032	37.95	27.46	0.03	26.87	0.03	26.04	0.03	25.92	0.03
033	21.97	26.38	0.05	25.74	0.05	25.23	0.05	25.13	0.05
038	25.96	26.41	0.05	25.65	0.04	25.18	0.04	24.98	0.04
039	17.97	27.63	0.06	27.00	0.06	26.59	0.06	26.36	0.06
040	41.94	27.06	0.03	26.58	0.03	26.11	0.03	25.96	0.03
041	41.94	26.48	0.03	26.20	0.03	25.32	0.03	25.13	0.03
042	23.97	26.99	0.05	26.07	0.05	25.36	0.05	25.15	0.05
043	23.97	27.48	0.05	26.99	0.05	25.90	0.05	25.81	0.05
045	19.97	27.41	0.06	26.54	0.06	25.94	0.06	25.71	0.06
046	19.97	27.48	0.06	26.97	0.06	26.24	0.06	26.29	0.06
047	27.96	27.09	0.04	26.50	0.04	25.78	0.04	25.85	0.04
048	21.97	27.48	0.05	27.05	0.05	26.56	0.05	26.25	0.05
049	23.97	26.57	0.05	26.05	0.05	25.47	0.05	25.14	0.05
050	19.97	27.38	0.06	26.46	0.06	25.96	0.06	26.22	0.06
051	31.95	27.41	0.04	26.85	0.04	26.30	0.04	26.16	0.04
053	25.96	27.60	0.05	26.92	0.04	26.07	0.04	25.73	0.04
054	45.93	26.61	0.03	26.13	0.03	25.79	0.03	25.50	0.03
055	27.96	26.91	0.04	26.00	0.04	25.34	0.04	25.14	0.04
056	35.95	27.15	0.04	26.48	0.03	26.03	0.03	25.47	0.03
057	37.95	27.05	0.03	26.57	0.03	25.79	0.03	25.55	0.03
058	17.97	27.50	0.06	27.04	0.06	26.49	0.06	26.21	0.06
059	15.98	27.33	0.07	26.80	0.07	26.27	0.07	26.15	0.07

LSBVCC	rad28 g	sb28 u	sb28 u error	sb28 g	sb28 g error	sb28 i	sb28 i error	sb28 z	sb28 z error
060	13.98	28.13	0.08	27.58	0.08	27.13	0.08	27.03	0.08
061	25.96	27.17	0.05	26.93	0.04	26.21	0.04	26.24	0.04
062	23.97	26.86	0.05	26.05	0.05	25.49	0.05	25.41	0.05
063	29.96	27.84	0.04	27.00	0.04	26.37	0.04	26.16	0.04
064	15.98	27.56	0.07	27.04	0.07	26.50	0.07	26.59	0.07
065	17.97	26.83	0.06	26.47	0.06	25.76	0.06	25.76	0.06
066	19.97	27.00	0.06	26.43	0.06	26.04	0.06	26.26	0.06
067	17.97	27.52	0.06	27.03	0.06	26.63	0.06	26.12	0.06
068	19.97	27.55	0.06	26.97	0.06	26.63	0.06	26.69	0.06
069	23.97	28.06	0.05	27.51	0.05	26.83	0.05	26.81	0.05
070	41.94	26.54	0.03	26.11	0.03	25.84	0.03	25.58	0.03
071	19.97	27.09	0.06	26.61	0.06	26.21	0.06	25.91	0.06
072	17.97	27.58	0.06	27.07	0.06	26.53	0.06	26.54	0.06
073	19.97	27.34	0.06	26.64	0.06	26.22	0.06	26.28	0.06
074	49.93	26.93	0.03	26.72	0.03	26.15	0.03	25.99	0.03
076	27.96	27.78	0.04	27.11	0.04	26.74	0.04	26.58	0.04
077	19.97	27.52	0.06	26.87	0.06	26.12	0.06	26.19	0.06
079	19.97	28.08	0.06	27.21	0.06	26.81	0.06	26.82	0.06
080	15.98	27.34	0.07	26.95	0.07	26.39	0.07	26.51	0.07
081	25.96	26.51	0.05	26.14	0.04	25.35	0.04	25.24	0.04
082	25.96	27.40	0.05	26.57	0.04	26.06	0.04	25.97	0.04
083	15.98	27.50	0.07	27.14	0.07	26.71	0.07	26.70	0.07
084	21.97	26.91	0.05	26.05	0.05	25.92	0.05	25.29	0.05
085	21.97	27.32	0.05	26.61	0.05	26.21	0.05	25.88	0.05
086	31.95	27.74	0.04	27.23	0.04	26.72	0.04	26.63	0.04
087	19.97	26.95	0.06	26.20	0.06	25.64	0.06	25.46	0.06
088	19.97	27.44	0.06	26.85	0.06	26.31	0.06	26.15	0.06
089	47.93	27.23	0.03	26.67	0.03	25.97	0.03	25.82	0.03
090	19.97	27.65	0.06	27.48	0.06	26.79	0.06	27.12	0.06
091	15.98	27.57	0.07	26.91	0.07	26.54	0.07	26.46	0.07
092	31.95	27.13	0.04	26.54	0.04	26.03	0.04	25.94	0.04
093	15.98	27.38	0.07	27.26	0.07	26.76	0.07	26.97	0.07
094	29.96	27.09	0.04	26.58	0.04	25.95	0.04	25.72	0.04
095	21.97	27.49	0.05	27.06	0.05	26.39	0.05	26.01	0.05
099	15.98	27.19	0.07	26.54	0.07	26.36	0.07	26.08	0.07
100	11.98	27.89	0.10	27.41	0.09	26.15	0.09	26.79	0.10
101	29.96	26.86	0.04	26.38	0.04	26.23	0.04	25.59	0.04
102	21.97	27.27	0.05	26.75	0.05	26.24	0.05	26.19	0.05
103	19.97	27.94	0.06	27.38	0.06	26.88	0.06	26.91	0.06
104	17.97	27.22	0.06	26.89	0.06	26.07	0.06	26.14	0.06
105	31.95	26.21	0.04	25.66	0.04	25.22	0.04	25.02	0.04

LSBVCC	rad28 g	sb28 u	sb28 u error	sb28 g	sb28 g error	sb28 i	sb28 i error	sb28 z	sb28 z error
106	29.96	27.28	0.04	26.43	0.04	26.12	0.04	25.57	0.04
107	19.97	27.80	0.06	27.39	0.06	27.24	0.06	27.01	0.06
108	29.96	26.73	0.04	25.94	0.04	25.29	0.04	25.16	0.04
109	25.96	26.85	0.05	26.29	0.04	25.73	0.04	25.63	0.04
110	13.98	27.59	0.08	27.27	0.08	26.65	0.08	26.73	0.08
111	33.95	26.62	0.04	26.03	0.03	25.40	0.03	25.40	0.03
117	31.95	26.36	0.04	25.62	0.04	24.93	0.04	24.68	0.04
118	19.97	27.53	0.06	27.05	0.06	26.34	0.06	26.44	0.06
129	13.98	27.50	0.08	27.09	0.08	27.16	0.08	27.14	0.08
151	23.97	27.81	0.05	27.40	0.05	26.37	0.05	26.24	0.05
152	19.97	26.31	0.06	25.93	0.06	25.91	0.06	25.68	0.06
153	19.97	27.22	0.06	26.29	0.06	25.36	0.06	25.25	0.06
154	23.97	27.33	0.05	26.71	0.05	26.18	0.05	25.74	0.05
156	39.94	26.38	0.03	25.69	0.03	25.13	0.03	24.97	0.03
157	19.97	27.62	0.06	27.22	0.06	26.68	0.06	26.49	0.06
158	33.95	27.11	0.04	26.28	0.03	25.82	0.03	25.49	0.03
159	23.97	27.07	0.05	26.52	0.05	26.23	0.05	26.10	0.05
161	15.98	27.82	0.07	27.21	0.07	26.57	0.07	26.56	0.07
167	23.97	26.59	0.05	25.91	0.05	24.54	0.05	23.80	0.05
168	19.97	27.28	0.06	26.74	0.06	26.17	0.06	26.47	0.06
169	21.97	26.87	0.05	26.14	0.05	25.47	0.05	25.32	0.05
170	29.96	27.40	0.04	26.89	0.04	25.99	0.04	25.98	0.04
171	21.97	26.71	0.05	26.14	0.05	25.44	0.05	25.28	0.05
172	23.97	26.62	0.05	26.28	0.05	25.90	0.05	25.76	0.05
173	21.97	27.63	0.05	27.17	0.05	26.62	0.05	26.60	0.05
174	15.98	27.73	0.07	27.38	0.07	26.40	0.07	26.62	0.07
175	31.95	26.91	0.04	25.96	0.04	25.20	0.04	25.15	0.04
176	19.97	28.09	0.06	27.62	0.06	26.98	0.06	26.84	0.06
177	21.97	26.34	0.05	25.79	0.05	25.50	0.05	25.43	0.05
178	27.96	27.12	0.04	26.40	0.04	25.98	0.04	25.72	0.04
179	15.98	28.36	0.07	27.44	0.07	25.83	0.07	25.42	0.07
180	17.97	27.22	0.06	26.62	0.06	26.11	0.06	25.75	0.06
181	21.97	27.07	0.05	26.47	0.05	25.92	0.05	26.05	0.05
182	25.96	26.82	0.05	26.15	0.04	25.52	0.04	25.67	0.04
183	25.96	27.12	0.05	26.35	0.04	25.72	0.04	25.82	0.04
184	39.94	26.54	0.03	25.66	0.03	25.12	0.03	24.97	0.03
185	25.96	27.78	0.05	27.23	0.04	26.74	0.04	26.69	0.05
186	21.97	27.00	0.05	26.54	0.05	26.02	0.05	25.80	0.05
187	21.97	27.23	0.05	26.85	0.05	26.47	0.05	26.00	0.05
188	23.97	26.53	0.05	25.79	0.05	25.26	0.05	25.23	0.05
189	17.97	27.02	0.06	26.63	0.06	25.94	0.06	26.13	0.06

LSBVCC	rad28 g	sb28 u	sb28 u error	sb28 g	sb28 g error	sb28 i	sb28 i error	sb28 z	sb28 z error
190	19.97	27.39	0.06	26.57	0.06	25.91	0.06	25.86	0.06
195	25.96	27.24	0.05	26.56	0.04	26.05	0.04	25.71	0.04
196	17.97	26.98	0.06	26.34	0.06	26.01	0.06	25.62	0.06
197	39.94	26.30	0.03	25.53	0.03	24.94	0.03	24.86	0.03
198	23.97	26.91	0.05	26.38	0.05	25.78	0.05	25.67	0.05
200	17.97	27.84	0.07	27.30	0.06	26.91	0.06	27.06	0.06
201	17.97	27.03	0.06	26.63	0.06	25.95	0.06	25.58	0.06
202	45.93	26.27	0.03	25.58	0.03	24.88	0.03	24.70	0.03
208	15.98	27.00	0.07	26.71	0.07	26.17	0.07	26.32	0.07
225	13.98	27.70	0.08	27.11	0.08	26.57	0.08	26.51	0.08
226	33.95	27.09	0.04	26.43	0.04	25.94	0.03	25.82	0.04
227	19.97	27.96	0.06	27.27	0.06	26.84	0.06	26.66	0.06
228	27.96	26.37	0.04	26.00	0.04	25.52	0.04	25.47	0.04
231	33.95	27.03	0.04	26.36	0.04	25.98	0.03	25.98	0.04
232	21.97	27.03	0.05	26.30	0.05	25.77	0.05	25.68	0.05
233	31.95	26.47	0.04	25.96	0.04	25.37	0.04	24.74	0.04
234	27.96	27.31	0.04	26.69	0.04	25.70	0.04	25.68	0.04
235	25.96	26.76	0.05	26.33	0.04	25.64	0.04	25.52	0.04
240	41.94	27.03	0.03	26.49	0.03	25.90	0.03	25.89	0.03
247	17.97	28.23	0.07	27.23	0.06	26.87	0.06	26.86	0.06
274	21.97	26.99	0.05	26.42	0.05	26.06	0.05	25.62	0.05
277	25.96	27.69	0.05	25.88	0.04	25.49	0.04	25.30	0.04
278	53.92	26.60	0.03	26.07	0.02	25.20	0.02	24.83	0.02
279	19.97	26.61	0.06	25.78	0.06	25.44	0.06	25.56	0.06
280	19.97	26.58	0.06	25.92	0.06	25.48	0.06	24.89	0.06
281	35.95	26.59	0.04	25.86	0.03	25.37	0.03	25.02	0.03
282	25.96	27.69	0.05	27.16	0.04	26.72	0.04	26.47	0.05
284	25.96	26.77	0.05	26.20	0.04	25.96	0.04	25.76	0.04
285	25.96	26.27	0.05	25.70	0.04	25.47	0.04	25.02	0.04
286	15.98	27.75	0.07	27.56	0.07	26.58	0.07	26.33	0.07
287	13.98	27.45	0.08	26.95	0.08	26.43	0.08	26.36	0.08
288	13.98	27.89	0.08	27.43	0.08	26.91	0.08	26.59	0.08
289	29.96	26.91	0.04	26.25	0.04	25.69	0.04	25.66	0.04
290	15.98	27.83	0.07	27.20	0.07	26.90	0.07	26.73	0.07
291	27.96	27.13	0.04	26.33	0.04	24.71	0.04	24.50	0.04
292	9.99	28.11	0.12	27.44	0.11	27.40	0.11	26.39	0.11
293	17.97	26.88	0.06	26.29	0.06	26.04	0.06	25.92	0.06
294	13.98	27.55	0.08	27.06	0.08	26.47	0.08	26.30	0.08
295	35.95	27.17	0.04	26.34	0.03	25.85	0.03	25.56	0.03
296	15.98	27.57	0.07	27.06	0.07	26.68	0.07	26.72	0.07
297	35.95	27.05	0.04	26.29	0.03	25.93	0.03	25.85	0.03

LSBVCC	rad28 g	sb28 u	sb28 u error	sb28 g	sb28 g error	sb28 i	sb28 i error	sb28 z	sb28 z error
298	21.97	27.56	0.05	27.12	0.05	26.45	0.05	26.43	0.05
299	21.97	27.14	0.05	26.46	0.05	26.20	0.05	26.07	0.05
300	29.96	26.52	0.04	25.69	0.04	25.23	0.04	25.51	0.04
301	15.98	27.33	0.07	26.68	0.07	26.52	0.07	26.59	0.07
302	27.96	26.83	0.04	26.16	0.04	25.68	0.04	25.22	0.04
303	23.97	27.19	0.05	26.35	0.05	24.90	0.05	24.68	0.05
304	17.97	27.44	0.06	26.83	0.06	26.70	0.06	26.60	0.06
305	35.95	26.64	0.04	26.24	0.03	25.48	0.03	25.48	0.03
306	17.97	27.29	0.07	26.81	0.06	26.27	0.06	26.31	0.07
307	11.98	28.45	0.10	27.87	0.09	27.35	0.09	27.13	0.10
308	25.96	27.34	0.05	26.81	0.04	26.10	0.04	25.88	0.05
309	15.98	27.73	0.07	27.22	0.07	27.01	0.07	26.63	0.07
310	19.97	27.29	0.06	26.70	0.06	26.22	0.06	25.89	0.06
311	39.94	27.05	0.03	26.39	0.03	25.83	0.03	25.26	0.03
312	23.97	26.47	0.05	25.80	0.05	25.16	0.05	25.12	0.05
313	19.97	27.18	0.06	26.45	0.06	26.03	0.06	25.85	0.06
314	19.97	27.51	0.06	26.91	0.06	26.50	0.06	26.39	0.06
315	31.95	27.11	0.04	26.83	0.04	26.46	0.04	26.08	0.04
316	21.97	27.43	0.05	26.83	0.05	26.55	0.05	26.14	0.05
318	15.98	27.99	0.07	27.42	0.07	27.03	0.07	26.94	0.07
319	15.98	27.55	0.07	27.01	0.07	26.62	0.07	26.69	0.07
320	25.96	27.48	0.05	26.90	0.04	26.28	0.04	26.30	0.04
321	23.97	26.88	0.05	26.01	0.05	25.49	0.05	25.46	0.05
322	17.97	27.43	0.06	26.75	0.06	26.27	0.06	26.14	0.06
323	39.94	26.82	0.03	25.90	0.03	25.10	0.03	24.93	0.03
324	17.97	27.51	0.06	27.00	0.06	26.37	0.06	26.34	0.06
325	27.96	26.86	0.04	26.18	0.04	25.55	0.04	25.53	0.04
326	21.97	27.46	0.05	26.94	0.05	26.09	0.05	26.05	0.05
327	33.95	27.22	0.04	26.67	0.04	25.90	0.03	26.03	0.04
328	23.97	26.88	0.05	26.22	0.05	25.77	0.05	25.89	0.05
329	21.97	26.58	0.05	25.78	0.05	25.90	0.05	25.63	0.05
330	37.95	26.51	0.03	25.89	0.03	25.57	0.03	25.07	0.03
331	29.96	27.16	0.04	26.65	0.04	26.01	0.04	26.06	0.04
357	13.98	27.66	0.08	27.22	0.08	26.62	0.08	27.04	0.08
358	15.98	27.70	0.07	27.28	0.07	26.87	0.07	24.87	0.07
359	23.97	26.81	0.05	26.16	0.05	25.62	0.05	25.06	0.05
360	37.95	26.64	0.03	26.08	0.03	25.55	0.03	25.37	0.03
361	21.97	26.95	0.05	26.39	0.05	25.87	0.05	25.78	0.05
390	23.97	27.49	0.05	27.25	0.05	26.77	0.05	26.42	0.05
394	33.95	26.43	0.04	25.88	0.03	25.33	0.03	25.30	0.03
395	15.98	27.68	0.07	27.02	0.07	26.46	0.07	26.48	0.07

LSBVCC	rad28 g	sb28 u	sb28 u error	sb28 g	sb28 g error	sb28 i	sb28 i error	sb28 z	sb28 z error
397	19.97	27.27	0.06	26.56	0.06	26.09	0.06	25.95	0.06
398	35.95	26.55	0.04	25.84	0.03	25.36	0.03	25.14	0.03
399	23.97	27.82	0.05	27.34	0.05	26.91	0.05	26.88	0.05
401	35.95	28.43	0.04	27.62	0.03	26.97	0.03	26.87	0.03
402	15.98	27.47	0.07	26.97	0.07	26.33	0.07	26.35	0.07
403	17.97	27.77	0.07	27.29	0.06	26.78	0.06	26.78	0.06
404	17.97	26.70	0.06	26.14	0.06	25.55	0.06	25.44	0.06
405	17.97	28.27	0.07	27.75	0.06	26.96	0.06	27.01	0.06
406	25.96	27.16	0.05	26.55	0.04	26.26	0.04	26.07	0.04
407	21.97	27.71	0.05	27.27	0.05	26.74	0.05	26.50	0.05
409	15.98	27.79	0.07	27.35	0.07	26.69	0.07	26.47	0.07
411	21.97	27.50	0.05	26.92	0.05	26.30	0.05	25.77	0.05
412	23.97	27.22	0.05	27.06	0.05	26.54	0.05	26.19	0.05
413	19.97	27.46	0.06	26.87	0.06	26.41	0.06	26.23	0.06
414	13.98	27.98	0.08	27.52	0.08	26.88	0.08	26.62	0.08
415	9.99	27.96	0.11	27.43	0.11	27.18	0.11	26.88	0.11
416	15.98	27.82	0.07	27.13	0.07	26.79	0.07	26.45	0.07
429	25.96	27.43	0.05	27.16	0.04	26.70	0.04	26.83	0.05
431	25.96	26.70	0.05	26.05	0.04	25.38	0.04	26.22	0.04
432	15.98	27.38	0.07	26.78	0.07	26.31	0.07	26.21	0.07
433	47.93	26.78	0.03	26.28	0.03	25.66	0.03	25.43	0.03
434	25.96	26.82	0.05	25.94	0.04	24.87	0.04	24.64	0.04
435	37.95	26.56	0.03	25.92	0.03	25.28	0.03	25.06	0.03
436	33.95	26.48	0.04	25.98	0.03	25.33	0.03	25.02	0.03
438	27.96	26.69	0.04	26.33	0.04	25.84	0.04	25.83	0.04
439	15.98	27.18	0.07	26.35	0.07	25.77	0.07	25.50	0.07
440	21.97	27.25	0.05	26.53	0.05	26.38	0.05	25.84	0.05
441	21.97	26.80	0.05	26.13	0.05	25.57	0.05	25.51	0.05
442	29.96	27.44	0.04	27.15	0.04	26.74	0.04	26.52	0.04
443	21.97	27.35	0.05	26.65	0.05	26.08	0.05	26.00	0.05

'She says nothing at all, but simply stares upward into the dark sky and watches, with sad eyes, the slow dance of the infinite stars.'

NEIL GAIMAN, STARDUST